Gravity based foundations for offshore wind turbines

Cyclic loading and liquefaction

M.J.P. van Wijngaarden

TU Delft
NUS National University of Singapore
Deltares Enabling Delta Life

Source of cover image: `http://www.baminnovation.eu/` (December 20th, 2016)

Gravity based foundations for offshore wind turbines

Cyclic loading and liquefaction

by

M.J.P. van Wijngaarden

To obtain the degree of Master of Science in

Hydraulic Engineering and Water Resources Management

at Delft University of Technology and National University of Singapore

To be defended on January 11, 2017 at 9:00 AM in Delft, The Netherlands.

Thesis committee:	Prof. dr. K.G. Gavin	Delft University of Technology
	ir. R. R. de Jager	Delft University of Technology/Boskalis
	ir. T. C. Raaijmakers	Delft University of Technology/Deltares
	dr. ir. P. Meijers	Deltares
	prof. dr. C. F. Leung	National University of Singapore

An electronic version of this thesis is available at `http://repository.tudelft.nl/`.

Preface

This thesis is the final part to obtain my Master of Science degree in Hydraulic Engineering and Water Resources Management, at Delft University of Technology and at the National University of Singapore. In this research the civil engineering fields of structural engineering and hydrodynamics are combined with soil mechanics. Bridging the gaps between different topics made my graduation work very diverse, but it especially gave me more insight into how a civil engineer should combine different disciplines. Although it is not possible to study each discipline to the same level, the civil engineer should know to which level the discipline needs to be studied to finally add a new piece of understanding to the scientific community. This will also be necessary when one is looking for the integrated understanding of a gravity based foundation for the offshore wind industry, in which turbine, support structure and foundation all need to be taken into account to come up with a competitive design.

I would like to thank all members of my graduation committee, but first of all Deltares to offer this graduation position at the Geo-unit. Furthermore I would like to thank Ken for chairing the committee, Richard for his input on liquefaction analysis and Tim for his input in the hydrodynamics and the developments of gravity based foundations for offshore wind turbines. And then in particular Piet, you have shown me how to apply your expertise on various topics, whether it's about cyclic loading from earthquakes, from vibratory sheet piling or from wave loads on an offshore structure, you know how to translate the problem back to its basics. I really appreciated your guidance in my work and especially the hint to stick to the main questions. Finally I would like to thank prof. Leung for representing the National University of Singapore in the committee.

Martijn van Wijngaarden
Delft, December 2016

Summary

The enormous development of the offshore wind industry has resulted in norms and regulations for the foundation design of offshore wind turbines. A rather large amount of knowledge has been gained on the static stability, while the relation between cyclic loads from wind, waves and turbine and the soil response receives less attention. The risk of losing stability due to partial liquefaction asks for a procedure to take multiple cyclic loads into account. In this thesis the cyclic loading on a gravity based foundation for an offshore wind turbine is investigated. The focus is on pore pressure developments under cyclic loading in storm conditions in homogeneous medium to dense sand.

The main processes in cyclically loaded sand are the generation and dissipation of excess pore pressures during a storm. Drainage results in a volume decrease and densification of the soil deposit. The latter phenomenon increases the resistance for further pore pressure generation. Finally, the process of preshearing or the history effect represents the changing soil structure during cyclic loading, which is found to be present in partially drained conditions. This effect is an addition to the strengthening of the soil due to densification.

Based on existing modelling approaches of cyclic loading of sand, it is found that both the irregular nature of the cyclic loads and the real development of a storm should be taken into account in the calculations of excess pore pressures. A group of load cycles with a high frequency and a large amplitude may result in significant pore pressure build-up. The amount largely depends on the moment in time when the load cycles are transferred to the seabed, since this determines the already obtained densification and the generated pore pressure in the soil. However, for most models and methods described in literature it is still necessary to translate the irregular load cycles into discretized sequences with equal amplitude, where the irregular nature and the real development of a storm are lost.

The previously mentioned soil processes of pore pressure generation, dissipation and preshearing are implemented in the in-house model DCycle of Deltares. This is a 1D-model extended with radial drainage to model the dissipation below a circular gravity based foundation. Furthermore, the program is capable of taking any irregular load time history into account. It is therefore suitable to take the irregular nature of the loads into account and has been used in this research.

A reference geometry of a 30 meter diameter gravity based foundation and offshore wind turbine has been defined for a water depth of 30 meter. The wind loads, wave loads and turbine loads are derived in the frequency domain for this geometry. By using a random phase-amplitude model it is possible to generate a large number of irregular load histories in the time domain. With this approach the irregular nature of the loads is taken into account, and using the CoastDat database (Weisse et al. (2005)) the real storm build-up at the reference location (Blyth, UK) is taken into account.

The largest liquefaction potential is found just outside the circular base area of the gravity based foundation, by using various definitions of the cyclic shear stress ratio in a FEM-calculation of a single extreme load cycle. In the areas around the edges of the structure, the cyclic shear stress amplitudes are still high while the initial effective stresses are significantly lower than below the GBF. This results in the largest cyclic shear stress ratios and therefore the largest liquefaction potential. The results have been used as input for DCycle.

The pore pressure developments below the reference geometry of the gravity based foundation have been assessed in DCycle for homogeneous sand with a relative density of 60%. The results show that the maximum excess pore pressure is found in the first storm in the load history, due to the significant densification, drainage and preshearing in the build-up of the first storm. Based on selected storms from the dataset, it was found that the storms with the largest cyclic load amplitude in the storm do not produce the largest excess pore pressures. Instead, the storms with the fastest build-up in terms of increasing cyclic load amplitude per unit of time result in the largest excess pore pressures. A faster build-up limits the processes of drainage, densification and preshearing, resulting in the maximum excess pore pressures.

For the same sand deposit loaded by the storm with the fastest build-up the maximum values of relative excess pore pressures are on average reached about one hour before the maximum cyclic load amplitudes in the storm. This is based on 200 irregular load histories of the storm. 90% of the maximum relative excess pore pressures are below 0.36. The 90% value of relative excess pore pressure reduces to 0.17 at the moment of the maximum cyclic load amplitude in the storm. For less permeable sands larger relative excess pore pressures are found, but the maximum excess pore pressure is on average reached before the maximum cyclic load amplitude in the storm. This shows that even for less permeable sands the effects of drainage and densification in the build-up of a storm are very significant, preventing full liquefaction and resulting in a maximum relative excess pore pressure before the maximum load amplitude. The results show a significant spread in the obtained maximum values of relative excess pore pressures due to the irregular load histories, indicating that multiple load histories should be taken into account to obtain a reliable pore pressure estimate.

The results of excess pore pressures should be validated with laboratory tests to see whether the predicted pore pressures compare well with measured values. This asks for a test which implements continuous drainage and in which also the cyclic load build-up based on a storm can be followed. Furthermore, field measurements should provide another way to validate the model results. In addition to a validation, a probabilistic approach is recommended to relate the probability distributions of maximum values of excess pore pressures with the probability density function of the cyclic load amplitudes. Together with a stability assessment this should be related to a failure probability, which can be linked to requirements in norms and standards.

Contents

Preface iii

Summary v

List of Figures xv

List of Tables xxi

1 Introduction 1

1.1 Motivation of the research . . . 1
1.2 Problem description . . . 3
1.3 Research objectives & questions . . . 5
1.4 Research methodology . . . 6
1.5 Restrictions . . . 6
1.6 Outline of the report . . . 7

2 Behaviour of sand under cyclic loading 9

2.1 Introduction . . . 9
2.2 Deformation of sands . . . 9
2.2.1 Contraction and dilation . . . 9
2.2.2 The critical state . . . 11
2.2.3 Undrained behaviour and consolidation . . . 11
2.2.4 Cyclic loading . . . 12
2.2.5 Asymmetric cyclic loading . . . 14
2.2.6 Preshearing . . . 15
2.3 Liquefaction . . . 17
2.3.1 Definition . . . 17
2.3.2 Excess pore pressures . . . 17
2.3.3 Liquefaction failure types . . . 19
2.4 Liquefaction of a horizontal seabed . . . 20
2.5 Liquefaction of marine structures . . . 24
2.5.1 Ekofisk Tank . . . 24
2.5.2 Wave loaded caisson . . . 25
2.5.3 Measures to reduce liquefaction potential . . . 28
2.6 Concluding remarks . . . 29

3 Modelling cyclic loading of sands 31

3.1 Introduction . . . 31
3.2 Challenges in modelling . . . 32
3.3 Seed and Rahman model . . . 34
3.3.1 Cyclic shear stress profile . . . 34
3.3.2 Pore pressure generation . . . 35
3.3.3 Assumptions and limitations . . . 36
3.3.4 The effect of a random wave field . . . 37
3.4 DCycle model . . . 38
3.4.1 Model description . . . 38
3.4.2 Preshearing . . . 41
3.4.3 The effect of a random wave field . . . 43
3.5 Other approaches . . . 45
3.5.1 API Standard . . . 45
3.5.2 DNV Standard . . . 45
3.5.3 NGI . . . 46

3.6 Concluding remarks 48

4 Reference case **51**
4.1 Introduction 51
4.2 Support structures for offshore wind turbines. 51
4.2.1 General concepts 51
4.2.2 Gravity based foundations 53
4.3 Reference case 53
4.3.1 Gravity based foundation 53
4.3.2 Offshore wind turbine 54
4.3.3 Soil conditions 54
4.3.4 Additional data 56

5 Load analysis **59**
5.1 Introduction 59
5.2 Load analysis 59
5.2.1 Loads: stochastic processes 61
5.2.2 Wind loads 64
5.2.3 Wave loads 68
5.2.4 Turbine loads 74
5.2.5 Current loads 76
5.2.6 Dynamic amplification 76
5.3 Final spectra 80
5.4 Verification 83
5.5 Reference case 84
5.6 Assumptions and limitations 87
5.7 Concluding remarks 89

6 Cyclic shear stress profile **91**
6.1 Introduction 91
6.2 CSSR-Definitions 91
6.3 Schematisation of the GBF 93
6.3.1 Load stages 95
6.4 Schematisation of the loads 95
6.5 Plaxis model 97
6.5.1 Model parameters 97
6.5.2 Model results 99
6.5.3 Model verification 101
6.5.4 Load contributions. 102
6.6 Assumptions and limitations 102
6.7 Concluding remarks 103

7 Excess pore pressures **105**
7.1 Introduction 105
7.2 General approach 105
7.3 DCycle input 107
7.3.1 Soil data 107
7.3.2 Loads at seabed level. 108
7.3.3 Storm definition 108
7.4 Results 109
7.4.1 Storm input 109
7.4.2 Threshold level. 112
7.4.3 Irregular load histories 113
7.5 Sensitivity study. 116
7.5.1 Preshear value 116
7.5.2 Gravel bed 119
7.5.3 Silt layer 120
7.6 Validation of the method 122

7.7 Assumptions and limitations . . . 125
7.8 Concluding remarks . . . 125

8 Conclusions, discussion and recommendations 127

8.1 Conclusions. . . . 127
8.1.1 Main research question . . . 127
8.1.2 Sub question 1 . . . 128
8.1.3 Sub question 2 . . . 128
8.1.4 Sub question 3 . . . 129
8.2 Discussion . . . 129
8.3 Recommendations . . . 131

Bibliography 135

A Appendix A: Multiple storms 139

A.1 Multiple storms . . . 139

B Appendix B: Model of Seed & Rahman 143

B.1 Model of Seed & Rahman . . . 143

List of Abbreviations

AAF	Aerodynamic Admittance Factor
BEM	Blade Element Momentum theory
CSSR	Cyclic Shear Stress Ratio
DNV	Det Norske Veritas
EPP	Excess Pore Pressure
FEM	Finite Element Model
FFT	Fast Fourier Transform
GBF	Gravity Based Foundation
HAT	Highest Astronomical Tide
HCA	High Cycle Accumulation model
IEC	International Electrotechnical Commission
IFFT	Inverse Fast Fourier Transform
MSL	Mean Sea Level
NGI	Norwegian Geotechnical Institute
OWT	Offshore Wind Turbine
PDF	Probability Density Function
PSD	Power Spectral Density
TRF	Transfer Response Function

Nomenclature

α	generalised Phillips' constant in JONSWAP spectrum	$[-]$
α_i	amplitude of wave signal i	$[m]$
$\bar{S}_{uu}$	normalized Kaimal spectrum of horizontal wind speeds	$[1/Hz]$
$\bar{S}_{ww}$	normalised JONSWAP spectrum	$[1/Hz]$
$\bar{U}$	10 minute averaged wind speed at 10 meter height	$[m/s]$
β	compressibility of water	$[-]$
β	relative pore pressure generation per cycle	$[kPa/cycle]$
$\Delta\sigma_d$	amplitude deviator stress	$[kPa]$
$\Delta\sigma_m$	amplitude in mean total stress	$[kPa]$
$\Delta\tau_{max}$	shear stress amplitude in maximum load cycle	$[kPa]$
$\Delta\tau_{xy}$	double amplitude of Cartesian shear stress	$[kPa]$
ΔF	load amplitude	$[N]$
ΔF_{max}	load amplitude in maximum load cycle	$[N]$
Δn	change in porosity	$[-]$
Δt	time step for numerical integration	$[s]$
ΔV	volume change due to drainage	$[m^3]$
Δz	vertical step for numerical integration	$[m]$
$\Delta\tau$	shear stress amplitude	$[kPa]$
ϵ_{vol}	volumetric strain	$[-]$
η	water level elevation	$[s]$
γ	peak enhancement factor in JONSWAP spectrum	$[-]$
γ	shear strain	$[-]$
γ_w	volumetric weight of water	$[kN/m^3]$
$\gamma_s^{'}$	effective volumetric weight of soil	$[kN/m^3]$
κ	Von Karman constant: 0.4	$[-]$
κ	intrinsic permeability	$[m^2]$
λ	wave length	$[m]$

ν	kinematic viscosity	$[m^2/s]$
ω	radial wave frequency	$[rad/s]$
ϕ_i	phase of frequency component i	$[rad]$
ψ	angle of dilation	[degrees]
ρ	density of air	$[kg/m^3]$
ρ_w	water density	$[kg/m^3]$
σ'_{v0}	initial vertical effective stress	$[kPa]$
σ_u	standard deviation of mean wind speed	$[m/s]$
σ'_x	horizontal effective stress	$[kPa]$
σ'_z	vertical effective stress	$[kPa]$
$\sigma'_{v,av}$	average vertical effective stress	$[kPa]$
$\sigma'_{v,max}$	maximum vertical effective stress	$[kPa]$
$\sigma'_{v,min}$	minimum vertical effective stress	$[kPa]$
σ'_v	vertical effective stress	$[kPa]$
τ	shear stress	$[kPa]$
$\tau_{xy,max}$	maximum Cartesian shear stress	$[kPa]$
$\tau_{xy,min}$	minimum Cartesian shear stress	$[kPa]$
τ_{xz}	shear stress on xz plane	$[kPa]$
θ	the rate of pore pressure increase in Seed&Rahman formula	$[-]$
ζ	ratio of actual damping versus critical damping	$[-]$
A	pore pressure generation term without preshearing and without drainage	$[kPa/s]$
A	rotor swept area	$[m^2]$
a, b	empirical constants for pore pressure generation	$[-]$
A_c	Charnock's constant, 0.011 for open seas and 0.034 for near-shore locations	$[-]$
A_q, B_q	Fourier coefficients	$[-]$
A_{plate}	surface area of base plate	$[m^2]$
A_{pp}	first empirical pore pressure generation coefficient	$[-]$
B_{pp}	second empirical pore pressure generation coefficient	$[-]$
c	coefficient of Kozeny-Carman	$[-]$
C_d	drag coefficient	$[-]$
c_l	lateral damping coefficient	$[Ns/m]$
C_m	inertia coefficient	$[-]$
c_r	rotational damping coefficient	$[Ns]$
C_T	thrust coefficient	$[-]$
c_v	consolidation coefficient	$[m^2/s]$
c_{corr}	correction factor for irregular waves	$[-]$
$CSSR$	cyclic shear stress ratio	$[-]$
D	dilatancy parameter	$[-]$
d	water depth	$[m]$
D_p	pile diameter	$[m]$
D_t	tower diameter	$[m]$
d_{grain}	grain size	$[m]$
D_{rotor}	rotor diameter	$[m]$
DAF	dynamic amplification factor	$[-]$
e	void ratio	$[-]$
e_{max}, e_{min}	maximum and minimum void ratio	$[-]$
f	frequency	$[Hz]$
f_0	natural frequency	$[Hz]$
f_p	peak frequency in JONSWAP spectrum	$[Hz]$
f_q	frequency of component q	$[Hz]$
f_0	natural frequency	$[Hz]$
f_{1p}	rotation frequency of the wind turbine	$[Hz]$
F_{3p}	amplitude of horizontal force at seabed level with frequency 3P	$[N]$
f_{3p}	blade passing frequency of the wind turbine	$[Hz]$
F_{drag}	drag load	$[N]$
$F_{inertia}$	inertia load	$[N]$

F_{thrust}	thrust force on wind turbine	$[N]$
G	shear modulus	$[MPa]$
H	height above MSL	$[m]$
h	flow distance to drain	$[m]$
H_s	significant wave height	$[m]$
H_{hub}	height of turbine hub above mean sea level	$[m]$
H_{tower}	tower height above MSL	$[m]$
H_{wave}	individual wave height	$[m]$
I	moment of inertia	$[m^4]$
I	turbulence intensity	$[-]$
I_d	relative density	$[-]$
I_m	mass imbalance of wind turbine	$[kgm]$
I_{plate}	moment of inertia of base plate	$[m^4]$
I_{ref}	reference turbulence intensity	$[-]$
K	bulk modulus	$[MPa]$
k	hydraulic permeability	$[m/s]$
k	spring stiffness	$[N/m]$
k	wave number	$[1/m]$
K_c	Keulegan-Carpenter number	$[-]$
k_l	lateral spring stiffness	$[N/m]$
k_r	rotational spring stiffness	$[Nm/rad]$
k_{eq}	equivalent spring stiffness	$[N/m]$
L	blade length	$[m]$
L_k	integral length scale of Kaimal spectrum	$[m]$
M	distortional stiffness modulus	$[MPa]$
m	mass	$[kg]$
m_v	coefficient of compressibility	$[1/kPa]$
M_{1p}	amplitude of bending moment at seabed level with frequency 1P	$[Nm]$
M_{3p}	amplitude of bending moment at seabed level with frequency 3P	$[Nm]$
m_{v0}	coefficient of compressibility at reference stress level	$[1/kPa]$
N	number of load cycles	$[-]$
n	porosity	$[-]$
N_{equi}	number of load cycles of the equivalent wave height	$[-]$
$N_{liq,0}$	number of load cycles to full liquefaction without preshearing	$[-]$
N_{liq}	number of load cycles to full liquefaction	$[-]$
N_{ref}	number of cycles up to full liquefaction for the selected equivalent wave height	$[-]$
N_{waves}	number of waves of the considered (random) wave height	$[-]$
p	instantaneous wave pressure at seabed	$[kPa]$
p_0	amplitude of wave pressure at seabed	$[kPa]$
p_{ref}	reference stress level	$[kPa]$
Q_i	inflow of pore water in mesh layer i	$[m^3/s]$
Q_{i-1}	inflow of pore water in mesh layer i-1	$[m^3/s]$
R	radius of the gravity based foundation	$[m]$
R_a	ratio of blade area versus the frontal tower area	$[-]$
R_u	cumulative pore pressure resistance against repeated loading (DNV)	$[-]$
r_u	relative excess pore pressure	$[-]$
Re	Reynolds number	$[-]$
rpm_{cutin}	rotations per minute of wind turbine at cut in wind speed	$[1/minute]$
rpm_{cutout}	rotations per minute of wind turbine at cut out wind speed	$[1/minute]$
$S_{ff,3p}$	spectral density of horizontal force at seabed with frequency 3P	$[N^2]$
$S_{ff,wave}$	spectral density of horizontal force at seabed due to wave loads	$[N^2/Hz]$
$S_{ff,wind}$	spectral density of horizontal force at seabed due to wind loads	$[N^2/Hz]$
$S_{mm,1p}$	spectral density of bending moment at seabed level with frequency 1P	$[(Nm)^2]$
$S_{mm,3p}$	spectral density of bending moment at seabed level with frequency 3P	$[(Nm)^2]$
$S_{mm,wave}$	spectral density of bending moment at seabed due to wave loads	$[(Nm)^2/Hz]$
$S_{mm,wind}$	spectral density of bending moment at seabed due to wind loads	$[(Nm)^2/z]$

S_{uu}	Kaimal spectrum	$[(m/s)^2/Hz]$
S_{uu}	Kaimal spectrum of horizontal wind speeds	$[(m/s)^2/Hz]$
S_{ww}	JONSWAP spectrum, spectral density of wave height	$[m^2/Hz]$
T	wave period	$[s]$
T_{char}	characteristic drainage time	$[s]$
T_p	peak wave period	$[s]$
T_{storm}	total storm duration	$[s]$
U	wind speed, mean and fluctuating component	$[m/s]$
u	(undisturbed) particle velocity profile	$[m/s]$
u	excess pore pressure	$[kPa]$
u	fluctuating wind speed	$[m/s]$
u_{cutin}	cut in wind speed of wind turbine	$[m/s]$
u_{max}	maximum horizontal particle velocity	$[m/s]$
u_{rated}	rated wind speed of wind turbine	$[m/s]$
u_{soil}	horizontal displacement of soil due to wave	$[m]$
V_g	total volume of grains	$[m^3]$
V_p	total volume of pores	$[m^3]$
V_t	total volume of soil	$[m^3]$
W_{plate}	section modulus	$[m^3]$
w_{soil}	vertical displacement of soil due to wave	$[m]$
X	preshear parameter or history parameter	$[-]$
z	vertical coordinate	$[m]$
z_0	surface roughness related to wind	$[m]$

List of Figures

1.1 Cumulative absolute and relative share of foundation types in installed offshore wind farms at the end of 2015 (EWEA (2016)) . . . 2
1.2 Settlement and tilting after liquefaction of the west port breakwater in Niigata, Japan (De Groot et al. (2006b)) . . . 3
1.3 General problem description of cyclic loading on a gravity based foundation for an offshore wind turbine . . . 4
1.4 Different steps in the assessment of a gravity based foundation for an offshore wind turbine under cyclic loading . . . 5

2.1 Rearrangement of soil particles due to shear (left figure) and monotonic shear in dry sand, relating shear stress, shear strain and volumetric strain (right figure) (De Groot et al. (2006a)) . . . 10
2.2 The failure line, $\tan(\phi)$, and the phase transformation line, $\tan(28° - 30°)$ (left) and influence of density on volume strain (right) (De Groot et al. (2006a)) . . . 10
2.3 Stresses in undrained monotonic shear (De Groot et al. (2006a)) . . . 12
2.4 Influence of density in case of undrained monotonic shear (De Groot et al. (2006a)). The stars indicate instability points . . . 12
2.5 Influence of density on volume strain (left) and influence of stress amplitude on volume strain (right) (De Groot et al. (2006a)) . . . 12
2.6 Cyclic loading in undrained situation, stresses and strains (left) and excess pore pressure development (right) (De Groot et al. (2006a)) . . . 13
2.7 Influence of density and load intensity (CSSR) on the number of cycles to full liquefaction, for parameters a = 0.48 and b = 0.2 in equation 2.3 . . . 14
2.8 Stress and strain diagrams for dense sand with asymmetric cyclic loading resulting in partial liquefaction and cyclic mobility (left) and for dense sand with very asymmetric cyclic loading resulting in negative pore pressures and cyclic mobility (right) (De Groot et al. (2006a)) . . . 14
2.9 Influence of preshearing on pore pressure increase during cyclic loading, based on samples with relative density of 80% (Bjerrum (1973)) . . . 15
2.10 Reduction of β with decreasing porosity (defined positive) (Smits et al. (1978)) . . . 16
2.11 Excess pore pressure development in time (De Groot and Meijers (2004)) . . . 18
2.12 Chart for the evaluation of liquefaction Robertson (2010) . . . 19
2.13 Residual excess pore pressures and CSSR value determines whether the failure line is reached (De Groot et al. (2006a)) . . . 21
2.14 Failure types, determined by relative density index I_d and relative characteristic drainage time T_{char}/T, with T a characteristic period for the cyclic load, based on De Groot et al. (2006b) . . . 21
2.15 Wave pressure on sea floor (Seed and Rahman (1978)) . . . 22
2.16 Vertical distribution of the amplitudes the pore-water pressure, the effective stresses, and the displacements for the limiting case G/K approaches zero (left, based on Yamamoto et al. (1978)) and vertical distribution of relative pore pressure and relative shear stress and its maximum at $kz = 1$ (right) . . . 23
2.17 Instantaneous pore pressures and pore flow under waves with incompressible pore fluid (De Groot et al. (2006a)) . . . 23
2.18 100 year design storm used for pore pressure build-up calculations (left) and wave heights and number of waves, associated shear stress and pore pressure generation (right) (Bjerrum (1973)) 24
2.19 Cyclic strength of soil versus design storms with various return periods. Taiebat (1999), based on data of Lee and Focht (1975) . . . 24
2.20 Predictions of relative excess pore pressures (in percentages) at the edge and centre of the Ekofisk tank by Bjerrum (both undrained) and Rahman (both partially drained) (Taiebat (1999)) . . . 25
2.21 Processes associated with the excess pore pressure development below a vertical breakwater loaded by waves (after Kudella et al. (2006)) . . . 26

2.22 Residual pore pressure developments beneath the caisson at different locations (Kudella et al. (2006)) . . . 27
2.23 Fluctuating moment due to wave loads (top), transient caisson motions and transient pore pressures (middle) and residual pore pressure and residual motions (bottom) (Kudella et al. (2006)) 27

3.1 Implicit and explicit steps to be taken in a coupled approach for pore pressure development (Safinus et al. (2011)) . . . 33
3.2 Maximum CSSR values for different wave lengths and water depths, corresponding to a breaker criterion of 0.78d . . . 35
3.3 Rate of pore pressure generation indicating the faster-slower-faster increase up to full liquefaction as presented in equation 3.4 for different values of θ . . . 36
3.4 Effect of soil softening on pore pressure response (Finn et al. (1983)) . . . 37
3.5 Stiffness degradation in DCycle as a function of excess pore pressure and relative density . . . 40
3.6 Effect of densification taken into account, but no preshearing (Meijers and Luger (2012)) . . . 42
3.7 Effect of densification and preshearing both taken into account, pre-storm present (Meijers and Luger (2012)) . . . 42
3.8 Effect of densification and preshearing taken into account, gradual wave build-up (Meijers and Luger (2012)) . . . 42
3.9 Input of the storm in terms of wave height (top). Wave induced pressure at seabed level, for regular waves (middle) and (random) wave induced pressure generated from a JONSWAP spectrum with random phase model (bottom) (Meijers and Luger (2012)) . . . 43
3.10 Pore pressure development over time for regular wave loading (Meijers and Luger (2012)) . . . 44
3.11 Pore pressure development over time for five irregular wave pressure histories, generated using a JONSWAP spectrum with a random phase model (Meijers and Luger (2012)) . . . 44
3.12 Pore pressure contour diagram as presented in DNV Foundations code (DNV (1992)) . . . 45
3.13 Development of a contour diagram, starting with element tests (top) into a plot of average and cyclic shear strain amplitude for combinations of average and cyclic shear stress amplitude (bottom) (Andersen (2007)). In blue average shear strain is indicated, and in red the cyclic shear strain amplitude. . . . 47
3.14 Transformation of a random load history (left) into a discretized load history (middle), and the resulting pore pressure development can be read from the contour diagram (right, Andersen (2007)) . . . 47
3.15 Effect of drainage in terms of excess pore pressure versus time (left), and how to take drainage into account using the pore pressure contour plot (right) (Andersen (2007)) . . . 48
3.16 Subdivision of the next chapters 4, 5 and 6 within the followed approach . . . 49

4.1 Currently used support structure concepts for offshore wind turbines, and definitions to be used (based on De Vries (2010)) . . . 52
4.2 Gravity based foundation with a steel tubular shaft, as proposed by BAM (left, Smaling (2014)) and reference geometry, side view (middle) and top view (right) . . . 54

5.1 Subdivision of the chapters within the followed approach, with the content of chapter 5 highlighted in blue . . . 59
5.2 Definitions of the dynamic loads on the offshore wind turbine, together with the axis definition, based on Arany et al. (2014) . . . 60
5.3 Frequency diagram for an Siemens 3.6 MW offshore wind turbine, including wind and wave spectrum and 1P and 3P load spectrum (Arany et al. (2014)) . . . 61
5.4 Visualisation of the Fourier transform and the inverse Fourier transform, and the relation with time and frequency domain . . . 62
5.5 Visualization of the spectrum transformation from input load spectrum to load spectrum at seabed level, for wave loads . . . 64
5.6 Wind speed spectrum with the spectral gap, indicating the low and high frequency fluctuations (van der Hoven (1957)) . . . 65
5.7 Kaimal spectrum on a logarithmic y-axis, in terms of the power spectrum density (wind speed squared per frequency interval) versus frequency . . . 65
5.8 Turbulence intensities versus 10 minute wind speeds at hub level for different turbulence classes according to IEC, both onshore and offshore . . . 66

5.9 Thrust coefficients for 4 turbines, using a turbine simulation model and the generic formula of equation 5.18 (red line). D/H is the ratio of rotor diameter over hub height (Frohboese and Schmuck (2010)) . . . 68
5.10 Wave theories as function of relative wave steepness and relative water depth . . . 70
5.11 The Morison criterion of D/L < 0.2 for structural elements of the GBF and for different wave periods . . . 71
5.12 Drag and inertia loads on the GBF, for a regular wave with height 4 meter and period 7 seconds. Please note the different vertical axis for drag and inertia load. . . . 73
5.13 Bending moments at seabed level due to the rotor mass imbalance, based on Arany et al. (2014) 75
5.14 Two dynamic schematisations of the system . . . 78
5.15 Dynamic amplification factor (DAF) for various damping ratios . . . 81
5.16 Generated spectra of horizontal shear force at seabed for rated wind speed (14 m/s) and wave conditions with H_s = 4m. and T_p = 8s. . . . 81
5.17 Generated spectra of horizontal shear force at seabed for parked wind turbine at 50yr wind speed (43 m/s) and wave conditions with H_s = 10m. and T_p = 12s. . . . 81
5.18 Generated spectra of bending moment at seabed for rated wind speed (14 m/s) and wave conditions with H_s = 4m. and T_p = 8s. . . . 82
5.19 Generated spectra of bending moment at seabed for parked wind turbine at 50yr wind speed (43 m/s) and wave conditions with H_s = 10m. and T_p = 12s. . . . 82
5.20 Generated time series of horizontal shear force at seabed level . . . 83
5.21 Generated time series of bending moment at seabed level . . . 83
5.22 Spectrum comparison between original spectrum and spectrum from the generated time series for bending moment at seabed level. N = 4096 . . . 84
5.23 Spectrum comparison between original spectrum and spectrum from the generated time series for horizontal shear load at seabed level. N = 4096 . . . 84
5.24 Spectrum development of bending moment at seabed level over time for increasing wave height, wave period and wind speed . . . 87
5.25 Spectrum development of horizontal force at seabed level over time for increasing wave height, wave period and wind speed . . . 87

6.1 Subdivision of the chapters within the followed approach, with the content of chapter 6 highlighted in blue . . . 91
6.2 Schematised GBF as a rectangular plate with width W and length L and with axis indicated . . . 94
6.3 The loads from wave, wind and turbine are transferred to seabed level (left) in fore-aft direction. The static loads and dead weight are applied in the second stage. During the extreme load cycle, the first half of the load cycle is applied (second from right) and the second half of the load cycle (right figure). The positive directions are indicated in the left figure. The stages correspond to the previously listed stages. . . . 95
6.4 Used mesh in the Plaxis calculations, also showing the static water pressure from a water level of +30 meter above seabed . . . 98
6.5 CSSR profiles at different locations below the GBF for correct modelling of A and W. In this case the plate is 22.5 meter wide. Figure 6.3 indicates the direction of loading: the static component acts in positive x-direction. x=[12;13] is just outside the GBF base area, while x=[9;10] just below the edge, and [-0.5;0.5] below the middle. . . . 100
6.6 CSSR profiles at different locations below the GBF for correct modelling of A and I. In this case the plate is 26 meter wide. Figure 6.3 indicates the direction of loading: the static component acts in positive x-direction. x=[14;15] is just outside the GBF base area, while x=[11;12] just below the edge, and [-0.5;0.5] below the middle . . . 100
6.7 CSSR profiles using multiple definitions (equations 6.2 and 6.3), for correct modelling of A and I. The profile is located just outside the edge of the GBF, at x-locations [14;15] . . . 100
6.8 Contour plot for correct modelling of A & I. The static load is applied in positive x-direction, as indicated in figure 6.3 . . . 101
6.9 CSSR profiles using a larger half space in Plaxis, for correct modelling of A and I . . . 101
6.10 CSSR profiles separated for wind and wave loads, bending moments and horizontal loads . . . 102

7.1 Subdivision of the chapters within the followed approach, with the content of chapter 7 highlighted in blue . . . 105
7.2 Visualised steps in the calculation procedure related to the GBF under consideration. The CSSR contour plot is shown below the GBF as derived in chapter 6, with the governing profile just outside the base plate that will be used. . . . 106
7.3 Load cycles are analysed by their period (from zero-crossings) and by the amplitude . . . 106
7.4 Storm definitions in terms of upper threshold level and lower threshold level, together with the hourly averaged horizontal cyclic load amplitude at seabed for the largest storm from the dataset indicated in blue. This storm is the largest storm from the CoastDat dataset at Blyth, corresponding to a significant wave height of 10.85m., peak period of 17.9s. and wind speed of 23 m/s. . . . 109
7.5 Relative excess pore pressure build-up for the three storms creating the largest relative EPP, at seabed level, for two random generations for each of the storms (top and bottom). The storm developments in amplitude horizontal force at seabed is hourly averaged but has a cyclic nature as well, but this is not plotted since this would result in an unclear plot. The storm developments is plotted at the left axis, and EPP at the right axis. . . . 110
7.6 Comparison between storms with the largest maximum relative excess pore pressure (top), and the largest storms in terms of amplitude in shear force at seabed level (bottom). The presented percentiles of duration to maximum relative EPP and maximum relative EPP values, are based on 200 calculations for 200 randomly generated time series for each of the six storms. The storms are based on the definition with a lower threshold level of 1250kN and upper threshold of 3000kN. The maximum values of pore pressures were are found at seabed level. . . . 111
7.7 Relative and absolute excess pore pressure below centre of GBF, for the time steps around the maximum relative excess pore pressure. Plotted for the storm with the 90% value of maximum excess pore pressure from figure 7.6. . . . 112
7.8 Storm build-up speed [kN/hr] versus maximum relative excess pore pressure reached, presented for a lower threshold level of 1250kN and upper threshold of 3000kN. The pore pressures are all at seabed level, below the centre of the GBF. Calculation results are averaged for 5 generated irregular load time histories for each storm and each of the threshold levels. . . . 113
7.9 90th percentile and best fit to data of maximum values of relative EPP (top) and to data of relative EPP at moment of maximum storm load (bottom). Both for a set of 200 irregular load time histories and homogeneous sand with relative density of 60%, for the storm with the fastest build-up . . . 114
7.10 90th percentile and best fit to data of horizontal force amplitudes at time of maximum relative EPP (top) and at the time of the maximum load in the storm (bottom). Both for a set of 200 irregular load time histories, for the storm with the fastest build-up . . . 114
7.11 90th percentile and best fit to data of maximum relative EPP values from 3 storms building up fastest (top) and horizontal force amplitudes at the time of the max. EPP in the storm (bottom). All for a set of 200 irregular load time histories. . . . 115
7.12 Storm build-up speed versus maximum relative EPP reached, for 205 storms with a lower threshold of 1250kN and upper threshold of 3000kN, averaged over 5 irregular load time series, for preshear values of 50 and 500. The results for a preshear value of 150 can be found in figure 7.8 . 117
7.13 Histogram, 90th percentile and best fit to data of maximum relative EPP values for 200 calculations of irregular load time histories, for preshear value X=50 (top) and preshear value X=500 (bottom) . . . 118
7.14 90th percentile and best fit to data of maximum values of relative EPP for preshear value X=50 (top) and X=500 (bottom). Both for a set of 200 irregular load time histories . . . 118
7.15 90th percentile and best fit to data of maximum values of relative EPP (top) and to data of relative EPP at moment of maximum storm load (bottom). Both for a set of 100 irregular load time histories, for a gravel bed . . . 119
7.16 Relative (top) and absolute (bottom) excess pore pressure in a vertical below centre of GBF, for the time steps around the maximum relative excess pore pressure. . . . 120
7.17 90th percentile and best fit to data of maximum values of relative EPP (top) and to data of horizontal force amplitudes at time of max. relative EPP (bottom). Both for a set of 100 calculations for a soil profile with silt layer . . . 121

7.18 Relative (top) and absolute (bottom) excess pore pressure in a vertical below centre of GBF, for the time steps around the maximum relative excess pore pressure. 121
7.19 Ekofisk tank with main characteristics (left) and design storm and equivalent storm (right, Rahman and Seed (1977)) 123
7.20 Cyclic shear stress ratio for a wave height of 12.5 meter. Dimensions are in feet (left, Rahman and Seed (1977)) Finite Element mesh used by Taiebat (right, Taiebat (1999)). In this figure also points A and B are indicated, were the output will be presented. Point A is located at the centre below the tank, at seabed level, while point B is located below the edge of the tank foundation, 1.5 meter below seabed. 123
7.21 Results of pore pressure calculations from Taiebat and Rahman (left, Taiebat (1999)) and based on DCycle calculations (right). In the left figure the legend "present analysis" refers to the results from Taiebat, and not to the results obtained in this thesis, since these are presented in the figure at the right. The results from DCycle are at the centre of the foundation and should be compared with the blue lines in the left figure. The results at centre level are in both cases at seabed level. . 124

A.1 Development of relative density in time for three storms creating the lowest relative density at the end of the storm, for multiple preshear parameters. Development over time is plotted for the duration of each of the storms, at a depth of 1.5 meter below seabed. 140
A.2 Maximum EPP in first and second storm, for multiple values of preshear parameter X. Results based on a single irregular time series. 140
A.3 90% value and best fit to data of maximum values of relative excess pore pressures for preshear value of X=50, in the first storm (top) and in the second storm (bottom). Based on 100 generated irregular load time histories. 141
A.4 90% value and best fit to data of maximum values of relative excess pore pressures for preshear value of X=150, in the first storm (top) and in the second storm (bottom). Based on 100 generated irregular load time histories. 141
A.5 90% value and best fit to data of maximum values of relative excess pore pressures for preshear value of X=500, in the first storm (top) and in the second storm (bottom). Based on 100 generated irregular load time histories. 142

List of Tables

3.1 Example calculation by Seed and Rahman (1978). The total storm duration, i.e. the sum of the number of waves multiplied by the wave period in each bin, is 3500 seconds. The resulting correction factor for 232 equivalent waves with an equivalent wave height of 2.44 meter and equivalent wave period of 6.5 seconds, becomes $3500/(232 * 6.5) = 2.32$. 38

4.1 Overview of installed gravity based foundations 53
4.2 Main dimensions of the concept gravity based foundation and the reference geometry 53
4.3 Main characteristics of Vestas 8MW wind turbine 55
4.4 Soil conditions for the reference case 56
4.5 Environmental data at the reference site (Irvine (2011)) 57

5.1 Applicable wave theories for wave height and wave period combinations 70
5.2 Morison coefficients, prediction using numerical wave modelling 73
5.3 Parameters for the 1-mass-spring-dashpot system 78
5.4 Masses forming the total seabed mass m_1 79
5.5 Parameters for the 2-mass-spring-dashpot system 79
5.6 Damping ratios relative to critical damping from literature 80
5.7 Wind loads for several wind speeds (5, 15, 25 and the 1/5 yr and 1/50 yr value), both static and dynamic components 85
5.8 Wave loads for several wave heights (2, 5, 10 and the 1/5 yr and 1/50 yr value), with and without dynamic amplification (DAF) 85
5.9 1P Fore-aft bending moments for several wind speeds with and without dynamic amplification factor (DAF). For wind speeds above 25 m/s the wind turbine is parked and the 1P loads are zero. 86
5.10 3P loads for several wind speeds with and without dynamic amplification factor (DAF). For wind speeds above 25 m/s the wind turbine is parked and the 1P loads are zero. 86

6.1 Dimensions for the two considered schematisations of the GBF 94
6.2 Resulting static and dynamic (fluctuating) loads for Plaxis calculations. Based on wind speed of 25 m/s and significant wave height of 10 meter 96
6.3 Resulting loads for Plaxis calculation, in total, and separately for wind and wave loads. The four columns on the left are the actual horizontal loads and bending moments acting on the GBF, while in the six columns on the right these loads have been recalculated to the loads per meter length of the schematised rectangular baseplate. Also the bending moments are recalculated into vertical loads and per meter length. The positive direction are indicated in the left figure of figure 6.3. 96
6.4 Baseplate parameters for Plaxis 98
6.5 Soil parameters in the FEM calculations 98

7.1 Soil conditions for DCycle, for a homogeneous sand layer of 30 meter deep. No soil improvements such as a gravel bed are implemented. 107
7.2 CSSR profile used in DCycle 108
7.3 2 separate soil profiles have been investigated, both a homogeneous sand layer of 30 meter deep with two preshear values 116
7.4 Soil conditions for DCycle, a homogeneous sand layer with a gravel bed of 0.5 meter on top . . . 119
7.5 Soil conditions for DCycle, a homogeneous sand layer with an intermediate 4 meter thick silt layer 120
7.6 Equivalent storm characteristics 122
7.7 CSSR profile used in DCycle 124

A.1 Soil conditions for DCycle, for a homogeneous sand layer of 30 meter deep. No soil improvements such as a gravel bed are implemented. . . . 139

1 Introduction

1.1. Motivation of the research

The motivation of this research comes partly from the offshore wind industry, applying relatively new and improved support structure concepts such as a gravity based foundation. Especially compared to the monopile foundations, often seen as proven technology, the gravity based concept is less applied but still in development. Another part of the motivation can be found in the cyclic loading of soils below marine structures, possibly leading to liquefaction. Since it is not yet clearly defined how the cyclic loading and resulting effects should be taken into account in design conditions, some important questions remain unanswered, as further described in the problem definition. Below the developments in offshore wind industry and the cyclic loading of soils will be discussed, motivating this thesis research. In the problem description both will be combined, resulting in the research questions.

Offshore wind industry

Growing population and faster economic development results in increasing energy demands. As the fossil resources are finite and harm the environment irreparably, increasing interest is developed in renewable energy. The European Union has therefore set its goal of 20% renewable energy of the total energy production in 2020 (European Commission (2010)), which should even be increased to 27% in 2030 (European Commission (2014)). In 2050 this should reduce the total emission of greenhouse gasses by 80-95 % compared to 1995 levels (European Commission (2011)).

According to the European Environmental Agency (Uslu (2009)), wind energy could power Europe many times over. Due to densely populated areas onshore in the European region, especially along the coasts where wind conditions are better, many offshore wind farms have been built. From 2008, Europe is even the leader in offshore wind farm development, mainly due to its shallow waters in the North Sea and Baltic Sea and the good wind conditions offshore. Furthermore, building offshore leads to less aesthetic pollution than onshore. Statistics show (EWEA (2016)) that wind farms in Europe are built further offshore and in deeper waters, rising on average from 30 kilometres offshore in 2013 to 43 kilometres in 2015. Water depths increased on average from 20 meter to 27 meter. Also the size of wind turbines have increased in 2015 by 13% compared to 2014, due to increasing interest and developments of wind turbines in the range of 4 to 6 MW. However, the increasing water depths and turbine sizes poses large challenges in the design and construction of foundations. In the past years the majority of foundations consisted of the monopile type, due to its easy fabrication, installation and suitability for soil conditions in the European waters. The monopile share still increases, but also the gravity based foundations are seen more often. The multi pile foundation, such as jackets, tripods and tripiles, are less often applied due to the high construction and installation costs. The cumulative shares of foundation types at the end of 2015 are presented in figure 1.1.

Construction and installation costs of offshore foundations may form a significant part of the total building costs of a wind farm, and are therefore very interesting to look at in order to reduce the total investment costs. According to (DTI (2001)) the foundation costs may take up to 30% of the total building costs, especially due to the heavy equipment necessary to install the foundations and wind turbines and related downtime due to

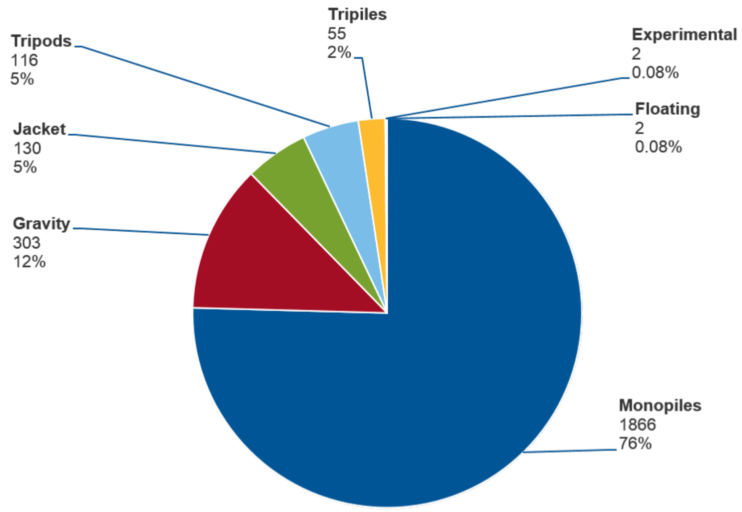

Figure 1.1: *Cumulative absolute and relative share of foundation types in installed offshore wind farms at the end of 2015 (EWEA (2016))*

weather conditions. Therefore the offshore installation activities should be kept to a minimum, which is however only possible if the foundation type allows an easy installation procedure. Furthermore, environmental restrictions become stricter, resulting in either less noise-generating offshore work methods, or noise mitigation measures (Jaspers Faijer (2014)). Offshore piling works are for instance only allowed during a certain piling-window in summer periods, and more and more noise mitigating measures such as bubble curtains have to be used.

Taking the developments and challenges into account, an interesting foundation type for larger offshore wind turbines in deeper waters might be a gravity based foundation (GBF) in combination with a steel tubular shaft, as proposed by BAM. The gravity base provides the main stability of the structure in deeper waters, while the steel tubular shaft is comparable to the monopile structure and keeps the hydrodynamic loads therefore relatively low. Since no piling works are required, the environmental impact is reduced considerable. Finally, the structure has relatively low material costs since the gravity base can be made of concrete.

Cyclic loading of soils

Thanks to the enormous development of the offshore wind industry, norms and regulations have been developed for the design process of the foundations and support structure, for instance by Det Norske Veritas - Germanische Lloyd (DNV-GL) and the American Petroleum Institute (API). A rather large amount of knowledge has been gained on static stability of the foundation, while the relation between cyclic loads on the structure and the soil response receives less attention. Together with the high consequences associated with possibility of full or partial liquefaction and loss of stability due to cyclic loading, this makes the topic highly relevant.

Cyclic loading of relatively densely packed soils results in contraction and the generation of excess pore pressures in the subsoil. If the effective stresses completely vanish, liquefaction is reached, although depending on the problem failure may be reached before liquefaction. The specific case of liquefaction induced by cyclic loads is called cyclic liquefaction, while static liquefaction can be induced by a single monotonic load applied to an initially unstable situation. The focus will be on cyclic liquefaction in this thesis, where the main processes of pore pressure generation, dissipation and consolidation, together determine the final build-up and depend on both the load conditions and soil conditions. The main research up till now has been gained on liquefaction of marine structures by wave loads and earthquake loads. Various examples of liquefaction of the subsoil below and around offshore structures can be found in literature. The main structures mentioned are pipelines, vertical breakwaters and gravity based foundations. Starting with pipelines, multiple examples are reported where the pipeline floated up to sea level after liquefaction of the seabed. This often occurred after severe storm conditions by wave loading (Christian et al. (1974)), or by earthquake loading such as in the Niigata earthquake in 1964 with a total pipeline length of 470 kilometres failing (Huang et al. (2014)). The large uplift deformations results in significant damage to the pipelines.

For vertical breakwaters and gravity based foundations the wave loading has had lots of attention within the European MAST III/Proverbs research program (Oumeraci et al. (1999)). This research program was initiated

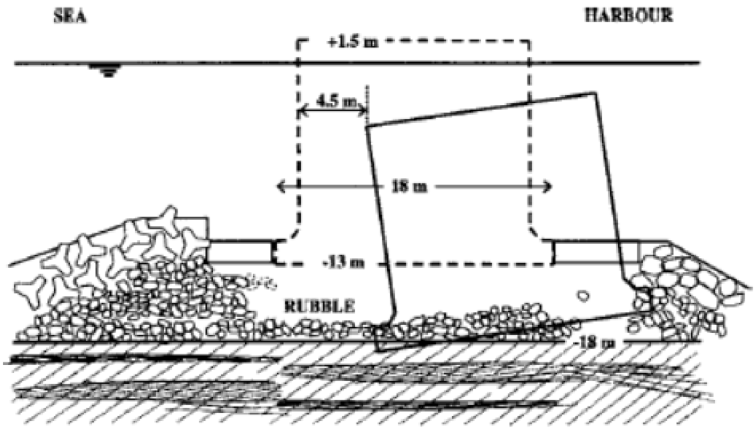

Figure 1.2: *Settlement and tilting after liquefaction of the west port breakwater in Niigata, Japan (De Groot et al. (2006b))*

after a lot of catastrophic failures in the 1970's and 1980's, although already in the 1930's multiple failures are reported (De Groot et al. (2006b) and Oumeraci (1994)). A case very well reported is the failure of the Niigata breakwater in Japan, in storm loading on October 29, 1976. The maximum wave loading in the storm was reported to be equal to the design wave loading. Twenty-one caissons of each 12 meter length moved about 4.5 meter in vertical and horizontal direction, also resulting in a significant tilting of the caissons (figure 1.2). After soil investigations, model test and model studies, it was concluded that one of the causes of the failure was the rapid increase in the residual pore pressure during the storm loading (De Groot et al. (2006b)), next to the contribution of the caisson motions itself.

Offshore gravity based foundations have also been studied extensively, of which the Ekofisk oil-storage tank from 1973 is well known (Lee and Focht (1975)). The 97 meter diameter tank was placed in 70 meter water depth, directly on sand without a drainage layer. In the design process liquefaction was extensively investigated for various storms and various sand conditions. The storm history was identified as a major parameter determining the final excess pore pressure to be reached, but since no measurements of wave height data where performed, only predictions of wave height distributions could be used to assess the excess pore pressure build-up in extreme conditions. It was also found that the caisson edges were most susceptible to liquefaction.

Summarizing and considering a gravity based foundation for an offshore wind turbine, the liquefaction risk asks for a procedure to take into account multiple cyclic loads from wind, waves and turbine, and an approach to assess the pore pressure developments in design (storm) conditions. This approach should lead to a better understanding of the excess pore pressure to be taken into account in the final stability assessment in extreme loads. This may finally result in further development of the gravity based foundations for offshore wind turbine and its application in more and more wind farms.

1.2. Problem description

Problem description in general
The starting point of the problem description is a general analysis of a gravity based foundation for an offshore wind turbine under cyclic loading. Investigating the cyclic loads acting on the total structure, the wind, turbine and wave loads are at first the most important cyclic loads. The loads are transferred to the subsoil, where they result in horizontal shear forces and bending moments with a cyclic character. The resulting soil behaviour under these cyclic loads asks for some more processes to be taken into account, for instance drainage and consolidation (figure 1.3). This will result in excess pore pressure build-up, influencing the stability of the structure, and cyclic settlements and tilting, influencing the operability of the structure. Also the dynamic motion of the structure and the interaction with the seabed might influence the excess pore pressure. Finally, the stability of the filter layer and scour protection might be influenced by the excess pore pressures, and by the instantaneous wave pressures around the structure as well.

Under cyclic loading soils tend to densify, resulting in the generation of excess pore pressures. If significant drainage is possible, this will allow the excess pore pressures to dissipate, and the soil subsequently to densify.

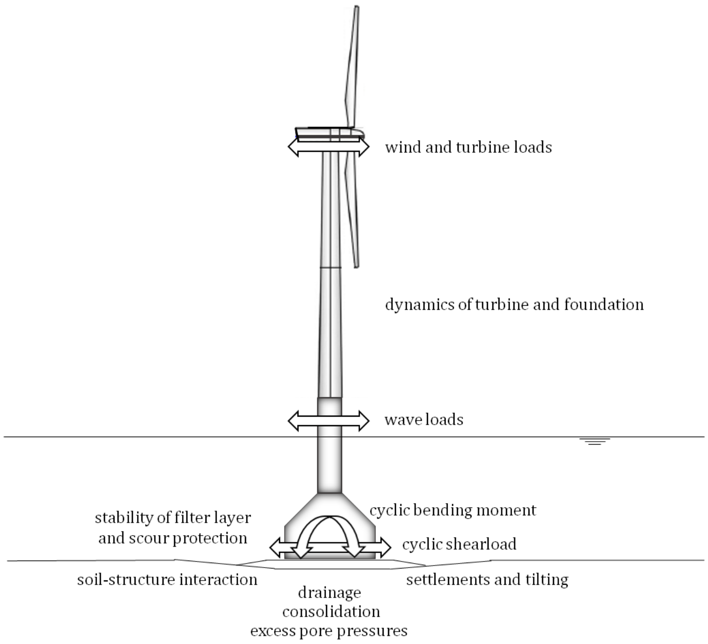

Figure 1.3: *General problem description of cyclic loading on a gravity based foundation for an offshore wind turbine*

The densification acts as an increase in strength to further cyclic loading and further pore pressure build-up. The soil conditions therefore continuously change during cyclic loading, in contrast to static loading, and as a consequence the order of loads may have a significant influence on the final pore pressure that is reached (Meijers et al. (2014)).

Since the cyclic loads from a gravity based foundation occur in a irregular nature, large cyclic amplitudes might be present at the start of loading resulting in a quick increase in excess pore pressures. After significant strengthening of the soil due to densification, the pore pressure generation may however be significantly less. Multiple load sequences should therefore be analysed to get an impression of the range of maximum excess pore pressures. Furthermore, also the sequences on a larger scale, on storm scale, are expected to determine the final excess pore pressure to be reached. A few smaller storms with densification as a result, act beneficial to the excess pore pressure build-up in a following larger (design) storm (Lee and Focht (1975)). A heavy storm at the start of the lifetime of the gravity base may be governing, but asks for a probabilistic approach to prevent a very conservative design based on loading with a very low probability.

As shown in figure 1.3 and 1.4, different fields of engineering are necessary to assess this problem. Starting with environmental input from wind and waves, multiple models are needed: a hydraulic model for wave loads, a turbine model for wind loads and a structural model for the transfer of loads to seabed level. The loads are input for the soil behaviour, while the soil itself asks for a different model for different processes. This can in general be subdivided into excess pore pressure developments and cyclic deformations. The excess pore pressures need to be taken into account in the final stability assessment of the structure in extreme loads, while the deformations mainly determine the operability of the turbine and are therefore relevant over the total lifetime of the structure. The settlements can furthermore be subdivided in vertical settlement and horizontal displacement, and may result in differential settlements and tilting of the structure. The vertical settlements may potentially lead to problems with the connection of electricity cables, and potentially cable failure, while differential settlements especially influence the operability of the wind turbine. The assessment should lead to a relation between cyclic loading and soil behaviour, and the impact on the stability of the structure in both the Ultimate Limit State (ULS) and the Serviceability Limit State (SLS).

Problem description for this research

The problem description for the current research consists in fact of a selection of the topics mentioned above. In figure 1.4 the topics that will be investigated further in this research are highlighted, and they will be described below.

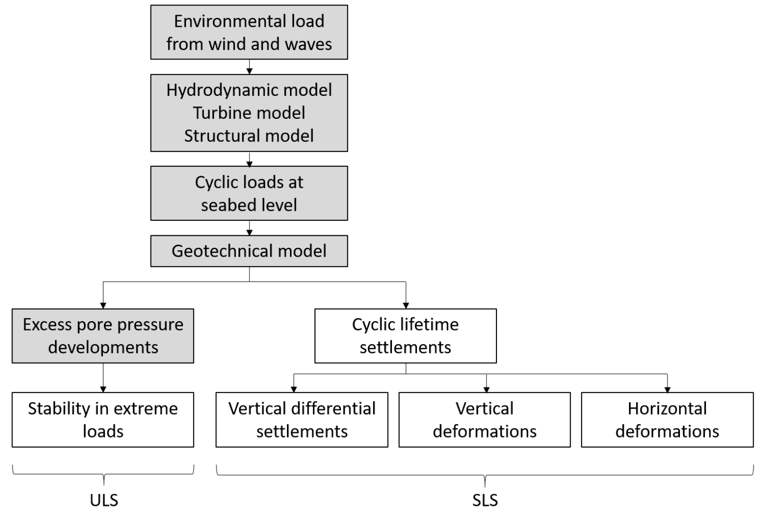

Figure 1.4: *Different steps in the assessment of a gravity based foundation for an offshore wind turbine under cyclic loading*

As already noted in the motivation of this research, the current norms and standards do not give a detailed method how this cyclic loading of marine structures should be taken into account in the design stage. The first question which therefore arises is how the cyclic loading on a gravity based foundation for an offshore wind turbine should actually be assessed. The gravity based foundation asks for an extension of the currently applied models, where only wave loads are taken into account, for instance on vertical breakwaters. For the gravity based foundation with an offshore wind turbine the large bending moments result in a completely different load situation.

From literature in the field of wave-induced liquefaction, the importance of the load history on the maximum excess pore pressure reached is stressed. Each combination of storms (in terms of significant wave height and peak period over time) results in different maximum values in excess pore pressure, since the effects of drainage, consolidation and preshearing versus the increasing loads from the storm occur simultaneously. Therefore it is not a priori known which storm or combination of storms produces the governing excess pore pressure (Meijers and Luger (2012)). In addition to this, the irregular load histories influence the resulting pore pressures response too (as observed for wave pressures on a flat seabed in Meijers et al. (2014)). A few load cycles with large amplitudes may result in a quick build-up of pore pressure at the onset of loading, while at a later stage after significant drainage the generation of pore pressure will be less. Therefore this aspect has to be taken into account as well.

Summarizing, the problem comes (1) from the gravity based structure, resulting in a structure which is different from the structures in the liquefaction assessments found in literature, and resulting in a different load configuration, and (2) from the load history which should be taken into account for a governing excess pore pressure in the stability assessment of a gravity based structure.

The problem definition can be summarized from the foregoing, and is formulated as:
No general method exists to assess the liquefaction potential of a gravity based foundation for an offshore wind turbine under cyclic loads. Therefore it is unclear whether cyclic loading poses a possible threat to the stability of the structure.

1.3. Research objectives & questions

The main objective of this study is therefore:
To assess the liquefaction potential of a gravity based foundation for an offshore wind turbine under cyclic loads

The outcomes of this research may first of all contribute to a more economical design since possible risks can be identified better, may secondly contribute to the international knowledge on stability of marine structures under cyclic loads and may thirdly therefore facilitate further design practices and may reduce possible failures of marine structures due to liquefaction.

The research questions that need to be answered to reach the objective, are:

- How to determine a cyclic shear stress profile below a gravity based foundation taking into account the load configuration and cyclic loads?
- How to determine a representative load history to assess the liquefaction potential of a gravity based foundation under cyclic loads?
- How should this be related to the current norms and standards?

1.4. Research methodology

In order to answer the research questions, first the existing knowledge from literature is investigated. This should clarify the different types of liquefaction, and whether failure due to liquefaction might actually be a possible threat for a gravity based foundation. Furthermore, it should clarify the nature of the problems, both pore pressure developments and settlements, and the different modelling approaches for each case.

After the literature review, a gravity based foundation for the case study will be defined based on a general lay-out as proposed by BAM. The location will be based on the location where the GBF will be placed, within the Blyth Offshore Demonstrator Project, offshore Blyth (UK). The case study will be used to derive the cyclic loads at seabed level, and to finally answer the research questions. The subsequent steps in the methodology are as follows:

- Definition of a reference case of a gravity based foundation and offshore wind turbine
- Load analysis in the frequency domain
- Derivation of a cyclic shear stress profile
- Calculations of excess pore pressures using multiple load histories
- Probabilistic approach for the excess pore pressures to determine a representative load history

1.5. Restrictions

The main restrictions of this research are listed below:

- The gravity based foundation for the case is based on the project of BAM with its application in the Blyth Offshore Demonstrator project, offshore Blyth (UK). The loads (storms) on the structure are based on site-specific data from the CoastDat database (Weisse et al. (2005)), and are only valid for the used dimensions of the gravity based foundation and for a certain type of turbine. The general results might be applicable to other gravity based foundations for wind turbines, but this certainly has to be investigated accordingly.
- The settlements of a gravity based foundation under cyclic loads don't have the main focus in this research. The main focus will be on the liquefaction failure by excess pore pressures and how to assess this problem, taking into account a representative load history. The development of settlements over the lifetime of the gravity based foundation requires different tools, especially related to the modelling approach.
- Following the restriction mentioned above, the focus is on storm conditions and the related periods to storms. The time over which pore pressures develop will be in the order of days. The total lifetime of the structure will not be considered.
- Furthermore, the focus is on the pore pressure developments in storm conditions. The final stability analysis of the gravity based foundation in extreme loading will not be part of this research.
- Considering the soil conditions, fictitious soil profiles will be used to answer the research question. The focus is on non-cohesive (uncemented) medium to dense sands (relative density of 60%). As part of the sensitivity studies, less permeable will be investigated, but these won't make up the larger part of this research. Furthermore, the main focus is on homogeneous soils.

1.6. Outline of the report

The starting point of this research is a literature review on the behaviour of sand under cyclic loading in chapter 2. Different liquefaction types of failure will be discussed and applied to the GBF. The often considered case in literature of a horizontal seabed loaded by waves will be shown, as well as the available knowledge with respect to the cyclic loading of marine structures. Chapter 3 will present the different modelling approaches for cyclic loading of sands, and will discuss why the used tools have been chosen and what the capabilities and limitations of other methods are. Subsequently, the basics of the program DCycle will be discussed. Other approaches presented in norms and standards and by NGI will be discussed too.

Chapter 4 kicks off with the definition of a reference geometry for the GBF and OWT, together with some basic properties. Chapter 5 marks the start of the application of theories and necessary ingredients to obtain the answer to the research questions, starting with the derivation of the cyclic loads on the GBF and OWT in the frequency domain. Chapter 6 treats the second ingredient to answer the research question: the derivation of a cyclic shear stress profile below the GBF in Plaxis. Chapter 7 finally combines the ingredients from chapters 5 and 6, resulting in DCycle calculations of excess pore pressures for various load histories. This results in the main conclusion related to the load history. Chapter 8 finally contains the conclusions, discussion and recommendations.

Before the start of this thesis, a short remark about the sign conventions is made. Since this thesis research includes both soil mechanics as well as hydraulic and structural engineering, different sign conventions for both fields of engineering are used together in this thesis. Soil mechanics takes pressure and compression positive, since soils are not able to resist tension loads. In hydraulic engineering and structural engineering on the other hand, tension loading is usually taken positive. In this thesis, the chapters 2, 3 and 6 are about the soil mechanics and will therefore use compression as positive. Chapter 5 is about the loads on the GBF, and will therefore use tension positive.

2

Behaviour of sand under cyclic loading

2.1. Introduction

In this chapter a basic description is presented of the cyclic behaviour of sands exposed to cyclic loads. This will give a sound basis for the further application to a gravity based foundation. The starting point of the chapter is the deformation of sands under shear forces, starting at monotonic loading and extending to cyclic loading. Furthermore the characteristics of dilative, contractive, drained and undrained behaviour will be introduced. This will subsequently be used in the description of multiple liquefaction types, of which a good understanding is essential to be able to place the current investigation within the field of liquefaction assessments. After this introduction, the basic problem of a horizontal seabed loaded by waves will be discussed. This problem shows the elementary processes and can be seen as a first step in the analysis, although the gravity based foundation asks for broader approach. Subsequently literature about cyclic loading of marine structures is investigated to identify the currently available knowledge from scale tests as well as from numerical modelling. This results in an overview of the main processes and remaining research questions, and places this thesis research in a wider perspective.

Before starting this chapter, liquefaction needs to be defined. In literature, an often used definition is the one given by the workshops on the evaluation of liquefaction resistance of soils of the National Center for Earthquake Engineering Research (NCEER): "the act or process of transforming any substance into a liquid" (Youd et al. (2001)). The transformation occurs due to an increase in pore pressure and a decrease in effective stress. The increase in pore pressure comes from the tendency of granular soils to contract under cyclic loading, and may occur in saturated or almost saturated soils. This definition will be used while describing the main properties of sands under cyclic loading in this chapter.

2.2. Deformation of sands

The soil behaviour is described in terms of vertical effective stresses $\sigma_v^{'}$, shear stresses τ, volume strains ϵ_{vol} and shear strains γ. These are only uniquely defined if the plane where the stresses and strains act is indicated, for instance the horizontal plane or the plane of the largest shear stress. In many cases, it is more practical to use the deviator stress, the difference between the largest and the smallest principal stress, as a measure of the largest shear stress in any soil element. This won't be used in this thesis however, instead the before mentioned stresses and strains will be used. Furthermore, soils in nature and in laboratories may not be isotropic, but the assumption of isotropy is used here to clarify the most essential phenomena for this research. Finally, the focus is on non-cohesive soils (i.e. sands) till further notice.

2.2.1. Contraction and dilation

During shearing in a single direction (monotonic shear) volume decrease and volume increase will occur due to rearrangements of the grains. Under a constant vertical effective stress, the grains will first get into a

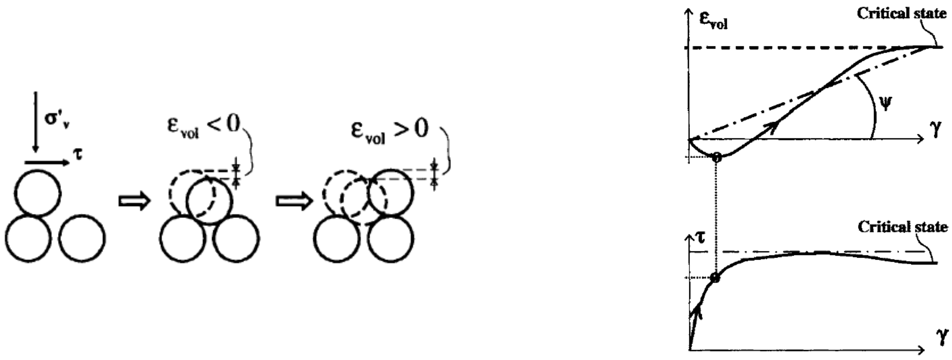

Figure 2.1: *Rearrangement of soil particles due to shear (left figure) and monotonic shear in dry sand, relating shear stress, shear strain and volumetric strain (right figure) (De Groot et al. (2006a))*

closer packing with increasing shear load, resulting in a volume decrease (compaction or contraction), while after shearing more, the grains will get into a looser packing again due to grain layers sliding over each other (figure 2.1 left). This results in a volume increase again (called dilation or dilatation). The resulting shear strains will be mainly elastic at relatively low shear stress values, but may be plastic when larger shear stresses are applied. During unloading and reloading, the shear strains will be mainly elastic, while the virgin loading will result in plastic shear strains.

For densely packed soils, the corresponding volumetric strain ϵ_{vol} versus the shear strain γ under monotonic shear, the upper right figure in figure 2.1, indicates this transition from contraction to dilation. In regular geotechnical engineering this behaviour is often linearised, using the dilation angle ψ. In the diagram of volume strain ϵ_{vol} versus shear stress τ, the transition between contraction and dilation can clearly be seen in the lower plot of the right figure of 2.1. The increasing stress ratio with increasing shear strain can be related to strain hardening, while the decreasing part after the peak can be related to strain softening (Arthur et al. (1977)). The peak shear strength in the diagram furthermore coincides with the maximum rate of dilation. Under continuous shearing, the post peak strength in the critical state is reached, which will be explained later.

The transition point from dilation to contraction largely depends on the relative density of the considered sand. Very dense sands will show contractive behaviour at the onset of monotonic shear loading. Loosely packed sands will show large contraction, and won't even start dilating after continuous shearing. This behaviour is shown in the volumetric strain versus shear strain diagram (figure 2.2 right). The transformation points from dilative behaviour to contractive behaviour appear to be on a straight line for various relative densities. The line which connects these points is called the phase transformation line and relates the shear stress to the vertical effective stress.

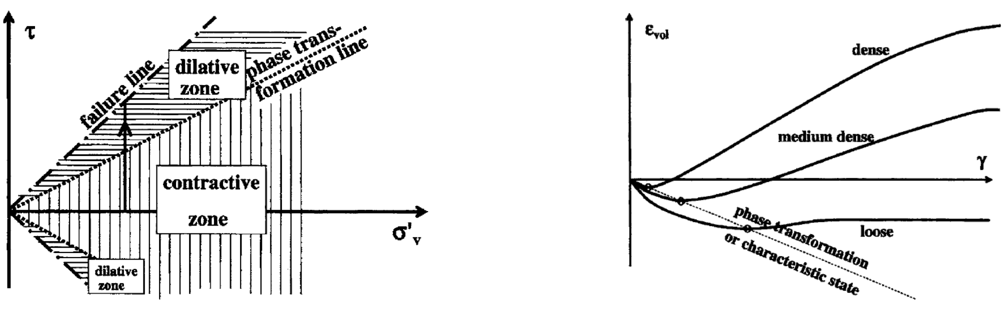

Figure 2.2: *The failure line,* tan(ϕ)*, and the phase transformation line,* tan(28° – 30°) *(left) and influence of density on volume strain (right) (De Groot et al. (2006a))*

If the shear stress τ versus the vertical effective stress ϵ_{vol} is plotted (figure 2.2 left), this phase transformation line separates a zone of dilative behaviour from a zone of contractive behaviour. Additionally, a failure line can be plotted in the same figure based on the maximum shear stress to be applied, depending on the angle of internal friction of the material: $\tau = \sigma_v^{'} tan(\phi)$. The zone between the failure line and the phase transformation line now indicates the total zone of dilative behaviour.

The degree of contraction or dilation is largely determined by the initial packing density of the material (figure 2.2 right). For loosely packed sands, large contraction will appear, while for densely packed sands far less contraction will appear. For loosely packed sand on the other hand, after the phase transformation point, far less dilation will occur compared to the dilation for densely packed sand after the phase transformation point. This can also be seen in figure 2.2 left, where for loosely packed sand with a lower angle of internal friction, the failure line and the phase transformation line will be closer to each other, indicating a smaller dilative zone. A final parameter influencing dilative or contractive behaviour is the initial mean effective stress σ'_{v0}, which is in terms of its absolute magnitude important. An increase in the vertical effective stress results in more contraction and less dilation under shear loading, which can also be seen in the left of figure 2.2.

2.2.2. The critical state

If the shear stress reaches the failure value in figure 2.1, the dilation ends and a constant volume remains. The shear stress will slightly decrease below the failure value. The state that is now reached is called the critical state, as indicated in the right lower plot in the right figure of figure 2.1). The term critical state has mainly been used in the UK, while in the US mainly steady state was used, after Casagrande and Castro (Been et al. (1991)). The critical state is thought to be an equilibrium in which stresses and void ratio are constant at large strains while the soil continues to deform. Further straining does not results in a change of state, Ie. stresses and void ratios, since the soil is already completely destructed. The critical state points of void ratio and stress state together form the critical state line, the line which indicates the stress path from an initial condition to the final stress state. The steady state however is defined when the soil mass is continuously deforming at constant volume, constant stress conditions and with constant velocity. The soil mass is assumed to be in a certain flow structure. The critical state line relates the void ratio and the stress level in the current state with the critical state, denoted in the state parameter. In this thesis, the corresponding line in the tau - σ'_v diagrams is called the failure line.

2.2.3. Undrained behaviour and consolidation

The shear- and volumetric deformations mentioned in the contractive and dilative theory, are not likely to occur in undrained conditions. Under these conditions the pore water is prevented to flow out from the boundaries or due to the fast application of the loads, and consequently the volume remains constant. Therefore the full load has to be carried by the pore water. The undrained behaviour is a specific case of drained soil behaviour, in which the soil still tends to dilate or contract. In dilative soils this will result in an increase in effective stress level and a suction force in the pores (decreasing pore pressure). After a while water is able to flow in and the pore pressures are restored again. For contractive soils a reverse process holds: soil particles want to get into a denser packing, while pore water is not yet able to flow out and consequently the pore pressure increases. The excess pore pressures, i.e. the difference between the pore pressure and the hydrostatic pressure, will also disappear after a while when drainage allows the excess water pressure to flow out. This process of restoring the pore pressures in undrained dilative and contractive soils is called consolidation. Whether drained or undrained behaviour is most likely, is largely determined by the loading rate and consolidation time, which will be used later for the definition of various liquefaction types.

Using simple shear tests, the stress path during undrained monotonic shear loading can be demonstrated. While increasing the shear stress and maintaining a constant vertical total stress, the vertical effective stress will gradually decrease due to a rise in pore pressure, together maintaining the constant total vertical stress. After the phase transformation line, the soil starts to dilate again, reducing the pore water pressure (figure 2.3). In undrained dilative soils, the vertical effective stress increases continuously, resulting in increasing shear stress even above the maximum shear stress in the drained test, inducing lots of shear deformation. This state is indicated as the steady or critical state in the right figure of figure 2.3.

Comparing a very loose packing and a very dense packing, for both packings the isotropic effective stress decreases during the increase in deviator stress and the increase in pore pressure. For very loose soils the reduction in effective stress is that large that no effective stresses may remain, resulting in full liquefaction. For loose soils the effective stress decreases, but not necessarily to zero, indicating only partial liquefaction. For medium dense and dense soils, the vertical effective stress increases in the steady state situation due to pore under pressures (left figure of figure 2.4).

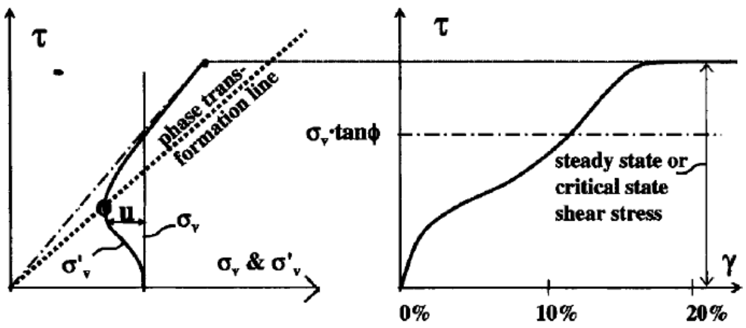

Figure 2.3: *Stresses in undrained monotonic shear (De Groot et al. (2006a))*

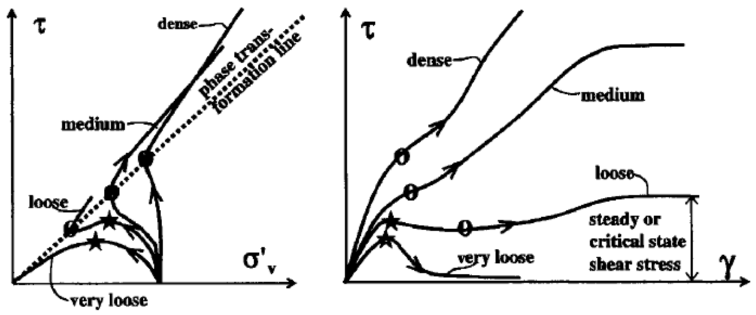

Figure 2.4: *Influence of density in case of undrained monotonic shear (De Groot et al. (2006a)). The stars indicate instability points*

The soils with a specific void ratio (loosely packed) and specific stress state are sensitive to liquefaction. Whether liquefaction occurs is related to the instability point, which is the point from where the shear stress continuously decreases, i.e. where instability is reached, as indicated in figure 2.4 with a star for loose and very loose soils. If this point is reached, only a very small loading is necessary to get over the instability point, resulting in the flow type of failure: a continuous deformation process is started by a slight increase in load over the instability point, resulting in liquefaction. All instability points for loosely packed soils with various void ratios and stress states, result in a instability line. For dense or contractive sands however, the failure mode is much more brittle. The strength of the soil cannot increase any more when the pore pressures reaches its lower limit, due to cavitation. Below the cavitation limit gas bubbles form and will result in completely different and far more complex phenomena.

2.2.4. Cyclic loading

Shear stress cycles in dense and moderately dense sand cause the progressive contraction of the skeleton. Dilative behaviour in these sands is only observed near to plastic failure in case of large cyclic shear stress amplitudes. If this state is reached at all, after a few load cycles part of the deformation becomes elastic, in which the resulting contraction might flatten out the dilation during the plastic deformation. The contractive behaviour of medium dense to dense sands under cyclic loading will subsequently be discussed.

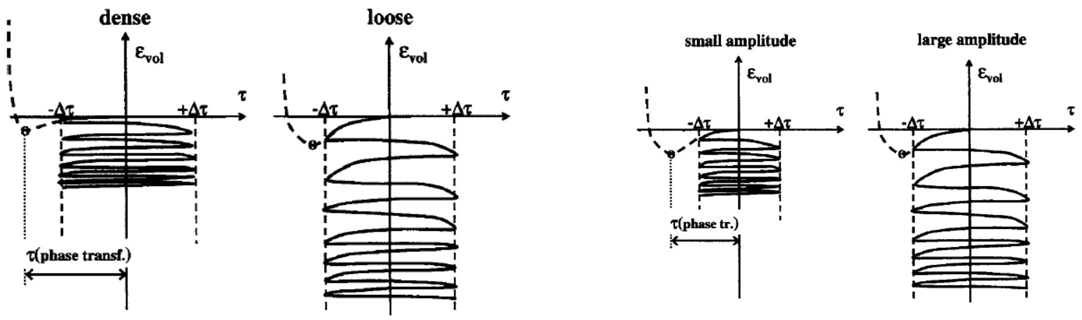

Figure 2.5: *Influence of density on volume strain (left) and influence of stress amplitude on volume strain (right) (De Groot et al. (2006a))*

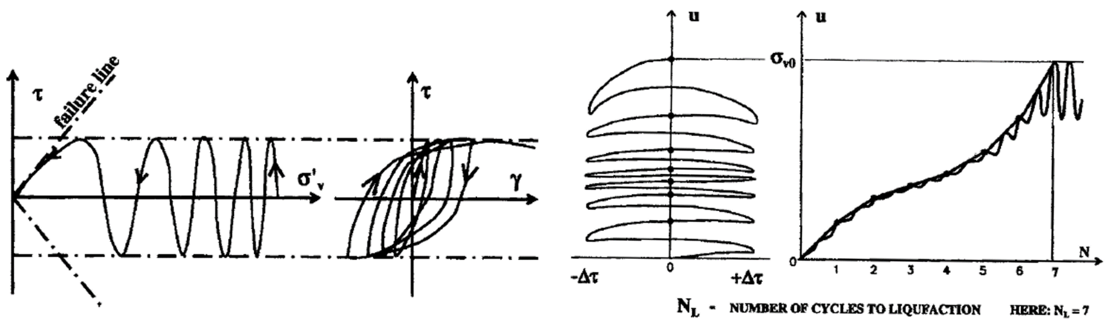

Figure 2.6: *Cyclic loading in undrained situation, stresses and strains (left) and excess pore pressure development (right) (De Groot et al. (2006a))*

The main characteristics of the cyclic load are the amplitude and the period of loading, resulting in a number of cycles in a certain duration of loading. The soil strength on the other hand, can be represented by the number of cycles required to reach full liquefaction, which is largely determined by the relative density. The cyclic shear load is often expressed in a cyclic shear stress ratio (CSSR), originating from earthquake engineering (equation 2.2). Starting with drained conditions, the resulting volume strain is mainly determined by the relative density (figure 2.5 left) and stress amplitude (figure 2.5 right). A denser packed soil will experience less volume strain per cycle compared to a looser packed soil, while a larger amplitude generates larger volume strains per cycle. In both cases however, the volume strain will decrease with increasing number of load cycles. This again only holds for isotropic conditions, and for example not if the soil skeleton was previously loaded in a certain direction.

In undrained conditions, the average pore water pressure development becomes an interesting output parameter. Increasing the number of load cycles, the average pore water pressure gradually increases (right figure of figure 2.6). The excess pore pressure is often expressed as the relative excess pore pressure, which is the ratio with the initial vertical effective stress (2.1). The build-up of excess pore pressure starts with a relatively large increase due to the large contraction in the first load cycles. Subsequently, the pore water pressure increases less, and as the number of load cycles is reaching the number of load cycles at liquefaction, the pore water pressure increase per cycle increases again. The latter effect is due to an increase in load (reduced vertical effective stress), represented by the cyclic shear stress ratio (CSSR) in equation 2.2. This also results in larger shear strains and a reduced stiffness. It should finally be noted that the schematised graph of figure 2.6 was derived for cyclic loads with a constant amplitude.

$$r_u = \frac{u}{\sigma'_{v0}} \tag{2.1}$$

$$CSSR = \frac{\Delta\tau}{\sigma'_{v0}} \tag{2.2}$$

$$\frac{\Delta\tau/\sigma'_{vo}}{I_d} = aN_{liq}^{-b} \tag{2.3}$$

with:

r_u	= relative excess pore pressure [-]
u	= excess pore pressure [kPa]
$CSSR$	= cyclic shear stress ratio [-]
$\Delta\tau$	= shear stress amplitude [kPa]
σ'_{vo}	= initial effective vertical stress [kPa]
I_d	= relative density [-]
N_{liq}	= number of cycles to full liquefaction (undrained) [-]
a, b	= empirical constants [-]

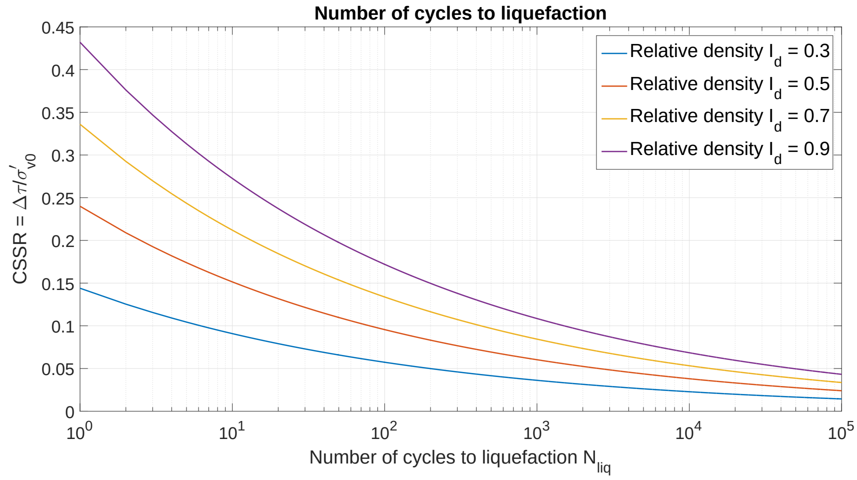

Figure 2.7: *Influence of density and load intensity (CSSR) on the number of cycles to full liquefaction, for parameters a = 0.48 and b = 0.2 in equation 2.3*

Again, the relative density and the relative stress amplitude determine the number of cycles up to full liquefaction. An increase in relative density has a similar influence as a decrease in initial vertical effective stress and results in an increase in the number of cycles to liquefaction, assuming a constant CSSR. This is due to the smaller amount of contraction in denser soils or at lower mean effective stresses, as also observed for dry tests, increasing the liquefaction resistance (figure 2.7). The relation between CSSR, number of load cycles and relative density is often described in a formula as denoted in equation 2.3, with empirical constants based on element tests.

2.2.5. Asymmetric cyclic loading

In many situations asymmetric loading might occur, which is defined as cyclic loading with a mean value of shear stress, i.e. the cyclic load cycles around a mean value. As was investigated by Lupea (2013), the amplitude of load determines whether pore pressure build-up occurs, while the average value can be up to the soils capacity as long as the amplitude remains low. This can also be seen in the $\tau - \sigma$ curves: no total loss of effective stress is reached as long as the average relative shear stress is sufficiently large, and the relative shear stress amplitude sufficiently small. An equilibrium conditions is found in this case, lying at the intersection of the phase-transformation line and the average shear stress, if a relatively large initial vertical effective stress was present (figure 2.8 left). If this was not the case, i.e. if the vertical effective stress is relatively small or the shear stress very large (very asymmetric loading), the stress state is located within the dilative zone from the start, and the pore pressure will become negative (figure 2.8 right).

In both cases a state of constant pore pressure is reached, but with an increasing strain in each load cycle, called cyclic mobility, as explained later. Furthermore, it can be seen that the maximum residual excess pore pressure is limited under asymmetric loading, since the vertical effective stresses will never completely reduce to zero.

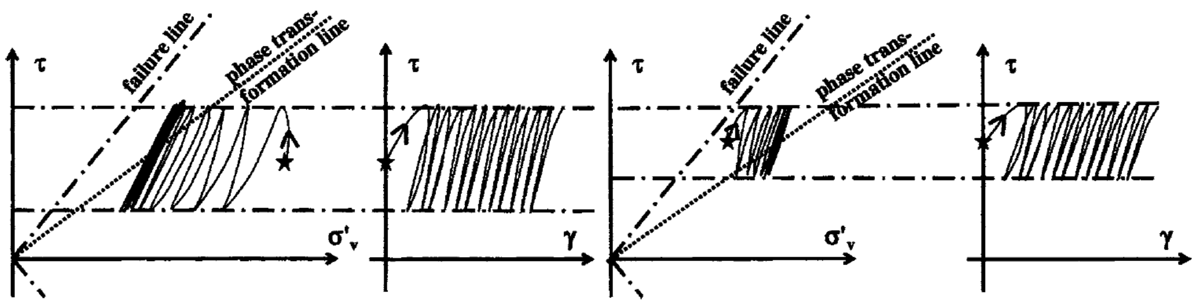

Figure 2.8: *Stress and strain diagrams for dense sand with asymmetric cyclic loading resulting in partial liquefaction and cyclic mobility (left) and for dense sand with very asymmetric cyclic loading resulting in negative pore pressures and cyclic mobility (right) (De Groot et al. (2006a))*

2.2.6. Preshearing

Cyclic loads will in reality neither be fully drained or fully undrained, resulting in intermediate drainage over time. The total effect of pore pressure generation and pore pressure dissipation consequently changes in time. From the start of loading a quick rise in pore pressure is developed, in which the generation of pore pressure exceeds the dissipation of pore pressure. With increasing number of load cycles however, the pore pressure increase decreases. This strengthening effect of the soil, also called preshearing, which occurs only in case of drained loading, can either be linked to the densification of the soil skeleton, or to the change in packing structure of the soil skeleton, as will be explained below.

An interesting investigation of pore pressure generation and dissipation was done in preparatory works for the foundation of Ekofisk Tank in the North Sea (Bjerrum (1973) and Lee and Focht (1975)). For this purpose, cyclic triaxial tests were performed in which after 12.5 and 50 cycles the pore pressure was released by 10%. The undrained number of cycles was limited to 12.5 and 50, since using an average wave period of 10 seconds, the total time during 12.5 and 50 cycles was approximately the drainage time for pore water under the tank in case of radial drainage and horizontal drainage respectively. After the intermediate drainage of 10%, the cyclic loading was continued in undrained conditions. After the intermediate drainage, the pore pressure generation during the subsequent cycles was largely reduced. The number of cycles up to liquefaction even doubled for some tests (figure 2.9). From the tests it was concluded that the preshearing effect could not only be caused by the slight increase in density, but should be related to a change in the structural arrangement of the grains as well (Lee and Focht (1975)). Due to the cyclic loading, the grains will be able to refine the packing in order to eliminate potential instabilities in the soil skeleton. This occurs without a significant change in the void ratio and is only observed in cyclic shear loading (Song (1990)).

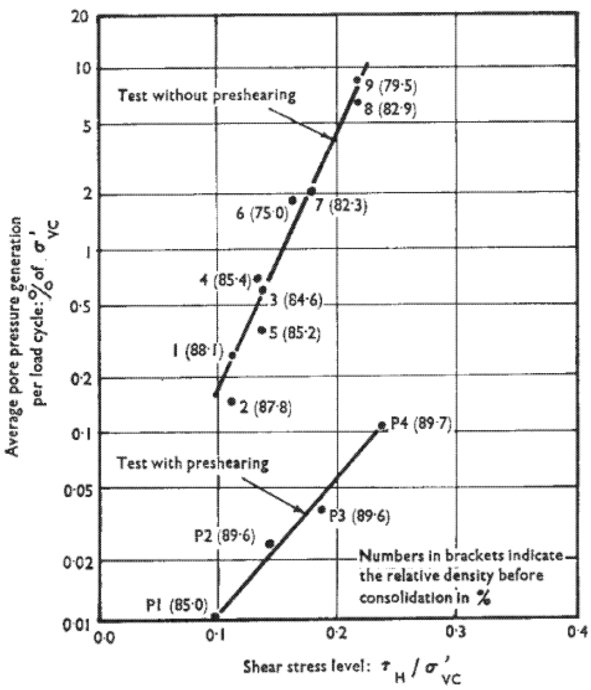

Figure 2.9: *Influence of preshearing on pore pressure increase during cyclic loading, based on samples with relative density of 80% (Bjerrum (1973))*

However, it was also noticed that the effect of preshearing and the reduced generation of excess pore pressure after (partial) drainage, does only occur if the load conditions in terms of shear stresses and shear strains remain below a certain limit (around 0.5% cyclic shear strain, Meijers and Luger (2012)). Finn et al. (1983) found a similar threshold value of the shear strain below which strengthening of the soil was found after reconsolidation, but above which the soil liquefied even faster. The results showed that when the shear strain is limited to the threshold value, the number of load cycles to full liquefaction increases after intermediate drainage, at least for relatively densely packed soils during contractive behaviour.

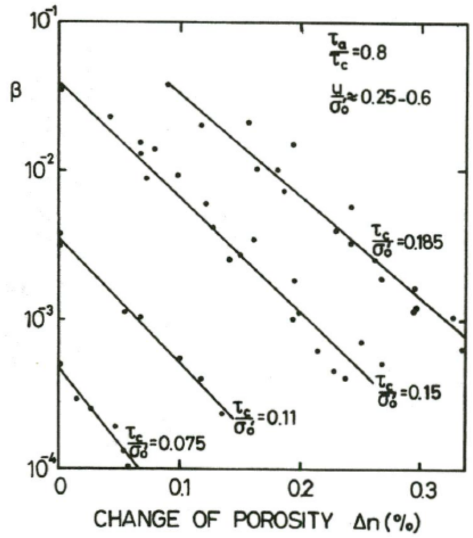

Figure 2.10: *Reduction of β with decreasing porosity (defined positive) (Smits et al. (1978))*

If the shear strain exceeds the threshold value, this number of cycles decreases even though the soil has been able to re-consolidate in between. Oda et al. (2001) proposed that the decrease in the number of cycles in case of shear strains above the threshold, is due to the shear bands with large void ratios that develop, which was also found in discrete element modelling. In the next load cycle, these large void ratios will suddenly be filled with soil particles, and a quick increase in pore pressure is developed.

According to Smits et al. (1978), a relation between the volumetric strain ϵ_{vol} and the shear strain γ can be formed using the elastic stiffness moduli, which relates incremental volumetric strain changes to incremental distortional changes. In undrained cyclic triaxial tests with intermediate drainage stages, Smits developed a relation to analyse the effect of preshearing. The preshearing is expressed as a change in porosity in the already applied load cycles (a decrease, which is defined to be positive), versus the loading expressed as the ratio of pore pressure increase over initial mean effective stress per load cycle, expressed in a normalised pore pressure generation coefficient β (figure 2.10).

Analysing the results, a logarithmic relation is obtained (Meijers and Luger (2012)) to relate the decreasing porosity to the pore pressure generation term (equation 2.4). The pore pressure generation term A represents the case without any preshearing or intermediate drainage, in that case Δ n is zero. The exponent of $X\Delta n$ represents the effect of preshearing and β the pore pressure increase per cycle ($\beta = \Delta r_u/\Delta N$). The value of X is an empirical constant which was determined by Meijers and Luger (2012) using tests of Bhatia (1982) with increasing stress amplitude, which was not included in the tests of Smits, which where based on a constant load amplitude. Based on the tests of Bhatia, a value for the preshear parameter X of 200-250 was found.

The equation can be rewritten to represent the increase in the number of load cycles to full liquefaction as a function of the porosity decrease (equation 2.5). However it should be noted that formula 2.4 is based on tests with intermittent drainage. In reality, continuous drainage will be present during cyclic loading. Equation 2.5 is only applicable if the shear strain remains below the mention threshold, and is furthermore only applicable to contractive behaviour under cyclic loading.

$$\beta = 10^{A+X\Delta n} \tag{2.4}$$

$$N_{liq} = N_{liq,0}10^{-X\Delta n} \tag{2.5}$$

With:

A = pore pressure generation term without preshearing and without drainage [-]
β = $\Delta r_u/\Delta N$ increase in relative pore pressure per cycle [-]
N_{liq} = number of undrained load cycles to full liquefaction [-]
$N_{liq,0}$ = number of load cycles to full liquefaction without preshearing [-]
X = preshear parameter or history parameter [-]

Threshold value for densification
Claimed by many researchers, a threshold value for both the cyclic shear stress and cyclic shear strain exists below which no densification occurs. If two spheres are considered, representing soil particles, a threshold value can be determined by exerting a shear force on one of them and finding the shear strain after which irreversible shearing occurs (the Hertz model, Meijers (2007)). This shear strain can now be related to the shear stress and shear force, leading to a threshold value for shearing and densification.

Based on this model, the threshold shear strain increases with increasing stress level (depth) but decreases for an initially present shear stress. Based on literature values for sand, the threshold varies between $0.5 * 10^{-4}$ and $1.0 * 10^{-4}$. These values however, are often based on extrapolation of data, and the values may well get within the measuring accuracy (Meijers (2007)). Especially for large numbers of cycles, still some densification will occur, indicating that the volume strain won't be zero in this case and no real threshold can be defined. The theoretical cyclic shear stress amplitude (CSSR) threshold however, which was derived to be 0.6, does not agree with measured values between 0.05 to 0.1.

2.3. Liquefaction

2.3.1. Definition

As mentioned in the introduction, an often used definition of liquefaction is given by the workshops on the evaluation of liquefaction resistance of soils of the National Center for Earthquake Engineering Research (NCEER) is "the act or process of transforming any substance into a liquid" (Youd et al. (2001)). The increase in pore pressure comes from the tendency of relatively densely packed granular soils to contract under cyclic loading, as was investigated in the previous section. Liquefaction may lead to large displacements or even complete failure of the soil or structure, depending on the size and location of the liquefied areas, and therefore plays an important role in marine structures. Since the definition matches the soil behaviour from the previous section, there is no need to use another definition.

In general, two types of liquefaction can be distinguished (Robertson (2000) and Robertson (2010)): flow liquefaction in loose soils in which strain softening leads to a reduction of shear strength quickly. In this behaviour the load can often not reduce, for instance in slopes with loosely packed sand. This results in a large scale movement, with little warning and rapid development. In literature this type of liquefaction is often denoted as flow liquefaction, indicating that the failure results in a flow slide of a significant amount of material from a slope or embankment. Flow liquefaction may be found in literature under the name of static liquefaction, pointing to the load conditions resulting in flow liquefaction: a monotonic, static load is often the trigger for flow liquefaction. The other type of liquefaction is the cyclic liquefaction, which even occurs in dense sands. This type results in accumulation of pore pressures and settlements during each load cycle, with a resulting loss of soil stiffness. For the latter process it is not necessary that the soil reaches complete liquefaction to cause stability problems. The reduction of shear stress by cyclic pore pressure build-up may be significant for the foundation stability.

It is noted that an undefined area is still present in between static and cyclic liquefaction: the trigger to the instability in case of static liquefaction does not necessarily have to be static, it can also be a cyclic load, as long as the process towards the instability is monotonic. This is for instance the case in a contracting sand close to the unstable stress situation under cyclic loads. The trigger for flow liquefaction results in an unstable situation, which cannot be turned back to a stable stress situation, while for cyclic liquefaction the stress situation after removal of the cyclic load may still be stable. In this study the focus will be on the cyclic liquefaction type.

2.3.2. Excess pore pressures

The increase in pore water pressure is named the excess pore pressure (EPP), and is the difference between in the actual pore water pressure and initially present hydrostatic pressure. In relation to marine structures, full liquefaction with zero effective stresses will hardly be relevant (De Groot et al. (2006b)). However, partial liquefaction may already reduce the shear strength significantly and may lead to large deformations.

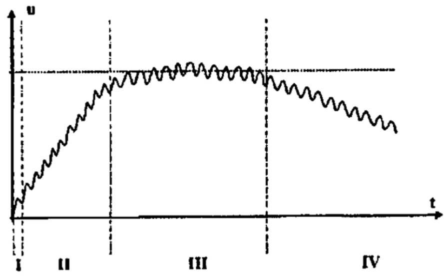

Figure 2.11: *Excess pore pressure development in time (De Groot and Meijers (2004))*

The pore water pressures under cyclic loading can often be separated in a fluctuating part and a residual part. The fluctuating part of the pore pressures is named transient or instantaneous pore pressure and has a relation with the loading at each single time step, for instance due to waves (Finn et al. (1983)). Next to the transient part, an increase in average pore pressure may develop, increasing during each load cycle or decreasing during drainage processes. These pore water pressures are named residual pore water pressures, and do not have a unique relation with the varying load at each time step. The residual pressures depend on the load conditions however, such as load duration and load amplitude. Furthermore, the residual pore pressures are largely influenced by the soil conditions, which determine the pore pressure generation and dissipation mechanisms. An example of the process of excess pore pressure generation is given in figure 2.11. The instantaneous pore pressures are fluctuating with the load, while the residual pore pressure is gradually increasing or decreasing. The different processes during the pore pressure development are described using figure 2.11 (De Groot and Meijers (2004)) in undrained conditions.

Stage I — Instantaneous pore pressures develop, due to elastic compression of the soil skeleton.

Stage II — Residual pore pressures develop, caused by effects of soil contraction due to cyclic shear. Furthermore, a decreasing stiffness of the soil skeleton should be taken into account, due to the decreasing effective stress.

Stage III — Drainage and generation of pore pressures together increase the excess pore pressure in stage II, eventually reaching zero stiffness and full liquefaction. A quasi-static stage is reached.

Stage IV — The drainage results in a decrease in soil skeleton volume and an increased density, increasing the liquefaction resistance (number of cycles). The generation of pore pressure therefore decreases in time and drainage of pore pressure is dominant over generation. Additionally, a stiffening or hardening of the soil occurs, which is named preshearing (section 2.2.6).

From literature lots of wave-induced and earthquake liquefaction assessments are known. Waves induce cyclic loads at the seabed, while they also induce instantaneous pressure variations at seabed level, leading to transient or residual pore pressure variations. The first is more interesting to upper soil layers around marine structures, while the latter is more relevant for residual pore pressure build-up in deeper layers with limited drainage. The first type is limited by the wave geometry, which is limited by the seabed topography, and will consequently not result in full liquefaction, as will be demonstrated in section 2.4. Full liquefaction due to residual pore pressures is rarely seen in literature (De Groot and Meijers (2004) and Kudella et al. (2006)). Based on analysis of more than 20 failures experienced by vertical caisson breakwaters by Oumeraci (1994), it was concluded that full liquefaction is never observed due to residual pore pressures only. This study showed that the geotechnical failure modes play a significant role in the final failure, while the residual excess pore pressures did not induce failure on its own. It was however stressed that the combined action of structure motions and residual deformations may lead to large build-up of excess pore pressure and consequently failure.

For earthquake loading however, drainage is not possible due to the very short periods of loading with horizontal accelerations, with approximately undrained behaviour as a result. Under wave loading, the soil won't behave completely undrained, due to relatively large wave periods and longer storm duration and consequently intermediate drainage. Earthquake loading therefore results in a fast build-up of residual pore pressure. Next to the difference in drainage conditions, for a marine structure it is highly probable that it will experience minor storm conditions before the design storm occurs. This will in general strengthen the liquefaction resistance of the soil (section 2.2.6). For earthquake loading the probability of strengthening due to smaller earthquakes is very low.

2.3.3. Liquefaction failure types

One of the first who separated various liquefaction failure types was Robertson (Robertson (1994) and Robertson (2010)). The two types are flow liquefaction and cyclic softening (2.12), the latter being subdivided depending on the size and duration of loading. If shear stress reversals are present, i.e. if the average value of the shear stress remains low, the vertical stresses may completely vanish and cyclic liquefaction will occur. If shear stresses do not reverse, if an average shear stress level is present, cyclic mobility will occur where the excess pore pressures cannot increase up to the level of the vertical stresses, since the phase transformation is reached: the contractive behaviour changes into dilative behaviour. This is in agreement with the described soil behaviour in undrained conditions under cyclic loading. Furthermore, the monotonic or cyclic trigger is indicated for flow liquefaction, resulting in an unstable situation which cannot be turned back. For cyclic softening the situation is not unstable initially, after removing the load the situation will still be stable.

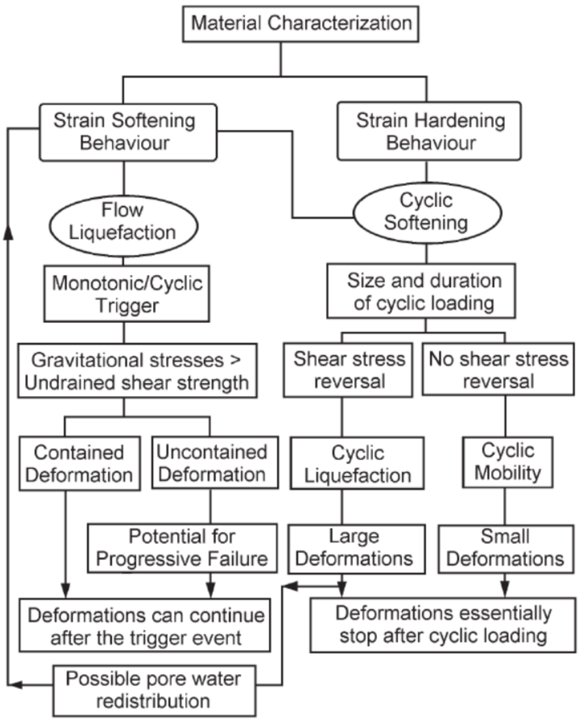

Figure 2.12: *Chart for the evaluation of liquefaction Robertson (2010)*

By De Groot et al. (2006b), a subdivision is made in four liquefaction failure types, mainly relating to marine structures. The first two are representing the two types defined by Robertson:

- Liquefaction flow failure: foundations experience large continuous deformations due to loss of effective soil stresses, driven by excess pore water pressures.
- Stepwise liquefaction failure: foundation displacements occur stepwise due to significant residual excess pore pressures. Instantaneous pore pressures do not play a role. The residual excess pore pressure induces a stress state on the failure line.
- Stepwise failure: failure due to the development of instantaneous pore pressures (no residual pore pressures), leading to a stepwise displacement of the foundation. It is thus possible to reach the failure line only by a large shear stress in undrained conditions, reaching the failure line in a few load cycles without significant residual pore pressure.
- Wobble failure: failure due to large instantaneous cyclic shear strains causing large cyclic deformations. The shear strains at the failure line can be far larger than the shear strains in the cycles where the failure line is not yet reached. The deformations during wobble failure are non-permanent.

Some basic soil properties related to drainage will be introduced to connect these properties with the most relevant failure mechanisms. The effect of drainage on pore water pressures should be taken into account, since in reality hardly any soil behaves completely undrained. Drainage can only take place if the time needed to drain the pore water pressure is shorter than the period to generate the pore pressure. The characteristic drain period can be calculated for sandy soils, with equation 2.6 and 2.7.

$$T_{char} = \frac{h^2}{c_v} \tag{2.6}$$

$$c_v = \frac{k}{\gamma_w (m_v + n\beta)} \tag{2.7}$$

T_{char} = characteristic drainage time [s]
h = flow distance to drain [m]
c_v = consolidation coefficient [m^2/s]
k = hydraulic permeability [m/s]
γ_w = volumetric weight of water [kN/m^3]
m_v = coefficient of compressibility [1/kPa]
n = porosity [-]

A short application of this theory to the earlier mentioned failure types will be discussed below.

Liquefaction flow failure:
This type of failure needs high residual pore water pressures, which can only develop if the characteristic drainage time is relatively large. Otherwise, intermediate drainage will occur with densification of the soil as a result, increasing the liquefaction resistance and preventing liquefaction flow failure further. Furthermore, it requires an initially very loose packing of the sand and a continuous monotonic loading. The liquefaction flow failure does not include any dilative effects, and assumes monotonic contraction.

Stepwise liquefaction and wobble failure:
During failure the soil deformations induces negative pore pressures, which increases the effective soil stresses and therefore strengthens the soil. This limits the shearing during a single (extreme) load cycle, but will not limit the shear strains during other cycles. Therefore these other cycles may cause residual shear strains inducing stepwise deformations. This is called cyclic mobility.

The conditions for cyclic mobility to occur, are:

- The necessity to have dilation during the state of cyclic mobility, which is in general only the case for soils with medium to large densities I_d, i.e. soils that have already densified a lot in the contractive zone up to point on the failure line.
- A limited amount of drainage, since pore water pressures have to build-up during densification, in order to reach the dilative zone and create the necessary negative pore pressures, which finally increases the effective stresses in the soil and the increase in soil strength. Whether the soil behaves undrained during a single load can be checked using $T_{char}/T_{load} > 5-20$ (De Groot et al. (2006b)).
- A sufficiently high value of the residual excess pore pressure and shear stress amplitude should be present to reach the failure line. If for instance the shear stress amplitude is limited, a higher residual pore pressure is necessary to get to the failure line. In figure 2.13 this is indicated with points B and C: for point B the failure line is reached with high pore pressures, while point C has less pore pressures and therefore needs a larger CSSR value to reach the failure line.

The four failure types are visualised in figure 2.14.

2.4. Liquefaction of a horizontal seabed

Yamamoto (Yamamoto et al. (1978)) derived the soil response to water waves travelling above a non-cohesive seabed in an analytical way, based on the theory of Biot, which takes into account both the (elastic) stiffness of the porous medium and the stiffness of the pore water and the flow of water trough the porous medium, using Darcy's theory. In this case, the pressure increase due to water waves is assumed to be small compared to the hydrostatic case, and therefore linear elastic behaviour is assumed for these small stress increases. A system of 3 partial differential equations is solved using appropriate boundary conditions at the soil-water interface

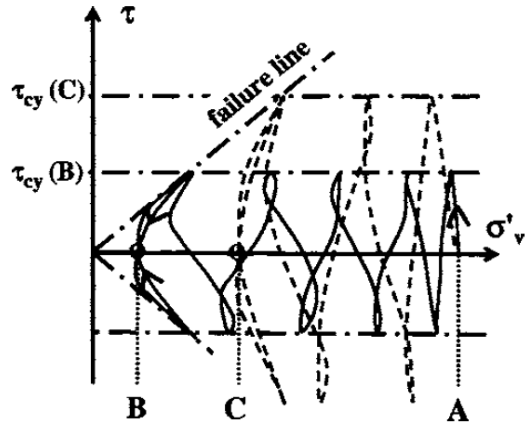

Figure 2.13: *Residual excess pore pressures and CSSR value determines whether the failure line is reached (De Groot et al. (2006a))*

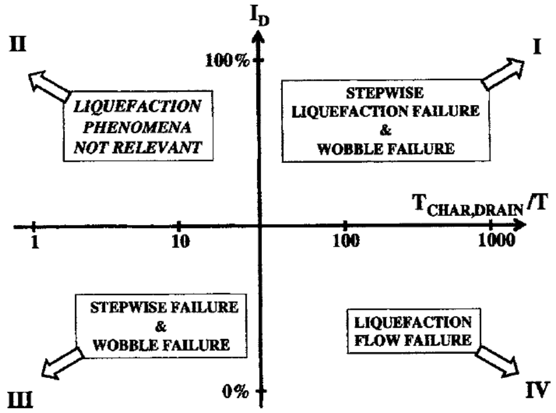

Figure 2.14: *Failure types, determined by relative density index I_d and relative characteristic drainage time T_{char}/T, with T a characteristic period for the cyclic load, based on De Groot et al. (2006b)*

and at the infinitely deep bottom layer, all in terms of horizontal displacement u, vertical displacement w, and pore water pressure p. The external forcing (figure 2.15) by the water wave is assumed to be in the form of a sinusoidal signal. The applied signal at the soil-water boundary is given in equation 2.8, with k the wave number and ω the radial frequency, and with amplitude as indicated in equation 2.9.

$$p = p_0 \sin(kx - \omega t) \tag{2.8}$$

$$p_0 = \frac{\gamma_w H_{wave}}{2\cosh(kd)} \tag{2.9}$$

p	= instantaneous wave pressure at seabed [kPa]
p_0	= amplitude of wave pressure at seabed [kPa]
k	= wave number $2\pi/\lambda$ [1/m]
λ	= wavelength [m]
ω	= radial wave frequency [rad/s]
γ_w	= volumetric weight of water [kg/m^3]
H_{wave}	= individual wave height [m]
d	= water depth [m]

Considering completely saturated soils, for which the shear modulus G over bulk modulus K approaches zero, at least if the water contains no gasses and the soil is not too dense (G small), this finally results in an exact solution to the problem. The result is given in three exact solutions (Yamamoto et al. (1978)) for the horizontal displacement u_{soil}, the vertical displacement w_{soil} and the pore pressure development (equation 2.10). Only the last is presented here:

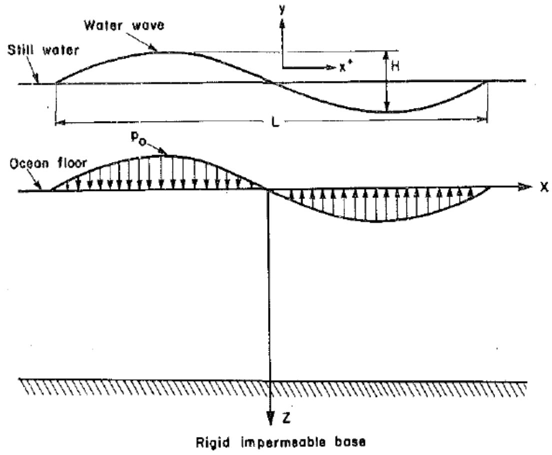

Figure 2.15: *Wave pressure on sea floor (Seed and Rahman (1978))*

$$p = p_0 - kz\exp(-kz) \tag{2.10}$$

As can be seen in equation 2.10, the pore pressure attenuation for increasing depth is small, and only determined by the wave number and not by the permeability. This is due to the fact that G/K is assumed to approach zero, which is approximately the case for completely saturated soil with incompressible pore water. For partially saturated dense sands, formulas were derived showing larger attenuation of pore pressure inside the seabed. Equation 2.10 is similar to the equation obtained earlier by Putnam (1949). Yamamoto et al. (1978) also obtained an expression for partially saturated dense sand with compressible pore water, i.e. resulting in a soil stiffness much larger than pore water stiffness, showing that the attenuation is much larger for this case and also largely determined by the permeability of the soil. Thus the compressible pore water does not travel that deep into the seabed compared to incompressible pore water. Furthermore, a phase delay in the pore pressure response was found increasing linearly with depth. So given the two extreme cases of dominant soil stiffness or dominant pore water stiffness, the transmission of the pore pressures and the stresses and deformations of the soil fall somewhere in between. Using the deformations of the soil body, the effective stresses were calculated using Hooke's law, using linear elastic behaviour, which finally resulted in the amplitudes of vertical, horizontal and shear stresses due to a single wave load as a function of depth (equation 2.11).

$$\Delta\sigma_x^{'} = -\Delta\sigma_z^{'} = \Delta\tau_{xz} = p_0 kz\exp(-kz) \tag{2.11}$$

With the symbols previously defined, and with:

$\Delta\sigma_x^{'}$ = amplitude in horizontal effective stress [kPa]
$\Delta\sigma_z^{'}$ = amplitude in vertical effective stress [kPa]
$\Delta\tau_{xz}$ = amplitude in shear stress [kPa]

The displacements, water pressure and effective stresses are plotted in the left figure of 2.16. Differentiating the relative shear stress τ_{xz}/p_0 to z, shows that a maximum is located at kz below seabed with a value of $0.36p_0$, shown with the dashed red line in the right figure of 2.16, also indicating the vertical distribution of relative pore pressure and relative shear stress. The solutions of Yamamoto et al. (1978) were validated in wave tank tests in the Delft Hydraulics Laboratory, which showed good agreement between the theory and the measurements. The same was found in the earlier experiments by Putnam, where especially the sandy bottoms showed a good agreement with the derived formulae.

Taking into account the negative exponential attenuation of pore pressure with depth, the pore pressures directly beneath the seabed when a wave crest is passing is vertical downwards, while it is vertically upwards under a wave trough. Under the wave crest, the increased pressure at the seabed will instantly induce a downward directed flow into the seabed, while under the wave trough, an outflow of pore water will occur.

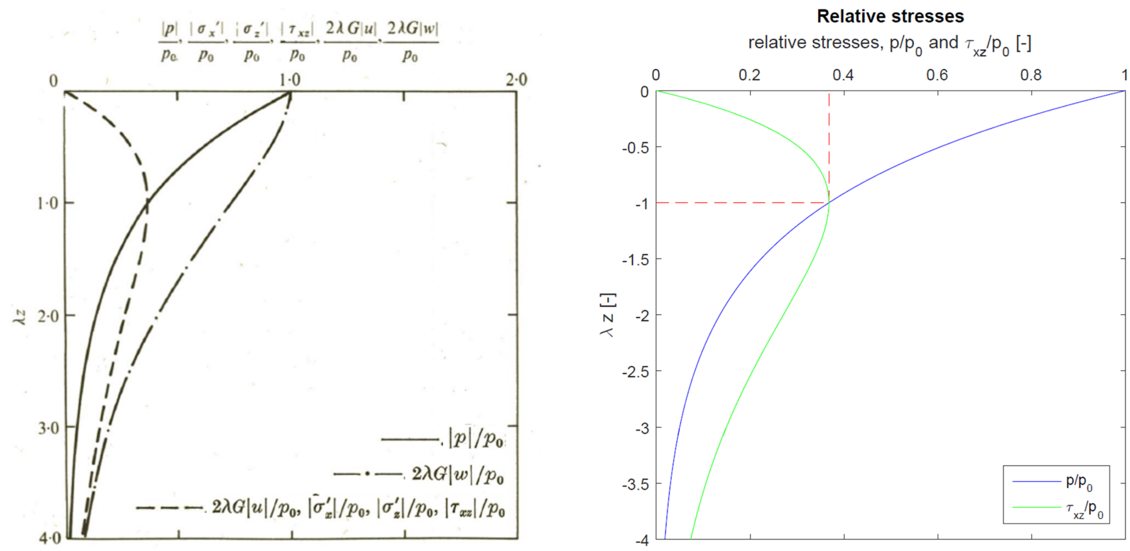

Figure 2.16: *Vertical distribution of the amplitudes the pore-water pressure, the effective stresses, and the displacements for the limiting case G/K approaches zero (left, based on Yamamoto et al. (1978)) and vertical distribution of relative pore pressure and relative shear stress and its maximum at $kz = 1$ (right)*

Under the wave crest the effective stresses are largest, while under the wave trough they are smallest, resulting in the highest liquefaction potential underneath the trough (De Groot et al. (2006a)). No shear stresses are induced at the moments of wave crest and wave trough, however they are at intermediate point between crest and trough (at the nodes). At these point the flow in the seabed is purely horizontal inducing cyclically varying shear stresses, in magnitude equal to the vertical stresses induced under crest and trough (figure 2.17). These shear stresses are exactly the stresses causing the soil to densify, resulting in the residual pore pressure build-up. As was already clear from formula 2.11, the magnitude of the horizontal, vertical and shear stresses are equal, showing that the principal stresses continuously rotate when a wave travels by.

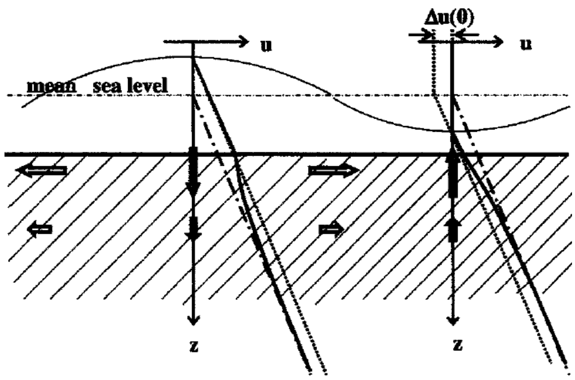

Figure 2.17: *Instantaneous pore pressures and pore flow under waves with incompressible pore fluid (De Groot et al. (2006a))*

It can now be investigated whether the instantaneous or transient wave pressure travelling over a horizontal seabed may actually induce liquefaction. For large wave lengths the wave induced pressure at seabed level reaches a maximum when $\cosh(kd) = 1$. Depending on the wave breaking criterion, for instance breaking at wave heights between 0.5 to 0.75 times the water depth (Holthuijsen (2007)), the pressure at seabed level reaches values between 0.25 to 0.38 times the hydrostatic pressure at seabed level. Taking into account that the maximum relative pore pressure below seabed is 0.36 p_0, which was derived in the right figure of 2.16, the instantaneous excess pore pressures can only reach 9-14% of the hydrostatic pressure. So even in case of very unfavourable waves, the instantaneous excess pore pressure remains relatively low, showing that (instantaneous) liquefaction of a horizontal seabed under a wave crest (where the maximum upward pressure occurs) is not very likely.

2.5. Liquefaction of marine structures

Before applying the theory to a gravity based foundation for an offshore wind turbine, some examples of structures and their liquefaction assessment from literature will be discussed. The first one is the Ekofisk Tank and the second wave loaded caissons. In addition to this, results from scale tests about soil-structure interaction is presented and measures to reduce liquefaction potential.

2.5.1. Ekofisk Tank

The often mentioned structure in literature that has been investigated extensively for liquefaction, is the Ekofisk Tank in the North Sea. The tank was designed as a production platform with oil storage possibilities. NGI (Bjerrum (1973)) developed a method to assess the pore pressure build-up during the design storm with a return period of 100 years. The storm builds up over a period of 6-9 hours, with a full length of about 3-9 hours, building off in the final 6-9 hours (figure 2.18 left). A linear relation was assumed between the wave height and the cyclic shear stress ratio, which has been determined for each wave height present in the design storm. The distribution of wave heights in the storm has been based on statistics. For a single wave the pore pressure generation was calculated, based on the already presented figure 2.9, derived from laboratory tests. The total pore pressure is summed up, resulting in a total pore pressure of 31% (figure 2.18 right). Bjerrum did not include any updated soil stiffness during pore pressure generation, and did also not include pore pressure dissipation.

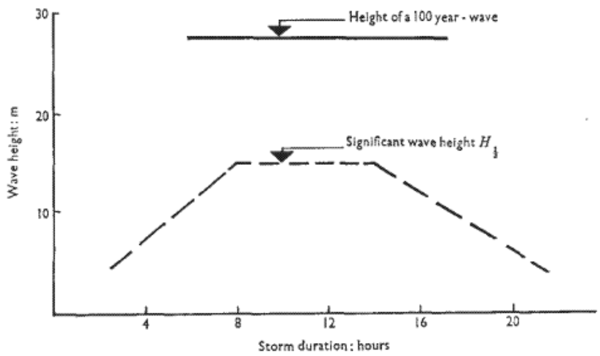

Height of waves: m	Number of waves, N	$\frac{\tau_H}{\sigma'_{vo}}$	β: % (From Fig. 31)	$\frac{\Delta u}{\sigma'_{vo}} \cdot N$: %
4–8	485	0·07	0·006	2·9
8–12	471	0·12	0·013	6·1
12–16	282	0·17	0·030	8·5
16–20	121	0·22	0·065	7·9
20–24	32	0·26	0·150	4·8
24–26	3	0·30	0·300	0·9
Total	1394			31·1

Figure 2.18: *100 year design storm used for pore pressure build-up calculations (left) and wave heights and number of waves, associated shear stress and pore pressure generation (right) (Bjerrum (1973))*

Lee and Focht continued on the Ekofisk terminal (Lee and Focht (1975)). They used the same 100 yr. design storm and derived multiple other design storm with lower return periods. The design curves for these storms were then compared to the cyclic strength curves of the soil from laboratory data. The strength curve of the soil should then be able to withstand the design storm for each number of load cycles. Using this approach it was also clear that the Ekofisk tank was able to resist the 100 yr. design storm (figure 2.19), however only for a relatively density of 100%. Lee and Focht finally also included the effect of preshearing.

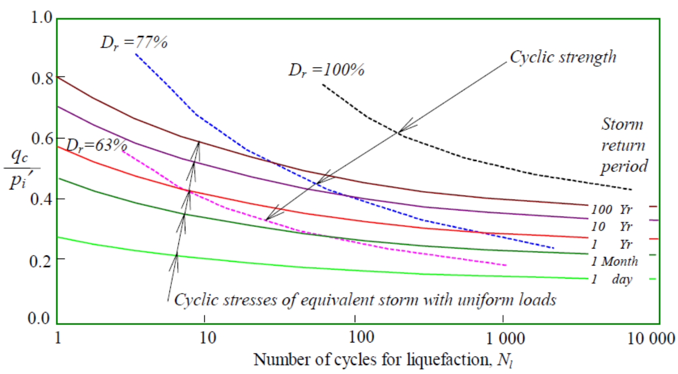

Figure 2.19: *Cyclic strength of soil versus design storms with various return periods. Taiebat (1999), based on data of Lee and Focht (1975)*

In addition to these investigations, Taiebat (1999) presented a comparison of results from Bjerrum (1973) and Seed and Rahman (1978), based on the Ekofisk tank as well (figure 2.20). The calculations from Bjerrum did not include drainage, however the calculations from Seed&Rahman did. For a relative density of 85%, Bjerrum's results indicated full liquefaction at the edge of the tank, but below the centre of the tank excess pore pressures would only reach 32%. However, these are still expected to be overestimated values due to the missing drainage. The model by Seed&Rahman predicted only 22% excess pore pressure at the edge, while only 6% would be reached at the centre. All values were predicted at the peak loading of the storm. The result show an interesting phenomenon: the largest relative excess pore pressures were found just outside the base area of the tank, where drainage conditions are expected to be better and therefore excess pore pressures lower. This will be compared later in this research with the observations for the gravity based foundation (GBF) with offshore wind turbine (OWT).

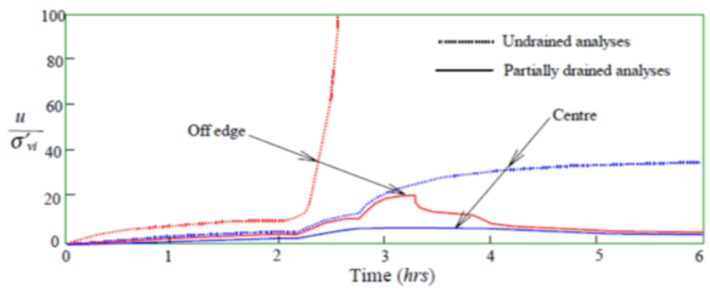

Figure 2.20: *Predictions of relative excess pore pressures (in percentages) at the edge and centre of the Ekofisk tank by Bjerrum (both undrained) and Rahman (both partially drained) (Taiebat (1999))*

The Ekofisk tank was installed on the seabed in June 1973. The pore pressures and settlement of the structure were measured during multiple storms. The structure was exposed to some minor storms first, after which the most severe storm occurred in November 1973. The measuring devices were at that time out of order. The heaviest storm during measurements was in November 1973, during which a wave height of 16 meter resulting in pore pressure increases up to 10-20 kPa.

2.5.2. Wave loaded caisson

Based on large scale model tests in the research program of Liquefaction around Marine Structures (LIMAS) some interesting conclusions can be drawn on the cyclic wave loading on caissons. Within the tests the main focus was on the various modes of interaction between the caisson and the soil, as described in Kudella et al. (2006). The resulting modes of interaction (figure 2.21 left) between soil and structure will be discussed below, and are:

- Wave motion mode: wave motions in terms of pore pressures are directly transferred to the foundation, resulting in time dependent pore pressures, both instantaneous and residual. This mode is mainly determined by the wave characteristics and the local water depth. The wave loads can either be of relatively low frequency (non-breaking), or of relatively high frequency in case of breaking wave loads on the caisson. The transmission of wave pressures into the subsoil is also determined by the porosity of the rubble mound (figure 2.21, second from left).
- Structure motion mode: the movements of the structure by the external loads, in this case wave loads, are transferred to the soil as total stresses. This mode is mainly determined by the loads and the characteristics of the structure and its foundation, determining the stresses at the structure-soil interface. The structure might experience oscillatory motions or small permanent displacements due to single extreme loads. The structure movements can be subdivided into sway (horizontal), heave (vertical) and rocking (rotational) (figure 2.21, second from right).

Superposition of both modes results in the loading at the seabed level (2.21 right). Furthermore, in terms of displacements, either oscillatory motions and permanent displacements can be found depending on the loads and the dynamic response of the structure. The total stresses at the seabed can also be subdivided into wave-motion induced pore pressures, and structure-motion induced normal effective stresses, shear stresses and pore pressures.

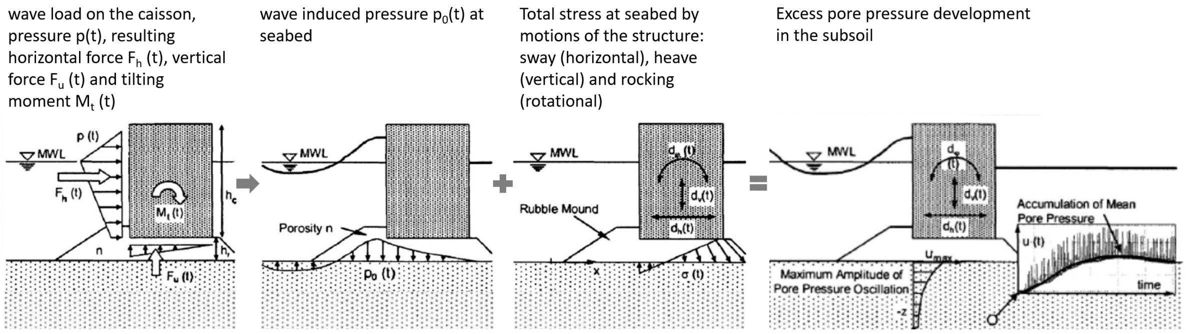

Figure 2.21: *Processes associated with the excess pore pressure development below a vertical breakwater loaded by waves (after Kudella et al. (2006))*

In the EU-funded LIMAS project (Liquefaction around Marine Structures) large scale model tests were performed to investigate the structure mode and the wave motion mode for a caisson breakwater case loaded by waves, with emphasis on the structure motion mode (Kudella et al. (2006)). Using pore pressure transducers and soil density rods the soil behaviour was measured during both pulsating wave loads and breaking wave impact loads. The soil conditions and drainage conditions correspond to a loose sand bed with a limited vertical permeability ($I_d \approx 0.4$), for instance due to thin clay layers. The main conclusions from the model tests are shortly described below. In order to describe the results, the caisson side loaded by waves will be named *sea side*, and the side not loaded by waves the *shore side*.

In general, the pore pressures beneath the structure shows a close correlation with the vertical movements of the structure (the structure motion mode) induced by wave loads. Especially the shoreward side of the structure shows larger transient pore pressures than at the seaward side, corresponding better with the movement of the structure. The largest excess pore pressures are found at the shore side since the soil is loaded in compression and the caisson moves downward, while the sea side is unloaded and the pore under pressures are limited due to the upward motion of the caisson at this side. For the sea side, the pore pressure developments show a correlation with a combination of wave pressure and structure movement. Furthermore, it was found from pore pressure measurements that the pore pressure response at locations outside the base area of the structure show a large correlation with the wave pressure itself (wave motion mode).

The following more specific conclusions were drawn as well (Kudella et al. (2006)):

- It was observed that the transient wave induced pore pressures are an order of magnitude smaller than the transient caisson induced pore pressures, at least for the shore side of the caisson. Consequently, it was concluded that the wave motion mode is of less influence on the transient pore pressure generation.
- A threshold value was found consisting of frequency and amplitude of the wave loads hitting the caisson, to generate any residual pore pressure. This threshold was in these large scale tests only reached in case of impact wave loads, since only these loads reach the threshold. For the pulsating wave loads no residual pore pressures were found.
- The development of residual pore pressures was found to be independent on the location beneath the caisson (seaside or shoreside or just outside the structure) (figure 2.22). The residual pore pressure generation can clearly be separated in an increasing stage, quasi-equilibrium stage and a drainage stage.

- A clear relation was found between residual settlements and residual pore pressure development (figure 2.23). The bending moments due to wave loads acting on the structure are compared to the pore pressure developments below the structure. A clear relation can be seen between the vertical caisson motions and the residual pore pressure. After a certain number of cycles the pore pressure starts to build-up, and the inflection point I can be defined when the residual pore pressure becomes significant, i.e. when the residual pore pressure start to increase faster than in the cycles before. The transient motions of the shoreward caisson edge start to increase at a higher rate as well at this point, which also holds for the transient pore pressures. The residual pore pressure ratio starts to decrease again after point S, but the residual soil settlement still increases. This could indicate that the pore pressure generation starts to decrease due to the continuous densification of the soil (Kudella et al. (2006)). At the peak of the residual pore pressure, the relative excess pore pressure (ratio with the vertical effective stress) was 0.25.

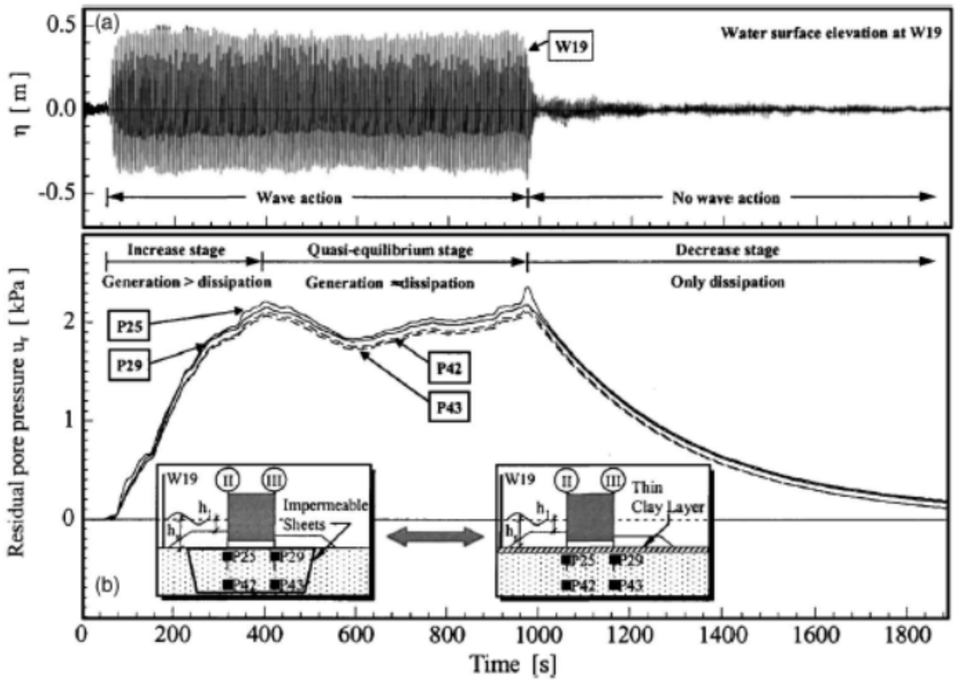

Figure 2.22: *Residual pore pressure developments beneath the caisson at different locations (Kudella et al. (2006))*

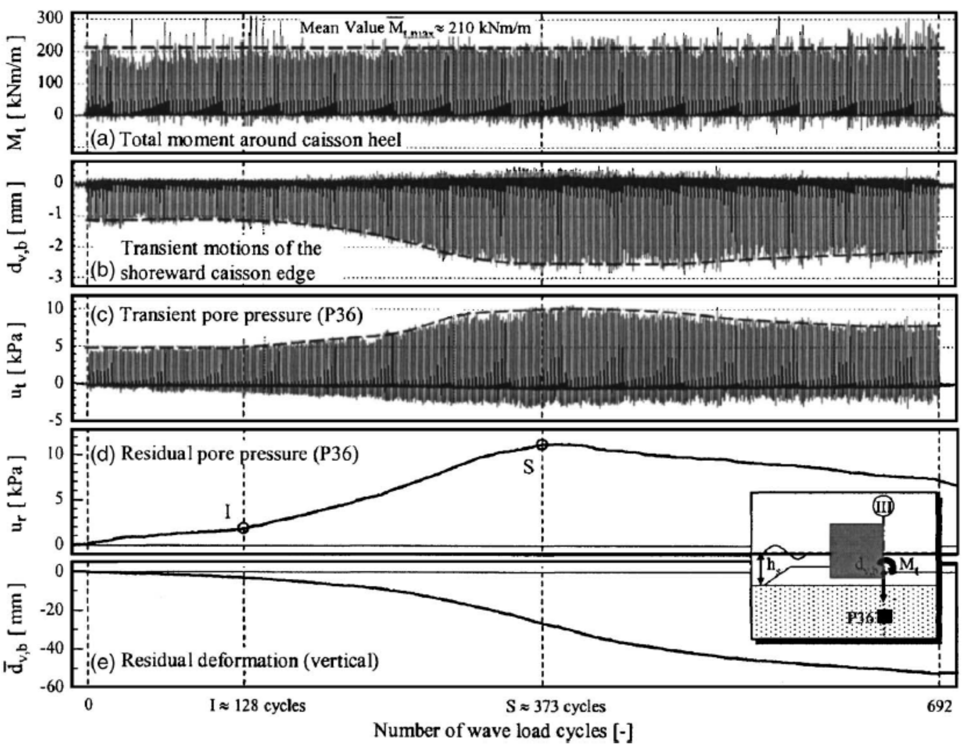

Figure 2.23: *Fluctuating moment due to wave loads (top), transient caisson motions and transient pore pressures (middle) and residual pore pressure and residual motions (bottom) (Kudella et al. (2006))*

Discussion of the results
From the model scale tests by Kudella et al. (2006), it can be concluded that the transient pore pressures are mainly related to the structure motion mode. The residual pore pressures did not seem to differ significantly between various locations below the structure, indicating that drainage is not significant. However, in the tests impermeable polyethylene sheets were used at the vertical and horizontal boundaries of the sand mass (figure 2.22). This was done to scale the drainage capacity correctly, and was assumed to represent thin clay layers. This might clarify why the pore pressures below the caisson do not differ between locations, since pore pressures are diffusing below the caisson and are not able to drain. It is still expected though that the pore pressure developments below the gravity based foundation for the offshore wind turbine shows differences between various locations, as a result of different drainage capabilities for the centre and edge of the foundation.

Furthermore, the breaking wave loads were the only source for residual pore pressure build-up, the pulsating wave loads did not induce residual pore pressures. There was a close correlation between the vertical caisson motions and the residual pore pressures, which might indicate that the breaking wave loads result in a vertical caisson motion from the cyclic bending moment, which subsequently results in residual pore pressure development in the subsoil. The question arises where the result of the cyclic shear forces at the soil-structure interface can be found back. Especially these loads are the driving force in excess pore pressure generation in literature, at least in element tests, and these indicate that also small load amplitudes may result in significant residual pore pressure, as long as a large number of cycles is applied. The breaking wave loads will have their impact at a higher level at the caisson wall, resulting in larger bending moments, indicating that these loads mainly induce a vertical load of the subsoil, which might ask for higher loads to induce any pore pressure. Horizontal loads might result in larger deformations and consequently larger pore pressures, but unfortunately no correlation between these loads and the pore pressure developments was made in this scale test. This might form a clarification why residual pore pressures were only induced by breaking wave loads.

From the tests it is concluded that the motion of the structure induced by the cyclic loads, has a large contribution to the excess pore pressures. The large contribution of the vertical motions induced by cyclic bending moments to the residual pore pressures is clearly shown. This loading type is especially relevant for the GBF with OWT, since the large bending moments resulting from wind loads might result in cyclic vertical movements of the GBF. It is still expected on the other hand that the horizontal shear forces at seabed also induce a significant contribution to the excess pore pressures, and consequently that not only extreme loads (breaking wave loads in this case) result in residual pore pressure.

Finally, it was found that the relative excess pore pressure did not increase above 0.25, indicating that even under these unfavourable drainage conditions full liquefaction is not to be expected. This was also found from the analysis of various marine structures that failed during storm loading (Oumeraci (1994)): in no single case full liquefaction was found to be responsible for failure, in all cases movements of the structure contributed.

2.5.3. Measures to reduce liquefaction potential

Several measures can be thought of to reduce liquefaction potential around marine structures:

Replace the top layer with a cover layer of a high permeability
By replacing the top layer of the soil with a relatively small layer of cover material with higher permeability compared to the original material, the drainage characteristics of the top layer are significantly improved. Within the design of the cover layer the focus should mainly be on the depth of the layer. The stability of the layer around the structure to be protected should however also incorporate the fluctuating wave pressures. Other factors that play a role, are (Seed and Rahman (1978)):

- Depth of the cover: an increase in depth reduces the pore pressure for the same permeability of the cover material.
- Permeability of originally present material: a higher permeability of the cover material increases the drainage capabilities of the top layer and reduces the liquefaction potential further.
- Permeability of cover material: the permeability of the cover layer does not significantly influence the pore pressure response. Therefore a cover layer of gravel or rock-fill will result in a reduction of liquefaction potential of similar size.

Densification of seabed
Several techniques are possible to densify sandy sea beds: vibroflotation, blasting, plate vibration, and dynamic consolidation (De Groot et al. (2006b)). The main principle is the same for every technique: induce the tendency of the soil to densify by means of cyclic shearing. The pore pressure should be able to drain off during or after the period of densification. If many fines are present, other solutions should be found, since the fines prevent the drainage and prevent the desired decrease in pore volume.

2.6. Concluding remarks

From the described deformations properties of sand various liquefaction types have been distinguished, based on a couple of boundary conditions: the type of loading (i.e. monotonic, cyclic), the drainage conditions (soil related, i.e. porosity and loading related, i.e. fast or slow) and the soil properties (i.e. relative density). These properties result in dilative or contractive behaviour and drained or undrained behaviour. In fact, the fully undrained behaviour won't occur in reality, but the drainage may be limited due to the soil properties or the speed of loading. Applying these boundary conditions to the gravity based foundation, the contractive soil behaviour with drainage is expected to occur, which holds for relatively densely packed sands (relative density higher than 50% according to De Groot et al. (2006b)).

From literature on scale tests for the EU-funded LIMAS project and research on more than 20 breakwater failures, it was found that the residual excess pore pressure build-up is not able to result in full-liquefaction. The motions of the structure may result in soil deformations that significantly contribute to the generation of pore pressure. It is therefore not expected that the residual excess pore pressure beneath the gravity based foundation for an offshore wind turbine results in full-liquefaction due to cyclic loading of the subsoil only. Therefore, the term of partial liquefaction is more appropriate for gravity based foundations, since the residual pore pressures will significantly increase but without reduction of the effective stresses to zero.

Relating the liquefaction types to the cyclic loading of a gravity based foundation for an offshore wind turbine, the cyclic liquefaction type is especially relevant. Flow liquefaction is not expected to occur, since drainage conditions will allow the subsoil to densify in the process of cyclic loading, particularly in the gradual build-up of loads in a storm. Even if very loose soil is present, this results in significant densification and finally in medium to dense sand, susceptible to cyclic liquefaction at the extreme loads. However, the settlements in case of loose soils resulting from the densification may then still result to problems related to serviceability. During cyclic loading the excess pore pressure is expected to rise, since drainage will not allow the pore pressure to flow off immediately, resulting in build-up and, using the definitions by De Groot et al. (2006b), resulting in stepwise liquefaction failure.

It is however possible that with a limited residual excess pore pressure (i.e. partial liquefaction), the extreme load cycle on the gravity base results in instability problems. If the failure line is reached in such an extreme load cycle, i.e. when cyclic mobility occurs, effects of dilation and negative pore pressures become relevant and might contribute significantly to the stability. Furthermore, for the extreme load cycle the shear strains should be limited to be able to count on the preshearing effect. Large shear strains are to be expected when the failure line is reached during a few extreme load cycles, and may partly be residual depending on the loading (symmetric or asymmetric). In this respect also the observed large movements of the breakwater failures can be declared, which can obviously not be declared by densification alone (Oumeraci (1994)). Whether cyclic mobility is reached should therefore be carefully assessed, since the stated requirements in section 2.3.3 can in fact be fulfilled in extreme loading, it is highly relevant for the gravity based foundation.

In order to analyse the problem further, it is desired to consider different modelling approaches for the cyclic loading of soils, starting with a broad scope but narrowing down to pore pressure developments in storm conditions. This will be the topic of the next chapter, where the basic capabilities of the models for this problem will be assessed and where an introduction to the available models will be given.

3

Modelling cyclic loading of sands

3.1. Introduction

In the previous chapter the deformation behaviour of soil was described. It has been linked to cyclic loading and the related liquefaction failure types. These types have subsequently be applied to cyclic loading of marine structures, including gravity based foundation as well, although still from a theoretical perspective. This research into cyclic loading of a gravity based foundation has however been placed within the theory, ans will be used later to relate outcomes from this research to the available theory again. It is now desired to make the approach more practical to start analysing the cyclic loading on a gravity based foundation, to be finally able to answer the research questions.

The starting point is a broad investigation of approaches to model excess pore pressures and settlements due to cyclic loading of marine structures, often applied to gravity based foundations. The aim is not to find the best approach for this purpose, but to place the approach that has been used in the DCycle model, developed by Deltares, between the other available models. The pore pressure generation model of Seed & Rahman (Seed and Rahman (1978)) is used in DCycle, and will subsequently be discussed. The other principles within DCycle will be explained afterwards. The proposed norms and standards from industry will finally also be discussed.

The aim of the models that will be discussed is in any case the modelling of cyclic loading of sands, specifically the pore pressure developments and settlements in the subsoil below and around marine structures.

According to (Lupea (2013)) three modelling approaches can be followed to assess the cyclic loading of soils and to investigate specifically excess pore pressures and settlements. These are the empirical, the constitutive and the hybrid models. These will shortly be introduced:

- *Empirical models*
  The fully uncoupled methods decouple the stresses and strains and the pore pressure build-up completely. First of all, the cyclic stresses are calculated, which serve as input for the pore pressure response. The pore pressure generation is based on empirical data from undrained cyclic triaxial tests, and does not model each load cycle separately but in terms of the total number of load cycles. An empirical formula is for instance the approach of Seed & Rahman (Seed and Rahman (1978)) which will be discussed in this chapter.
- *Constitutive models*
  In constitutive models each individual load cycle is modelled separately. These models are often embedded in a finite element package.
- *Hybrid models*
  The hybrid models use a combination of the empirical models and the constitutive models during the calculations. The accumulation of pore pressures is taken into account by an empirical model. Subsequently, the constitutive model is used during a few load cycles to assess the degradation of strength and stiffness.

The output of the constitutive model serves as input for the next batch of cycles in the empirical pore pressure model. It is possible to take the dependency of soil stiffness versus mean effective stresses into account, however this leads to an expensive procedure of calculations. Finally, according to Safinus et al. (2011) the steps in the hybrid models can be separated into implicit and explicit procedures, with the implicit procedures representing the steps in the constitutive model, and the explicit steps the pore pressure development in an empirical model.

3.2. Challenges in modelling

Three major challenges exist in the modelling of excess pore pressures and settlements under cyclic loading, which in fact holds for both cohesive and non-cohesive soils. Although the settlements under cyclic loading won't be investigated in this research, the related challenges in predicting settlements are closely related to excess pore pressures, and therefore also included in this overview. These challenges also hold for cyclic loading of marine structures in general, and also for the gravity based foundation for an offshore wind turbine. The challenges are the load history, the number of cycles (to be subdivided into settlements and pore pressure response) and the random or irregular nature of the loading. These will subsequently be discussed.

The load history
The main design criteria for an OWT are the stability and operability during its entire lifetime, often 25 years. Considering the subsoil, the stability is related to pore pressure development and the operability is related to settlements of the foundation and possible tilting caused by differential settlements, influencing the operability of the wind turbine. In regular engineering practice the stability and operability of the structure is proven with static monotonic loads, but for cyclic loads the soil conditions change continuously due to processes of consolidation and drainage. The load history therefore determines the initial densification and initial excess pore pressure of the subsoil before the design storm occurs, and plays a major role in the stability assessment in extreme conditions (Pederstad et al. (2015)).

Number of cycles
For a lifetime of 25 years and for instance a cyclic load period of 7 seconds for waves, the number of cycles already becomes 112 million. The number of cycles can be largely reduced by a threshold definition, below where no densification and pore pressure build-up occurs. Even then the number of cycles still remains high, resulting in unacceptable calculation times. The number of cycles is relevant for the settlements and for the pore pressure build-up, described below:

- Settlements
  Due to cyclic loading accumulation of strains will occur, resulting in permanent strains and settlements. A large number of cycles can be modelled with a High-Cycle Accumulation (HCA) model (Safinus et al. (2011)). This model predicts the strain accumulation of non-cohesive soils for a large number of cycles ($N > 10^3$) with small strain amplitudes ($\epsilon < 10^-3$). The HCA model can for instance be implemented in a Finite Element Model (FEM). The method can also take the pre-loading history into account. However, the model asks for uniform cyclic loads, and therefore the irregular nature of the loads cannot be taken into account.
- Pore pressure build-up
  Modelling the soil behaviour under cyclic loading in terms of effective stress requires knowledge about pore pressures, generated by the cyclic load. To model pore pressure build-up, constitutive models have to deal with a large number of load cycles. This however often results in increasing numerical errors in each cycle, making them less suitable (Safinus et al. (2011)). The number of load cycles in the implicit part of a hybrid model, i.e. in the constitutive model, should not be larger than 100 (Lupea (2013)). Furthermore the calculation time becomes very long. Finally there is a more fundamental reason why the currently available constitutive models lack the ability to calculate the pore pressure response: in the elastic region the energy dissipation due to rearranging soil particles in the soil skeleton is not included, which is required to model the energy dissipation due to cyclic loading (Taiebat (1999)). Therefore the calculation of excess pore pressure can better be based on empirical formulations, taking the total number of cycles into account but without modelling each cycle separately.

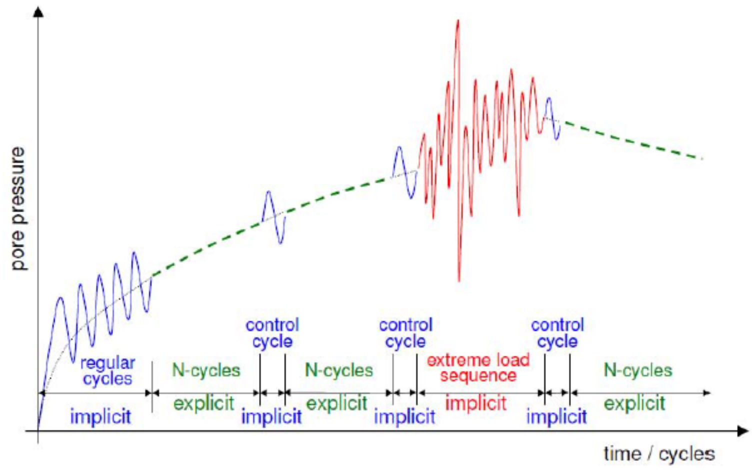

Figure 3.1: *Implicit and explicit steps to be taken in a coupled approach for pore pressure development (Safinus et al. (2011))*

As mentioned before, a combination of an empirical model (explicit steps) and an constitutive model (implicit steps) can be used as well. The implicit approach considers the systems equilibrium using the already developed pore pressure, and can be performed in a finite element calculation. Using this approach the numerical errors and large calculation time are prevented, and the stress changes during pore pressure response are taken into account. Furthermore, the implicit finite element calculations can be used to calculate the strain developments, for instance if the HCA model is used (figure 3.1).

The general steps to be taken for such a hybrid model are:

- Determine the cyclic loads acting on the structure in terms of frequencies and amplitudes.
- Divide the cyclic loads into a number of load parcels with equal amplitude and frequency, each containing many load cycles. This implies also to take a representative developments of loads into account, since this will have a major effect on the pore pressure response.
- For each load parcel, determine the cyclic stress profile below the structure, for instance in a finite element model.
- For each load parcel, determine the pore pressure generation and dissipation of pore pressure in an explicit manner.
- For each load parcel, determine the stress changes and displacements in a finite element model, taking into account the developed pore pressure from the previous phase.

This already shows that the irregular nature of the loading is lost in the approach. The order of the load parcels is often based on a schematic storm development form literature (as shown in figure 2.18), even though it is known that it highly influences the maximum excess pore pressure that is reached (Meijers and Luger (2012)). These are two major drawbacks in this approach. Finally, it is still very hard to determine the error in the obtained pore pressure and settlement, although the error is expected to be smaller than a constitutive model for a large number of cycles.

Random or irregular nature of loads
In analysis of settlement using the HCA model, the random (irregular) nature of loads cannot be taken into account. An often used approach is based on earthquake engineering where an equivalent load is defined, according to the procedure of Seed and Rahman (described in section 3.3.4), which results in the same soil response for the irregular loads. However, it will be hardly possible to find the equivalent load, since the subsoil response largely depends on the actual loads in terms of amplitude and frequency, resulting in a different stress distribution below a structure than for an equivalent load of constant amplitude and frequency. The equivalent load will therefore always be an approximation.

Summarizing this part on modelling approaches and its challenges, it seems essential to capture two effects in the excess pore pressure developments: (1) the irregular nature of the loads has to be taken into account to take the changing soil properties over time in cyclic loading into account. This however can not be done using a constitutive model, which in fact lacks the ability to model excess pore pressure generation, due to the fact that the energy dissipation from cyclic loading is not included, as discussed above (Taiebat (1999)). A hybrid model cannot capture the irregular nature either, since for these models the loads need to be discretized in bins of equal amplitude. Second, (2) the real development of a storm should be taken into account to get a realistic pore pressure development. The schematised storm development over time from literature does not represent real storms realistically, while it is known that the influence of the storm development over time is large (Bjerrum (1973)). Both effects can be taken into account in an adapted version of the program DCycle from Deltares, at least for the excess pore pressures, of which the basics will be presented in this chapter. The settlements will not be investigated in this thesis, since this requires a completely different approach (i.e. a HCA model) this will be left out of the remainder of this research.

3.3. Seed and Rahman model

Based on the derived pressure amplitude at seabed level, as discussed in 2.4, Seed and Rahman (1978) derived a profile of cyclic shear stress ratios (CSSR) as a function of depth, and derived an expression for residual pore pressure generation as a function of the number of load cycles. These will subsequently be discussed, since these results will be used and extended for the cyclic loading on the gravity based foundation.

3.3.1. Cyclic shear stress profile

The CSSR is the ratio of shear stress amplitude to vertical effective stress. It has been used in earthquake engineering to define the loads from horizontal accelerations, by means of a vertical profile of shear stresses, to be used subsequently in liquefaction assessments. For earthquakes the mechanism is different, since these originate in deeper layers and the signal travels a long distance before reaching a structure. The physical derivation of a cyclic shear stress profile below a single wave will be explained below, and it shows how a cyclic load at seabed is transferred to the subsoil. The CSSR profile will be used in this research as well, since the shear stresses from waves at seabed level can easily be converted to any other combination of loads. It is especially useful for the loading from the GBF with bending moments from the OWT, since the CSSR profile can be derived for an extreme load cycle in a FEM.

The starting point for the derivation of the cyclic shear stress profile is the shear stress below the seabed, generated by a single wave travelling over a horizontal seabed (equation 2.11), of which the amplitude is used and presented again in equation 3.2. Equation 3.1 gives the vertical effective stress. The resulting ratio of shear stress over vertical effective stress (CSSR) becomes a negative exponential function with depth z (equation 3.3). The CSSR ratio is in fact not defined at seabed level, since the vertical effective stress is zero at seabed level.

$$\sigma'_{v0} = \gamma'_s z \tag{3.1}$$

$$\Delta\tau = p_0 k z \exp(-kz) \tag{3.2}$$

$$CSSR = \frac{\Delta\tau}{\sigma'_{v0}} = \frac{p_0 z}{\gamma'_s z} \exp\{-kz\} = \frac{p_0 k}{\gamma'_s} \exp\{-kz\} \tag{3.3}$$

With:

σ'_{v0} = initial vertical effective stress [kPa]
γ'_s = effective volumetric weight of soil [kN/m^3]
$CSSR$ = Cyclic shear stress profile [-]
$\Delta\tau$ = shear stress amplitude [kPa]
p_0 = amplitude of wave pressure at seabed [kPa]
k = wave number $2\pi/\lambda$ [1/m]
z = vertical coordinate, positive downwards [m]

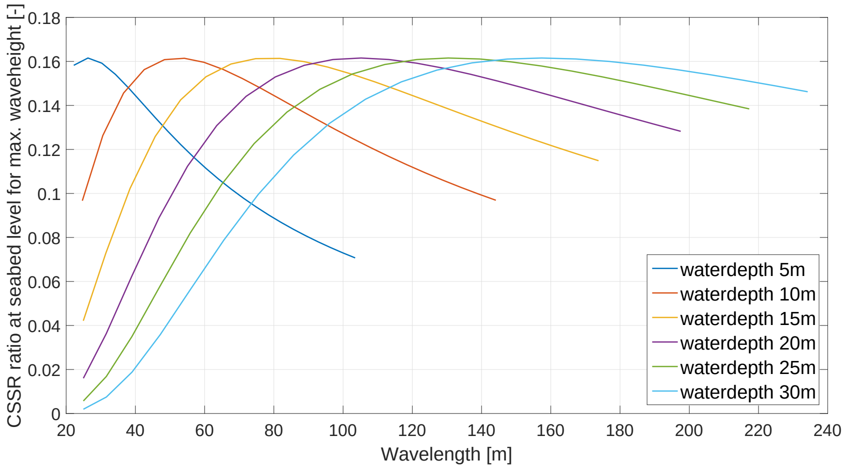

Figure 3.2: *Maximum CSSR values for different wave lengths and water depths, corresponding to a breaker criterion of 0.78d*

The negative exponential function indicates that the wavelength, related to the wave period by the dispersion equation, determines the rate at which the CSSR diminishes with depth. For smaller wave periods (shorter wave lengths) the decrease is faster. For each wave length a maximum CSSR value can be calculated for the corresponding wave height, just below the wave breaking criterion (for instance 0.78d, with d the water depth (Holthuijsen (2007))). For wave periods between 5 to 15 seconds the corresponding CSSR-values at seabed level have been calculated for water depths between 5 to 30 meter (figure 3.2). The following observations can be made:

- The maxima in the CSSR-curves is found at larger wave lengths (and corresponding larger wave periods) if the water depth increases.
- For a certain water depth and corresponding maximum wave height, the CSSR profile increases for decreasing wave lengths.
- If a threshold CSSR-value for densification is used, for instance 0.08 (although based on a shear strain amplitude, Meijers (2007)), this value is reached for a certain water depth and wave length combination when the water depth reaches about half the wave length. Therefore if the water depth becomes larger than half of the wave length, no liquefaction is to be expected. This is a often used rule of thumb to assess wave induced liquefaction of a seabed (Raaijmakers (2005)).

3.3.2. Pore pressure generation

The extent to which the pore-pressures develop, will depend on (Seed and Rahman (1978)):

- The storm characteristics, such as wave length, wave height and wave period, defining the forcing in magnitude and number of cycles.
- The soil characteristics under cyclic loading, i.e. relative density and permeability, defining the pore pressure generation.
- The drainage characteristics of the soil during consolidation, defining the dissipation of pore pressures
- Loading history of the soil, the effect of preshearing and the already developed pore pressure.

Seed & Rahman deduced a formula for the pore pressure increase as a function of the number of load cycles in undrained conditions, derived for a horizontal seabed loaded by waves (equation 3.4). The basis for the observed development of the excess pore pressure are stress-controlled cyclic triaxial and DSS-tests on virgin sand samples of various densities. The formula was derived for the full range of excess pore pressures, up to full liquefaction. By changing the value of θ, the formula may be applied to soils with various densities. A value of 0.7 was found reasonably for average sands. The number of cyclic to full liquefaction as used in formula 3.4 can be calculated with the often used formulation in equation 3.5, already presented in chapter 2, but for the sake of completeness repeated. The latter equation relates the soil strength in terms of relative density to the cyclic load in terms of the CSSR ratio, the shear stress amplitude over initial vertical effective stress.

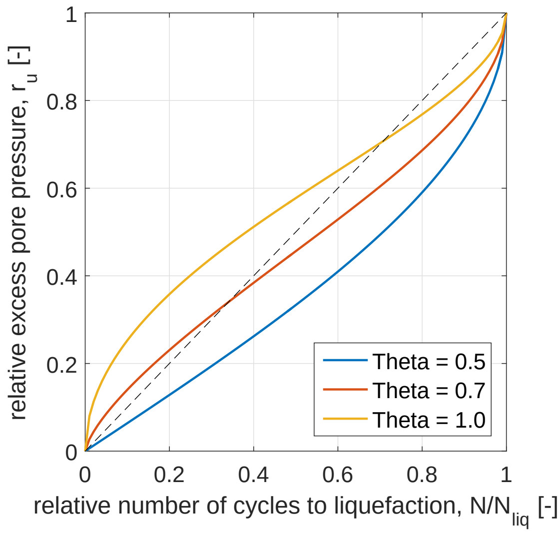

Figure 3.3: *Rate of pore pressure generation indicating the faster-slower-faster increase up to full liquefaction as presented in equation 3.4 for different values of θ*

$$r_u = \frac{2}{\pi}\arcsin\left(\frac{N}{N_{liq}}\right)^{\frac{1}{2\theta}} \tag{3.4}$$

$$\frac{\Delta\tau/\sigma'_{vo}}{I_d} = aN_{liq}^{-b} \tag{3.5}$$

r_u = relative excess pore pressure: ratio of excess pore pressure over initial vertical effective stress [-]
θ = the rate of pore pressure increase, 0.7 for many sands, indicated in figure 3.3 [-]
N = number of load cycles [-]
N_{liq} = number of load cycles up to full liquefaction (in undrained conditions) [-]
a, b = empirical constants [-]

From the proposed empirical formula it can be seen that initially a fast rate of pore pressure increase is present, which gradually decreases and close to full liquefaction (at least for $\theta > 0.5$) only a few more load cycles are necessary to cause liquefaction (fast increase). The initial fast increase is caused by the relatively large contraction during the first few load cycles, resulting in a relatively fast increase in excess pore pressure (EPP), while the latter effect is caused by the increased loading rate due to the reduced vertical effective stress by the already increased EPP.

Smits et al. (1978) argues that the shape of the pore pressure generation can be expressed in the $\beta = \Delta r_u/\Delta N$ coefficient (equation 2.4), representing two non-linear phenomena:

- The non-linearity of the compression curve: if a certain amount of densification is reached, the potential for further densification will be continuously decreased.
- The growing CSSR-value in each undrained load cycle due to pore pressure generation, which increases the pore pressure generation in following cycles again.

3.3.3. Assumptions and limitations

The pore-pressure generation model by Seed and Rahman (1978) is based on some assumptions and limitations, listed below:

- Linear elastic soil theory is the basis of the derived pore pressure generation model. For significant pore pressure generation however, non-linear soil behaviour should be taken into account. The soil itself stiffness itself can however be updated during the pore pressure build-up.

Finn investigated the difference between updating the soil properties (bulk and shear modulus) at intermediate time steps with actual stress levels and pore pressures (denoted as modified in figure 3.16), and without updating (denoted as not modified in figure 3.4). With the degradation of the moduli taken into account, the excess pore pressures are 20% higher for the permeability of $2 * 10^{-3} cm/s$, and the depth up to liquefaction increases as well. This shows the importance of updating the soil moduli during cyclic loading.

- The induced shear stress in the seabed by the wave pressure is not influenced by the soil permeability, which was also derived by Yamamoto et al. (1978). Finn et al. (1983) derived that this is only true as long as the soil is not very dense and consisting of fine particles. This also depends on the loads: during a single wave, the condition can be considered to be undrained, but for a complete storm drainage will occur in between load cycles.

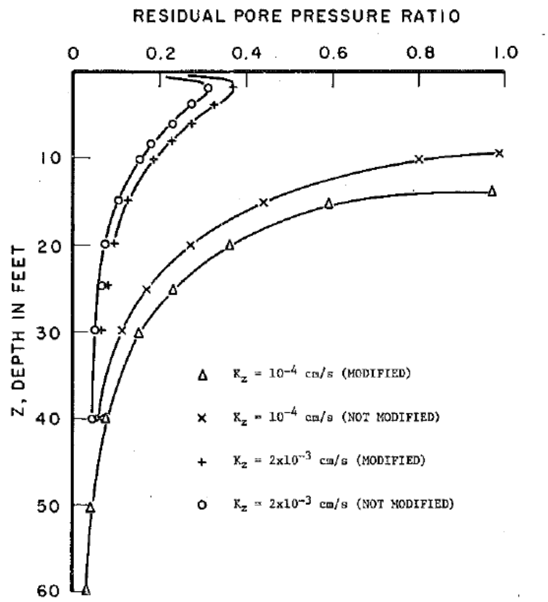

Figure 3.4: *Effect of soil softening on pore pressure response (Finn et al. (1983))*

3.3.4. The effect of a random wave field

Seed and Rahman (1978) furthermore propose a method to use a random wave field instead of an (unrealistic) regular wave field. Therefore, the random wave field is transformed into a regular wave field with equal wave heights, for instance the significant wave height. For this purpose the time series of irregular wave heights is split up in several batches with equal wave heights and wave periods. Seed and Rahman now propose to use the earlier developed formula for the number of cycles to liquefaction to determine this number for each wave height bin.

The equivalent number of waves is now determined by the ratio of the number of waves till full liquefaction for the reference wave height and the actual wave height, and used as a scale factor to the number of waves with the actual wave height. This is presented in formula 3.6. Using the number of equivalent load cycles, in fact a correction factor is applied on the number of load cycles which follows from the total storm duration and the peak wave period, represented by correction factor c in equation 3.6.

$$N_{equi} = N_{waves} \frac{N_{liq}}{N_{ref}} = \frac{T_{storm}}{T_p * c_{corr}} \tag{3.6}$$

With:

N_{equi} = number of cycles of the equivalent wave height [-]
N_{liq} = number of cycles up to full liquefaction for the considered wave height [-]
N_{waves} = number of waves of the considered wave height [-]
N_{ref} = number of cycles up to full liquefaction for the selected equivalent wave height [-]
T_{storm} = total storm duration [s]
T_p = peak wave period in the storm [s]
c_{corr} = correction factor for irregular waves [-]

The specific example of Seed and Rahman as presented in Seed and Rahman (1978) is presented in table 3.1. The number of waves of each wave height bin is given and the corresponding CSSR value is calculated at seabed level For different chosen values for the reference wave height, the equivalent number of cycles to liquefaction is determined. The correction factor in the example becomes 2.32 for a reference wave height of 2.44 m and a corresponding CSSR-value of 98% of the maximum CSSR-value. This value is proposed by Seed and Rahman (1978) to account for the irregular nature of the load. Meijers et al. (2014) used a value of 2, which was considered to be conservative, since this in fact results in more load cycles in the total storm duration, and therefore a higher excess pore pressure (right side of equation 3.6).

However, the correction factor largely depends on the reference number of load cycles and corresponding reference value of the CSSR, as can be seen in table 3.1 where different correction factors are found for different equivalent load cycles. In general, the correction factor should be larger than 1 and the number of equivalent load cycles should therefore not be larger than the number of irregular load cycles. According to Lee and Focht (1975) the reference CSSR value should therefore be between 20% and 50% of the maximum value occurring in the storm.

	Wave height (m)	Nr of waves (-)	Wave period (s)	CSSR z=0 (-)	N_{liq} (-)	N_{equi} (-)
	2.75	50	7.0	0.198	3.2	53
	2.44	80	6.5	0.196	3.4	80
	1.83	155	6.0	0.163	7.2	73
	1.22	180	5.0	0.130	24.0	25.5
	0.61	200	4.0	0.071	10000	0.068
Nr. of equi. waves		665				232
c_{corr}						2.32

Table 3.1: *Example calculation by Seed and Rahman (1978). The total storm duration, i.e. the sum of the number of waves multiplied by the wave period in each bin, is 3500 seconds. The resulting correction factor for 232 equivalent waves with an equivalent wave height of 2.44 meter and equivalent wave period of 6.5 seconds, becomes* $3500/(232*6.5) = 2.32$.

The approach is only applicable if waves with heights describing the complete spectrum are present. This is not the case if the spectrum evolves during the storm, in that case the correction factor should be updated during each stationary period of time. This was not taken into account by Seed & Rahman. Second, the equivalent wave height and wave period should be determined according to the drainage characteristics of the soil, since for a short drainage time a too long equivalent wave period results in completely different results. Third, also wave grouping effects are lost in this averaging procedure. Wave grouping occurs due to frequency dispersion, i.e. waves with low frequencies and therefore large velocities travel faster than waves with high frequencies, resulting in the large waves grouping together. A series of these concentrated larger waves might however be the governing situation for fast draining soils. In general, it can be concluded that the method of Seed and Rahman (1978) has some major drawbacks.

3.4. DCycle model

3.4.1. Model description

Meijers and Luger (2012) and Meijers et al. (2014) implemented the Seed and Rahman pore pressure generation term together with a dissipation term and the effect of preshearing into the model DCycle, an in-house Deltares program. The model is derived for a 1D stress state but can be applied to a 3D dissipation problem.

The model was validated with results of cyclic element tests. The following aspects are taken into account to calculate the development of excess pore pressure in time:

- Compaction or densification of the soil is taken into account
- Effect of preshearing (due to a pre-storm or a gradual storm build-up), representing the change in soil skeleton structure, and therefore separated from densification (see 2.2.6)
- Dissipation or drainage of the soil is taken into account with the consolidation process

The general equation to solve is the one-dimensional consolidation equation with an added pumping term, initially derived for undrained conditions, representing the generation and dissipation of pore pressures (equation 3.7). Furthermore, elastic behaviour is assumed and acceleration terms are neglected. The pumping term A(z,t) is represented by the Seed and Rahman model for pore pressure generation (equation 3.4), which gives for every mesh layer the relative number of cycles and the relative pore pressure build-up during each (undrained) load cycle. The pumping term A can be found by using the pore pressure generation equation of Seed & Rahman (equation 3.4), and differentiating the equation to time after expressing the number of cycles as a function of time. The derivation is presented in appendix B.

$$\frac{\partial u}{\partial t} = A(z,t) + c_v \frac{\partial^2 u}{\partial z^2} \tag{3.7}$$

With:

A = pore pressure generation term without preshearing and without drainage [kPa/s]
u = excess pore pressure [kPa]
z = vertical coordinate [m]
c_v = consolidation coefficient [m^2/s]

The related assumptions of DCycle are:

- Vertical consolidation is dominant, which allows for a one-dimensional calculation.
- The number of waves needed to generate the pore pressure is large, i.e. no large pore pressure generation after only one or a few waves, since in this case the 1-dimensional approach is not suitable anymore: the problem then becomes 3-dimensional.
- Compressibility of the pore water is assumed to be small compared to the grain size compressibility.
- The pore water flow is based on Darcy.
- Linear elastic behaviour is assumed.
- Acceleration terms are negligible.

The consolidation coefficient would during normal consolidation calculations be kept constant for the considered stress range, but is in DCycle a function of the stress level, relative density and the relative excess pore pressure (equation 3.8 and 3.9). The consolidation coefficient is user input at a stress level which has to be specified as well. Since both the pore pressure generation and dissipation depend on the stress level, a vertical mesh is generated based on the input of value of the upper soil layer thickness, which will be the thinnest layer. This layer will determine the stability requirement for the numerical calculation scheme together with the initial value of the consolidation coefficient. The consolidation coefficient depends on the stress level via the vertical compressibility coefficient m_v in equation 3.9, which was originally proposed by Martin (Martin (1975)) and also used in the model of Seed & Rahman. For various relative densities and relative excess pore pressures, the formula is plotted in figure 3.5. The figure shows how for increasing excess pore pressure the 1-dimensional stiffness $E_{oed} = \frac{1}{m_v}$ decreases. During pore pressure dissipation, the relative density will increase, which decreases the rate at which the stiffness decreases. This effect becomes especially significant for relative excess pore pressures above 0.5.

The stress dependent relations are (3.8 to 3.10):

$$c_v = \frac{k}{m_v \gamma_w} \tag{3.8}$$

$$m_v = \frac{m_{v0} \exp\left(A_{pp} r_u^{B_{pp}}\right)}{1 + A_{pp} r_u^{B_{pp}} + 0.5 A_{pp}^2 r_u^{2B_{pp}}} \tag{3.9}$$

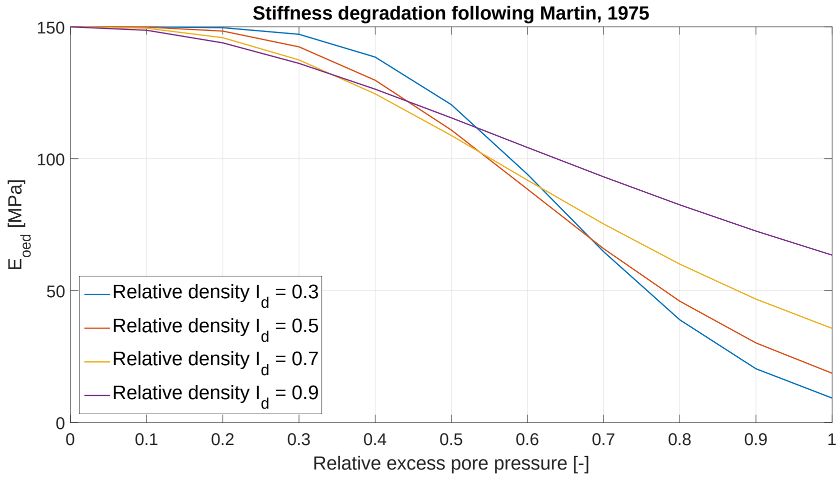

Figure 3.5: *Stiffness degradation in DCycle as a function of excess pore pressure and relative density*

$$A_{pp} = 0.5(1.5 - I_d) \qquad B_{pp} = \frac{3}{2^{2I_d}} \tag{3.10}$$

With:

k = permeability in z-direction [m/s]
m_v = coefficient of compressibility, defined in equation 3.9 [1/kPa]
γ_w = volumetric weight of water [kg/m^3]
$m_{v0} = m v_{00}\sqrt{\frac{\sigma'_{v0}}{p_{ref}}}$ [m^2/kN]
r_u = relative excess pore pressure [-]
A_{pp} = first empirical pore pressure generation coefficient [-]
B_{pp} = second empirical pore pressure generation coefficient[-]
I_d = relative density [-]
p_{ref} = reference stress level to determine for which the value of m_{v00} holds [kPa]

The decrease of porosity and the increase in relative density is calculated with the change in volume due to the inflow and outflow of pore water (equation 3.11), since this is assumed to be the only way in which a volume change can be reached.

$$\Delta V = (Q_i - Q_{i-1})\Delta t \tag{3.11}$$

With:

ΔV = volume change due to drainage [m^3]
Q_i = inflow of pore water in mesh layer i [m^3/s]
Q_{i-1} = inflow of pore water in mesh layer i-1 [m^3/s]
Δt = time step in numerical integration [s]

The change in porosity results in an increased number of cycles to liquefaction. This change is used in Smits et al. (1978) to take the effect of preshearing into account as described in equation 2.5. DCycle allows different ways to enter the CSSR profile. It can for instance be calculated for waves travelling over a horizontal seabed (equation 3.3). If a specific structure is to be included, the CSSR profile should be entered manually in DCycle. The CSSR profile can for instance be obtained using a FEM package. DCycle will subsequently linearly scale this CSSR-profile to different loads at all time steps during the calculation. The loading can be any load, and is represented by a force F in equation 3.12, but it can also be a bending moment for instance.

$$\frac{\Delta\tau}{\sigma'_{v0}}(z,t) = \frac{\Delta\tau_{max}}{\sigma'_{v0}}(z)\frac{\Delta F(t)}{\Delta F_{max}} \tag{3.12}$$

Where:

$\Delta\tau$ = shear stress amplitude [kPa]
$\Delta\tau_{max}$ = shear stress amplitude in maximum load cycle [kPa]
σ'_{v0} = initial vertical effective stress [kPa]
ΔF = load amplitude [N]
ΔF_{max} = load amplitude in maximum load cycle [N]

Structure on the seabed
DCycle has mainly been used for horizontal sea beds with a buried pipeline, but also the option for caisson breakwaters has been implemented. The structure is modelled as a closed flow boundary at the seabed, which results in an adapted dissipation of pore pressure: instead of only in a vertical, it will now dissipate in vertical plane in both the vertical and in the sideward (horizontal) direction.The horizontal dissipation was implemented using a correction factor on the 1D consolidation equation (equation 3.7).

For a circular gravity base structure however, the dissipation is not in a vertical plane but in radial directions, essentially 3D. This is expected to result in lower excess pore pressures since dissipation occurs in vertical and radial directions instead of only vertical and horizontal, as was the case for a caisson breakwater. The radial dissipation is derived for a circular gravity base structure and is implemented in DCycle as well. Results were compared with the vertical and horizontal dissipation beneath a caisson and showed larger dissipation rates and shorter dissipation times. However, since no scale model tests are available it is not possible to validate the corrected dissipation term, but the results are in line with the expectations. The resulting model is in fact a 1D model for the stress state and excess pore pressure generation, while drainage is modelled in vertical and radial direction based on a correction factor for the 2D dissipation beneath a caisson.

When a structure (either a caisson or a GBF) is modelled in DCycle, the user may define a CSSR profile below the structure. This profile will be used to assess the pore pressure generation in a single vertical below the middle of the structure, by scaling the amplitude of each load cycle with the maximum load cycle in the time series of loads and multiplying the CSSR profile over depth with this scaling factor. In this way a caisson or GBF with in fact any load acting on it can be modelled.

Numerical stability
To guarantee the stability of the numerical scheme for the consolidation equation, the following stability rule is used to determine the time step used in the calculation (equation 3.13). For the used defined upper soil layer thickness this will result in the governing time step in the first steps of the calculation, when the consolidation coefficient is highest.

$$\Delta t = \frac{(\Delta z)^2}{2c_v} \tag{3.13}$$

Where:

Δt = time step for numerical integration [s]
Δz = vertical step for numerical integration [m]
c_v = consolidation coefficient [m^2/s]

3.4.2. Preshearing

If partial drainage is present, the earlier described effect of preshearing occurs. This results in a change in soil-skeleton, which becomes visible in densification or reduced pore pressure generation. In terms of modelling the preshearing effect, two ways are possible (Meijers (2007)).

Either adjusting the relative density after each load cycle and determine the number of cycles to full liquefaction again for the adjusted relative density, or adjust the value of the number of cycles to full liquefaction directly, using an empirical relation as for instance proposed by (Smits et al. (1978)). Meijers and Luger (2012) investigated the pore pressure increase taking into account the approach of Smits et al. (1978). The effect of preshearing was investigated using 2 cases:

- during a pre-storm occurring before the design storm
- during the storm development before reaching the maximum wave in the design storm

In each of the cases a design storm with maximum wave height of 4 meter and wave period of 10 seconds is used, increasing linearly from 0 to 4 meter in 3 hours, remaining constant during 9 hours, and decreasing to zero again in the last 3 hours. Three cases were investigated:

Case 1: Effect of densification is taken into account, but no preshearing
In the result (figure 3.6) both the pre-storm and the design-storm can clearly be seen in the pore pressure increase. Since the preshearing is not taken into account, the pore pressure increases much more during the design storm and no increase in liquefaction resistance can be seen. Liquefaction can be observed since the pore pressure reaches a maximum above which it cannot increase further.

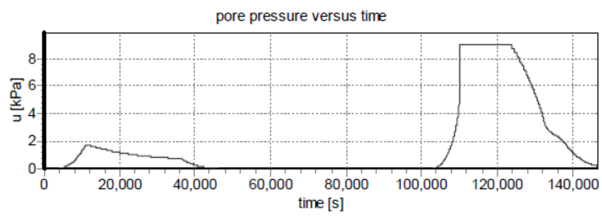

Figure 3.6: *Effect of densification taken into account, but no preshearing (Meijers and Luger (2012))*

Case 2: Both the effects of densification and preshearing are taken into account
In this case (figure 3.7) the pore pressure increase during the second storm is clearly less than in case 1, which can only be due to the effect of preshearing, indicating an increase in liquefaction resistance.

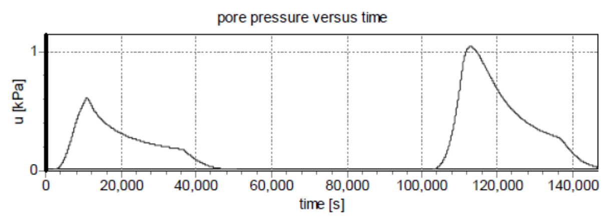

Figure 3.7: *Effect of densification and preshearing both taken into account, pre-storm present (Meijers and Luger (2012))*

Case 3: Both the effects of densification and preshearing are taken into account, but instead of a pre-storm, only a gradual increase in the design storm is present
No pre-storm is applied now (figure 3.8), only the possible effect of a gradual wave height increase in the first hours of the design storm is considered. The pore pressures are now higher than in case 2, but still far lower than in case 1. It can therefore be concluded that preshearing also occurs during the gradual build-up of wave height in a storm.

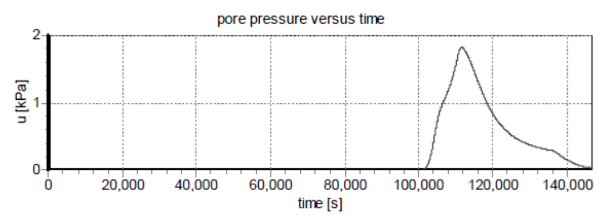

Figure 3.8: *Effect of densification and preshearing taken into account, gradual wave build-up (Meijers and Luger (2012))*

The preshearing effect has a significant (positive) effect on the generated excess pore pressures. Since the basics of preshearing are related to the soil deformation and the re-structuring of the soil body during shear deformation, the process should only be applied if the shear strains remain below 0.5% (see also 2.2.6). Whether the positive effect of preshearing can be taken into account should therefore be checked carefully. For larger shear strains than the threshold, the preshear effect has a negative effect and the soil is observed to liquefy even faster (Meijers (2007)).

3.4.3. The effect of a random wave field

In addition to this simplified approach of Seed & Rahman to use a correction factor to represent the irregular loading, also a more sophisticated approach can be followed in which a wave spectrum is used to generate a random wave signal. This was done in Meijers et al. (2014). For relatively short periods of time, about 10 to 20 minutes, a wave signal can be assumed to be stationary with constant wave energy, meaning that for such a short period the wave energy can be described with a single spectrum. After this period the spectrum should be updated. Therefore, the modelled storm should be discretized into periods of 10 to 20 minutes and for each bin the spectrum should be established, resulting in a trapped wave build-up and build-off. From the spectra, a time series of water level elevations is created based on the random-phase-amplitude model (equation 3.14), which is a summation of signals with various frequencies, amplitudes and phases. The summation over all frequency components results in the total wave signal With the water elevation, the pressure at the seabed can be calculated, from where the already discussed procedure is continued.

$$\eta = \sum_{i=1}^{end} \alpha_i \cos(\omega_i t + \phi_i) \tag{3.14}$$

η = water level elevation [m]
α_i = amplitude of frequency component i[m]
ω_i = radial frequency of component i [rad/s]
ϕ_i = phase of frequency component i [rad]

From each spectrum the time series is generated by the summation of different frequency components, with their own amplitude and phase. The phases are assumed to be uniformly distributed. Meijers et al. (2014) used this procedure for a 6 hour storm, with 2 hours build-up and 2 hours build off with a maximum wave height of 6 m. The simplified model with a correction factor of 2 on the total number of waves (following Seed and Rahman (1978), section 3.3.4) and the random wave signal are compared (figure 3.11). Starting with the input of the wave loads, the regular pressure time series at seabed can be seen (middle of figure 3.9), and can be compared to the random time series generated from a JONSWAP spectrum (bottom of figure 3.3). Each randomly generated time series will be different due to the random phase model, as discussed previously.

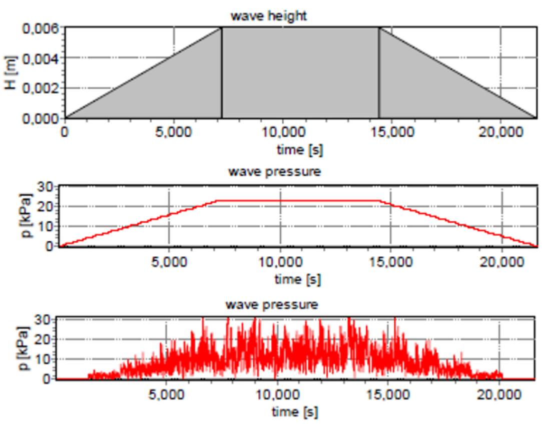

Figure 3.9: *Input of the storm in terms of wave height (top). Wave induced pressure at seabed level, for regular waves (middle) and (random) wave induced pressure generated from a JONSWAP spectrum with random phase model (bottom) (Meijers and Luger (2012))*

It can be seen that each generated wave history results in different pore pressure responses due to the random phases (figure 3.11). Furthermore, the random wave signal results in larger pore pressures in the build-up of the storm, possibly due to some cycles in the build-up of the storm with shorter wave period and therefore a larger number of waves, resulting in larger pore pressures. For the lower signal in 3.11 very high excess pore pressures are generated, which can only be attributed to an instantaneous combination of wave height and period resulting in a high pore pressure build-up with very limited drainage possibilities. Due to their sudden character, these pore pressures will be caused by short waves. These extreme pressures quickly decrease with increasing depth (Meijers et al. (2014)).

From different wave periods it was concluded by Meijers et al. (2014) that the excess pore pressure increases with decreasing wave period, probably due to less drainage possibilities at shorter time scales. Since it was observed that the random wave signals lead to larger pore pressures compared to a regular wave signal, this should be taken into account for design purposes.

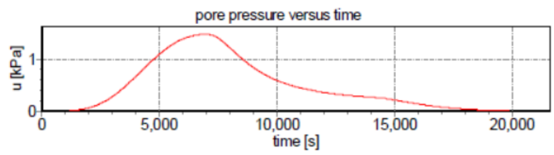

Figure 3.10: *Pore pressure development over time for regular wave loading (Meijers and Luger (2012))*

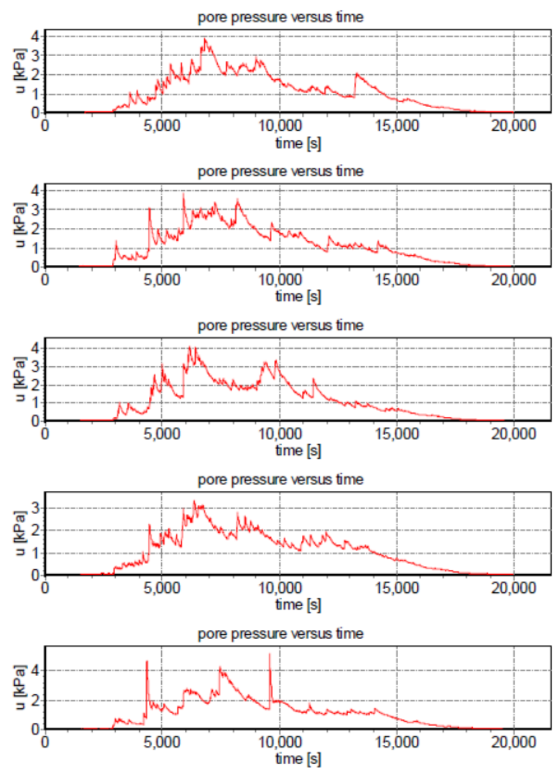

Figure 3.11: *Pore pressure development over time for five irregular wave pressure histories, generated using a JONSWAP spectrum with a random phase model (Meijers and Luger (2012))*

Summarizing, the proposed method to incorporate the random nature of (wave) loads in the excess pore pressure calculations in DCycle has some major advantages over the method by Seed&Rahman. By making multiple load calculations a range of maximum excess pore pressures can be found, allowing a probabilistic approach to take the resulting random excess pore pressures into account. There is no need to discretize the build-up in bins of equal wave height. Furthermore, the method is able to take the real storm development or even a load histories of multiple storms into account. These can for instance be based on a dataset of environmental data, in contrast to the schematised storm build-up that is often used for design purposes (for instance by Bjerrum (1973)). The method can subsequently also be adapted to site-specific data.

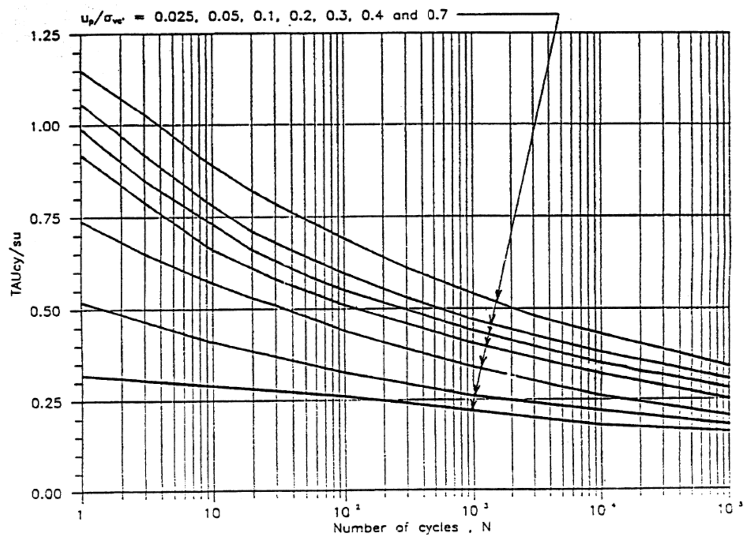

Figure 3.12: *Pore pressure contour diagram as presented in DNV Foundations code (DNV (1992))*

3.5. Other approaches

For other approaches the norms and standards can be used. These methods are in general written from a far more practical perspective than the previous sections, but since they give insight in the current design practice and its limitations, they are presented below. For design of gravity based structures, the codes of the Norwegian classification firm Det Norske Veritas (DNV) (DNV (2014) and DNV (1992)) is preferred. However, other codes exist, for instance from the American Petroleum Institute (API) and the International Organization for Standardisation (ISO). These are however mainly intended for the offshore oil- and gas industry, while DNV has a code specifically developed for offshore wind turbines and their support structures and foundations. The basis of the code is however still the experience gained in offshore oil- and gas structure design. In this paragraph the parts of the codes on cyclic loading on marine structures will be discussed. Finally also the developed method Norwegian Geotechnical Institute (NGI) will shortly be discussed.

3.5.1. API Standard

The American Petroleum Institute (API) (ISO 19901-4 (2000)) asks for investigation of the dynamic loads due to currents, waves, ice, wind and earthquakes. Also the response of the structure-foundation system should be taken into account in the dynamic analysis. No further information how this should be performed is presented.

3.5.2. DNV Standard

DNV gives more information compared to API. According to DNV both a total stress analysis and an effective stress analysis are appropriate ways to investigate cyclic loads on offshore wind turbine foundations. However, the effective stress analysis is explicitly preferred, since pore pressures can then be taken into account and potential liquefaction phenomena will be discovered. The DNV code for foundation design (DNV (1992)) was developed for offshore oil- and gas superstructures, and includes an extensive treatment of gravity based structures. The DNV code for design of offshore wind turbine structures DNV (2014) was specifically developed for offshore wind turbines, but gives no detailed information on the design of foundation types. The section on gravity based structures from DNV (1992) will be described below.

In order to determine pore pressure response it is recommended to use pore pressure contour diagrams derived from undrained cyclic testing. The element tests should be developed according to the site specific conditions. In the case of low to moderate stress levels DNV recommends the assessment for the pore pressure response as in equation 3.15, only to be applied for low to moderate stress levels. A pore pressure contour diagram is shown in figure 3.12, which gives a number of cycles at a certain stress level (defined by the ratio of cyclic shear stress versus undrained shear strength) to reach a certain pore pressure.

$$R_u = \Delta\sigma_d \frac{dN}{du} \tag{3.15}$$

R_u = cumulative pore pressure resistance against repeated loading: $R_u = r_u N$ [-]
N = the number of load cycles at stress level $\Delta\sigma_d$ [-]
r_u = pore pressure generation term, determined from laboratory tests [-]
$\Delta\sigma_d$ = change in deviator stress: $\Delta\sigma_d = \Delta\sigma_1 - \Delta\sigma_3$ [kPa]

r_u should be determined by laboratory tests. The change in pore pressure may be written as equation 3.16.

$$\Delta u = \Delta\sigma_m - D\Delta\sigma_d \tag{3.16}$$

Δu = change in pore pressure [kPa]
$\Delta\sigma_m$ = change in mean total stress: $1/3\ \sigma_1 + \Delta\sigma_2 + \Delta\sigma_3$ [kPa]
$\Delta\sigma_d$ = change in deviator stress: $\Delta\sigma_1 - \Delta\sigma_3$ [kPa]
D = dilatancy parameter, to be determined by stress path from undrained triaxial tests [-]

DNV also recommends including drainage, but without giving any guidelines how to add this to the given formulas. Furthermore, settlements due to cyclic loading should also be predicted to determine stability of the structure. Both undrained shear deformations and consolidation of pore pressures due to cyclic loading should be taken into account. In order to estimate these settlements they recommend the usage of analytical methods that use soil models with the ability to assess average shear stresses and cyclic shear stress history in all soil elements.

An interesting note is made in the total stress analysis, which states that when the ULS storm is considered, the storm event should be considered to take place directly after installation of the structure, with corresponding soil conditions. The beneficial effect of drainage during installation may be taken into account. For large structures on thick clay layers it is allowed to take smaller storms prior to the design storm into account, since DNV states that the deteriorating effect (i.e. pore pressure generation or reduction in shear strength) of smaller storms prior to the design storm may be counteracted by the beneficial effect of consolidation.

3.5.3. NGI

In the past 40 years, the Norwegian Geotechnical Institute (NGI) has developed an extensive database of cyclic laboratory tests from which cyclic contour diagrams have been derived (Andersen (2007)). The diagrams for DSS and triaxial tests are plotted as a function of average and cyclic shear stress and the number of load cycles. The stresses are normalized to undrained static shear strength for DSS tests. The average shear stress is applied undrained to the sample, and after 1 to 2 hours the cyclic load is applied. The cyclic loading has a period of 10 seconds. All samples are loaded to failure, defined to be when the average and cyclic shear stresses reach 15% strain in total. This might be too large for marine structure, since failure could be reached earlier (with smaller strains) due to operability requirements. Especially for a wind turbine this is relevant. The contour diagrams are based on a large number of tests, from which for each tests the average and cyclic shear strain is used to to express the failure mode: the ratio of average over cyclic shear strain. Also the number of cycles needed to reach this strain is measured. The results for each test, in this case DSS-tests on Drammen Clay, are presented in figure 3.13. From all the tests with interpolation and extrapolation the number of cycles to failure for different values of average and cyclic shear stress are determined and plotted. This results in the contour diagram, with also the failure modes indicated. From this DSS diagram is can be seen that for small to moderate average shear stresses the final failure mode is large cyclic shear strains, while for large average shear stresses the failure mode will be large average shear strains.

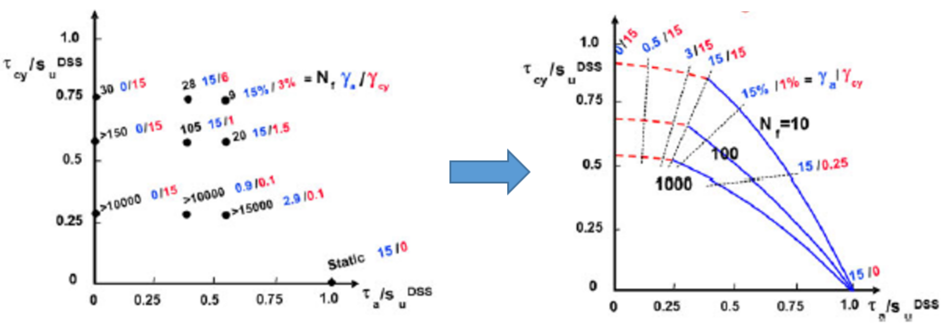

Figure 3.13: *Development of a contour diagram, starting with element tests (top) into a plot of average and cyclic shear strain amplitude for combinations of average and cyclic shear stress amplitude (bottom) (Andersen (2007)). In blue average shear strain is indicated, and in red the cyclic shear strain amplitude.*

In order to take the development of a design storm into account in the cyclic loading, a procedure was developed to transform the irregular load history into bins of equal loads (figure 3.14). The order of the loads is assumed to be increasing from the smallest amplitude to the largest amplitude, which causes the maximum soil degradation according to Andersen (2007) prior to the extreme load cycle. The total load sequence should be summarized into an equivalent number of cycles which results in the same cyclic degradation as the actual load history. Two methods are available, either the pore pressure accumulation, suited for cases where drainage is present during loading, and the strain accumulation procedure, more suited for clay. The starting point of the pore pressure accumulation procedure is the scaling of each bin with a load amplitude with the maximum load amplitude, resulting in a shear stress for each load cycle. Starting at the lowest load amplitude and continuously increasing to the maximum load amplitude, the pore pressure contour diagram is used to determine the gradual build-up by stepping through the diagram. Starting at point A with a scaled load amplitude of 0.042, applying 582 cycles, reaching point B. From this point the contour is followed to the next load amplitude at point C, 0.057. From this point 339 cycles are applied. All steps are visualised in figure 3.14. Finally the equivalent number of cycles is found at the end of the last load cycle with amplitude 0.15, showing a number of 21 cycles in this case. This is the number of equivalent cycles to reach the same excess pore pressure as the irregular load history.

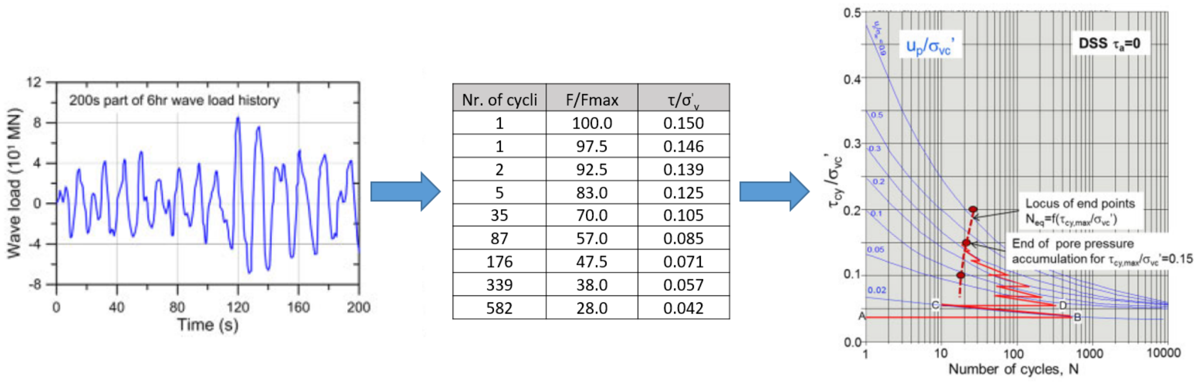

Nr. of cycli	F/Fmax	τ/σ'_v
1	100.0	0.150
1	97.5	0.146
2	92.5	0.139
5	83.0	0.125
35	70.0	0.105
87	57.0	0.085
176	47.5	0.071
339	38.0	0.057
582	28.0	0.042

Figure 3.14: *Transformation of a random load history (left) into a discretized load history (middle), and the resulting pore pressure development can be read from the contour diagram (right, Andersen (2007))*

Drainage can also be included in the procedure. The pore pressure will then follow curve AC instead of curve AB which was for fully undrained conditions (figure 3.15). From point C the next load amplitude will bring the excess pore pressure to point E if the conditions were undrained, but with drainage this will only come to point F. However also the excess pore pressure from point C will continue to dissipate, lowering the excess pore pressure to point G. The drainage can for instance be determined by a finite element consolidation analysis, according to Andersen (2007). The data from the contour diagrams is implemented in the UDCAM and PDCAM models in Plaxis 3D (Jostad and Page (2014)), respectively for undrained and partially drained soils.

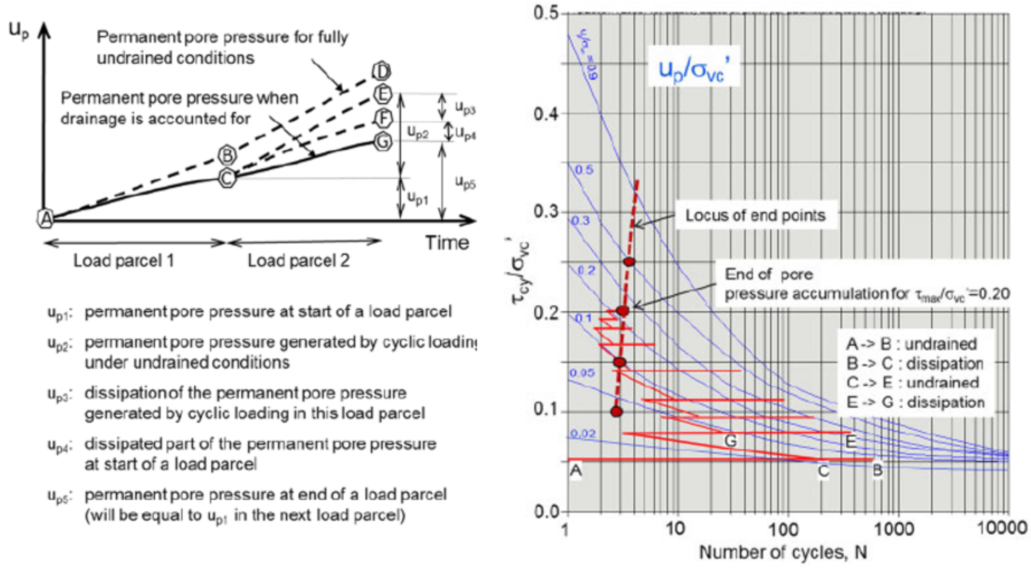

Figure 3.15: *Effect of drainage in terms of excess pore pressure versus time (left), and how to take drainage into account using the pore pressure contour plot (right) (Andersen (2007))*

3.6. Concluding remarks

This chapter started with the discussion of various models and the main challenges in models for cyclic loading of soils. Based on this investigation, and based on the research question related to the load history, it is desired to implement the irregular or random nature of the loads and the real development of a storm. The irregular nature can only be taken into account if there is no need to discretize the loading in bins of equal amplitude, which is for instance the case in hybrid models. The real build-up of a storm can be based on a synthetic data set or on measured storm data. Both effects can be taken into account in DCycle, the model developed by Deltares. The basics of the model have been described in the this chapter. The main features are the drainage during cyclic loading, and the adapted drainage below a circular gravity based foundation.

The norms and standards as well as the NGI approach have been investigated as well. It is interesting but surprising that API as well as DNV stress the significance of cyclic loading on stability of marine structures, but do not propose a detailed method. DNV proposes a model to take the pore pressure generation into account, but drainage is missing. Since this is expected to be highly relevant in a real storm build-up, the method is not suited for this research. Finally the NGI method has been analysed. The main advantage of the method is its sound basis on a large number of element tests and therefore on observed behaviour, instead of a prediction by a model. Furthermore, drainage can be taken into account, but an irregular load history still needs to be transformed into an discretized load history with bins of equal amplitude. In this procedure the irregular nature is lost, which is thought to be highly relevant due to the constantly changing soil properties (density, stiffness). Next to this and maybe even more important, it is assumed that the (discretized) loads build-up gradually till maximum amplitude. Therefore, the real development of a storm is not fully taken into account.

Therefore, the DCycle model will subsequently be used in this research to answer the research question related to the load history and the governing excess pore pressure in an extreme storm. The model might seem the most important part, but the input for the model is for the case of a gravity based foundation for an offshore wind turbine maybe as complicated. As mentioned, the real storm build-up including its randomness needs to be modelled to answer the research question.

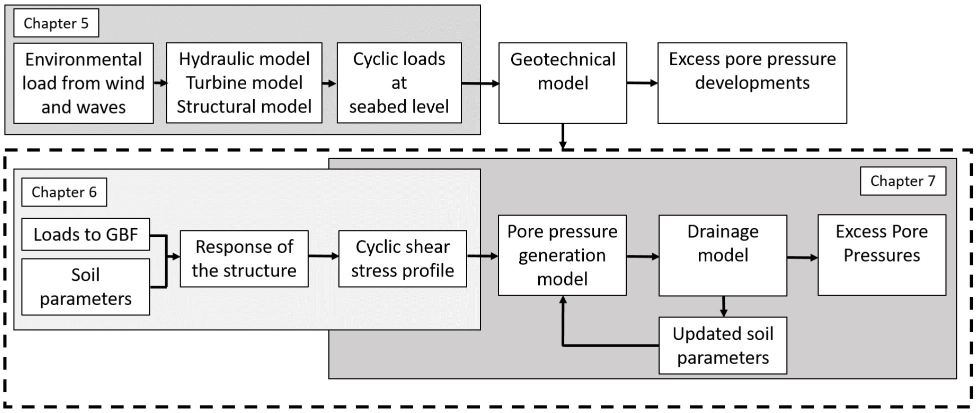

Figure 3.16: *Subdivision of the next chapters 4, 5 and 6 within the followed approach*

After defining a reference case for a GBF and OWT in chapter 4, the chapters 5 and 6 will focus on the necessary input for DCycle to be able to model the real storm build-up and include the randomness of the loads. These two steps are:

- Chapter 5: Derivation of the loads at seabed level for a selected reference geometry of the gravity based foundation with offshore wind turbine
- Chapter 6: Derivation of a cyclic shear stress profile below the gravity based foundation

The general approach that will be followed in the chapters 5, 6 and 7 is indicated in figure 3.16.

4

Reference case

4.1. Introduction

A reference case is defined in this chapter to start the analysis of the GBF with OWT and to finally answer the research questions. A case is necessary since a sound basis is required for the topics in the following chapters, as was already indicated in figure 3.16 in the previous chapter. The case will be largely based on the design by the BAM. The location is offshore Blyth (UK), where five gravity bases will be built within a demonstrator project, with corresponding environmental data from a synthetic dataset of CoastDat (Weisse et al. (2005)). This chapter starts with a general introduction to support structures for offshore wind turbines, converging to gravity based foundations subsequently, and finally the definition of a reference case with the required information for the following chapters.

4.2. Support structures for offshore wind turbines

4.2.1. General concepts

Foundations for offshore wind turbines (OWT) need to transfer loads from wind, turbine and waves to the subsoil. The design should be cost effective for large scale production in order to compete with other energy sources such as oil, gas or onshore wind. Therefore the ease of fabrication and speed of installation are important for application in offshore wind farms. Different foundation types have been developed and may be applied depending on local conditions. An overview of currently applied support structure concepts is given in figure 4.1, together with some definitions. The main support structures have originally been developed for application in offshore oil- and gas industry. The main differences between support structures for oil- and gas and OWTs are:

- The water depth where OWTs are currently installed is relatively small compared to water depths for offshore oil- and gas platforms.
- The ratio of horizontal load over vertical load on a support structure for an OWT is larger compared to oil- and gas platforms, where the horizontal load is in general smaller and the vertical load larger.
- Large bending moments occur at the base of support structures for OWTs due to horizontal wind loading at large heights above the still water level, while the bending moments are not present for support structures for oil- and gas industry.
- The dynamic behaviour of the OWT is in general a relatively soft system compared to offshore oil- and gas structures, indicating a lower natural frequency. This is due to the slender wind turbine design with low stiffness, resulting in natural frequencies close to the excitation frequencies of the loads. In the design of support structures therefore the resulting natural frequency of the system is an important parameter to prevent resonance phenomena, much more compared to the relatively stiff oil- and gas platforms placed on truss (tower) structures or jackets.

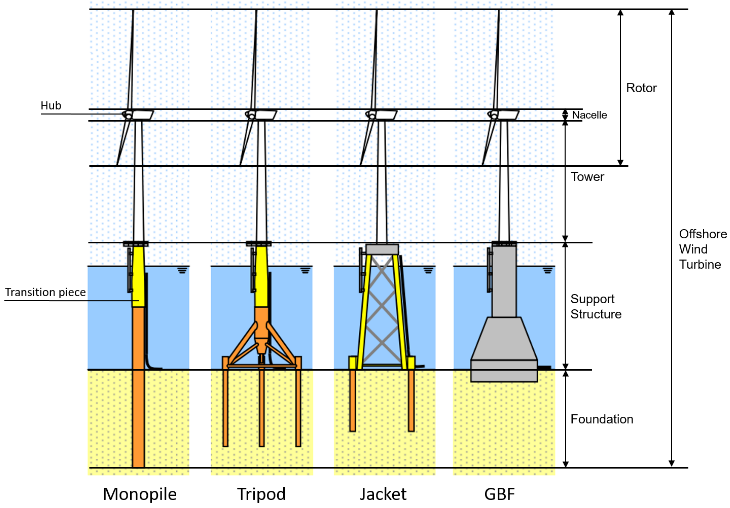

Figure 4.1: *Currently used support structure concepts for offshore wind turbines, and definitions to be used (based on De Vries (2010))*

Especially the monopiles have been applied in offshore wind industry regularly, due to the easy fabrication and installation aspects. If the water depth increases, larger hydrodynamic loads are experienced and consequently a larger base resistance is necessary to transfer the loads to the subsoil. Also stiffer structures are necessary to prevent very flexible structures with natural frequencies in the range of wave frequencies. In this case the multi-pile foundation may be interesting, such as tripods, jackets or tower constructions (figure 4.1). The stability of these structures is based on axial loading of foundation piles, either in tension or compression depending on the load conditions. Furthermore, stiffer structures can be accomplished, which results in less potential for resonance problems. Jackets also reduce the environmental load due to the open type of structure, while the ever increasing monopile diameters will keep increasing the hydrodynamic loads.

Considering the foundation types, distinction can be made between deep foundations by piles, or shallow foundations by gravity based structures. Gravity based foundations (GBF) gain their stability by the dead weight and transfer the environmental loads to the subsoil by normal- and shear stresses. GBFs are usually constructed onshore and towed out to their final destination, where only little offshore activities are required since no piling works have to be performed. In terms of environmental impact, a GBF therefore has an advantage over a piled foundation. However, in general a large volume is needed to ensure the stability and consequently a GBF experiences relatively large environmental loads. Therefore one of the major challenges in gravity based structures is the geotechnical design, taking into account the static and dynamic stability, soil behaviour under cyclic loads and settlements.

Whether a specific foundation and support structure is cost-effective at a specific location, is mainly determined by:

- The soil conditions and variability within soil conditions: soil conditions largely determine the bearing capacity of the foundation type and the possible installation methods. Variability in soil conditions determines whether a certain standardized support structure is suitable for a complete wind farm.
- The water depth: the water depth determines the hydrodynamic loads on the support structure, and consequently the loads at foundation level to be transferred to the subsoil.
- The wind turbine: the wind turbine determines the aerodynamic load and dead load on the support structure and foundation, which also has to be transferred to the subsoil.
- The construction and installation costs: the foundation costs determine about 30% of the total costs (DTI (2001)), and therefore reducing these costs can reduce the overall costs significantly. The foundation costs depend on construction costs of the support structure and foundation, but also on installation costs and finally in decommissioning costs.

A gravity based foundation in particular becomes competitive with the proven technology of monopiles for deeper waters and for larger wind turbines, where the stiffness of the monopile gets too close to the excitation frequencies of the environmental loads, or where bending moments from the wind turbine asks for excessive diameters of monopiles, although the industry shows that the limit in diameter has not been reached yet.

4.2.2. Gravity based foundations

The first GBF for offshore wind turbines were installed in Denmark in 1991, in a water depth of 5 meter. Afterwards more GBFs have been installed in the shallow Baltic Sea. An overview of more recent GBFs installed is given in table 4.1. Only the GBFs at the Thornton sandbank (Belgium) are located in relatively deep waters, up to 28 meter. Up to now the gravity based foundations are made of concrete up to the level of the transition piece, but another possibility is to use a concrete caisson with a steel tubular shaft up to the transition level. This concept is put forward by BAM and will be used as a case study in this research.

Wind farm	Country	Year	Installed MW	Water depth	GBF diameter
Thornton	Belgium	2008	30	12-28	24
Lillgrund	Sweden	2007	110	4-10	19
Nystedt I (Rodsand I)	Denmark	2003	166	6-10	11
Middelgrunden	Denmark	2001	40	3-5	17

Table 4.1: *Overview of installed gravity based foundations*

The major advantage using a steel tubular shaft instead of a concrete shaft is to reduce the dimensions where wave loads act, reducing the environmental loads. Furthermore large bending moments can be better transferred by steel than by concrete. Although a steel shaft is more expensive, this is compensated by the possibility to tow the structure towards its final destination. This is possible since the weight is largely reduced using a slender steel shaft and stability is increased due to a lower centre of gravity. The possibility of towing makes an expensive heavy lift vessel unnecessary, compensating the larger costs of steel.

4.3. Reference case

The reference case consists of a gravity based foundation, an offshore wind turbine, general soil properties and environmental data. These topics will be discussed in this order below.

4.3.1. Gravity based foundation

A reference geometry is defined based on the design of BAM, which will be used in this study to investigate the behaviour under cyclic loads. In this section the geometry used for this research as well as the reference location, reference turbine and environmental data will be presented. The gravity based foundation consists of a concrete caisson with a base slab diameter of 30 meter. The steel tubular shaft is founded on the base slab and ranges up to the interface level, where the connection with the tower will be made. A general overview of the conceptual design and the reference geometry is given in figure 4.2. The main characteristics of the concept design and reference geometry are listed in 4.2 and are based on the work of Smaling (2014).

Considering the design of the base slab, several possibilities exist depending on local conditions:

- If a very flat seabed is present, a flat gravity base can be placed directly on top of the seabed. However, scour problems may occur around the base slab of the structure, undermining the stability.
- In case scour is found to be a problem, vertical skirts below the base may be applied to improve the erosion resistance. The skirts can either penetrate into the sea floor, or land on top of the sea floor. In case the sea floor has irregularities, the areas between the skirts can be filled with grout to meet requirements of verticality.
- Finally, a solution with a complete seabed preparation is possible using a pre-installed gravel bed. The gravel bed improves drainage capabilities. In this case any irregularities in the seabed should first be removed.

		Concept design	Reference geometry
Diameter base	[m]	30	30
Total height base and cone	[m]	16.5	17
Diameter steel tubular pile	[m]	5.5 up to 7	6
Submerged weight base, cone and pile incl. ballast	[tons]	13000	13000

Table 4.2: *Main dimensions of the concept gravity based foundation and the reference geometry*

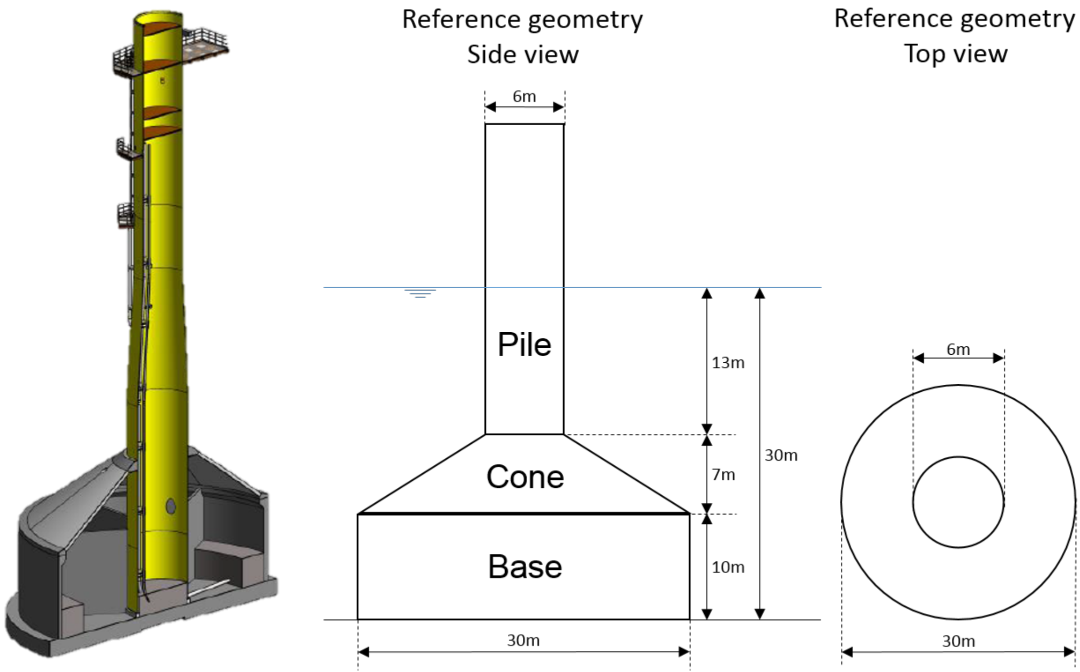

Figure 4.2: *Gravity based foundation with a steel tubular shaft, as proposed by BAM (left, Smaling (2014)) and reference geometry, side view (middle) and top view (right)*

In the current study a start will be made with a GBF placed on a flat seabed, without any gravel bed or skirts. As part of the sensitivity study, the effect of a gravel bed will be investigated. The general procedure before installation will be the dredging of a pit with a trailing suction hopper dredger, after which a filter layer will be placed with a fall-pipe vessel. In fact this gravel layer has different functions, i.e. not only increasing the drainage capabilities and therefore reducing risk on cyclic liquefaction, but it also creates a better levelled bed and it fulfils the function of a filter layer below the armour layer (for scour protection) to be applied around the GBF. After seabed preparation and placement of the gravel bed, the GBF will be installed and ballasted and the armour layer (scour protection) will be placed around the structure on top of the gravel bed.

The location where 5 GBFs will be installed is at the Blyth Offshore Demonstrator Project, offshore Blyth (Northumberland, UK), in an average water depth ranging between 30 to 58 meter and located 5.7 to 13.8 km from the coast (Irvine (2011)). In total 3 arrays have been defined of each maximum 5 turbines between 5 MW and 8.5 MW. The GBF will be economically interesting in relatively large water depths where other foundations, such as monopiles, become too big and too expensive. In this research a water depth of 30 meter will subsequently be used, although the GBF might be suitable for even deeper waters.

4.3.2. Offshore wind turbine

For the turbine type a 8MW 3-bladed Vestas wind turbine is selected (Vestas Wind Systems (2012)). This is a relatively large wind turbine which is however interesting for application on support structures in deeper waters to reduce the foundation costs per installed MW. The main characteristics of the turbine are listed in table 4.3. The tower diameters are site specific according to Vestas, and therefore tower diameters have been based on values from literature (Jonkman et al. (2009)). This also holds for the rotor, nacelle and hub mass and turbine tower. The turbulence class is based on the definition of the International Electrotechnical Commission (IEC (2014)).

4.3.3. Soil conditions

Since no detailed information about the soil conditions is available, reference soil properties will be used to answer the research question. First of all, some basic soil properties will be discussed which will mainly be related to the relative density of homogeneous sand. The starting point in this study will be homogeneous sand, which will be extended to less permeable sands in the sensitivity study. To get an indication of the soil

Turbine rotational speed	[rpm]	4.8-12.1
Operational wind speed range	[m/s]	4-25
Rated wind speed	[m/s]	14
Hub height above mean sea level (MSL)	[m]	124
Tower diameter top	[m]	4.5
Tower diameter bottom	[m]	6.5
Turbine rotor diameter	[m]	164
Rotor overhang	[m]	5
Rotor mass imbalance	[kg m]	4000
Mass of rotor, hub and nacelle	[ton]	425
Mass of turbine tower	[ton]	700
IEC-61400 Turbulence class	-	A (16%)

Table 4.3: *Main characteristics of Vestas 8MW wind turbine*

properties and the values for different relative densities, these will be derived below, but first of all some basic definitions are introduced.

The porosity is defined as the quotient of pore volume V_p divided by the total soil volume V_t (equation 4.2). The void ratio is the quotient of the pore volume divided by the volume of the grain particles, and is also a measure for the porosity (equation 4.1).

$$e = \frac{V_p}{V_g} \tag{4.1}$$

$$n = \frac{V_p}{V_t} = \frac{e}{1+e} \tag{4.2}$$

The relative density is expressed in terms of void ratios (4.3):

$$I_d = \frac{e_{max} - e}{e_{max} - e_{min}} \tag{4.3}$$

V_p = total volume of pores $[m^3]$
V_g = total volume of grains $[m^3]$
V_t = total volume of soil $[m^3]$
e = void ratio [-]
e_{max}, e_{min} = maximum and minimum void ratio [-]
I_d = relative density [-]

The minimum and maximum void ratios can be related to the maximum and minimum porosities, and can be determined by laboratory tests. In general, the range of packing densities can be based on the theoretical porosities of a cubical packing and a rhombic packing. For the cubic packing with a particle with diameter D, the volume of a soil particle is $\pi D^3/6$, and the total volume will be D^3, resulting in a ratio of volume of solids over total volume of $\pi/6 = 0.5236$, and the corresponding porosity of 0.4764. For the rhombic array a similar calculation can be made, which results in a porosity of 0.2595 (Verruijt (2012)). The corresponding void ratios are $e_{max} = 0.9099$ and $e_{min} = 0.3504$. The hydraulic permeability k (equation 4.4) is expressed as a function of the intrinsic permeability and the volumetric weight and viscosity of the fluid. The intrinsic permeability (equation 4.5) depends on the measure of the grain size d_{grain} and the porosity n and on the coefficient c, based on the Kozeny-Carman formula.

$$k = \frac{\kappa \gamma_w}{\nu} \tag{4.4}$$

$$\kappa = c d_{grain}^2 \frac{n^3}{(1-n)^2} \tag{4.5}$$

I_d	e	n	E	E_{ur}	ν	G	K	m_v	k	c_v
[-]	[-]	[-]	[MPa]	[MPa]	[-]	[MPa]	[MPa]	$[Pa^{-1}]$	[m/s]	$[m^2/s]$
0.5	0.63	0.39	35	150	0.3	13	29	2.12E-08	1.1E-04	0.52
0.6	0.57	0.36	40	170	0.3	15	33	1.86E-08	1.0E-04	0.56
0.7	0.52	0.34	45	190	0.3	17	38	1.65E-08	9.8E-05	0.59
0.8	0.46	0.32	50	210	0.3	19	42	1.49E-08	9.1E-05	0.61
0.9	0.41	0.29	55	230	0.3	21	46	1.35E-08	8.4E-05	0.62

Table 4.4: *Soil conditions for the reference case*

k = hydraulic permeability or conductivity [m/s]
κ = intrinsic permeability $[m^2]$
ν = kinematic viscosity $[m^2/s]$
c = coefficient of Kozeny-Carman: 0.01 [-]
d_{grain} = grain size [m]

The consolidation coefficient (equation 4.7) can be determined using the hydraulic permeability, and the compressibility coefficient m_v (equation 4.6). The bulk modulus K and shear modulus G are expressed in terms of the Young's modulus E and Poisson ratio ν.

$$m_v = \frac{1}{K + \frac{4}{3}G} \tag{4.6}$$

$$c_v = \frac{k}{\gamma_w (m_v + n\beta)} \tag{4.7}$$

$$K = \frac{E}{3(1-2*\nu)} \quad G = \frac{E}{2(1+\nu)} \tag{4.8}$$

m_v = coefficient of compressibility [1/MPa]
K = bulk modulus [MPa]
G = shear modulus [MPa]
E = Young's modulus [MPa]
c_v = consolidation coefficient $[m^2/s]$
k = hydraulic permeability or conductivity $[m/s]$
β = compressibility of water [-]
ν = kinematic viscosity $[m^2/s]$

Using the mentioned formulae, for different relative densities the sand conditions have been determined. By specifying a reference permeability at a reference porosity, the permeabilities at other porosities can be calculated too. A value of k = 1E-04 at n=0.35 was considered reasonable for sand. Using equation 4.4 the permeabilities at other porosities were calculated. The coefficient of consolidation is calculated by assuming incompressible pore water, making $\beta = 0$ in equation 4.7, and with the permeability and the coefficient of compressibility m_v the consolidation coefficient can be calculated. These properties and values will be used in the excess pore pressure calculations and are presented in table 4.4.

4.3.4. Additional data

For the reference site, the environmental data was obtained from (Irvine (2011)) and is presented in table 4.5. The water depth related to mean sea level (MSL) is rounded up to 30 meter and will be used throughout this study. The interface level and hub height have been estimated. The platform level is calculated to determine the resulting hub level of the wind turbine, which in turn determines the wind loads.

The platform level should not be located in the splash zone according to DNV (2014), and its height above MSL can therefore be calculated with equation 4.9. As can be seen 65% of the wave height with a return period of 50 years should be taken into account. The air gap should be the maximum of 1.0 meter or 20%

Water depth	[m]	30
Highest Astronomical Tide	[m + MSL]	3.35
Storm surge	[m]	0.6
Wave height 50 yr	[m]	19.6
Wave height 5 yr	[m]	16.3
Wave period 50 yr	[s]	11.6
Wave period 5 yr	[s]	10.7
Current velocity 100 yr	[m/s]	1.82
Current velocity 5 yr	[m/s]	0.90
Wind speed 5 yr at hub	[m/s]	37
Wind speed 50 yr at hub	[m/s]	43
Interface level	[m + MSL]	18.7
Hub height	[m + MSL]	124

Table 4.5: *Environmental data at the reference site (Irvine (2011))*

of the significant wave height with a return period. Since the significant wave height corresponding to the maximum individual wave with a return period of 50 years (19.6 meter) was not given, it was estimated to be $1/2H_s$ (Holthuijsen (2007), resulting in 9.8m) and for the air gap this results in a value of 1.96m., rounded up to 2m. This finally resulted in a platform level at 18.7 m+MSL. The platform level is assumed to be the same level as interface level, where the connection with the tower will be made. In reality this might however be a few meter higher. The hub height of the Vestas 8MW wind turbine in an onshore demonstrator project in Denmark was approximately 105 m. (Vestas Wind Systems (2012)) above ground level. Using this hub height as the approximate tower length, the hub height for the offshore conditions under consideration becomes 123.7 m+MSL, which will be round up to 124 m+MSL.

$$z_{platform} = HAT + \Delta z_{surge} + \Delta z_{air} + 0.65H_{1/50yr} \tag{4.9}$$

Where:

$z_{platform}$	= platform level [m + MSL]
HAT	= highest astronomical tide [m + MSL]
Δz_{surge}	= storm surge level with a 50yr return period [m]
Δz_{air}	= air gap [m]
$H_{1/50yr}$	= maximum wave height with a 50yr return period [m]

5

Load analysis

5.1. Introduction

Chapters 2 and 3 dealt with the elementary behaviour of sand under cyclic loading and the modelling of it. This has placed the approach followed in this research in a broader context of liquefaction phenomena and in a broader context of modelling approaches. DCycle was found to be suitable for the main processes that need to be taken into account to answer the research question related to the load history and the irregular nature of the loading. This already indicates the importance of the cyclic loads for the defined reference case in chapter 4. Therefore, the aim of this chapter is to derive these cyclic loads for this case. The followed approach is indicated in figure 5.1, with chapter 5 highlighted.

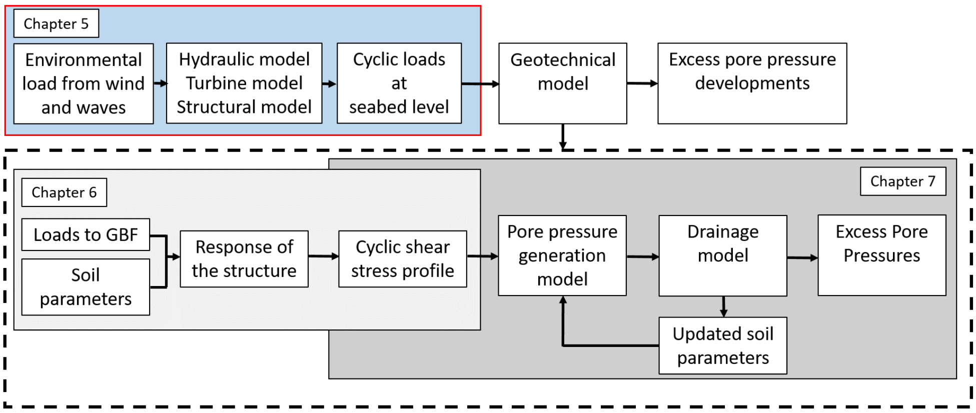

Figure 5.1: *Subdivision of the chapters within the followed approach, with the content of chapter 5 highlighted in blue*

It should be noted that this simplified load derivation is mainly focussing on loads in terms of frequencies and amplitudes, applied to various storms from the dataset. The limitations of the resulting load analysis will be presented in this chapter too. The load analysis will start with the general procedure: the loads will be derived in the frequency domain and transformed to the time domain with a random phase model, in order to capture the mentioned irregular nature of the loads as well. This procedure will be followed for wind, wave and turbine loads, and can be used to follow real storm developments from the synthetic dataset. Maybe most important, the chapter will end with the assumptions and limitations of the load analysis.

5.2. Load analysis

Offshore wind turbines experience both static loads (constant during a certain period of time) and dynamic loads (fluctuating in time), the latter one with a frequency and amplitude. In order to assess the stability

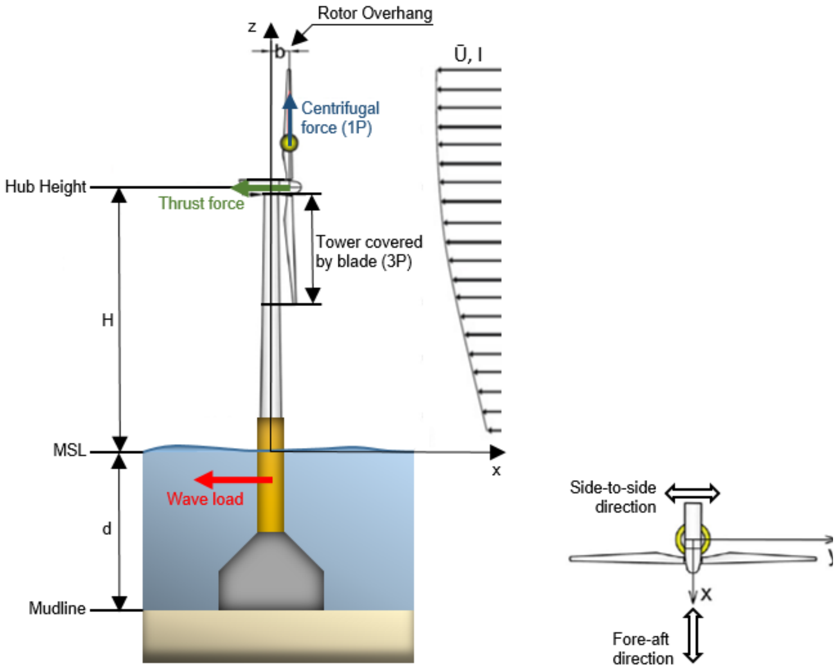

Figure 5.2: *Definitions of the dynamic loads on the offshore wind turbine, together with the axis definition, based on Arany et al. (2014)*

of the structure in relation to cyclic loading of the subsoil, mainly the dynamic load components in terms of amplitude, frequency and number of load cycles are of interest. In the current chapter a simplified load analysis will be performed which is largely based on the method of Arany et al. (2014) and Van der Tempel (2006). The main design code that is used is the Det Norske Veritas (DNV) offshore standard 'Design of Offshore Wind Turbines' (DNV (2014)). Other standards have only been used as a comparison because they are not specifically written for design of offshore wind turbines.

The dynamic loads acting on the structure are the environmental loads from turbulent wind eddies and the fluctuating wave loads, and the loads from the operating wind turbine. The static loads are imposed by the tidal current and the load from a mean wind speed (the stationary part of the wind speed). The dynamic loads are visualised in figure 5.2, where the axis are indicated as well.

- Fluctuating wind loads, depending on the mean wind speed and the turbine response characteristics to wind eddies passing the blades.
- Wave loads, of which the magnitude depends on the wave height, wave period and wave length, which is in turn related to the water depth. Also the geometry of the structure is of large influence.
- 1P loads: the loads from the rotor, with a frequency equal to the frequency of rotation (1P frequency), and the magnitude depends on the mass imbalance of the rotor. The frequency of rotation depends on the mean wind speed and is bounded by the operating system of the rotor, which results in a 1P frequency range for the operating wind speeds. The 1P frequency is constant for a certain mean wind speed.
- 3P loads: the loads from the blades passing the turbine tower, called the blade shadowing effect. The frequency of excitation is for a three bladed turbine 3 times the 1P frequency and therefore called 3P frequency. When a blade passes the tower, a loss in wind load on the tower is produced. It is therefore a load loss with frequency 3P. Since the 1P frequency depends on the mean wind speed, the 3P frequency also depends on the mean wind speed. For a variable wind speed turbine, the 3P frequencies result in a frequency range, equal to three times the 1P range.

In general the dynamic loads are most easily analysed in the frequency domain, represented as a power spectral density (PSD) of the loads versus frequency. This method is a convenient way to represent the contributions from different frequencies to the total dynamic loads. The PSDs of environmental loads such as wind and wave loads can best be obtained from site specific data, but also theoretical spectra can be used such as a Kaimal spectrum for wind and a JONSWAP spectrum for waves. These spectra can be converted to a load spectrum, for both horizontal forces and bending moments, using turbine characteristics for wind loads and support structure characteristics for wave loads. The 1P and 3P frequencies from the turbine are largely

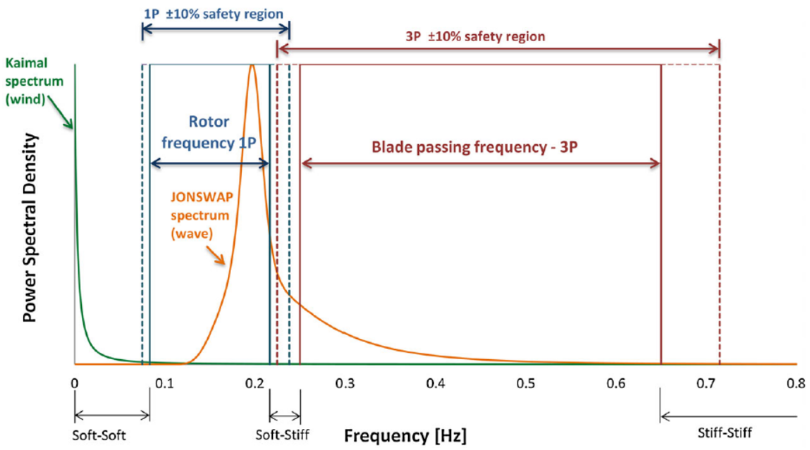

Figure 5.3: *Frequency diagram for an Siemens 3.6 MW offshore wind turbine, including wind and wave spectrum and 1P and 3P load spectrum (Arany et al. (2014))*

dependent on the turbine operating system but can be converted to horizontal forces and bending moments at seabed level as well. According to DNV (DNV (2014)) an additional margin of 10% on the upper and lower limits of the 1P and 3P frequencies should be applied, in order to stay on the conservative side, but whether this is conservative largely depends on the accuracy of the natural frequency that is determined.

Since the wind turbines are characterized by a large mass at a large height above sea level and a relatively slender turbine tower, a soft structure with a natural frequency comparable to the frequencies of wind, waves and the 1P/3P load is obtained. Therefore, the support structure design should result in a natural frequency of the total system which is not interacting with the environmental loads and the 1P and 3P frequencies. This should prevent resonance and damage to the structure due to large deformations, or fatigue failure. Three types of systems (the turbine, support structure and foundation in total) can be defined, depending on the natural frequency f_0 as indicated in figure 5.3.

- soft-soft: f_0 below the 1P frequency range, asking for a very flexible support structure and foundation
- soft-stiff: f_0 between 1P and 3P frequency range, most often applied in current support structure and foundation design
- stiff-stiff: f_0 above the 3P frequency range, which can only be reached using a very stiff support structure and foundation

From the figure it becomes clear that the dynamic behaviour of the offshore wind turbines together with the loads, results in a complex system and consequently an important role of dynamics in the design stage. This also involves the tuning of the design of the support structure and foundation to the dynamic behaviour of the total system including wind turbine, to prevent resonance eventually. And this consequently asks for an integrated design approach between load engineers and foundation engineers.

A very flexible support structure could for instance be a monopile in relatively deep water, but even with these structures it is hard to stay below the 1P frequency (Arany et al. (2014)). The soft-stiff structures are often applied, for instance the currently installed monopiles belong to these types of structures. The stiff-stiff part can only be reached with very stiff structures, for instance jackets and towers with 3 or 4 foundation piles and a steel frame structure. It should be noted that the natural frequency f_0 might also be time dependent, depending on the local soil conditions. Form literature it is known that the natural frequency may increase in strain hardening soils such as medium dense sands, resulting in a stiffer soil-foundation behaviour, and may similarly decrease in strain softening soils such as normally consolidated clays (Arany et al. (2014)).

The before mentioned four dynamic loads will subsequently be described and spectra for horizontal shear forces and bending moments at seabed level will be derived in the frequency domain.

5.2.1. Loads: stochastic processes

The loads on an OWT can be described in the time domain and frequency domain (Van der Tempel (2006)). The frequency domain can far more easily be used to analyse contributions from different loads, both in

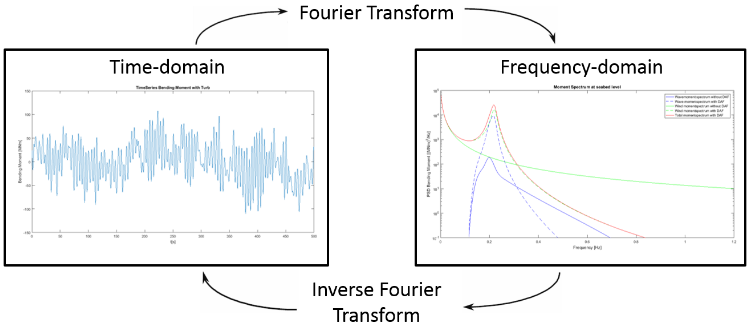

Figure 5.4: *Visualisation of the Fourier transform and the inverse Fourier transform, and the relation with time and frequency domain*

terms of frequency and in terms of amplitude. Furthermore, the major loads on offshore wind turbines of wind and waves, are random events (also called stochastic events in probabilistics). The stochastic loads can however still be analysed if all possibilities of occurrence are taken into account. Each realisation of the random process can be presented in a spectrum, as long as the process can be assumed to be stationary (not changing in time). This makes a spectrum suitable to represent the irregular loads.

Fourier transformation

A random load signal consists of a number of frequencies and amplitudes, all summed up to result in the total random or irregular load signal. From such a signal the frequencies and amplitudes can be derived using a Fourier transformation. It is assumed that the irregular signal consists of a summation of cosine and sine signals (equation 5.1), with a respective amplitude equal to the Fourier coefficients A_q and B_q (equation 5.2). The Fourier transformation produces a signal in the frequency domain from a signal in the time domain (figure 5.4).

$$z(t) = \sum_{q=1}^{end} A_q \cos(2\pi f_q t) + B_q \sin(2\pi f_q t) \tag{5.1}$$

$$\begin{aligned} A_q &= \frac{2}{N} \sum_{n=1}^{end} z_n \cos\left(\frac{2\pi q n}{N}\right) \\ B_q &= \frac{2}{N} \sum_{n=1}^{end} z_n \sin\left(\frac{2\pi q n}{N}\right) \end{aligned} \tag{5.2}$$

Considering a load signal, with:

A_q, B_q	= Fourier coefficients [N]
q	= Fourier component counter 1,2, ... q_{end} [-]
f_q	= frequency of component q [Hz]
t	= $n\Delta t$, time [s]
Δt	= time step [s]
n	= time step counter 1,2,..N [-]
N	= total number of time steps [-]

The Fourier coefficients are found by summing up over the total duration of the signal, and the random signal is found by summing up over all Fourier coefficients. The random wave signal can now be found back using the Fourier coefficients as defined above, which gives a load amplitude and phase (equation 5.3, 5.4 and 5.5) for each component. The latter procedure is called the inverse Fourier transform, since it is the inverse of the above described Fourier transform and produces a signal in the time domain from a given signal in the frequency domain (figure 5.4). The latter procedure will be used in this study to generate time series of loads, and the Fourier transform itself will only be used to verify the procedure of the inverse Fourier transform.

$$F(t) = \sum_{q=1}^{end} A_F \sin(2\pi f_F t + \phi_F) \tag{5.3}$$

With:

A_F = amplitude of load signal [N]
f_F = load frequency [Hz]
ϕ_F = phase of load signal [rad]

And with:

$$A_F = \sqrt{A_q^2 + B_q^2} \tag{5.4}$$

$$\tan(\phi_F) = \frac{B_q}{A_q} \tag{5.5}$$

The equations 5.1 up to 5.4 are implemented in the standard Matlab function for a fast Fourier transform (FFT) and an inverse Fourier transform (IFFT). The procedure of the Fourier transform is similar to the above mentioned equations, however the output is often presented in a power spectral density per frequency interval and not in terms of an amplitude of a load or signal. For instance for a wave spectrum, a better parameter to describe the variability in the signal is the variance of the signal instead of the amplitude of the signal itself. Subsequently the variance is binned in a spectrum and a variance density per frequency interval can be obtained, which is for a component with amplitude A_i equal to $\frac{1}{2}A_i^2/\Delta f$. With Δf approaching to zero, the spectrum can be made continuous instead of discrete. Therefore, for a power spectral density of wave heights the units will be $[m^2/Hz]$ and for wind speeds $[(m/s)^2/Hz]$.

Power Spectral Densities

The power spectral densities of wave heights and wind speeds can be used to construct power spectral densities (PSD) of loads, in terms of horizontal force and bending moment at seabed level. In order to do so a transfer response function (TRF) should be used which relates wave height and wind speeds to forces and bending moments. The squared transfer functions can be multiplied with PSDs of wave heights and wind speeds to obtain PSD of loads.

$$S_A(f) = \lim_{\Delta f \to 0} \frac{1}{2}\frac{\bar{A}(f)^2}{\Delta f} = \lim_{\Delta f \to 0} \frac{1}{2}\left(\frac{\bar{A}(f)}{\bar{F}(f)}\right)^2 \frac{\bar{F}(f)^2}{\Delta f} = \left(\frac{\bar{A}(f)}{\bar{F}(f)}\right)^2 S_F(f) \tag{5.6}$$

As an example the procedure is given in equation 5.6. For instance consider a system which is loaded with a signal with an amplitude F. The signal can be analysed in the frequency domain with a Fourier transformation giving a input load spectrum $S_F(f)$. Also the system itself can be analysed in the frequency domain by analysing its response A to different loads with different frequencies, giving a spectrum $S_A(f)$ (equation 5.6). Both spectra can be linked with a Transfer Response Function (TRF). If the TRF is known, the output spectrum of the system to the input spectrum of the load can be determined, and subsequently be analysed in the time domain.

This can be further generalised into equation 5.7:

$$S_A(f) = \mathrm{TRF}(f)^2 S_F(f) \tag{5.7}$$

Subsequently, the created spectrum of wind and wave loads can be used to reconstruct time series of loads for different input parameters of the wave- and wind spectrum. A randomly distributed phase angle of the different components in the summation is used to generate random time series from the spectral parameters. The amplitude is obtained from the spectrum and the phase is randomly generated between 0 and 2π, which results in a signal in the time domain. The general procedure is visualized in figure 5.5. These load time series will subsequently be used to assess the liquefaction potential of the gravity based foundation for an offshore wind turbine.

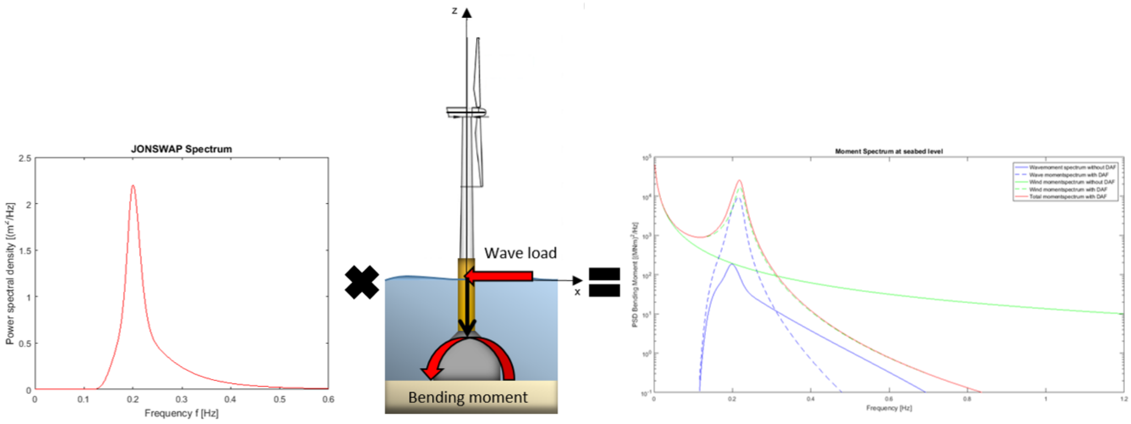

Figure 5.5: *Visualization of the spectrum transformation from input load spectrum to load spectrum at seabed level, for wave loads*

Important aspects

When a Fourier transformation is applied to a time series, a frequency component can be introduced with a higher frequency than the time record contains. This is named the aliasing effect and can be prevented by using a cut-off frequency above which no frequency components are taken into account. For a time record of length T, sampled at interval Δt with $N = T/\Delta t$ the number of samples, the smallest frequency present is $f_{min} = 1/T$ and the highest frequency is $f_{max} = N/(2T)$. The latter frequency is the Nyquist cut-off frequency. Therefore the frequency interval should be limited between $1/T$ and $N/(2T)$ to prevent non-existing frequencies being analysed in the frequency domain. For the fast Fourier transform (FFT) in Matlab the power N should also be a power of 2.

In order to catch the signal in the frequency domain correctly around the peak at the natural frequency of the system, a maximum value for the frequency bins can be derived. If the frequency step is too big, the Fourier transform could miss the sharp peak at the resonance frequency (Van der Tempel (2006)). The half power bandwidth determines which frequency interval can best be used to prevent this. It is related to the damping of the system and the natural frequency of the system (equation 5.8).

$$\Delta f \leq 2\zeta f_0 \tag{5.8}$$

Where:

Δf = frequency interval [Hz]
ζ = ratio of actual damping versus critical damping, equation 5.37 [-]
f_0 = natural frequency [Hz]

5.2.2. Wind loads

The fluctuating wind component is expressed with the turbulence intensity I, which is the ratio of the standard deviation of the mean wind $\bar{U}$ speed versus the mean wind speed $\bar{U}$ (equation 5.9). Turbulence is defined as the wind speed fluctuation with frequencies above the spectral gap. The spectral gap is an interesting characteristic of distribution of wind energy in the frequency domain, known as the Van der Hoven spectrum (van der Hoven (1957)). This indicates two main peaks in wind energy distribution, independent of the location, at a 4-days cycle and at a 1-minute cycle (figure 5.6). The 4 day cycles represent the geostrophic winds, while the 1-minute cycles represent the turbulence. Both peaks are separated by the energy gap with periods of wind fluctuations between 10 minutes and 2 hours. Wind turbulence has a minor influence on the annual power output of the wind turbine, but determines the aerodynamic loads significantly (Bianchi et al. (2007)).

$$I = \frac{\sigma_u}{\bar{U}} \tag{5.9}$$

With:

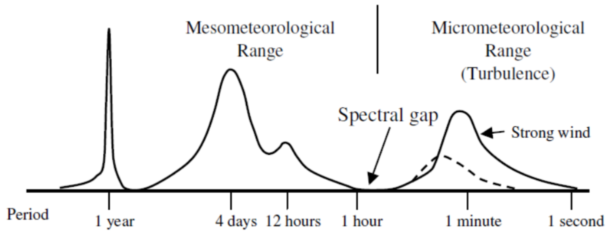

Figure 5.6: *Wind speed spectrum with the spectral gap, indicating the low and high frequency fluctuations (van der Hoven (1957))*

I = turbulence intensity [-]
$\bar{U}$ = 10 minute averaged wind speed [m/s]
σ_u = standard deviation of mean wind speed [m/s]

The turbulence intensity depends on the mean wind speed, but also largely depends on the location, for instance the surface roughness. Offshore turbulence intensities are in general smaller compared to onshore turbulence intensity due to smaller surface roughness. Also the turbine itself influences the turbulence intensity by deforming the turbulent eddies. In this study a representative turbulence intensity will be used which neglects the latter effects. Different theoretical wind spectra can be used, for instance the Von Karman spectrum or the Kaimal spectrum. DNV suggests to use the Kaimal spectrum (figure 5.7), which will therefore be used. The spectrum is represented by equation 5.10. The Kaimal spectrum is only valid for high frequency fluctuations, i.e. for small time scales below 10 minutes (>0.0017 Hz).

$$S_{uu}(f) = \sigma_u^2 \frac{4\frac{L_k}{\bar{U}}}{(1+6f\frac{L_k}{\bar{U}})^5/3} \tag{5.10}$$

Where:

S_{uu} = Kaimal spectrum, spectral density of wind speed $[(m/s)^2/Hz]$
L_k = integral length scale [m]
f = frequency [Hz]
$\bar{U}$ = 10 minute averaged wind speed [m/s]
σ_u = standard deviation of mean wind speed [m/s]

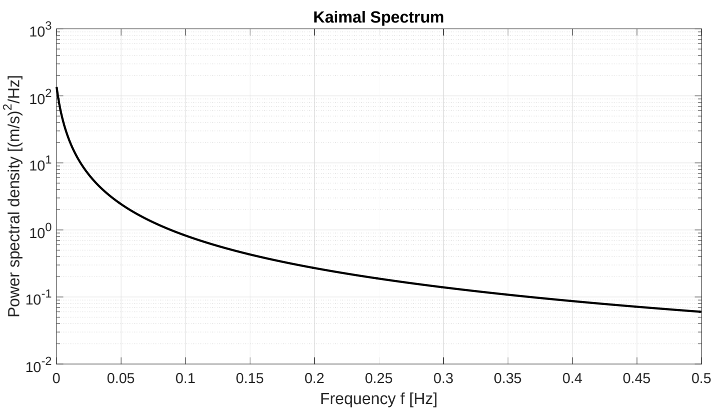

Figure 5.7: *Kaimal spectrum on a logarithmic y-axis, in terms of the power spectrum density (wind speed squared per frequency interval) versus frequency*

L_k is an integral length scale, which is according to DNV (DNV (2014)) 340.2 meter for heights larger than 60 meter above mean sea level, and will therefore be used. The standard deviation of the wind speed can be derived from site measurements of wind speeds, or can be calculated according to the standard of the International Electrotechnical Commission (IEC (2014)). Three classes of I_{ref} have been defined of respectively 16%, 14% and 12% reference turbulence intensity, which is defined at a 10 minute averaged 15 m/s wind

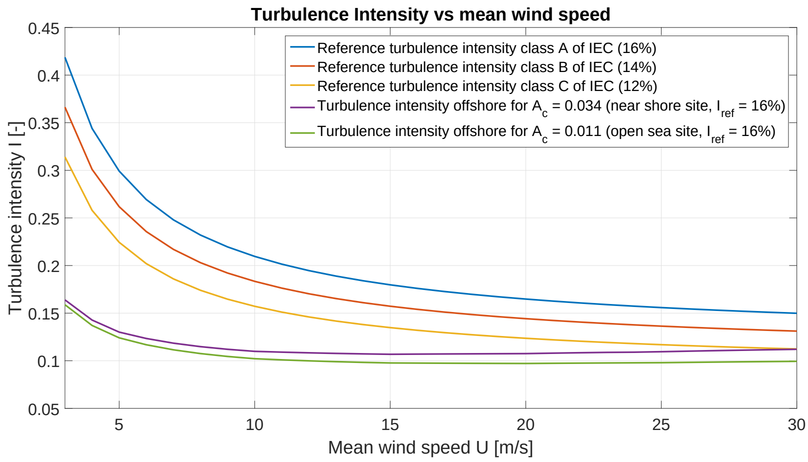

Figure 5.8: *Turbulence intensities versus 10 minute wind speeds at hub level for different turbulence classes according to IEC, both onshore and offshore*

speed. The standard deviation σ_u can be calculated with I_{ref} in equation 5.11. With the standard deviation the turbulence intensity at other 10 minute averaged wind speeds can be calculated using equation 5.9.

$$\sigma_u = I_{ref}(0.75\bar{U} + 5.6) \tag{5.11}$$

With the variables as defined above, and:

I_{ref} = reference turbulence intensity [-]

For offshore conditions, IEC derived another expression to account for the lower turbulence intensities offshore (equation 5.12 and 5.13). z_0 represents the surface roughness. The turbulence intensities decrease for increasing wind speeds and are offshore lower than onshore, as observed in figure 5.8.

$$\sigma_u = \frac{\bar{U}}{\ln(H/z_0)} + 1.84 I_{ref} \tag{5.12}$$

With:

$$z_0 = \frac{A_c}{g}\left(\frac{\kappa\bar{U}}{\ln(H/z_0)}\right)^2 \tag{5.13}$$

And with the variables as defined above, and:

A_c = Charnock's constant: 0.011 for open seas and 0.034 for near-shore locations [-]
κ = Von Karman constant, 0.4 [-]
$\bar{U}$ = 10 minute averaged wind speed at 10 meter height [m/s]
z_0 = surface roughness [m]
H = Hub height, or any other desired height [m]

The wind speeds can be related to different heights z above sea level and can be translated using equation 5.14 with a reference wind speed $U_{z_{ref}}$ at height z_{ref}. For the wind speed $\bar{U}$ in the subsequent equations, the 10 minute averaged wind speed at hub level should be used in order to determine the wind loads on the turbine.

$$U_z = U_{z_{ref}} \frac{\ln\frac{z}{z_0}}{\ln\frac{z_{ref}}{z_0}} \tag{5.14}$$

Using the Kaimal spectrum, a spectrum of wind loads can be derived. The thrust force on a wind turbine is proportional to the square of the wind speed U (Zaaijer (2008)). The wind speed U consists of a mean wind speed and a fluctuating wind speed u (depending on the turbulence intensity).

$$F_{thrust} = \frac{1}{2}\rho A C_T U^2 \tag{5.15}$$

Where:

F_{thrust} = thrust force on wind turbine [N]
ρ = density of air $[kg/m^3]$
A = rotor swept area = $\frac{1}{4}\pi D_{rotor}^2 [m^2]$
D_{rotor} = rotor diameter [m]
C_T = thrust coefficient [-]
U = $\bar{U}$ + u [m/s]
$\bar{U}$ = 10 minute averaged wind speed at hub level [m/s]
u = fluctuating wind speed [m/s]

This can be rewritten into a static thrust force from the mean wind speed $\bar{U}$ and a fluctuating dynamic component from the fluctuating wind speed u (equation 5.16, with the definitions of equation 5.15). This is however only valid for quasi steady assumptions, i.e. if the wind speed can be described as a constant mean and fluctuating component during a certain period of time.

$$F_{thrust} = F_{thrust,static} + F_{thrust,dynamic} = \frac{1}{2}\rho A C_T(\bar{U}^2 + 2\bar{U}u + u^2) \approx \frac{1}{2}\rho A C_T \bar{U}^2 + \rho A C_T \bar{U} u \tag{5.16}$$

The spectral density is defined as the amplitude squared per frequency interval. It can now be obtained by multiplying the squared dynamic amplitude of the thrust force with the normalized Kaimal spectrum, where the latter is the Kaimal spectrum divided by the standard deviation σ_u^2. This procedure in general, was presented in equation 5.6. If the fluctuating component of the wind speed (u) is approximated by the standard deviation σ_u, the spectral density of horizontal force at seabed level due to dynamic wind loads is obtained in equation 5.17.

$$\begin{aligned} S_{ff,wind}(f) &= (\rho A C_T \bar{U} u)^2 \bar{S}_{uu}(f) = \rho^2 \frac{D^4 \pi^2}{16} C_T^2 \bar{U}^4 I^2 \bar{S}_{uu}(f) \\ \bar{S}_{uu}(f) &= \frac{S_{uu}}{\sigma_u^2} \end{aligned} \tag{5.17}$$

Where:

$S_{ff,wind}(f)$ = spectral density of horizontal force at seabed level due to wind loads $[N^2/Hz]$
$\bar{S}_{uu}(f)$ = normalized Kaimal spectrum of horizontal wind speeds [1/Hz]
$S_{uu}(f)$ = Kaimal spectrum of horizontal wind speeds $[(m/s)^2/Hz]$
σ_u = standard deviation of mean wind speed [m/s]

The thrust coefficient is an important parameter since it now represent the dynamic behaviour of the blades of the turbine to dynamically varying wind speeds. For a detailed analysis this simple relation between fluctuating wind speed and thrust force should be captured in a blade element momentum theory (BEM-theory) to model the wind turbine in a 3D fluctuating wind field. According to Frohboese and Schmuck (2010), the thrust coefficient can be approximated by equation 5.18, which can be considered to be a worst case value for thrust loading as was shown in a comparison between a turbine simulation model and the approximation with equation 5.18 (figure 5.9). Only the turbine sizes with a rotor diameter over hub height ratio (D/H) of 1.1 and 0.8 have a slightly larger thrust coefficients at wind speeds between 10-12 m/s and 9-11 m/s respectively. It is however assumed in this study that the thrust coefficient gives an upper value for the thrust load. For real thrust coefficients of wind turbines a detailed blade element model should be used, which asks for

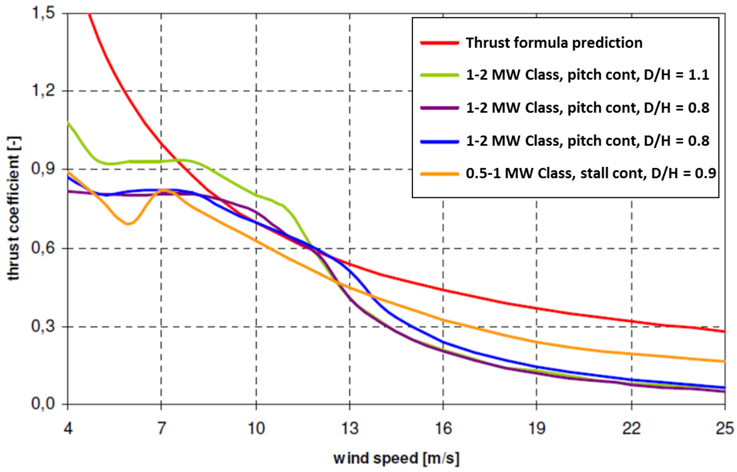

Figure 5.9: *Thrust coefficients for 4 turbines, using a turbine simulation model and the generic formula of equation 5.18 (red line). D/H is the ratio of rotor diameter over hub height (Frohboese and Schmuck (2010))*

detailed information about the blade characteristics and operating procedures of the wind turbine. Both are not available in this study, and it was therefore considered to be accurate enough to use the upper value of equation 5.18.

$$C_T = \frac{3.5(2\bar{U} - 3.5)}{\bar{U}^2} \tag{5.18}$$

In a similar manner for horizontal forces, a spectrum of bending moments at seabed level can be derived by multiplying the squared force amplitude by the squared distance to seabed level in equation 5.19.

$$S_{mm,wind}(f) = (\rho A C_T \bar{U} u)^2 (H_{hub} + d)^2 \frac{S_{uu}}{\sigma_u^2} = \rho^2 \frac{D^4 \pi^2}{16} C_T^2 \bar{U}^4 I^2 (H_{hub} + d)^2 \bar{S}_{uu}(f) \tag{5.19}$$

Where:

$S_{mm,wind}(f)$ = spectral density of bending moment at seabed due to wind loads $[(Nm)^2/Hz]$
H_{hub} = height of turbine hub above mean sea level [m]
d = water depth [m]

From both spectra (equation 5.17 and 5.19) it can be observed that it is dependent on the mean wind speed $\bar{U}$, since the turbulence intensity and therefore the fluctuating component of the wind speed varies with the mean wind speed. Furthermore, an Aerodynamic Admittance Factor (AAF) $\chi(f)$ can be added to the thrust force to model the admittance of fluctuating wind loads to the wind turbine blades in the frequency domain. The AAF factor is ≤ 1, and therefore without taking the AAF into account a conservative estimate is found for the dynamic thrust force and for the resulting spectra (Arany et al. (2014)).

5.2.3. Wave loads

Sea states can be be described in the frequency domain by wave spectra, for instance the well-known JONSWAP spectrum for young sea states or the Pierson-Moskowisch spectrum for fully developed sea states. Under idealised conditions in deep water the spectral parameters of significant wave height H_s and wave peak period T_p are dependent on the fetch, the duration of the wind blowing over the seas and the wind speed itself. Further away from the generation area of the wind waves, swell waves are developed due to frequency and direction dispersion. The swell waves can be described in the frequency domain too, and form a narrow peak located at lower frequencies than the JONSWAP spectrum.

During the development of wind waves in time the waves develop from high frequencies towards lower frequencies, but retaining the shape of the JONSWAP spectrum (Hasselmann et al. (1973)). If the spectrum is normalised, a general shape results which remains constant during the development of the sea state. Furthermore, due to the energy transfer between waves state the JONSWAP spectrum is a universal spectrum that can also be applied to the non-idealised conditions during storms, at least in the North sea environment for which is was derived. The JONSWAP spectrum can be expressed in equation 5.20 as proposed by DNV (DNV (2014)):

$$
\begin{aligned}
S_{ww}(f) &= \frac{\alpha g^2}{(2\pi)^4 f^5} \exp\left(-\frac{5}{4}(\frac{f}{f_p})^{-4}\right) * \gamma^r \\
\alpha &= 5\frac{H_s^2 f_p^4}{g^2}(1-0.287\ln(\gamma))\pi^4 \\
r &= \exp\left(\frac{-(f-f_p)^2}{2\sigma^2 f_p^2}\right) \\
\sigma &= \begin{cases} 0.07, & f < f_p \\ 0.09, & f > f_p \end{cases}
\end{aligned}
\tag{5.20}
$$

where:

S_{ww} = JONSWAP spectrum $[m^2/Hz]$
γ = peak enhancement factor, 3.3 [-]
α = generalised Phillips' constant [-]
f = frequency [Hz]
f_p = peak frequency [Hz]
H_s = significant wave height [m]
σ = spectral width parameter [-]

Wave theories
The next step to be taken is to transfer the JONSWAP spectrum to a wave load spectrum. To determine the wave load, first an appropriate wave theory should be taken into account. Depending on the local wave conditions and the water depth, the linear (Airy) wave theory is applicable or other appropriate theories should be used for velocities and accelerations. If waves get too steep, i.e. if the ratio of wave height over wave length gets too large, steepness-induced breaking may occur. Depth induced breaking may occur if the ratio of wave height (H) over water depth (d) gets too large. Both ratios also determine the appropriate wave theory, as was investigated by LéMéhauté in 1976 (Holthuijsen (2007)), expressed as relative wave height H/gT^2 and relative water depth d/gT^2, with H the wave height, d the water depth and T the wave period. In figure 5.10 the wave theories can be found as a function of both ratios.

At the reference location at Blyth (UK) the wave theories have been investigated for a range of realistic wave height and wave periods (table 5.1). A subdivision in wave theories has been used: Stokes higher order (denoted as stokes HO), breaking waves, either steepness induced (denoted as breaking steepness) or depth induced (denoted as breaking depth) and cnoidal waves (denoted cnoidal). Most of the combinations show that higher order stokes theories are applicable. For large wave heights breaking may occur. Linear wave theory is obviously not applicable for this range of wave periods and wave heights. Although this was noted it was not further taken into account, especially since other assumptions such as the application of the Morison equation might be even less accurate. Linear wave theory will be used subsequently.

Morison formula for wave loads
The force exerted on a slender structure can be determined using the semi-empirical Morison equation, as proposed by DNV (DNV (2014), equation 5.21). The equation is based on the assumption that the total force consists of a linear superposition of the drag and inertia forces, of which the drag force is in phase with the square of the instantaneous flow velocity and the inertia load in phase with the flow acceleration. For linear waves, the phase difference between velocity and acceleration is 90°, since the velocity is maximum when the acceleration is zero (only drag load) and acceleration is maximum when velocity is zero (only inertia load). The drag force has its maximum when the crest or trough passes the structure, while the inertia force has its maximum when a node passes (at the still water line). The horizontal force on an element with height dz at level z, can be determined by integrating equation 5.21 over z (Morison et al. (1950)).

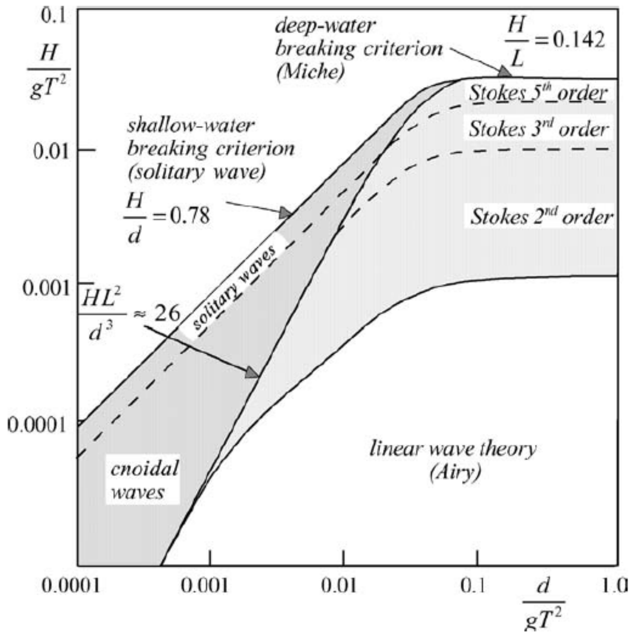

Figure 5.10: *Wave theories as function of relative wave steepness and relative water depth*

	T=5s		T=10s		T=15s		T=20s	
	d/gT^2	H/gT^2	d/gT^2	H/gT^2	d/gT^2	H/gT^2	d/gT^2	H/gT^2
H=5m.	0.1223	0.0204	0.0306	0.0051	0.0136	0.0023	0.0076	0.0013
	stokes HO		stokes HO		stokes HO		stokes HO	
H=10m.	0.1223	0.0204	0.0306	0.0051	0.0136	0.0023	0.0076	0.0013
	breaking (steepness)		stokes HO		stokes HO		stokes HO	
H=15m.	0.1223	0.0612	0.0306	0.0153	0.0136	0.0068	0.0076	0.0038
	breaking (steepness)		stokes HO		cnoidal		breaking (depth)	
H=20m.	0.1223	0.0815	0.0306	0.0204	0.0136	0.0091	0.0076	0.0051
	breaking (steepness)		stokes HO		breaking (depth)		breaking (depth)	

Table 5.1: *Applicable wave theories for wave height and wave period combinations*

$$dF_T = dF_{\text{drag}}(z,t) + dF_{\text{inertia}}(z,t) = \frac{1}{2}C_d\rho_w D_p|u(z,t)|u(z,t)dz + \frac{1}{4}C_m\pi\rho_w D_p^2\frac{\partial u}{\partial t}(z,t)dz \tag{5.21}$$

Where:

C_d = drag coefficient, suggested values between 0.7 and 1.2 [-]
C_m = inertia coefficient, suggested values between 1.5 and 2.0 [-]
ρ_w = water density $[kg/m^3]$
u = (undisturbed) particle velocity profile [m/s]
D_p = pile diameter [m]

It should be taken into account that the water level up to the maximum crest elevation is used when integrating over z, at least for the calculation of the drag load reaching its maximum when a crest passes the structure. The linear (Airy) wave theory does not take this into account, and for instance a Wheeler stretching method could be used which stretches the velocity profile to the instantaneous water level. This is however not further taken into account, and might therefore result in a under estimated wave load.

Depending on the wave load characteristics and geometrical characteristics, either the drag or inertia might be dominant. The drag force represents the force of flow on a structure and can in general be subdivided into forces due to pressure and forces due to friction. The pressure force is generated by the pressure difference at the front and rear-side of the structure due to difference in flow velocity. The friction force is generated

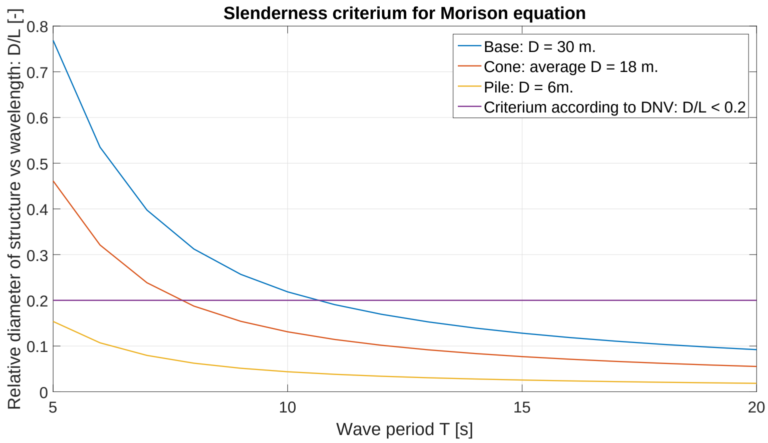

Figure 5.11: *The Morison criterion of D/L < 0.2 for structural elements of the GBF and for different wave periods*

by the wall roughness of the structure itself. The inertia force represents the force due to the movement of water, which consists partly of the displaced water mass of the structure itself, and partly of water around the structure which is also displaced.

The Morison equation was experimentally derived for slender piles, and therefore the equation is only valid for slender structures. It is however engineering practice to use the Morison equation, even up to or above the slenderness criterion, at least in the preliminary design. If the slenderness criterion is violated, one could use numerical models to calculate wave loads on non-slender structures. Structures are defined to be slender when no refraction or diffraction processes are induced by the structure. According to DNV (2014) this is the case if the characteristic diameter of the structure is smaller than 20% of the wavelength, $D < 0.2\lambda$, with λ the wave length. This comes down to $kD < 1.3$, with k the wave number.

If the diameters of the three main parts (base, cone and pile) of the GBF versus a range of wave periods are considered, the boundaries of the validity of the Morison equation can be made clear (figure 5.11). The linear dispersion relation was used to calculate the wave length from the wave period (equation 5.22). For a range of wave periods between 5 and 20 seconds, the slenderness criterion is exceeded for the large base of the GBF at wave periods below 10-11 seconds. Also for the still relatively large cone, for which an average diameter of 18 meter was used, the slenderness criterion is violated at wave periods below 7-8 seconds. For storm waves therefore, the Morison equation may still be valid.

$$\omega^2 = g k \tanh kd \tag{5.22}$$

where:

$k = 2\pi/\lambda$, wave number [1/m]
$\omega = 2\pi/\mathrm{T}$, radial frequency [rad/s]
d = water depth [m]

In general it is expected that the Morison equation overestimates the inertia load on the big base and cone of the GBF. This is due to:

- The inertia force is proportional to the cross sectional area of the structural element in the horizontal plane. The Morison equation assumes that the structural element does not influence the profile of velocities and accelerations in depth and time, but for the large gravity base with a large cross sectional area this does not hold anymore. Therefore the inertia force is expected to be overestimated.
- Furthermore, a phase difference may occur between the maximum wave load on the base and on the cone and pile, due to the large differences in diameter. The total load during a wave passing may therefore be lower than the sum of the loads on individual elements. Looking at the stability of the structure, not the total load on a single structural element is relevant but the maximum occurring total wave load on the structure.

- The large gravity base disturbs the flow around the structure and will therefore also influence the wave load on the cone and pile. The Morison formula implicitly assumes that in vertical direction the flow is undisturbed too, i.e. in vertical direction the structure should also be slender. This is however not the case, and might also lead to a larger force on the cone and pile than the Morison formula predicts.
- However, no wheeler stretching is applied to take the loading by the wave crest into account, and also the wave run-up on the gravity base and breaking wave loads are not taken into account. This might result in an under prediction of the wave load on the (slender) pile. Whether the overall result is therefore an overestimation or underestimation is unclear.

In fact the Morison equation is also valid for breaking waves as long as the structure is fully submerged and the full integration along the vertical coordinate z is executed. However, the equation is based on linear wave theory, which may not be applicable anymore in breaking wave conditions.

Morison coefficients
The coefficients in the Morison equation are determined on the basis of a drag coefficient for steady state flow (C_{ds}) according to DNV (DNV (2014)). This coefficient is a function of the relative roughness of the structure, the Keulegan-Carpenter number and the Reynolds number. The Reynolds number represents the inertia forces versus the viscous forces, while the Keulegan-Carpenter number represents the drag forces versus inertia forces. If K_c is smaller than 5 inertia is dominant, while if K_c is larger than 15 drag is dominant.

$$Re = \frac{u_{max} D_p}{\nu} \tag{5.23}$$

$$K_c = \frac{u_{max} T}{D_p} \tag{5.24}$$

Where:

Re = Reynolds number [-]
K_c = Keulegan-Carpenter number [-]
u_{max} = maximum horizontal particle velocity [m/s]
D_p = diameter of structure
ν = kinematic viscosity of water [m^2/s]
T = wave period [s]

The horizontal particle velocities $u(z,t)$ and horizontal accelerations $\frac{\partial u}{\partial t}(z,t)$ as functions of depth and time can be found by linear (Airy) wave theory. It can be seen that the velocities and accelerations occur out of phase. Under a wave crest and wave trough the particle velocities reach their maximum but in opposite direction, while the acceleration is maximum under the wave trough, and also changes sign during each cycle (figure 5.14).

$$u(z,t) = \frac{\pi H_s \cosh(k(d+z))}{T \sinh(kd)} \cos(2\pi t/T) \tag{5.25}$$

$$\frac{\partial u}{\partial t}(z,t) = \frac{2\pi^2 H_s^2 \cosh(k(d+z))}{T^2 \sinh(kd)} \sin(2\pi t/T) \tag{5.26}$$

Where:

u = particle velocity [m/s]
k = $2\pi/\lambda$, the wave number [1/m]
λ = wave length [m]
z = vertical coordinate, positive upwards from MSL [m]
H_s = significant wave height [m]
T = wave period [s]
d = water depth [m]

Both Re and K_c, and therefore the drag and inertia coefficients, are frequency dependent. This is however not further taken into account, i.e. they are determined for an extreme wave load but subsequently applied to other wave frequencies as well. What is taken into account however, is the reduction of the wave load due to the overestimated inertial load. This is done by applying adapted Morison coefficients, the coefficients used are tuned to the maximum wave load found by numerical modelling in Finlab (Smaling (2014)). Based on the wave load on the structure as predicted by the numerical model an prediction of the Morison coefficients was made to reduce the overestimation of the inertial load. The coefficients are shown in table 5.2.

	pile	cone	base
C_d [-]	0.95	0.95	0.95
C_m [-]	2	1.6	1.6

Table 5.2: *Morison coefficients, prediction using numerical wave modelling*

The Morison equation is integrated over the height of the reference geometry. For a wave height of 4 meter, a wave period of 7 seconds and a water depth of 30 meter, the horizontal wave loads were investigated in their magnitude (drag versus inertia), for each of the three components of the reference geometry (base, cone and pile). As can be seen in figure 5.12, the drag and inertia load occur out of phase and the inertia force is dominant, for all parts of the GBF (base, cone and pile), however the real phase difference between the base, cone and pile are not taken into account. The figure shows that the inertia load on the base, cone and pile contribute significantly to the total wave load, while the drag load contributes far less.

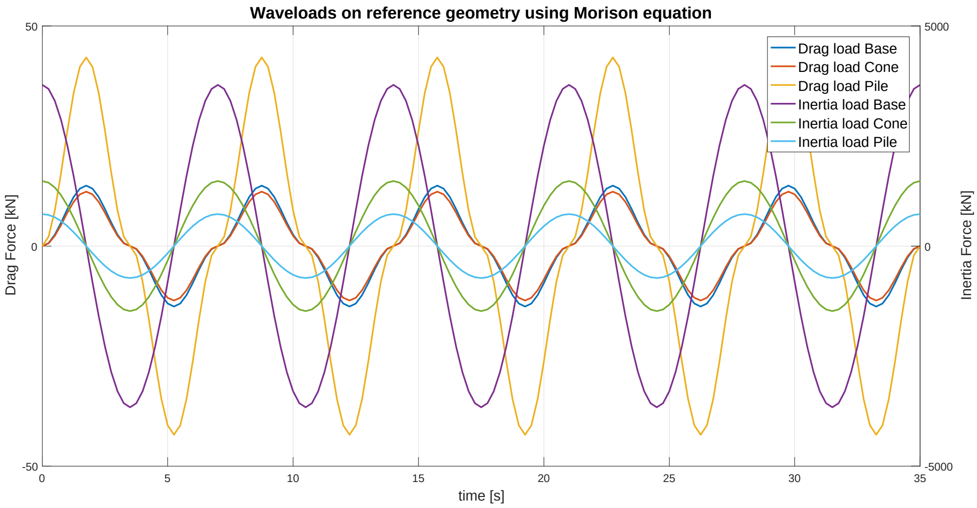

Figure 5.12: *Drag and inertia loads on the GBF, for a regular wave with height 4 meter and period 7 seconds. Please note the different vertical axis for drag and inertia load.*

Spectral description

To obtain a spectral density of the wave loads, the maximum wave load on the structure is determined for each single significant wave height with corresponding peak period. The wave loads are both expressed in a horizontal force at seabed level and a bending moment at seabed level, comparable to the wind loads. Both loads are squared and multiplied with the JONSWAP spectrum divided by H_s^2, representing the normalised JONSWAP spectrum. This finally results in a spectral density of horizontal force $[N^2/Hz]$ and bending moment $[(Nm)^2/Hz]$ (equations 5.27 and 5.28). As can be seen, the drag and inertia loads on the individual elements are summed up and the maximum value is selected. In fact this maximum is based on the inertia loads, since these appear to make up the larger part of the forces as can be seen in figure 5.12, but for the sake of completeness both parts are denoted. The general procedure for the multiplication with the TRF was already presented in equation 5.6.

$$S_{ff,wave}(f) = \left(\sum_{i=1}^{n} F_{drag}(i,t) + F_{inertia}(i,t) \right)_{max}^{2} \bar{S}_{ww}(f) \tag{5.27}$$

$$S_{mm,wave}(f) = \left(\sum_{i=1}^{n} F_{drag}(i,t)z(i) + F_{inertia}(i,t)z(i)\right)^2_{max} \bar{S}_{ww}(f) \tag{5.28}$$

With:

$$\bar{S}_{ww}(f) = \frac{S_{ww}}{H_s^2} \tag{5.29}$$

Where:

$S_{ff,wave}(f)$ = spectral density of horizontal force at seabed due to wave loads [N^2/Hz]
$F_{drag}(i,t)$ = drag load on element i, integrated over height of the structure [N]
$F_{inertia}(i,t)$ = inertia load on element i, integrated over height of the structure [N]
$\bar{S}_{ww}(f)$ = normalised JONSWAP spectrum [1/Hz]
$S_{mm,wave}(f)$ = spectral density of bending moment at seabed due to wave loads [$(Nm)^2/Hz$]
$z(i)$ = distance from centreline of element i to seabed level [m]

5.2.4. Turbine loads

Due to the rotation of the blades of the turbine, turbine loads are transferred to the support structure and soil as well. The loads can be subdivided into the 1P loading and the 3P loading.

1P frequency load
The 1P loading develops due to the rotor mass imbalance and the aerodynamic mass imbalance. The rotor mass imbalance can be visualised as an added lumped mass rotating at a distance R from the centre of the hub. The aerodynamic mass imbalance develops due to differences in pitch angle of the individual blades. In order to analyse the latter effect a detailed blade model should be used, which will not be further taken into account in this study. The rotor imbalance however will be taken into account in a simplified manner.

The centrifugal force F_{cf} from a rotating mass at distance R from the centre can be written in terms of the centrifugal acceleration. For the wind turbine, the centrifugal acceleration can be related to the frequency of rotation Ω by $a = R\Omega^2$ (Arany et al. (2014)). The centrifugal force can now be expressed in equation 5.30.

$$F_{cf} = ma = mR\Omega^2 = I_m\Omega^2 = 4\pi^2 I_m f^2 \tag{5.30}$$

Where:

I_m = m R = mass imbalance [kg m]
f = $\Omega/(2\pi)$, frequency of rotation of the turbine [Hz]

The centrifugal force does not induce a shear force at seabed level. A cyclically varying bending moment however is present at seabed level due to the centrifugal force, in two directions: in the fore-aft direction (M_y generated by F_z) and in the side-to-side direction (M_x generated by F_y and F_z, figure 5.13). The bending moment in the side-to-side direction is larger than the fore-aft direction, since the arm is equal to the hub height (above MSL) plus water depth, while the arm for the bending moment in the fore-aft direction is only the rotor overhang b. Even torsion in the turbine tower is produced by the centrifugal force, which is however neglected. Also the effect of gravity on the rotating mass is neglected, since the centrifugal effect is far larger.

The maximum bending moment in fore-aft direction can now be expressed (5.31), with b the rotor overhang (m). In the frequency domain this is represented by the amplitude squared at a single rotor frequency (1P). This results in a Dirac-delta function, with an infinite value at the 1P frequency and zero at all other frequencies. The integral under the Dirac-delta function is one, and therefore the spectral density is simply the amplitude squared. For turbines with a variable rotational frequency, the centrifugal force and bending moment are still a function of the 1P frequency, which is also the case for the Vestas 8MW turbine. The 1P frequency is related to the mean wind speed at hub height, and a higher wind speeds results in a higher 1P

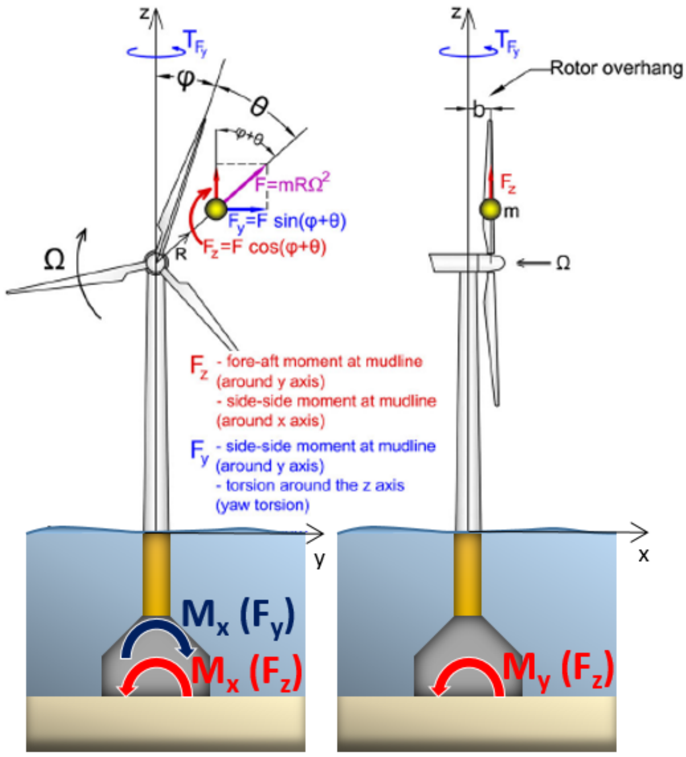

Figure 5.13: *Bending moments at seabed level due to the rotor mass imbalance, based on Arany et al. (2014)*

frequency. This eventually produces a larger centrifugal force (equation 5.30) and therefore a larger bending moment at seabed level (equation 5.31).

$$M_{1p} = 4\pi^2 I_m f^2 b \tag{5.31}$$

$$S_{mm,1p}(f) = M_{1p}^2(f)\delta(f - f_{1p}) \tag{5.32}$$

Where:

M_{1p} = bending moment amplitude at seabed level [Nm]
$S_{mm,1p}$ = spectral density of bending moment at seabed with frequency 1P [Nm^2]

3P frequency load

Every time one of the blades passes the turbine tower, the drag load on the tower is reduced. The frequency of the load is equal to three times the 1P frequency for a three bladed turbine. The amplitude of the load can be estimated by a simple approximation of the surface area of the blade. If the blade is in a downward position, it covers the tower over the full blade length L. The horizontal force and bending moment resulting from the load loss can be found by integrating along the tower height H_{tower} where the blade passes. The spectral densities for horizontal forces and bending moments at seabed level can subsequently be derived (equation 5.35).

$$F_{3p} = R_a \int_{H_{tower}-L}^{H_{tower}} \frac{1}{2}\rho_{air} C_d D_t(z) U^2(z) dz \tag{5.33}$$

$$M_{3p} = R_a \int_{H_{tower}-L}^{H_{tower}} \frac{1}{2}\rho_{air} C_d D_t(z) U^2(z)(z+d) dz \tag{5.34}$$

$$
\begin{aligned}
S_{ff,3p}(f) &= F_{3p}^2(f)\delta(f - f_{1p}) \\
S_{mm,3p}(f) &= M_{3p}^2(f)\delta(f - f_{1p})
\end{aligned}
\tag{5.35}
$$

where:

F_{3p} = amplitude of the horizontal force with frequency 3P [N]
M_{3p} = amplitude of the bending moment at seabed level with frequency 3P [Nm]
R_a = ratio of blade area versus the frontal tower area [-]
H_{tower} = tower height above MSL [m]
L = blade length [m]
C_d = drag coefficient [-]
D_t = tower diameter [m]
U = wind speed, as function of height: $U(z) = \bar{U}(z/H)^{0.143}$ [m/s]
$S_{ff,3p}$ = spectral density of horizontal force with frequency 3P [N^2]
$S_{mm,3p}$ = spectral density of bending moment at seabed level with frequency 3P [$(Nm)^2$]

The factor R_a depends on the blade design and tower design. Since no detailed information is available about blade dimensions and tower dimensions, it is assumed that both the blade area and tower area are proportional the turbine size, resulting in a constant factor R_a. For a Siemens 3MW turbine, the factor is 130 $m^2/188.2\ m^2$, resulting in $R_a = 0.69$ (Arany et al. (2014)). This factor will also be used for the reference turbine of 8MW in this study.

5.2.5. Current loads

Before continuing to the dynamic amplification of the above mentioned most important loads, the last loads on the structure will shortly be described. According to DNV (DNV (2014)) also the current loads should be included in the three basic load cases. The current load can be calculated with the Morison's equation too, using only the drag related part. The inertia related part will be zero, since no instantaneous accelerations are present.

The current load can be calculated with equation 5.36. For combined wave and current the velocity u should be the summation of the particle induced velocity and the current velocity. Various current profiles over depth exist, for instance a linear profile or a power law profile. The velocity profile will determine the bending moment at seabed level.

$$
dF_c = \frac{1}{2}\rho_w D C_d u^2 dz \tag{5.36}
$$

5.2.6. Dynamic amplification

When frequencies of loads are getting closer to the natural frequency of the offshore wind turbine, the amplitudes of the loads increase, eventually leading to resonance of the system. The final amplitude when dynamic amplification is taken into account largely depends on the damping present in the system. DNV (DNV (2014)) proposes formula 5.37 for the dynamic amplification factor (DAF) for fatigue loads when no detailed model of the structure is available. In this study the focus is not on fatigue loads, however the amplification of loads in the frequency domain can also be used for other purposes than fatigue loads. Therefore equation 5.37 will be used to determine the amplification in the frequency domain. The above mentioned spectra for wind, wave and turbine loads have to be multiplied by the square of the dynamic amplification factor (DAF), as was pointed out in equations 5.6 and 5.7.

$$DAF = \frac{1}{\sqrt{(1-\beta^2)^2 + (2\zeta\beta)^2}}$$
$$\beta = \frac{f}{f_0} \qquad (5.37)$$
$$\zeta = \frac{c_{damping}}{c_{critical}}$$

where:

DAF	= dynamic amplification factor [-]
β	= ratio of actual frequency versus natural frequency [-]
f	= excitation frequency [Hz]
f_0	= natural frequency [Hz]
$c_{damping}$	= actual damping coefficient [Ns/m]
$c_{critical}$	= critical damping coefficient [Ns/m]

According to DNV (DNV (2014)), formula 5.37 is only applicable to wave loads and only if the natural frequency of the system is larger than 0.4 Hz. The natural frequency should be derived using a single degree of freedom system. If the natural frequency is larger than 0.4 Hz a time domain analysis should be carried out. In the current study the natural frequency will be determined using two different schematisations, but it will be applied to all loads (i.e. wave, wind and 1P and 3P loads) taking the limited time for this study into account.

Multiple schematisations can be thought of, the first difference is whether masses, springs and dashpots are lumped or distributed. Since the purpose of this study is to quickly estimate the natural frequency of the system to use for dynamic amplification, lumped masses, springs and dashpots are used. Furthermore, a 1-mass-spring-dashpot (MSD) with only the mass in the top of the tower, or a two-mass-spring-dashpot with also a schematised mass of the GBF can be made. Both will be worked out to assess the differences and are visualised in figure 5.14.

From the turbine characteristics it can beforehand already be concluded that the natural frequency of the system should fall between the 1P and 3P ranges. A soft-soft structure (below 1P) and a stiff-stiff structure (above 3P) can hardly be obtained, at least not with the current wind turbines installed and with the current support structure concepts (Arany et al. (2014)). For the reference case of the 8MW turbine with rotational speeds between 4.8 rpm and 12.1 rpm, the frequency range for the 1P ranges between 0.0800-0.2017 Hz and a 3P ranges between 0.2400 - 0.6050 Hz. Therefore the hypothesis is that the natural frequency should lie between 0.2017 and 0.2400 Hz.

1-mass-spring-dashpot system
The 1-mass-spring-dashpot models the turbine tower clamped at seabed level and having a single mass in the top of the turbine. The upper lumped mass is schematising the nacelle, hub and rotor mass in the top of the turbine tower. For a monopile the clamped level can be at an estimated depth below seabed, which depends on the soil conditions and the pile diameter (for instance 3.5 times the pile diameter below seabed for sands with relative density of 50%, Van der Tempel (2006)). For the GBF a first estimate can be made by assuming the tower clamped at the seabed level, where the steel shaft is founded at the bottom of caisson. According to Van der Tempel (2006), the tower mass itself should be partly (23%) taken into account in the top mass m_2, together with the top mass of the rotor, hub and nacelle (equation 5.38).

$$m_2 = 0.227 m_{tower} + m_{top} = 0.227 * 700 + 425 = 584\text{ton} \qquad (5.38)$$

Using a simple structural formula for the deformation of a one-sided fixed beam with stiffness E and moment of inertia I, the stiffness k can be derived (equation 5.39). With the turbine characteristics listed in table 5.3, a wall thickness of 85 mm. (Jonkman et al. (2009)), stiffness modulus for steel of $2.1 * 10^8$ kN/m, this results in a stiffness k and mass m_2 as indicated in table 5.3. For a single degree of freedom system the natural frequency can now be determined by $\omega^2 = k/m_2$ with m_2 the lumped mass. The damping is neglected since it is assumed to have a minor influence on the natural frequency.

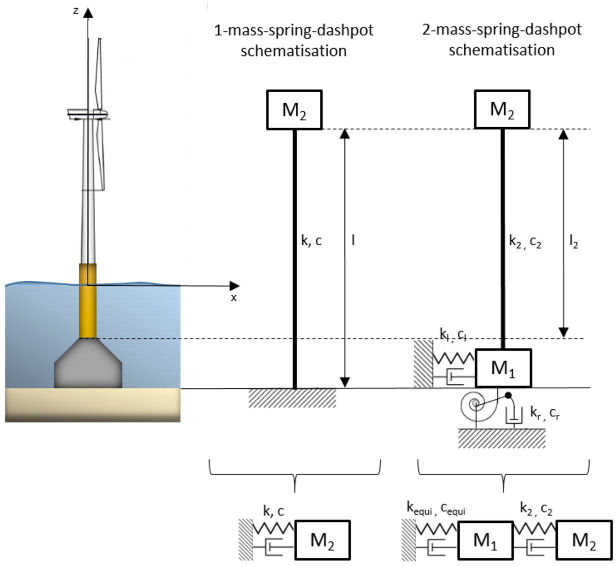

Figure 5.14: *Two dynamic schematisations of the system*

$$
\begin{aligned}
I &= \frac{1}{8}\pi D^3_{tower} t_{wall} \\
k &= \frac{3EI}{l^3}
\end{aligned}
\tag{5.39}
$$

Moment of inertia I	$[m^4]$	5.5535
Length l	[m]	165
Tower stiffness k	[kN/m]	$7.7885 * 10^2$
Mass m_2	[ton]	584

Table 5.3: *Parameters for the 1-mass-spring-dashpot system*

2-mass-spring-dashpot system
However to make a better model the soil stiffness should be taken into account and also the large mass of the gravity base filled with ballast. Therefore a 2-mass-spring-dashpot system would be a better representation. The stiffness of the soil acts both laterally (in horizontal direction) and rotationally, with damping in corresponding directions as well, and an equivalent stiffness can be used according to (Vugts and Harland (1996)). The equivalent stiffness was derived for a stepped tower with both a lateral and rotational spring at one end, which can now be replaced by a single lateral spring with an equivalent stiffness (Figure 5.14). The corresponding stiffness, damping and the mass m_1 can be found according to Zaaijer (2005) taking into account the soil properties (equation 5.40).

$$
\begin{aligned}
k_r &= \frac{GD^3}{3(1-\nu)} \\
c_r &= \frac{0.65D^4\sqrt{\rho G}}{32(1-\nu)} \\
k_l &= \frac{6GD(1-\nu)}{7-8\nu} \\
c_l &= \frac{4.6D^2\sqrt{\rho G}}{4(2-\nu)} \\
k_{eq} &= \frac{k_{rot}k_{lat}L^2}{k_{rot}+k_{lat}L^2} \\
m_{soil} &= \frac{0.76\rho D^3}{8(2-\nu)}
\end{aligned}
\tag{5.40}
$$

Where:

G	= shear modulus of the soil $[N/m^2]$
D	= diameter of circular gravity base [m]
ν	= Poisson ratio of the soil [-]
ρ	= volumetric weight of the soil $[N/m^3]$
L	= tower length [m]
k_r	= rotational spring stiffness [Nm/rad]
k_l	= lateral spring stiffness [N/m]
c_r	= rotational damping [Ns]
c_l	= lateral damping [Ns/m]
k_{eq}	= equivalent lateral spring stiffness [N/m]
m_{soil}	= soil mass [kg]

The 2-mass-spring-dashpot system with 2 degrees of freedom can be solved analytically by drawing the displacements and forces of the 2 degrees of freedom independent, and subsequently add both. This results in a coupled system of equations, with a symmetrical stiffness matrix (equation 5.41). The displacement will be of a harmonic type with amplitude $\bar{u}$, radial velocity ω and phase θ. Replacing $u = \bar{u}\cos(\omega t + \theta)$ in equation 5.41, rewriting the matrix and setting the determinant to zero to find the homogeneous solution, the characteristic equation is found from which the natural frequency can be determined (equation 5.42). The damping is neglected in the latter equation since it is assumed to have a minor influence on the natural frequency.

$$\begin{bmatrix} m_1 & 0 \\ 0 & m_2 \end{bmatrix} \begin{bmatrix} \ddot{u}_1 \\ \ddot{u}_2 \end{bmatrix} + \begin{bmatrix} c_{eq}+c_2 & -c_2 \\ -c_2 & c_2 \end{bmatrix} \begin{bmatrix} \dot{u}1 \\ \dot{u}_2 \end{bmatrix} + \begin{bmatrix} k_{eq}+k_2 & -k_2 \\ -k_2 & k_2 \end{bmatrix} \begin{bmatrix} u_1 \\ u_2 \end{bmatrix} = \begin{bmatrix} 0 \\ 0 \end{bmatrix} \tag{5.41}$$

$$m_1 m_2 \omega^4 - \omega^2 (m_1 k_2 + m_2(k_{eq} + k_2)) + k_{eq} k_2 \tag{5.42}$$

The top mass m_2 is the same as for the 1-mass-spring-dashpot system. The spring stiffness k_2 is now based on a different tower length l_2 since the caisson mass is now taken into account as well. It is assumed that the tower length ranges up to the top of the roof of the caisson, which is 148 meter in total. However, the other part of the tower mass which was not taken into account in the total mass m_2 is now taken into account in the mass at seabed level (m_1) (which is 77% of the tower mass, equation 5.38). Therefore the total mass m_1 results from 77% of the tower mass, the mass of the caisson and the mass of the soil m_{soil}. The total mass is calculated based on the reference characteristics of the turbine, the mass of soil according to equation 5.40 and the weight of the caisson and steel shaft of 13000 tons. The latter makes up the largest part of the total seabed mass m_2 of 16559 tons (table 5.4). It should be noted that no additional water mass moving along with the schematic mass has been taken into account.

77% tower mass	[ton]	541
Caisson mass	[ton]	13000
Soil mass	[ton]	3018
Total mass m_1	[ton]	16559

Table 5.4: *Masses forming the total seabed mass* m_1

Tower length l_2	[m]	148
Tower stiffness k_2	[kNm]	$1.0793 * 10^3$
Mass m_2	[ton]	584
Shear modulus of the soil G	[MPa]	30
Poisson ratio of the soil ν	[-]	0.3
Volumetric weight of the soil	$[kN/m^3]$	20
Rotational spring stiffness k_r	[kNm/rad]	$3.8571 * 10^8$
Lateral spring stiffness k_l	[kN/m]	$2.1913 * 10^6$
Equivalent lateral spring stiffness k_{eq}	[kN/m]	$3.8264 * 10^8$
Mass at seabed m_1	[ton]	$1.6559 * 10^4$

Table 5.5: *Parameters for the 2-mass-spring-dashpot system*

Natural Frequencies
Using the 2 models the first natural frequencies can be obtained:

- 1-mass-spring-dashpot system: f_0 = 0.1850 Hz
- 2-mass-spring-dashpot system: f_0 = 0.2164 Hz

The first natural frequency of the 2-MSD system falls between the 1P and 3P range, while the 1-MSD system shows a value inside the 1P range. The 2-MSD system in fact indicates a stiffer structure. Although the frequencies differ by 17%, this is mainly due to the difference in tower length taken into account in both approximations and not due to the difference of using a single mass or multiple masses. If the tower length of the 1-MSD system is taken equal to the length of the 2-MSD system, i.e. if the clamped connection is thought to be at the roof of the caisson, the natural frequencies obtained are 0.2178 and 0.2164 respectively for the 1-MSD and 2-MSD system (0.6% difference).

Therefore it is not necessary to take the masses and stiffness at seabed level into account due to their relatively large size compared to the mass and stiffness of the tower. A clamped connection such as the 1-MSD might not seem to model the soil reactions in the system, but due to the soils' large stiffness compared to the tower it may be neglected and schematised as a clamped connection. However, the tower length and therefore the level of the clamped connection is an important parameter, and from both schematisations it can be concluded that a clamped connection at seabed level produces a too soft structure with a too low natural frequency. In this case the level of the clamped connection could better be located at the "roof" of the concrete caisson, since this is where the steel support shaft can be considered to be fixed without any rotational freedom. This results in a frequency between the 1P and 3P range. A natural frequency of 0.216 Hz will be used.

Furthermore, from the simplified analysis it was observed that the first natural frequency is largely determined by the wind turbine characteristics (mass and stiffness). Using a larger mass at the top (larger turbine) a lower natural frequency will be found, while a large turbine also implies a larger hub height and therefore longer tower, reducing the stiffness and natural frequency further. The support structure of the GBF itself is not influencing this frequency with relative large mass and stiffness.

Damping
The damping ratio (relative to critical damping) itself is another important parameter in equation 5.37, which should include structural damping, soil damping, hydrodynamic and aerodynamic damping (Arany et al. (2014)). From literature different values were found by Arany et al. (2014), listed in table 5.6. In general it is hard to estimate the total amount of damping, as can be seen from the large ranges found in literature. The damping ratios depend on detailed design of the structure, and will also vary with the direction of loading. Taking into account that the influence of damping on the spectral amplitudes is rather large, a conservative total damping value (a relatively low value) was taken and based on the proposed value by Arany et al. (2014), which is 5%.

Structural damping	0.3 - 2 %
Soil damping	0.4 - 1.5 %
Hydrodynamic damping	4 - 7 %

Table 5.6: *Damping ratios relative to critical damping from literature*

For various damping ratios the DAF is plotted in figure 5.15 for a natural frequency of 0.35 Hz. A higher damping ratio clearly indicates less amplification. For the current study a damping ratio of 0.05 is assumed, which indicates that up to 10^2 times amplification occurs at the natural frequency. This should clearly be prevented.

5.3. Final spectra

Final spectra can be obtained by summing up the spectrum of wind and wave load, taking into account the dynamic amplification. The 1P and 3P frequencies can be added to the spectrum with the corresponding amplitudes (equation 5.32 and 5.35). In this paragraph some examples of generated spectra will be shown and will be discussed. The input parameters that will be used for the load derivations have been derived in

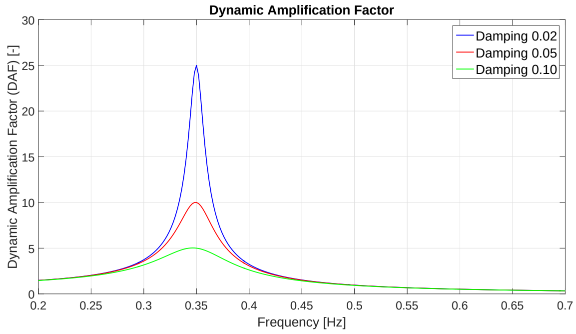

Figure 5.15: *Dynamic amplification factor (DAF) for various damping ratios*

the current chapter, and are a natural frequency of 0.22 Hz, a damping ratio of 5%, and a number of time steps per time duration of one hour of N = 4096 (section 5.2.1).

In extreme conditions, above the cut-out wind speed, the turbine will be parked. In that case the turbine loads (1P and 3P frequency) are not taken into account. Instead a fluctuating drag load on the tower is taken into account, in the same manner as done for the case the turbine is operating. For two conditions the resulting spectra are presented in figures 5.16 and 5.17:

- Operating wind turbine at rated speed (14 m/s) and wave conditions H_s = 4m. and T_p = 8s. (figure 5.16 and 5.18).
- Parked wind turbine at ultimate wind speed (50 m/s) and wave conditions H_s = 10m. and T_p = 12s. (figure 5.17 and 5.19).

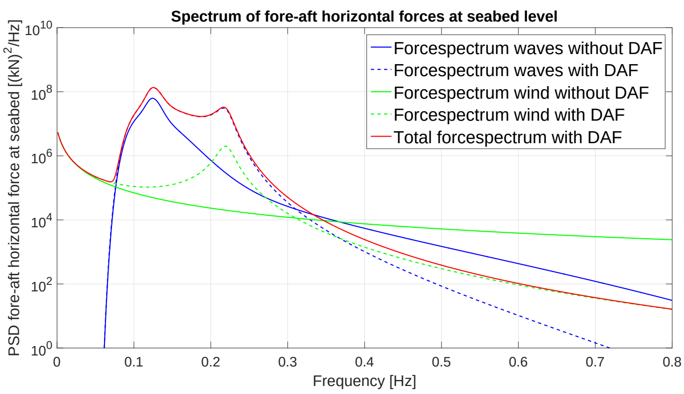

Figure 5.16: *Generated spectra of horizontal shear force at seabed for rated wind speed (14 m/s) and wave conditions with H_s = 4m. and T_p = 8s.*

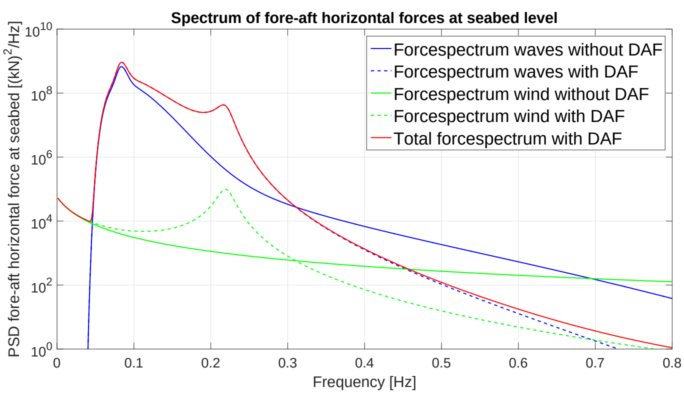

Figure 5.17: *Generated spectra of horizontal shear force at seabed for parked wind turbine at 50yr wind speed (43 m/s) and wave conditions with H_s = 10m. and T_p = 12s.*

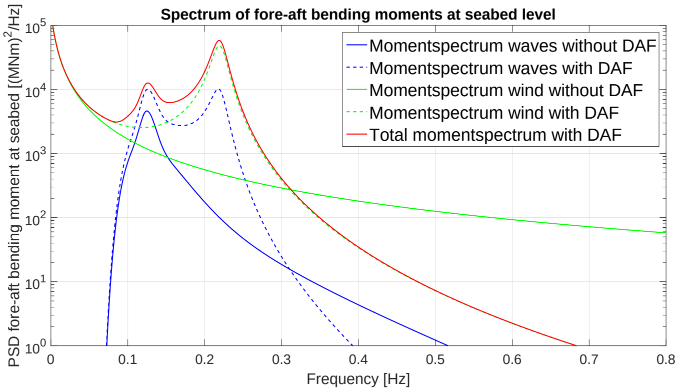

Figure 5.18: *Generated spectra of bending moment at seabed for rated wind speed (14 m/s) and wave conditions with H_s = 4m. and T_p = 8s.*

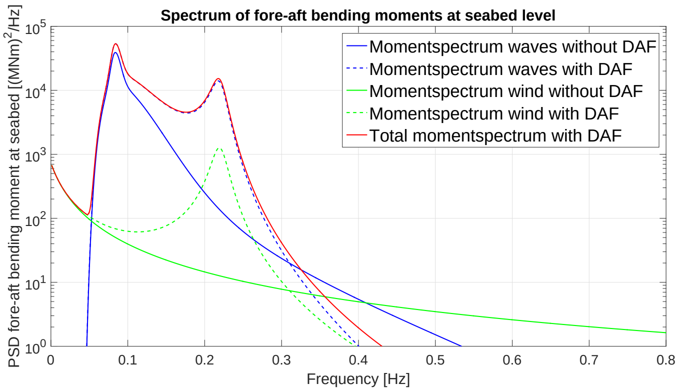

Figure 5.19: *Generated spectra of bending moment at seabed for parked wind turbine at 50yr wind speed (43 m/s) and wave conditions with H_s = 10m. and T_p = 12s.*

Some general observations from the spectra give more insight in the loads at seabed level during different conditions of wind speed and wave height. First of all, in the spectra the amplification at both the frequencies of the peak wave period and the natural frequency of the structure can be found. Furthermore:

- The amplitude corresponding to the loads at the natural frequency of the system of foundation and tower depend on the load conditions (wave height and wind speed) and whether the turbine is operating. The latter fact determined the area at which the loads act, reducing from the swept area to only the frontal area of the blades and tower.
- In general, the wave loads make up the largest part of the spectral density, only for frequencies below the peak wave frequency this is determined by the wind loads. Above which frequency the wind loads start dominating again is mainly determined by the wave height: for the 4 meter wave height, this is already above 0.15Hz while for the 10 meter wave the wind loads don't dominate above a certain frequency. This holds for both horizontal forces and bending moments.
- For the extreme wind speed of 50 m/s it can be observed that the loads are still lower than at the wind speed of 14 m/s when the turbine is operating, both for bending moments and horizontal forces.
- For the loads at frequencies close to the wave period, the loads are mainly determined by the wave height. For larger waves the horizontal forces and bending moments at seabed level increase, while the dynamic amplification at the natural frequency of the system also increases the loads from waves around this frequency. Depending on the conditions of wave height and wind speed, either the peak at the wave frequency or the peak at the natural frequency of the system shows the highest spectral density.

- Comparing bending moments and horizontal forces at seabed level when the turbine is operating (for the rated wind speed of 14 m/s), the peak in spectral density in the bending moment is found at the natural frequency of the system, indicating that the dynamic behaviour of the structure largely determines at which frequencies the loads are transferred to the subsoil. For the horizontal shear force, the peak around the natural frequency of the system is lower than the peak around the wave frequency. This indicates that the wave loads largely determine the horizontal force at seabed level, and that the dynamic behaviour of the system is most relevant to bending moments. Whether the largest bending moment density is found at the wave frequency or at the natural frequency depends on whether the turbine is operating or parked.

5.4. Verification

A time series of 600 seconds was generated based on the above described approach (Figure 5.20 and 5.21). The wind, wave and turbine loads are taken into account. For a wind speed of 14 m/s at hub height and a significant wave height of 4 meter and peak period of 8 seconds the results are shown in figure 5.20 and 5.21.

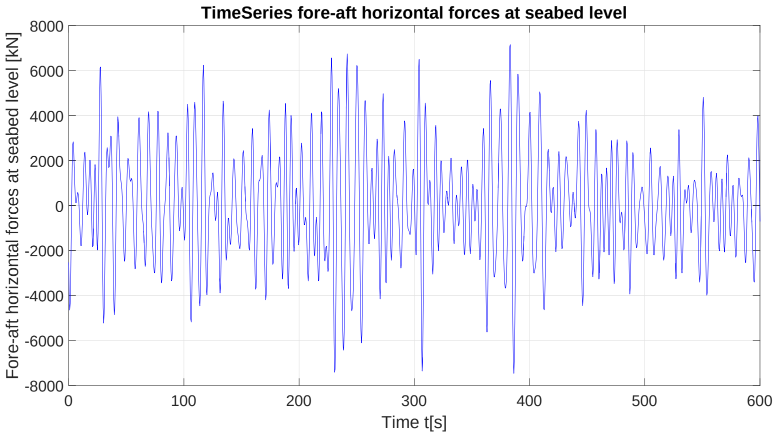

Figure 5.20: *Generated time series of horizontal shear force at seabed level*

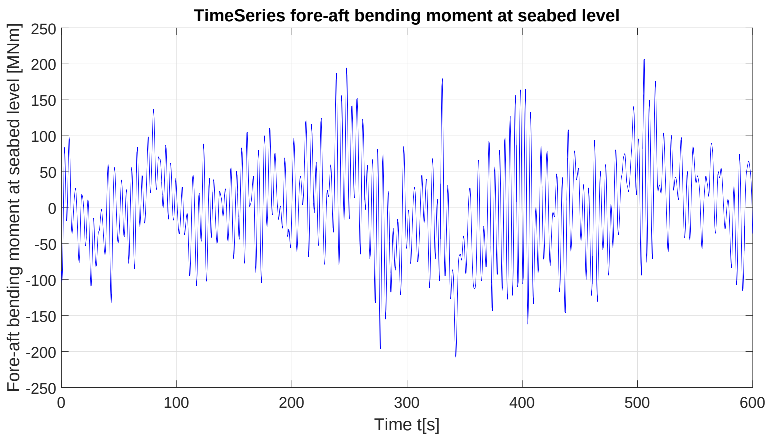

Figure 5.21: *Generated time series of bending moment at seabed level*

With a Fourier transformation on the generated time series a spectrum can be made, which is expected to match well with the spectrum from which the time series were derived. This is indeed the case as can be observed in figure 5.22 and 5.23. The time series have been made using a number of points in a one hour duration of 4096. If the number of points in the time series is increased the match gets better. No significant difference between horizontal force and bending moments at seabed can be found. It should be noted that the number N (number of samples in the time series) should always be a multiple of 2 in the fast Fourier transform in Matlab. A number of 4096 will be used in the subsequent calculations.

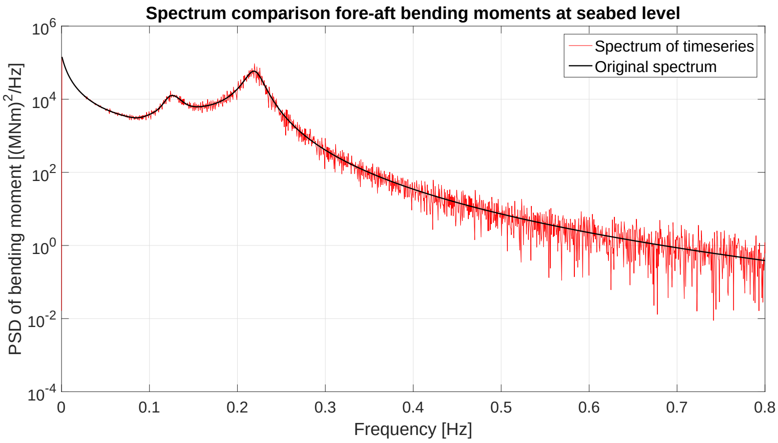

Figure 5.22: *Spectrum comparison between original spectrum and spectrum from the generated time series for bending moment at seabed level. N = 4096*

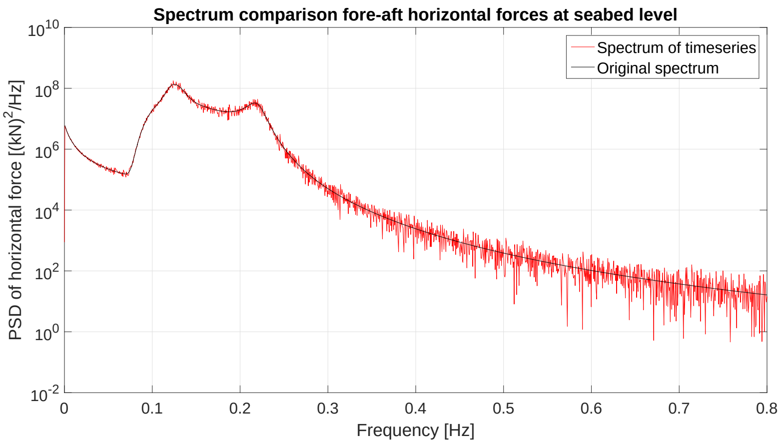

Figure 5.23: *Spectrum comparison between original spectrum and spectrum from the generated time series for horizontal shear load at seabed level. N = 4096*

5.5. Reference case

In order to estimate the contributions of each load, for some wind speeds and wave heights the loads have been calculated. The loads are calculated in terms of horizontal force in fore-aft direction and bending moment in fore-aft direction, both at seabed level. The loads have been calculated for the load cases according to DNV, with return periods of 5 yr. and 50 yr. for both wind and wave loads. The corresponding wind speeds are 37 and 43 m/s and wave heights 16.3 and 19.6 meter with periods of 10.7 and 11.6 seconds (4.5). For three other cases with lower wind speed and milder wave conditions the loads have been calculated as well. The wind and wave loads are expressed in static and dynamic parts, in which the static part is the constant (mean) value, while the dynamic part is the fluctuating part around the mean.

Wind and wave loads

The dynamic wind loads have been calculated using the turbulence intensity for a near-shore offshore site, with corresponding roughness height (equation 5.13, table 5.7). The turbulence intensity first decreases for increasing wind speed, but for relatively large wind speeds, up to the wind speed with a return period of 50 years, the turbulence intensity increases again. This was also observed in figure 5.8. It should be noted that no dynamic amplification is taken into account in the calculations for wind loads, since the frequencies are very low and the dynamic amplification factor (DAF) will be 1. For the wave loads the dynamic amplification is highly relevant, and shows values above 2, indicating a four times amplified load (table 5.8).

If the wind and wave loads are compared for a wind speed of 25 m/s (just below the cut out wind speed) and a wave height of 10 meter, some observations can be made:

Wind speed	Turbulence Intensity	Static thrust force	Dynamic thrust force	Static fore-aft bending moment	Dynamic fore-aft bending moment
[m/s]	[-]	[MN]	[MN]	[MNm]	[MNm]
5	0.128	0.45	0.12	47.55	12.19
15	0.104	1.36	0.28	142.65	29.67
25	0.106	2.26	0.48	237.74	50.5
37	0.112	0.11	0.02	11.66	2.6
43	0.115	0.13	0.03	13.55	3.1

Table 5.7: *Wind loads for several wind speeds (5, 15, 25 and the 1/5 yr and 1/50 yr value), both static and dynamic components*

Wave height	Wave period	DAF	Horizontal wave force w/o DAF	Horizontal wave force with DAF	Fore-aft moment w/o DAF	Fore-aft moment with DAF
[m]	[s]	[-]	[MN]	[MN]	[MNm]	[MNm]
2	4	2.82	0.69	5.54	15.80	126.05
5	6.3	2.14	5.46	24.94	58.06	265.35
10	8.9	1.37	17.03	31.77	139.44	260.10
16.3	10.7	1.23	28.47	42.90	221.20	333.33
19.6	11.6	1.19	33.66	47.45	257.78	363.39

Table 5.8: *Wave loads for several wave heights (2, 5, 10 and the 1/5 yr and 1/50 yr value), with and without dynamic amplification (DAF)*

- From the obtained values of static and dynamic wind loads it can be seen that the static wind load is multiple times larger than the dynamic wind load, which also results in a larger static bending moment form wind than dynamic bending moment from wind.
- The average ratio of horizontal wave force versus dynamic wind load is around 60, indicating a far larger fluctuating wave load than fluctuating wind load.
- The ratio of bending moment at seabed level for wave load versus dynamic wind load is slightly less than 5, indicating a larger fluctuating bending moment due to wave loads than wind loads. The far larger ratio of 60 for the horizontal forces is largely reduced by the larger arm of the wind load compared to the wave load.
- If the static horizontal wind component is compared with the (dynamic) horizontal wave components, the ratio of horizontal forces is around 12, also indicating that the horizontal dynamic wave force is even larger than the static horizontal wind force.
- The average ratio for bending moments of wave (including DAF) versus static wind only leads to a value of 1, indicating that the bending moment from the static wind component is comparable to the (dynamic) bending moment of waves.

Turbine loads

The rotation of the turbine produces the 1P loads (table 5.9). No fore-aft horizontal component is induced however, only a bending moment at seabed level is generated. The rotor mass imbalance was calculated based on a comparison with a Vestas 2 MW turbine for which the rotor mass imbalance was known. The mass imbalance is caused by the blade mass rotating at a distance from the hub, and can according to Arany et al. (2014) be related to the rotor diameter (indicating the distance from the hub) and the mass of the blades. A linear relation is assumed and the mass imbalance of the 2MW turbine is simply scaled with the rotor diameter and the blade mass (equation 5.43).

$$I_{m,8MW} = I_{m,2MW}\frac{M_{8MW}}{M_{2MW}}\frac{D_{8MW}}{D_{2MW}} = 500\frac{150}{37.5}\frac{164}{80} = 4100kgm \tag{5.43}$$

The bending moments at seabed level can be calculated with equation 5.31 for multiple wind speeds. The rotational frequency of the wind turbine is linearly interpolated between the cut-in wind speed, the rated wind speed and the operating frequencies (rpm) of the turbine (equation 5.44). The rated wind speed is the wind speed above which the rotor will not increase its frequency. Therefore, above the rated wind speed the 1P frequency, and therefore also the load, will remain constant. This can also be observed in table 5.9 and also results in a constant DAF for higher wind speeds. This DAF is quite high, an amplification of 25 times can be reached since the higher frequencies in the 1P range are quite close to the natural frequency of the system (0.20 Hz versus 0.2164 Hz), which was concluded from the dynamic analysis.

Wind speed	Rotor speed	Frequency	DAF	1P Fore-aft bending moment w/o DAF	1P Fore-aft bending moment with DAF
[m/s]	[rpm]	[Hz]	[-]	[MNm]	[MNm]
5	5.7	0.095	1.24	0.007	0.011
15	12	0.2	5.79	0.032	1.073
25	12	0.2	5.79	0.032	1.073

Table 5.9: *1P Fore-aft bending moments for several wind speeds with and without dynamic amplification factor (DAF). For wind speeds above 25 m/s the wind turbine is parked and the 1P loads are zero.*

Wind speed	Rotor speed	DAF	3P Frequency	3P Horizontal Force w/o DAF	3P Horizontal Force with DAF	3P Fore-aft moment w/o DAF	3P Fore-aft moment with DAF
[m/s]	[rpm]	[-]	[Hz]	[MN]	[MN]	[MNm]	[MNm]
5	5.7	1.34	0.29	0.0017	0.0030	0.123	0.222
15	12	0.15	0.60	0.0152	0.0004	1.110	0.025
25	12	0.15	0.60	0.0422	0.0009	3.084	0.069

Table 5.10: *3P loads for several wind speeds with and without dynamic amplification factor (DAF). For wind speeds above 25 m/s the wind turbine is parked and the 1P loads are zero.*

$$rpm = rpm_{cutin} + \frac{rpm_{cutout} - rpm_{cutin}}{u_{rated} - u_{cutin}} (U_{wind} - u_{cutin}) \tag{5.44}$$

The 1P load also produces bending moments in side-to-side direction (Figure 5.2). The arm of these loads is far larger than the rotor overhang (5m), since in the side-to-side direction the arm is the total hub height and water depth up. Therefore these bending moments will simply be a factor $(H_{hub} + d)/b = (125+30)/5 = 31$ larger. The wave and wind loads produce still far larger (cyclic) bending moments. Since the latter effect will be governing the cyclic loads on the subsoil, the 1P loads in side-to-side direction are neglected in this study.

Finally also the 3P loads have been calculated for the reference case (table 5.10). The 3P loads consist of a horizontal force and a bending moment at seabed level. The frequency of the rotor is again related to the wind speed by using a linear interpolation between the rotor cut-in and cut-out rpm and the cut-in and rated wind speed (equation 5.44). For higher wind speeds the rotational frequency of the rotor (1P) is kept constant by the turbine operating system, and therefore the 3P frequency will also be constant but three times higher. For the 3P loads it can be observed that the DAF reaches values below one, indicating damping of the 3P loads with a relatively high frequency. Therefore the loads with DAF included become smaller than the loads where no DAF is taken into account. The 3P load is in fact a load loss, since it reduces the drag load on the turbine. Therefore the 3P loads are not added in the spectrum and time series.

Analysing the turbine loads, the following can be observed:

- The bending moments of 1P loads are relatively small compared to the wind and wave loads, even with dynamic amplification they will be of minor influence on cyclic load effects below the seabed.
- The 3P loads are also relatively small compared to wave and wind loads, but already larger than the 1P loads.

The current loads have been calculated using a drag coefficient of 2.5. A linear depth profile of the current velocity was used to calculate the bending moment at seabed level. The total frontal area of the GBF is approximately 500 m^2, which results in a current load for the 1/50 yr conditions of 2.1 MN and for the 1/5 yr 0.5 MN. The corresponding bending moments are 42 MNm and 10 MNm. The current load is however a static load, and will not induce any densification of the soil bed. In amplitude however it is larger than the 1P and 3P induced loads.

Spectra development

An interesting investigation is the development of the spectra of horizontal force and bending moment at seabed level during the build-up of a storm. This is shown for a regular build-up of a storm in figures 5.24 and 5.25. Both wave height, peak period and wind speed are increasing, following a general storm development from the CoastDat database that will be used for the storm data (Weisse et al. (2005)).

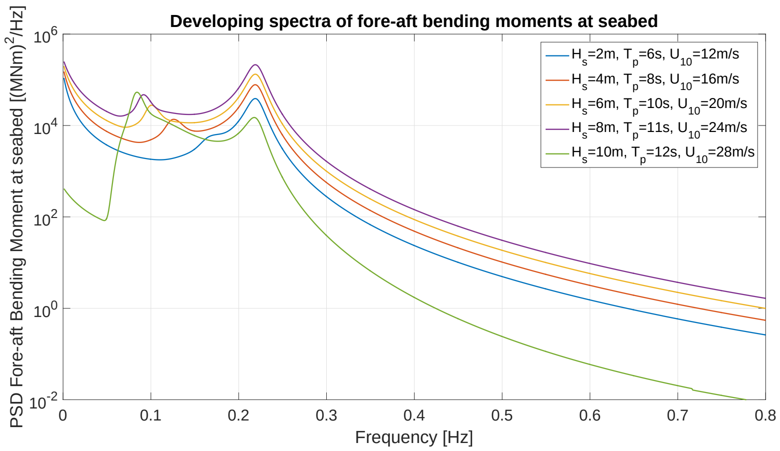

Figure 5.24: *Spectrum development of bending moment at seabed level over time for increasing wave height, wave period and wind speed*

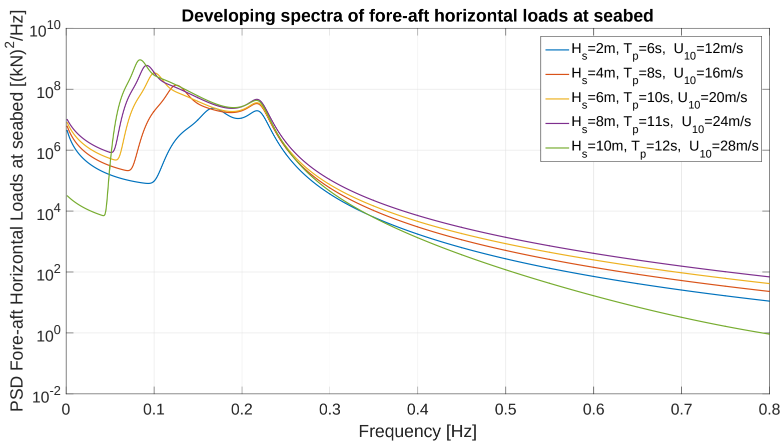

Figure 5.25: *Spectrum development of horizontal force at seabed level over time for increasing wave height, wave period and wind speed*

From the bending moments is can clearly be seen that the increasing wave height and wind speeds results in higher spectral densities around the natural frequency of the system (0.22 Hz). However, if the wind speed increases above the cut-out wind speed, the spectral density at the natural frequency decreases, and the major spectral density can only be found around the wave frequency. This shows the large contribution of the system dynamics in the dominant frequency of the bending moments transferred to the subsoil when the turbine is operating, which reduces significantly when the turbine is shut down. When the turbine shuts down, also the smaller frequencies below 0.5 Hz, resulting from the wind loading, show a large reduction in spectral density.

Looking now at the spectrum development of the horizontal force at seabed, this behaviour is in fact opposite. The spectral density around the natural frequency (0.22 Hz) is nearly constant during the storm build-up, while the spectral density around the wave frequency obviously increases with storm build-up. Also the peak shifts, since the wave period is increasing in the storm build-up. This shows that for the horizontal force the contribution of the system dynamics is of less influence, while the wave frequency is far more significant.

5.6. Assumptions and limitations

The main assumptions and limitations of the load analysis will be summed up, divided in dynamics, wind loads, wave loads and turbine loads:

Dynamics

- The dynamic analysis has been based on a lumped mass method, i.e. no distribution of masses along the height of the structure has been taken into account. This also holds for the springs and damping.

This should be done in a detailed dynamic analysis and should result in a more accurate prediction of the natural frequency.

- Considering the dynamic amplification factor, it should be noted that the fixed dynamic amplification factor for each frequency can only be applied if the stiffness remains constant during the considered dynamic load. If for instance high amplification or even resonance is reached, the stiffness will not remain constant and a more sophisticated analysis is required.
- The effect of soil degradation due to cyclic loading and pore pressure generation is not taken into account on the dynamics of the OWT. However is was found that due to the large mass of the GBF at seabed level and the relatively large soil stiffness compared to the tower stiffness, that the first natural frequency is mainly determined by the tower. Therefore it is not expected that the soil degradation has a significant influence on the natural frequency of the system.
- The final system dynamics have been taken into account with a dynamic amplification function. This may only be used in a preliminary design according to DNV (2014) and should otherwise be based on accurate dynamic modelling. It is expected that the dynamic amplification function at least shows at which frequency the largest amplification are to be expected, and will especially be more accurate if the natural frequency can be predicted in a more accurate way.

Wind Loads

- The dynamic loads from wind gusts depends on the dynamic response of the blades of the turbine. This is currently only taken into account with a thrust factor C_t. Additionally a frequency dependent factor can be added to represent the blade response in the frequency domain. To be more accurate a blade element model (BEM) should be used to determine the response of the blades, and to subsequently determine the loads to be transferred to the soil. Taking the limited time for this study into account, this is however not further elaborated, but is expected to have an important influence on the dynamic loads from the wind turbine.
- The wind loads were divided into a static and a dynamic component. The dynamic component is summarized in the Kaimal spectrum, but the static component will in reality also vary. The frequency of the static component will be very low and therefore it is reasonable to assume that the soil does not experience any densification due to this load.
- The wind and waves are assumed to be aligned. In reality this is not necessarily the case, especially in coastal areas where wave propagation depends on the local topography and where winds might also blow in offshore direction, while this won't be the main wave direction.

Wave Loads

- Linear wave theory (Airy wave theory) is the basis of the wave load calculations. For intermediate or shallow water depths however this should be changed to a higher-order-wave theory to have a better estimate of the loads on the GBF. It was shown that in many wave height and wave period combinations higher order wave theories or cnoidal theories should be applied (table 5.1). This should result in a more accurate prediction of the wave load. Also breaking waves will occur, but with a low probability, and therefore a low number of cycles.
- The Morison equation is the basis for the wave load calculation, but was originally derived for slender piles. It was shown that for storm waves, with large wave lengths and large wave periods the approximation is better than for short waves.
- No phase differences in the contributions from base, cone and pile in the total wave load have been taken into account. Therefore, the wave loads have been overestimated, since due to the different moments of maximum wave loads on the individual elements, the maximum total wave loads is not equal to the sum of the maximum wave loads on the individual elements. This results in a significant overestimation of the wave loads.
- The Morison coefficients are frequency dependent, but are kept constant during the calculations for various wave frequencies. This is due to the fact that the Morison coefficients are based on numerical wave studies, and the Morison coefficients have been tuned to the numerical results to reduce the overestimation of inertia forces from. Since this has only been done for the maximum wave height and corresponding wave period, and since the drag and inertia parts in the total wave load are not linear with the wave period, the Morison coefficients have been kept constant.

Turbine loads

- The mass imbalance of the wind turbine is estimated based on a 2 MW turbine. This should be based on accurate data from the wind turbine manufacturer, again showing the highly interconnected field of engineering within this topic.
- The turbine operating system will determine the operating frequency of the turbine (rpm) in relation to the wind speed. This is currently only linearly interpolated, but should be updated based on the (complex) operating system of the turbine.

Finally it should be noted that the vertical loads have not been taken into account. Due to the varying water level during a wave passage, the buoyancy force varies cyclically as well. The variation will however be small compared to the static weight of the structure. Also the 1P loads from the turbine induce cyclic vertical loads, but it was shows that these are considerably smaller than the cyclic wind and wave loads. The vertical loads are therefore ignored in the analysis.

5.7. Concluding remarks

In the current chapter the cyclic loads from wind, wave and turbine have been derived at seabed level. The procedure showed that it is possible to determine these loads in the frequency domain, and add different environmental loads into a single spectrum of either horizontal forces or bending moments at seabed level. These spectra can be prepared for each significant wave height, peak period and wind speed. The previously discussed loads were all implemented in a Matlab script to obtain the load spectra for a real storm. Each storm needs only to be specified by a significant wave height H_s, peak period T_p and wind speed U_{10}. In chapter 7 the CoastDat database (Weisse et al. (2005)) will be used for the storms at the location of Blyth where the OWT is to be placed. With hourly values of the storm data, the real storm development can be specified in terms of the spectra of resulting loads at seabed level. The spectra can finally be transformed into the time domain, to be used for excess pore pressure calculations.

From the load analysis it can be concluded that for the horizontal forces the contribution of the system dynamics is of less influence, while the wave frequency is far more significant. The wave frequency makes up the larger part of the dynamic horizontal force at seabed level. Furthermore, a large contribution of the system dynamics in the dominant frequency of the bending moments at seabed level was found, at least when the turbine is operating. The contribution of the system dynamics reduces significantly when the turbine is shut down. The relative contribution of wave loads to the dynamic bending moment at seabed level is furthermore largely reduced due to the large arm of the wind loads, however the wave related bending moment was still found to be larger than the wind load.

Although the load analysis is based on a large number of assumptions, especially related to the wind loads and the dynamic behaviour of the structure, the most important frequency components are captured in this approach. With this approach the irregular nature of the loads and the real storm build-up can be taken into account. In order to apply the derived loads, first a cyclic shear stress profile below the GBF needs to be calculated to complete the input for DCycle. This will be discussed in the next chapter.

6

Cyclic shear stress profile

6.1. Introduction

The previous chapter dealt with the cyclic loads from wind, waves and turbine that are transferred to seabed level. The resulting shear loading of the subsoil below the GBF can be described by a cyclic shear stress profile over depth. The cyclic shear stress amplitude is no longer represented correctly by the analytical formula of Yamamoto, given in equation 2.11. This profile was derived for a single wave load on a horizontal seabed, but the stress distribution has changed due to the transferred loads from the GBF to the sea floor. In this chapter a cyclic shear stress profile will be derived for the GBF using the Finite Element Model Plaxis. This is the final step necessary for the input in DCycle, and is visualised in figure 6.1.

The starting point in this chapter will be a comparison of multiple definitions of the cyclic shear stress ratio, from which various cyclic shear stress profiles can be derived. In addition to the definition, the loads need to be determined which will be used in the derivation of the profile. With both a definition and the loads, the Plaxis model can be set up. This will be discussed next, together with a discussion on the input parameters. Finally the results will be discussed for several load combinations.

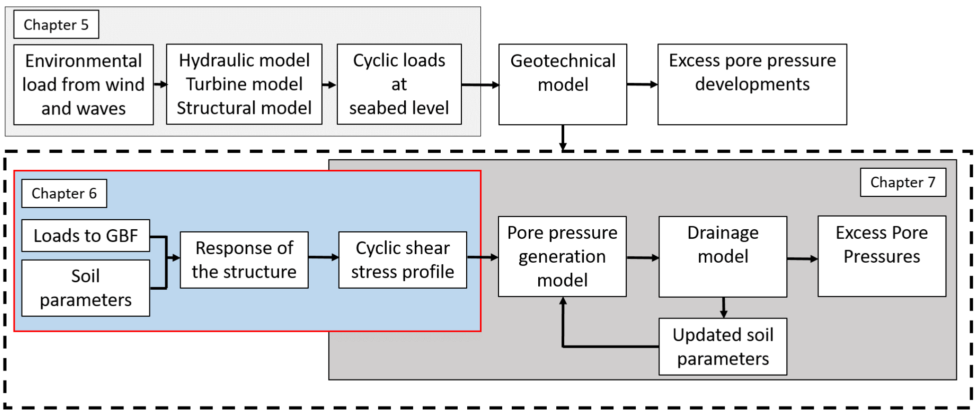

Figure 6.1: *Subdivision of the chapters within the followed approach, with the content of chapter 6 highlighted in blue*

6.2. CSSR-Definitions

The Plaxis model will be used to derive the CSSR profile in a single load cycle. A single load cycle will produce a single cycle of cycle shear stresses in the soil, from which the amplitude in shear stress can be derived. Different methods and definitions will first be introduced to derive the shear stress amplitude. The general 1-dimensional cyclic shear stress ratio often found in literature is presented in equation 6.1 (Youd et al. (2001)):

$$CSSR = \frac{\Delta\tau_c}{\sigma'_{v0}} \tag{6.1}$$

With:

$CSSR$ = cyclic shear stress ratio [-]
$\Delta\tau_c$ = shear stress amplitude [kPa]
σ'_{vo} = initial effective vertical stress [kPa]

This definition can now be used in different ways to obtain the cyclic shear stress ratio from the maximum and minimum load level in a single load cycle. To investigate the sensitivity of the obtained cyclic shear stress ratios from various definitions, three definitions will be used:

- Determine the shear stress amplitude using the (Cartesian) shear stresses directly, without looking for the plane with the largest shear stresses. Divide the shear stress amplitude by the average vertical effective stress (equation 6.2).

$$CSSR = \left|\frac{\Delta\tau_{xy}}{\sigma'_{v,av}}\right| = 0.5\left|\frac{(\tau_{xy,max} - \tau_{xy,min})}{\sigma'_{v,av}}\right| \tag{6.2}$$

  Where:

  $\Delta\tau_{xy}$ = difference between maximum and minimum Cartesian shear stress [kPa]
  $\sigma'_{v,av}$ = average vertical effective stress [kPa]
  $\tau_{xy,max}$ = maximum Cartesian shear stress [kPa]
  $\tau_{xy,min}$ = minimum Cartesian shear stress [kPa]

- Instead of defining the amplitude of the shear stress using a maximum and minimum load level in a single (extreme) cycle, the difference in ratio of shear stress over vertical effective stress between the maximum and minimum load can be used as amplitude. These ratios in the maximum and minimum load are subtracted to find the amplitude in the maximum load cycle.

$$CSSR = 0.5\left|\frac{\tau_{xy,max}}{\sigma'_{v,max}} - \frac{\tau_{xy,min}}{\sigma'_{v,min}}\right| \tag{6.3}$$

  Where:

  $\tau_{xy,max}$ = maximum Cartesian shear stress [kPa]
  $\tau_{xy,min}$ = minimum Cartesian shear stress [kPa]
  $\sigma_{v,max}$ = maximum vertical effective stress [kPa]
  $\sigma_{v,min}$ = minimum vertical effective stress [kPa]

- Method proposed in (Boeije et al. (1993)), finding the plane under angle α with the largest shear stress amplitude in an extreme load cycle. From the maximum and minimum shear stresses the amplitude is derived, which is divided by the initial effective stress in vertical and horizontal direction to get the CSSR ratio. This finally results in a formula for the shear stress amplitude. The formula was presented in the paper, however the derivation is missing. In order to clarify the thoughts, it is derived again below. The formula was originally written in Cartesian coordinates with y-axis vertical upwards from the seabed, but in this thesis the z-axis will be the vertical axis upwards from the seabed. It should however be noted that it is often stated that the shear stress amplitude is divided by the initial vertical effective stress, while the latter initial effective stress is not only vertical, but contains a horizontal component as well.

  The shear stresses acting on a plane under angle α can be derived from the equilibrium of forces on a soil element, all expressed in Cartesian coordinates. The shear stress is given by Poulos and Davis (1974) (equation 6.4). In formula 6.4 τ in fact represents two times the amplitude. Therefore, the shear stress amplitude between two different load situations (maximum load and minimum load) can be found by subtracting both shear stresses (equation 6.5).

$$\tau = \tau_{xy}(\cos(\alpha)^2 - \sin(\alpha)^2) + (\sigma_{zz} - \sigma_{xx})(\sin(\alpha)\cos(\alpha)) \tag{6.4}$$

$$2\tau_c = (\tau_{xy,max} - \tau_{xy,min})(\cos^2(\alpha) - \sin^2(\alpha)) + (\sigma_{zz,max} - \sigma_{zz,min} - \sigma_{xx,max} + \sigma_{xx,min})(\sin(\alpha)\cos(\alpha)) \tag{6.5}$$

Now the angle α of the plane with the largest shear stress amplitude can be found by differentiating equation 6.5 to α and solving for $d\tau/d\alpha = 0$ (equation 6.6). Using the double angle formulas, equation 6.6 can be rewritten to equation 6.7.

$$\begin{aligned} d\tau_c/d\alpha = {} & (\tau_{xy,max} - \tau_{xy,min})(-2\cos(\alpha)\sin(\alpha) - 2\sin(\alpha)\cos(\alpha)) + \\ & (\sigma_{zz,max} - \sigma_{zz,min} - \sigma_{xx,max} + \sigma_{xx,min})(\cos^2(\alpha) - \sin^2(\alpha)) = 0 \end{aligned} \tag{6.6}$$

$$d\tau_c/d\alpha = (\tau_{xy,max} - \tau_{xy,min})(-2\sin(2\alpha)) + (\sigma_{zz,max} - \sigma_{zz,min} - \sigma_{xx,max} + \sigma_{xx,min})(\cos(2\alpha)) = 0 \tag{6.7}$$

This finally results in equation 6.8.

$$\tan(2\alpha) = \frac{(\sigma_{zz,max} - \sigma_{zz,min} - \sigma_{xx,max} + \sigma_{xx,min})}{2(\tau_{xy,max} - \tau_{xy,min})} \tag{6.8}$$

The angle α for the maximum shear stress amplitude can now be determined and can be used in equation 6.5 to get the amplitude. Boeije (Boeije et al. (1993)) now defines the cyclic shear stress amplitude using equation 6.9.

$$\tau_c = \frac{1}{2}\left|(\tau_{xy,max} - \tau_{xy,min})(\cos^2(\alpha) - \sin^2(\alpha)) + (\sigma_{zz,max} - \sigma_{zz,min} - \sigma_{xx,max} + \sigma_{xx,min})(\sin(\alpha) * \cos(\alpha))\right| \tag{6.9}$$

To determine the CSSR-profile, the initial vertical and horizontal effective stress should also be known at the moment that the static stresses due to the GBF are present. According to Boeije (Boeije et al. (1993)) an appropriate value is found with the average of vertical and horizontal stress due to the static loading. For the other two approaches the definition is used from equation 6.2 and 6.3.

$$\sigma'_{v0} = \frac{\sigma'_{xx,0} + \sigma'_{zz,0}}{2} \tag{6.10}$$

From the various definitions of the CSSR-profile, it becomes clear that the GBF needs to be modelled in a single load cycle to derive the stresses for the maximum and minimum half of a load cycle respectively. In order to do so, first the circular GBF needs to be schematised to a rectangular baseplate, to model it in 2D plane strain in Plaxis. An axial symmetric model is not possible, since bending moments should be taken into account too. This will be discussed in the next section.

6.3. Schematisation of the GBF

A 2D plane strain Plaxis model is set up with the main goal to find the CSSR profile below the gravity based foundation for the extreme (ULS) load cycle. A 3D model will result in a more accurate stress distribution below the GBF. Due to effects of stress spreading a 3D model is expected to result in lower cyclic shear stress ratios. To obtain a conservative estimate of the cyclic shear stress profile, and because of time restrictions, a 2D model was set up. Before this can be done, a 2D schematisation should be made of the structure, which basically represents the circular baseplate of the GBF with a rectangular baseplate (based on DNV (1992) and DNV (2014)). From the rectangular baseplate a strip of 1 meter width is used to model in Plaxis (figure 6.4). The loads on the GBF are transformed to equivalent loads on the 1m. wide strip. The main properties of the GBF that should be transformed to an equivalent rectangular baseplate are the surface area, the moment of inertia and the section modulus. For the reference structure with a diameter of 30 m. the surface area, moment of inertia and section modulus become (equation 6.11):

		A & I correct	A & W correct
Width W	$[m]$	26	22.5
Length L	$[m]$	27.2	31.4
Surface area A_{plate}	$[m^2]$	707	707
Moment of Inertia I_{plate}	$[m^4]$	39747	29820
Section modulus W_{plate}	$[m^3]$	3060	2650
EI	$[10^{10} kNm^2]$	5.85	3.80
EA	$[10^9$ kN$]$	1.04	0.90

Table 6.1: *Dimensions for the two considered schematisations of the GBF*

$$\begin{aligned} A_{plate} &= \pi R^2 = \pi 15^2 = 707 m^2 \\ I_{plate} &= \frac{1}{4}\pi R^4 = 1/4\pi 15^4 = 39761 m^4 \\ W_{plate} &= \frac{2I}{R} = 5301 m^3 \end{aligned} \tag{6.11}$$

Where:

A_{plate} = surface area of base plate $[m^2]$
I_{plate} = moment of inertia of base plate $[m^4]$
W_{plate} = section modulus $[m^3]$
R = radius of the gravity based foundation [m]

Since the main purpose of the Plaxis model is to determine the shear stresses correctly, at least the surface area of the modelled base slab should be kept equal to the surface area of the circular base slab. Two possibilities remain, either with correct surface area and moment of inertia or with correct surface area and section modulus. No dimensions of a rectangular base slab can be determined with all 3 properties equal to a circular base slab. The corresponding dimensions for both cases are listed in table 6.1 following equations 6.11. The parameters EI and EA for both schematised baseplate's have been calculated, and are used in Plaxis as well. The uncracked concrete stiffness of 40 GPa is used. The parameters are visualised in figure 6.2.

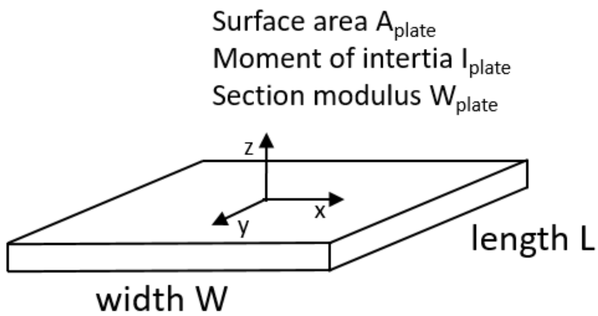

Figure 6.2: *Schematised GBF as a rectangular plate with width W and length L and with axis indicated*

The loads (forces and bending moments) that will be applied to the baseplate have to be divided by the length L of the baseplate to arrive at a load per meter strip, which can be used in the 2D Plaxis model. The resulting bending moment is subsequently applied as two vertical loads in opposite direction. This will be discussed after the load stages.

6.3.1. Load stages

The following stages were implemented in Plaxis. In all cases a static water level of +30 meter above the seabed was applied. The stages are visualised in figure 6.3 (except for stage 0) and are listed below:

Stage I	Initial stresses are calculated without any structure present (K0-procedure).
Stage II	The baseplate with static loads is present, including the dead weight of the GBF and OWT. This phase is drained, since the time between placement of the GBF and installation of the turbine and loads acting on the GBF is large enough to consider it to be drained. The static components of the loads, to be determined in the next paragraph, are also applied in this load stage.
Stage III	The first half of a load cycle (horizontal force and vertical forces representing bending moment) is applied, which represents the maximum load (middle of figure 6.3). The loading is undrained.
Stage IV	The second half of a load cycle is applied (horizontal force and vertical forces representing bending moment), which represents the minimum load during the extreme load cycle (right of figure 6.3). This loading is also undrained.

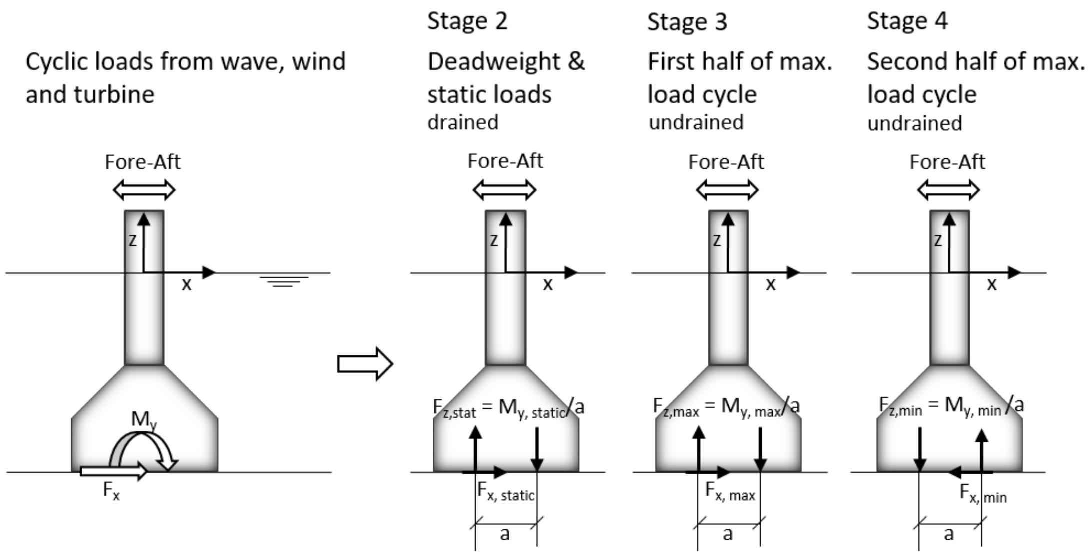

Figure 6.3: *The loads from wave, wind and turbine are transferred to seabed level (left) in fore-aft direction. The static loads and dead weight are applied in the second stage. During the extreme load cycle, the first half of the load cycle is applied (second from right) and the second half of the load cycle (right figure). The positive directions are indicated in the left figure. The stages correspond to the previously listed stages.*

First of all, calculations were made to assess whether the two options for a 2D schematisation are comparable, and therefore whether it can be considered to be an accurate representation of the 3D structure. This was done for a homogeneous soil layer of 30 meter deep. The gravity based foundation is modelled as a simple baseplate with the properties mentioned in table 6.1. The horizontal force and bending moments (represented by two vertical loads) are applied directly to the baseplate. The results showed no significant differences in the obtained CSSR-profiles, and therefore the calculations were continued for the rectangular baseplate with correct representation of A and I. The results for the two schematisations will be presented after the discussion on the schematisation of the loads and the model set-up in Plaxis.

6.4. Schematisation of the loads

The largest cyclic load cycle will be found when the turbine is still operating, and consequently inducing cyclic wind loads at seabed level, and when an extreme wave hits the GBF. It could be argued whether or not the wind turbine is operating in the weather conditions in which an extreme wave hits the GBF. However, it is desirable to derive the CSSR profile for an upper limit of the cyclic load amplitude, since this represent the soil behaviour and thus the CSSR profile under these extreme conditions correctly.

Both the cyclic loads from wind, waves and turbine have to be taken into account. The loads were derived in chapter 5, and the results from the reference geometry will be used to derive the total cyclic loads. The wave with a return period of 50 years will be used, which corresponds with a wave height of 19.6 meter and peak period of 11.6 seconds (table 5.8). The wind loads and turbine loads are based on a wind speed of 25 m/s, just below the cut-out speed (table 5.7). Also the static part of the load is derived, and all loads are split in horizontal loads at seabed level and in bending moments at seabed level. The various components are presented in table 6.2. It should be noted that the dynamic part in the tables represents the fluctuating part of the load, while the static part represents the constant part. This should not be confused with the DAF, which takes into account the dynamic amplification effects.

	Static Horizontal load [MN]	Dynamic Horizontal load [MN]	Static Bending load [MNm]	Dynamic Bending load [MNm]
Wind loads	2.26	0.48	238	51
Wave loads	0	48	0	363
1P Turbine loads	0	0	0	1.1
3P Turbine loads	0	0.001	0	0.07
Total loads	2.3	48.5	238	415

Table 6.2: *Resulting static and dynamic (fluctuating) loads for Plaxis calculations. Based on wind speed of 25 m/s and significant wave height of 10 meter*

The static and dynamic part of the load are subsequently combined to a total load in a single load cycle, with the first half of the cycle in positive direction, F_{max} and the second in negative direction (F_{min}, equation 6.12). Similar equations hold for the bending moments. The loads are transformed to the equivalent loads for the rectangular structure with a length of 27.2 meter and a width of 26 meter. The horizontal loads are therefore divided by the length of 27.2 meter to arrive at a load per meter length, and the bending moments by the length and the factious arm a between the two vertical loads (figure 6.3). The static components, originating from the wind load, are also recalculated to a strip of 1 meter length. All resulting loads are presented in table 6.3, both summed up and separately for wind and wave loads, to be used in the assessment of the contribution later. The loads have been applied in Plaxis as static loads, i.e. no inertia and damping is taken into account.

$$\begin{aligned} F_{max} &= F_{stat} + F_{dynamic} \\ F_{min} &= F_{stat} - F_{dynamic} \end{aligned} \tag{6.12}$$

Where:

F_{max} = maximum horizontal load in cycle [N]
F_{min} = minimum horizontal load in cycle [N]
F_{stat} = static horizontal load in cycle [N]
$F_{dynamic}$ = dynamic, fluctuating load in cycle [N]

	$F_{x,max}$	$F_{x,min}$	$M_{y,max}$	$M_{y,min}$	Plaxis $F_{x,stat}$	Plaxis $F_{x,max}$	Plaxis $F_{x,min}$	Plaxis $F_{z,stat}$	Plaxis $F_{z,max}$	Plaxis $F_{z,min}$
	[MN]	[MN]	[MNm]	[MNm]	[MN/m]	[MN/m]	[MN/m]	[MN/m]	[MN/m]	[MN/m]
Total	50.7	-46.2	653.2	-177.2	0.08	1.87	-1.70	1.09	3.00	-0.81
Wind	2.7	1.8	289	187	0.08	0.10	0.06	1.09	1.33	-0.86
Wave	48	-48	363	-363	0	1.76	-1.76	0	1.67	-1.67

Table 6.3: *Resulting loads for Plaxis calculation, in total, and separately for wind and wave loads. The four columns on the left are the actual horizontal loads and bending moments acting on the GBF, while in the six columns on the right these loads have been recalculated to the loads per meter length of the schematised rectangular baseplate. Also the bending moments are recalculated into vertical loads and per meter length. The positive direction are indicated in the left figure of figure 6.3.*

6.5. Plaxis model

In order to determine the shear stresses in an extreme load cycle, a Plaxis model is used to model the GBF. In the previous sections, the schematisations of the structure and the loads have been discussed, which will be used as input for the Plaxis model. In the subsequent sections first of all the soil parameters will be discussed, after which the results will be presented.

6.5.1. Model parameters

It is desired to superimpose two stress conditions in an extreme load cycle. Therefore, a linear elastic soil model should be used to prevent stress peaks being smoothed due to plasticity. This is the reason why the Mohr-Coulomb model will be used to derive the CSSR-profile. On the other hand, it might be better to use a hardening-soil model to take the differences in soil stiffness below and around the structure into account, which would be the case if a hardening soil model is used. It is however desired to remain in the linear elastic range, and therefore a linear elastic model is used. Since plasticity does not reduce peak stresses, in general a conservative value for the cyclic shear stress ratio will be found.

Appropriate stiffness moduli E should represent the stress state correctly during the stages as described before. The placement of the baseplate at the seabed is assumed to be an initial loading of the soil and is therefore represented by a lower stiffness compared to the phases where loads are applied. The loading phases actually are loading/unloading situations with corresponding stiffness. The soil properties are mainly related to the relative density of the soil body, at least for sandy soils. It is assumed that only relatively densely packed sands are present, since the loosely packed top layers will be removed and replaced by a gravel bed. For the initial placement of the baseplate a value of 50 MPa is chosen and for loading and unloading a value of 150 MPa is chosen. The Poisson ratio ν is set to 0.3, representing a realistic lateral stress coefficient of $K_0 = 0.43$. Higher relative densities can be described by higher friction angles. For the current derivation of the CSSR-profile, the value is set to 35 °.

As stated before, the soil model used in Plaxis is the linear-elastic model with a Mohr-Coulomb failure criterion It is observed that a large number of calculation points failed due to the large forces in ULS condition, especially in the upper soil layers. In order to be able to apply the method as proposed in Boeije et al. (1993), elastic soil behaviour is desired since otherwise the calculated amplitude derived from two different stress states would be influenced by plastic failure. It is stated in Boeije et al. (1993) that elastic soil behaviour might be used by applying a very (unrealistically) high value of the cohesion. This would result in elastic soil behaviour, without any indication of failure, but for the purpose of deriving the CSSR profile this is not important. Therefore, the calculation is repeated with a cohesion of $10^{10} kPa$, both in drained and undrained calculations. In reality the soil won't behave linear elastic, but plasticity will reduce peak stresses instead. The adopted linear elastic modelling therefore results in conservative values of cyclic shear stress ratios.

The angle of dilation has a significant influence on the soil strength. A small negative value represents loosely packed sands with ongoing densification during shear deformation. Small positive values might model densely packed sand. The dilation angle is related to the mobilised friction angle and a critical friction angle defined by the user. It is subsequently used in the hardening soil model to relate volumetric strains and shear strains. After large shearing the soil arrives in a state with a critical density, above which no dilation takes place anymore (critical state). This is modelled in Plaxis by setting the angle of dilation back to zero when the dilation cut-off is used, which can only be used in the Hardening Soil model. The dilation cut-off cannot be used in the linear-elastic soil model, and therefore it should be taken into account that the dilation does not continue for ever during shearing. Especially for undrained conditions no volume change is present, and due to dilation large tensile pore pressures may occur, exceeding the cavitation under pressure. For the purpose of deriving the CSSR profile, the angle of dilation is set to 0 in both drained and undrained calculations.

Undrained modelling can be done in two models in Plaxis: undrained A and undrained B. Model undrained A requires input of the effective stiffness parameters $E^{'}$ and $\nu^{'}$ and the strength parameters $\phi^{'}$ and $c^{'}$. The undrained B model offers the opportunity to enter the undrained shear strength s_u along with the $\phi = 0$ approach. In this case the mobilised shear strength is limited to the entered value, although the stress path may not be correct. In fact both a fully drained and a fully undrained calculation are simplifications of the real situation, which is only partially drained (or partially undrained). Since during the extreme load the conditions

Dead weight	[kN/m/m]	200
EA	[kN/m]	$1 * 10^9$
EI	$[kNm^2/m]$	$58 * 10^9$

Table 6.4: *Baseplate parameters for Plaxis*

might be better modelled with an undrained calculation due to the very short time scale, all calculations during the single load cycle are performed undrained in model A. For the top soil layers this might not be correct though.

The GBF is modelled as a plate for the two cases in table 6.1 with a width of 26 and 22.5 meter. The total weight of the ballasted GBF and wind turbine is taken into account in the dead weight of the plate. A stiffness of 40 GPa was used for the baseplate, not taking into account any reduced stiffness due to effects of concrete cracks. In reality the stiffness might be lower due to cracking, reducing the stresses transferred to the subsoil, and therefore a conservative estimate is obtained. With the corresponding surface area A and moment of inertia I the parameters for the baseplate can be calculated (table 6.4). An impermeable interface is used at the boundary between baseplate and soil.

The gravel bed is not modelled, since the high drainage capabilities cannot be modelled in the plastic calculation mode of Plaxis. In that case a groundwater flow model should be chosen. The gravel bed is not expected to affect the CSSR profile in this undrained calculation, since the strength and stiffness parameters are similar to the homogeneous sand body. In table 6.5 the main soil parameters have been summarised in table 6.5. The used mesh is presented in figure 6.4.

γ_{unsat}	$[kN/m^3]$	16
γ_{sat}	$[kN/m^3]$	20
$E'_{initial}$	[MPa]	50
$E'_{unload/reload}$	[MPa]	150
cohesion c	[kPa]	10^{10}
friction angle ϕ	[°]	35
dilation angle ψ	[°]	0
Poisson ratio ν'	[-]	0.3

Table 6.5: *Soil parameters in the FEM calculations*

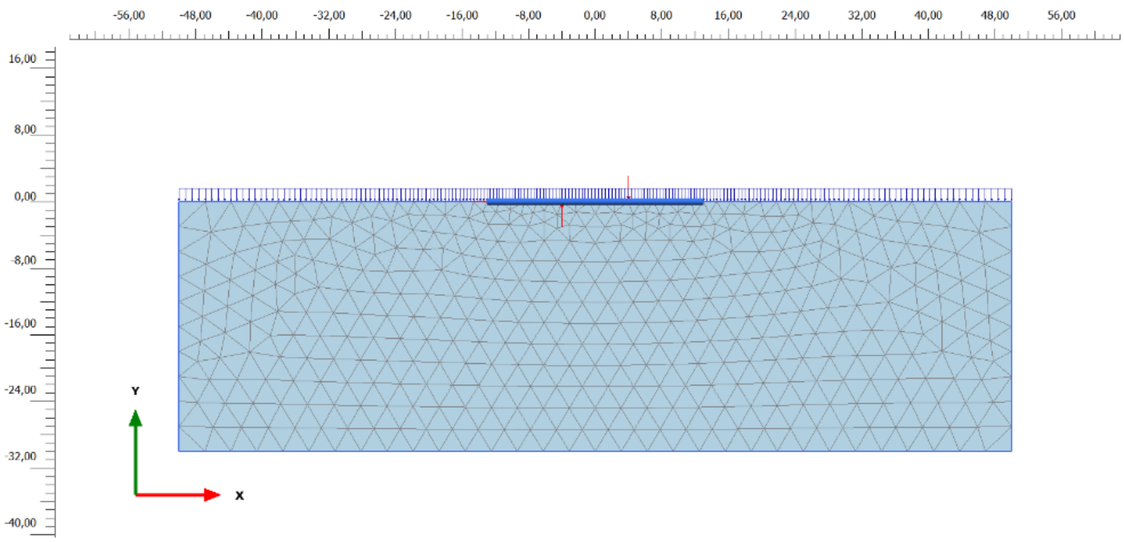

Figure 6.4: *Used mesh in the Plaxis calculations, also showing the static water pressure from a water level of +30 meter above seabed*

6.5.2. Model results

The CSSR profile is derived from the Cartesian stress components in the output of Plaxis using the various definitions of CSSR-ratios. In total 5 depth profiles were chosen, two of them a few meter away from the edge of the baseplate at both sides, two a few meter away from the edge but below the structure at both sides, and a single one in the centre of the baseplate. For each profile, the stresses have been selected in a 1 meter wide profile, and averaged over this meter, to obtain a reliable profile without local peak stresses. It therefore be the case that the cyclic shear stress ratio reaches higher values in certain points, which cannot be found back in the obtained CSSR-profile used in this study. In reality these peaks may be reduced as a result of stress spreading. Using the current 2D approach this results in a conservative estimate of the CSSR profile, due to a reduced stress spreading compared to a 3D situation.

The results for two different 2D schematisations are presented in figures 6.5 and 6.6. The figures show only small differences in the CSSR profiles. All subsequent calculations have been made with similar surface area A and moment of inertia I (A & I correct in table 6.1).

Looking closer at both schematisations (figure 6.5 and 6.6) and comparing different locations below the GBF, the largest CSSR-values are found in the top soil layers around the structure. The soil layers below the GBF show smaller CSSR-ratios and are therefore less sensitive to liquefaction. Just around the GBF the vertical stress is smaller than below the structure, and therefore the CSSR-value is higher. The maximum shear stress amplitudes are found below the edges of structure. The vertical isotropic stress also shows peak values below the edges of the structure. This results in lower CSSR-values compared to locations just outside the structure. Due to the static component of the wind load on the turbine, a slightly different CSSR profile is found at both sides of the GBF, with slightly higher values at the side in which the static component acts (in positive x-direction in figure 6.3).

The location in the middle of the GBF shows a minimum value at a depth around 5 meter. Below the middle of the structure lower shear stresses and initial effective stresses are present, however these lower values can only be reached if the stress spreading towards the edges takes place. This will gradually happen with increasing depth. The shear stress apparently spreads faster than the vertical effective stress, since the CSSR-value decreases up to a depth of 5 meter. In the upper soil layers mainly the dead weight of the GBF creates the vertical effective stress and with increasing depth the dead weight of soil layers is increasing, resulting in decreasing CSSR-values as well. After the minimum value around 5 meter depth, the stress spreading of the weight of the GBF starts to dominate above the increasing dead weight of soil layers, dominating the decreasing shear stress with depth and resulting in an increase in CSSR-values when depth increases from 5 to 10 meter. The profiles just below the edges of the GBF show low CSSR ratios in the upper meter, quickly increasing to values around 0.2. Apparently the large vertical stresses below the edges spread under a large angle, while the shear stresses remain high, increasing the CSSR values. At depths larger than 5 meter, the CSSR ratios decrease again, due to the spread in shear stress.

In order to check whether the approach mentioned in (Boeije et al. (1993)) and the Plaxis calculations are comparable to a simplified stress spreading assumption, a calculation was made based on a stress spreading under an angle of $\tan(1/2) = 27°$ (2V:1H). The shear stress is calculated from the horizontal load on the GBF and is divided by the area on which it is acting. The area increases with depth due to the spreading, which gives a depth profile of shear stress. From the weight of the GBF and the soil weight, a profile of vertical stresses can be derived, which together with the shear stress results in an average CSSR-profile below the structure (also plotted in figures 6.5 and 6.6). It should be noted that the bending moments are not taken into account in this case. For the upper layers this simplified calculation gives too low values, while for deeper layers too lager values are predicted.

For the other two approaches, as presented in equations 6.2 and 6.3, other results were found in terms of the CSSR-profile (figure 6.7). The approach of equation 6.2, taking the Cartesian shear stress directly without searching for the plane with the largest amplitude, obviously gives lower values. The method as presented in equation 6.3 gives even smaller values. Only in the upper layers larger values are found compared to the other methods. Defining the amplitude as the ratio of shear stress over vertical effective stress in both load cases results in lower values than defining the amplitude as the difference in shear stress in both half (maximum and minimum) load cycles. The approach from Boeije et al. (1993) results in higher values than the other two methods since the plane is found with the largest shear stress amplitude. This method will therefore be used.

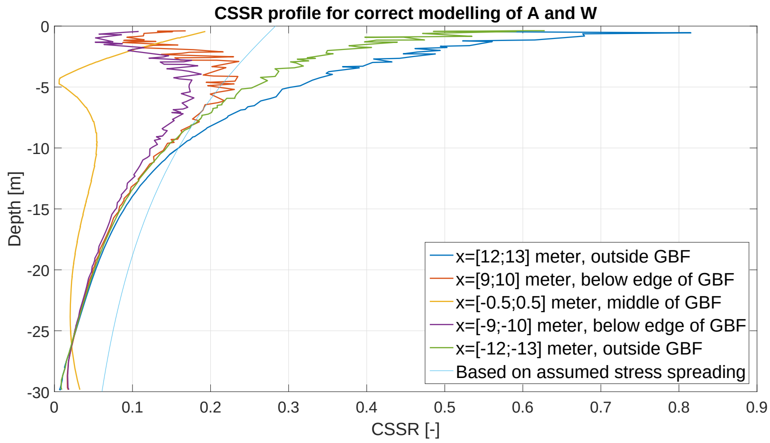

Figure 6.5: *CSSR profiles at different locations below the GBF for correct modelling of A and W. In this case the plate is 22.5 meter wide. Figure 6.3 indicates the direction of loading: the static component acts in positive x-direction. x=[12;13] is just outside the GBF base area, while x=[9;10] just below the edge, and [-0.5;0.5] below the middle.*

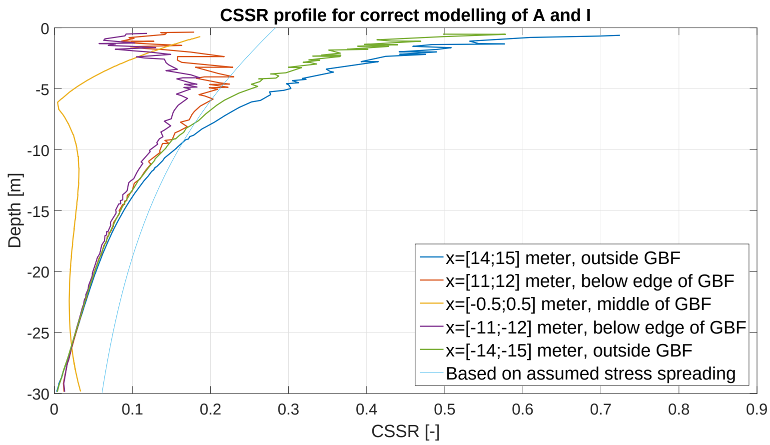

Figure 6.6: *CSSR profiles at different locations below the GBF for correct modelling of A and I. In this case the plate is 26 meter wide. Figure 6.3 indicates the direction of loading: the static component acts in positive x-direction. x=[14;15] is just outside the GBF base area, while x=[11;12] just below the edge, and [-0.5;0.5] below the middle*

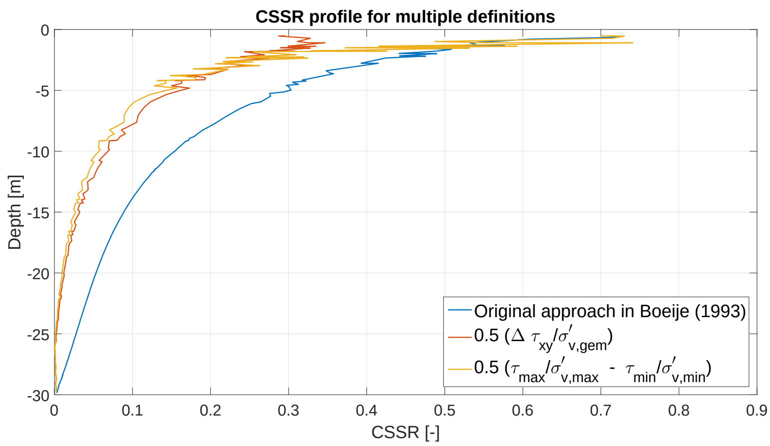

Figure 6.7: *CSSR profiles using multiple definitions (equations 6.2 and 6.3), for correct modelling of A and I. The profile is located just outside the edge of the GBF, at x-locations [14;15]*

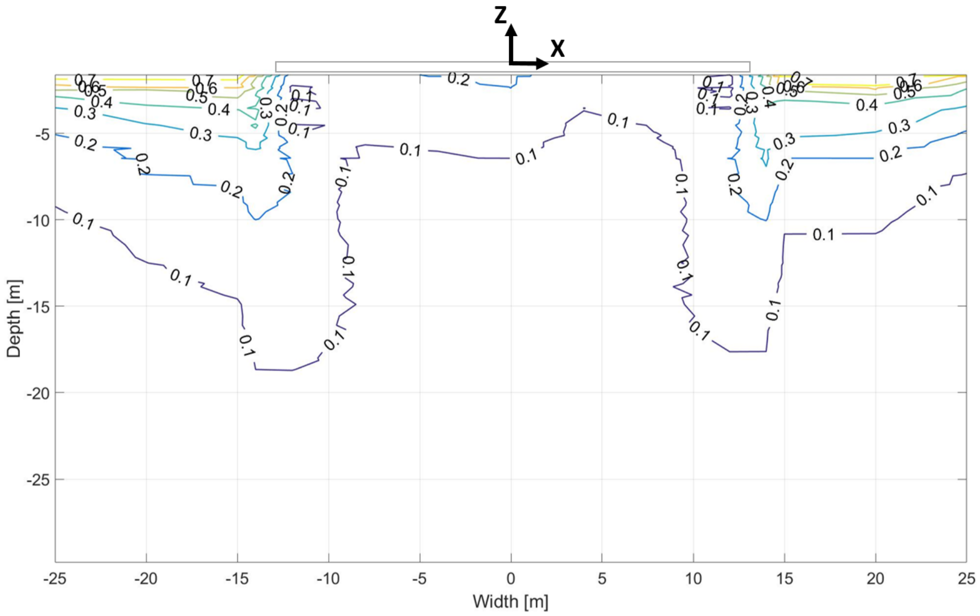

Figure 6.8: *Contour plot for correct modelling of A & I. The static load is applied in positive x-direction, as indicated in figure 6.3*

The results for the correct modelling of A & I are visualised in a contour plot too (figure 6.8). This also clearly shows the higher values around the edges of the structure. Only a slight asymmetry from the load direction (static loading in positive x-direction, figure 6.3) can be seen. This will not be further taken into account. The CSSR profile from outside the edge of the GBF will be discretized to be used further in DCycle.

6.5.3. Model verification

It was investigated whether any influence of the boundary conditions was present in the calculation results. By enlarging the model from 100 meter width to 200 meter width and increasing the depth from 30 to 60 meter, calculations where made (figure 6.9). A slightly reduced CSSR value can be observed in the top layer for the x-range between 14 and 15 meter, just outside the structure. The results for the larger model show furthermore smaller fluctuations in the CSSR-profile, but since the average value remains the same this was not further analysed. No horizontal stress differences at the boundaries before and after loading were observed, and the model was therefore concluded to be large enough to prevent any boundary effects. Also a finer grid size was used to assess whether it would influence the results. The medium and fine grids showed hardly any difference. The medium grid was used for all presented calculations.

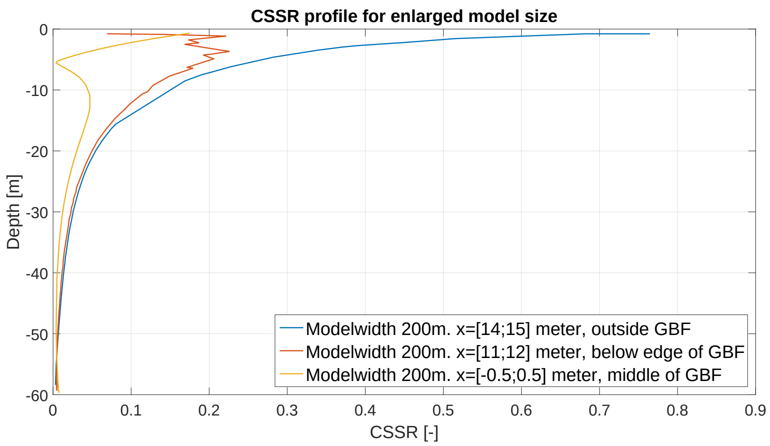

Figure 6.9: *CSSR profiles using a larger half space in Plaxis, for correct modelling of A and I*

6.5.4. Load contributions

The loads at seabed level result in horizontal forces and bending moments. The relative influence of both is assessed by a separate calculation using only horizontal loads and only bending moments respectively (figure 6.10). The loads from table 6.3 are used. To investigate the contribution from wave and wind loads, these loads are also used in separate calculations. The similar procedure is used as outlined in figure 6.3.

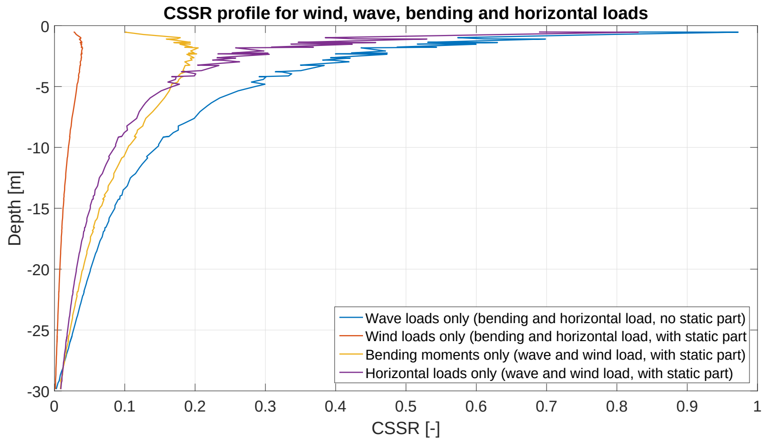

Figure 6.10: *CSSR profiles separated for wind and wave loads, bending moments and horizontal loads*

The following is observed from figure 6.10:

- The wave loads produce the largest contribution to horizontal loads, and also result in the largest CSSR ratios.
- The wind loads produce mainly bending moments, but due to their very small cyclic load amplitude the resulting CSSR ratio remains very small.
- The horizontal loads produce the largest CSSR ratios. The bending moments significantly less. In a combined analysis both will however contribute to the total load distribution and the resulting CSSR values.

6.6. Assumptions and limitations

The main assumptions of the described modelling approach, for a single load cycle in Plaxis, are:

- It is assumed that all stresses and deformations occur in phase. This makes it possible to determine the shear stress development by only looking at the minimum and maximum values, and which consequently allows to make a static calculation in Plaxis.
- The stresses are based on a linear-elastic calculation, which is necessary to use the superposition of stresses for minimum and maximum loading. Due to plastic soil behaviour peaks in stresses may be flattened out, which is currently not taken into account. Using a linear-elastic calculation will give an upper bound (conservative value) of the CSSR-profile.
- The soil behaves completely undrained during the extreme load cycle, which may not be fully correct for the top soil layers.
- The pore pressure development during a single load cycle in Plaxis is negligible.
- The pressure at seabed due to the wave itself is not modelled, neither next to the structure nor due to penetration of the pressure wave into the gravel bed below the structure. Only the forces transferred by the structure towards the seabed are considered. Also the difference in water pressure at seabed level at both side of the structure during maximum and minimum loading is not taken into account, only two time-instants are modelled.

6.7. Concluding remarks

The aim of this chapter was to derive a cyclic shear stress profile below the GBF during a single load cycle. From the FEM-calculations, some interesting conclusions can be drawn about the areas around and below the structure with the highest liquefaction potential. The largest shear stresses are found in the area below the edges of the structure. The initial effective stress increases with depth, and shows maximum values below the edges of the structure. Using the definition of the CSSR, this results in the largest CSSR-values just outside the base slab of the structure, since at this location the initial effective stresses are less and shear stresses are still high. Below the base slab, the vertical stresses are high and reduce the CSSR ratio, reducing the liquefaction potential below the structure. Since the vertical effective stresses are still low in the top soil layers, the maximum CSSR-value in a vertical profile will be found in the top layers.

Using various definitions of the cyclic shear stress ratio, it was found that the ratio defined in Boeije et al. (1993) results in the governing profile. The plane under angle α is found and the cyclic shear stress ratio is defined in this plane. The method ensures that due to the stress rotations next to the GBF still the governing cyclic shear stress profile can be found. The contributions of wave and wind loads on the reference geometry was investigated. It was found that the horizontal loads are dominating the shear stresses and the resulting CSSR profile, while the bending moments produce far lower ratios. The wave loads are dominating the CSSR profile since they form the major horizontal load. The wind loads mainly result in bending moments, but due to their small cyclic amplitude these loads are far less significant compared to wave loads.

With the results from the various CSSR profiles, the next step to DCycle can be made. Both the necessary parts, i.e. the cyclic loads from chapter 5 and the CSSR profile from this chapter, will be used in the next chapter for the calculation of excess pore pressures.

7

Excess pore pressures

7.1. Introduction

In chapters 5 and 6, the cyclic loads and the cyclic shear stress profile have been derived. Both will be used in the current chapter to calculate excess pore pressures (EPP) below the GBF. The aim of this chapter is to answer the research question related to the load history, which load history should be taken into account to determine a representative excess pore pressure to take into account in a stability analysis. The general steps are visualized in figure 7.1.

The starting point of this chapter will be how the cyclic loads and the cyclic shear stress profile will be combined and used in DCycle. The input for DCycle will be discussed, including soil profiles and the loading in terms of storms. The final results of the excess pore pressures, from which the main conclusions for this research will be drawn.

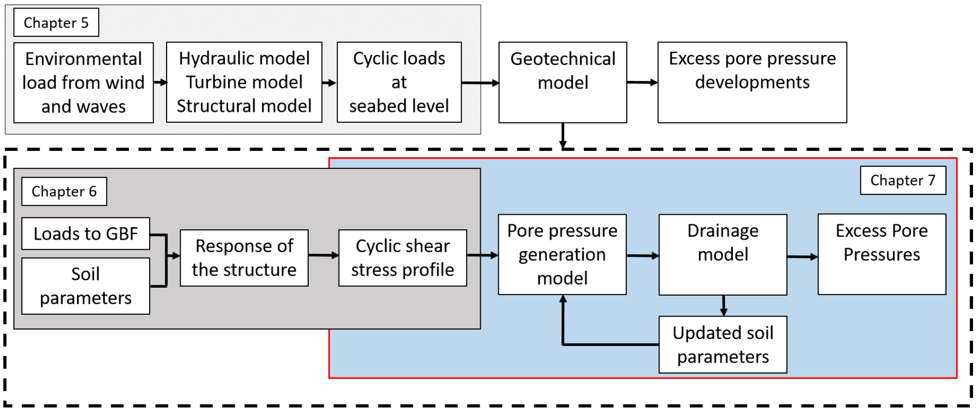

Figure 7.1: *Subdivision of the chapters within the followed approach, with the content of chapter 7 highlighted in blue*

7.2. General approach

The program DCycle was developed to calculate excess pore pressure in horizontal sea beds loaded by wave pressures. Subsequently it was extended to be used for other loads by using a CSSR profile as load input, which is scaled with a time series of loads, specified in a load history input file. The loads need therefore to be specified as a scale factor of the CSSR profile, resulting in a certain load amplitude, and a corresponding period of the each load cycle. The loads can in fact be any cyclic load as long as it can be scaled with the CSSR profile. This is indicated in figure 7.2.

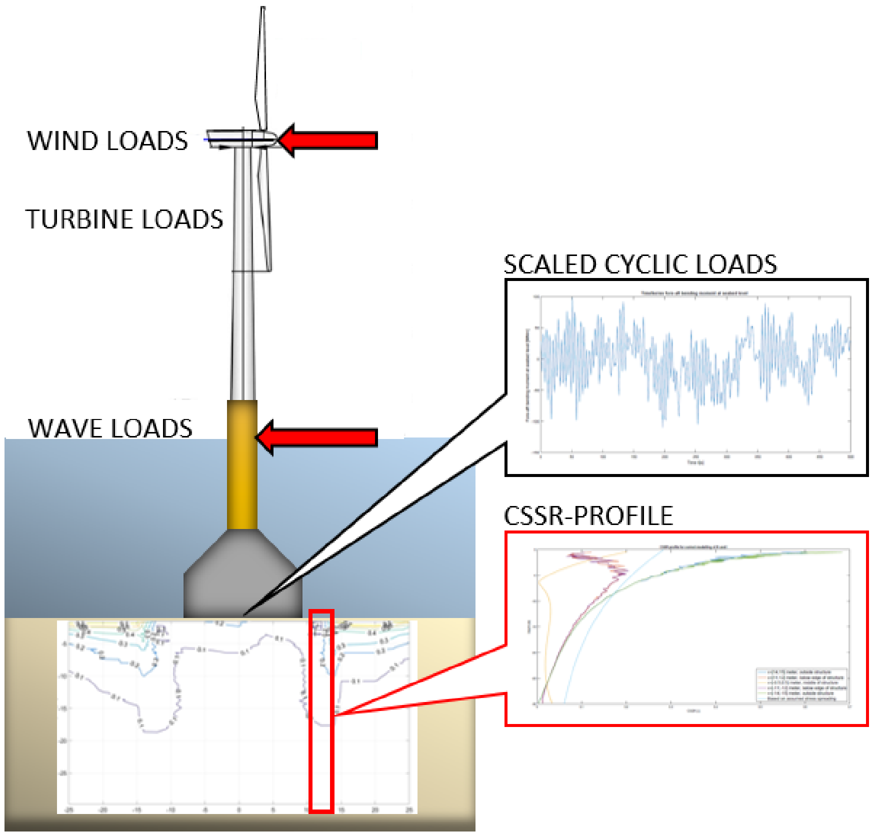

Figure 7.2: *Visualised steps in the calculation procedure related to the GBF under consideration. The CSSR contour plot is shown below the GBF as derived in chapter 6, with the governing profile just outside the base plate that will be used.*

The time series of loads at seabed level (derived in chapter 6), both horizontal forces and bending moments, need to be transformed to individual cycles to be used in DCycle. This is done by finding the zero-crossings (up-crossings) and calculating the amplitude. The amplitude is calculated as the average of the absolute values of maximum and minimum loads in a single period. The periods are calculated as the difference in time between individual zero-crossings. This is visualised in figure 7.3.

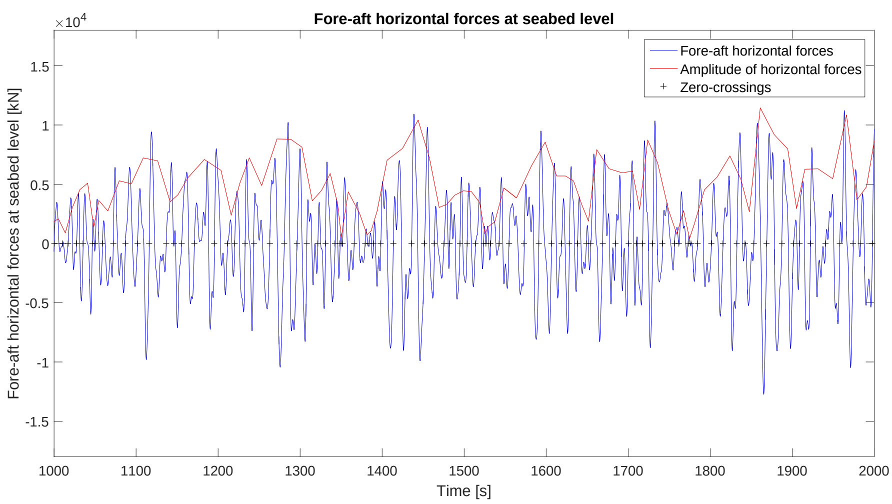

Figure 7.3: *Load cycles are analysed by their period (from zero-crossings) and by the amplitude*

DCycle asks for a load history file with a time series of periods and scaling factor for the amplitude of the cyclic loads. Each amplitude of a load cycle is scaled with the CSSR profile, which can for instance be derived using the maximum amplitude. Each load cycle has a certain period, which is compared to the number of load cycles up to liquefaction for the specified amplitude in the load cycle. This results in a pore pressure generation for each individual load cycle. Dissipation is also taken into account during the time series. For more information reference is made to chapter 3 in which the DCycle model is further specified.

Since every generated time series will be different, due to the random phase model of the loads from chapter 5, every pore pressure time series will be different too. It is therefore necessary to make multiple calculations to obtain a statistically reliable outcome. This represents the random or irregular nature of the loads, which can be taken into account in DCycle by using multiple randomly generated load histories for the same storm. This can be done for each storm in terms of significant wave height H_s, peak period T_p and wind speed U_{10}, based on hourly values for these storm parameters taken from the CoastDat database (Weisse et al. (2005)).

7.3. DCycle input

The basic equation of DCycle were presented in chapter 3, where the pore pressure generation model by Seed and Rahman (1978) has been discussed, as well as the drainage and preshearing that can be taken into account in DCycle. In the current section the input used in the DCycle calculations will be presented. The input consists of:

- Soil data
- CSSR profile
- History file with time series of load amplitudes and periods

7.3.1. Soil data

For the soil data the reference profile from chapter 4 with a relative density of 0.6 is used. A homogeneous soil layer of 30 meters deep is modelled, for which the CSSR profile was derived as well. The parameters are listed again in table 7.1. The coefficient of consolidation is set to $0.1m^2/\text{s}$ and the coefficient of permeability to 1E-04 m/s. The reference stress level for the coefficient of consolidation is 100 kPa. The pore pressure generation coefficients to calculate the number of cycles to liquefaction and subsequently the relative EPP build-up, are a = 0.48 and b = 0.2 and theta = 0.7 (equation 2.3 and 3.4, following Seed and Rahman (1978)). The preshear parameter X was assumed to be 150, following the recommended value for increasing load amplitudes representing a storm build-up (Meijers and Luger (2012)). It should finally be noted that the drainage in DCycle is corrected for the radial drainage below the GBF, as mentioned in chapter 3.4.

bottom [m]	RD [-]	n_{min} [-]	n_{max} [-]	γ_{wet} $[kN/m^3]$	c_v $[m^2/s]$	k [m/s]	a [-]	b [-]	θ [-]
30	0.6	0.33	0.45	20	0.5	1E-04	0.48	0.2	0.7

Table 7.1: *Soil conditions for DCycle, for a homogeneous sand layer of 30 meter deep. No soil improvements such as a gravel bed are implemented.*

The on-bottom stress is required for the calculation of relative the excess pore pressure from the calculated absolute excess pore pressure. The on-bottom stress at seabed level is determined by the effective (submerged) weight of the GBF. This was 13000 tons (table 4.2), and with the on-bottom area of the GBF of 707 m^2, this results in an on-bottom stress of 180 kPa. The first sublayer thickness was set to 0.5 m., which is subsequently used in the mesh generator in DCycle.

CSSR-Profile
The governing CSSR-profile that was found in chapter 6 will be used. This (vertical) profile is located just outside the edge of the GBF, based on horizontal forces and bending moments derived at seabed level at the middle of the circular GBF. The homogeneous sand profile will be loaded with this governing CSSR-profile, while the sand profile for which DCycle will calculate the EPPs is located below the middle of the circular GBF baseplate. The governing profile from just outside the base area of the GBF is applied in the vertical in the centre below the GBF. The resulting EPPs are therefore a conservative estimate.

The used CSSR profile needs to be discretized following the results from chapter 6. The resulting profile is discretized into 7 points (table 7.2).

Depth [m]	CSSR-value [-]
0	0.70
5	0.30
10	0.15
15	0.08
20	0.05
25	0.03
30	0.01

Table 7.2: *CSSR profile used in DCycle*

7.3.2. Loads at seabed level

For the loads at seabed level, the model derived in chapter 5 has been implemented in Matlab and is used to create load spectra of horizontal forces and bending moments at seabed level below the GBF. The spectra are transformed into the time domain and subsequently the amplitude and periods of individual load cycles are calculated. The environmental data of wind and waves used in this study comes from the German CoastDat hindcasted wave and wind data (Weisse et al. (2005), `http://www.coastdat.de/data_all/index.php`. The data ranges from 1958 until 2007 on an hourly basis, on a grid with a resolution of about 0.10° by 0.05°. The data is extracted at latitude 55.166°N and longitude -1.369°E, which is the location of the Blyth Offshore Demonstrator Project, offshore Blyth (Northumberland, UK).

The CSSR profile has been derived for a maximum load combination consisting of both shear forces and bending moments at seabed level, in the fore-aft direction. In the current procedure in DCycle the loads are scaled to this CSSR profile. Therefore two options remain, the first one is to scale the amplitude of the shear forces at seabed level with the maximum amplitude of shear forces. The second option is to scale the amplitude of the bending moment at seabed level with the maximum amplitude of the bending moment. From the CSSR profile in chapter 6 it became clear that the horizontal forces have the largest role in the cyclic shear stress ratio. The influence of bending moments is significantly less in the final ratio (figure 6.10). Therefore it was decided to use the cyclically varying horizontal shear forces to scale with the CSSR profile, since these loads make up the larger part of the CSSR profile. The cyclically varying bending moments play only a minor role in the CSSR profile and would therefore be less suitable to scale with the CSSR profile that is mainly determined by horizontal forces. Furthermore, a static load component is present in both the horizontal shear forces and in the bending moments at seabed level. The static component is also present in the loads used to derive the CSSR profile, and is therefore implicitly scaled together with the amplitude of the loads. This results in a pore pressure development in which the influence of the static part of the loads cannot be found back, although it is taken into account in the CSSR profile and subsequently in each load cycle by scaling this profile.

7.3.3. Storm definition

Using the CoastDat dataset of wind and wave data Weisse et al. (2005), different storm scenario's can be investigated in terms of the EPP developments in the subsoil. This should finally lead to a representative storm history to be taken into account in design conditions. From chapters 2 and 3, it was concluded that the load history of the subsoil largely determines the final EPP build-up. From literature various theoretical storms have been used in the assessment of liquefaction (Bjerrum (1973) and Lee and Focht (1975)). A real storm development might however result in completely different EPPs, and should therefore be taken into account to finally come up with a representative load history.

Before any analysis is possible, a storm threshold level needs to be set above which the load sequence is called "storm". All loads reaching values in horizontal force amplitude at seabed level above this threshold will be taken into account. This threshold will subsequently be called upper threshold. In order to select the starting point of storm, another threshold level needs to be defined, so that all storms that will be investigated start below a threshold level of a horizontal force amplitude. The start of a storm is found by following the horizontal force amplitude at seabed level from the maximum value in a storm back in time until the value does not continuously decrease anymore. If the lowest value that is found is below the threshold for the starting point, this will be used as the starting point. If this is not the case, the storm will be followed further back in time until a lowest value is found below the threshold value. The latter threshold level will be called lower threshold. Taking this into account, various threshold levels for a storm and various threshold levels for a starting point are possible to use. For the storm threshold horizontal force amplitudes of 2500, 3000 and 3500 kN have been used, which subsequently results in respectively 397, 205 and 86 storms, while for the starting value horizontal force amplitudes of 1250 and 1500 kN were used. This is visualised in figure 7.4.

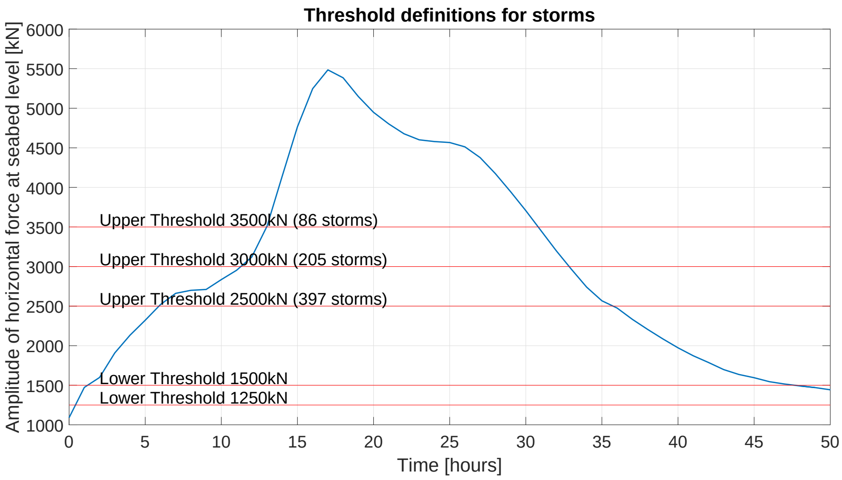

Figure 7.4: *Storm definitions in terms of upper threshold level and lower threshold level, together with the hourly averaged horizontal cyclic load amplitude at seabed for the largest storm from the dataset indicated in blue. This storm is the largest storm from the CoastDat dataset at Blyth, corresponding to a significant wave height of 10.85m., peak period of 17.9s. and wind speed of 23 m/s.*

7.4. Results

7.4.1. Storm input

Using the homogeneous sand deposit, the calculations in DCycle were made for the before mentioned upper and lower threshold levels of storms. The output of the DCycle calculations is given in excess pore pressures over time, at various depths in the 30 meter profile. From the excess pore pressures the relative excess pore pressures are obtained by dividing with the initial vertical effective stresses over depth. From the relative excess pore pressures the maximum values can be found, both in depth and in time. The maximum values are therefore only representing a specific point in the subsoil where this excess pore pressure is reached, and are located below the centre of the GBF.

The starting point of the calculations has been a series of three storms following after each other. Between the storms, a sufficiently long period for complete drainage was found to be present in the dataset. This can be proved with the characteristic drainage period in equation 7.1. The horizontal dissipation length is equal to half the base diameter, 15 meter, while the vertical dissipation length is estimated to be 15 meter as well. The latter estimate is reasonable since the CSSR-profile will generate the largest EPP in the upper 15 meter. Below 15 meter, the CSSR value has already decreased to 0.1 for the ultimate load cycle. For the consolidation coefficient the value of the sand layer of 0.1 m^2/s is used. This finally results in a characteristic drainage time of 2250 seconds (equation 7.1). Since all intermediate periods between the lower threshold levels of storms are larger, the EPPs between storms will be able to fully dissipate. In order to reduce computation time, the intermediate periods between storms are reduced to 2 hours.

$$T_{char} = \frac{h^2}{c_v} = \frac{15^2}{0.1} = 2250s. \tag{7.1}$$

The calculations for multiple storms following each other with the intermediate drainage time in between, showed that the maximum relative excess pore pressure in the selected storms from the CoastDat database is reached in the first storm. The large duration from the start of the storm up to the heaviest loading in the storm (largest amplitude of horizontal shear force at seabed), takes very long (on average over the selected storms 17 hours), resulting in a significant densification before the heaviest loading takes place. Unfavourable combinations of two storms after each other are further investigated in appendix A.

Therefore, the calculations for the various storm have been made for single storms from the dataset only, i.e. no combinations of storms are considered anymore. The starting point is the storm definition following figure 7.4 with a lower threshold of 1250kN and an upper threshold of 3000kN. The results for three single storms with each two generated irregular load time histories are shown in figure 7.5. In the results the variation of excess pore pressure with the cyclic loads can clearly be seen. The loads derived in chapter 5 showed the effect of grouping in load cycles with larger amplitudes due to frequency dispersion. This results in periods with a heavier loading and consequently a peak in excess pore pressure build-up. These peaks in relative EPP can clearly be observed, while in periods with lower loading rates, dissipation leads to lower excess pore pressures, but the cyclic variation of EPP in time remains. Furthermore, it can be seen that each irregular load time history shows a different development and different maximum value in excess pore pressure. Therefore it is already clear that one cannot considerer only a single load time history to obtain a reliable estimate of the maximum excess pore pressure.

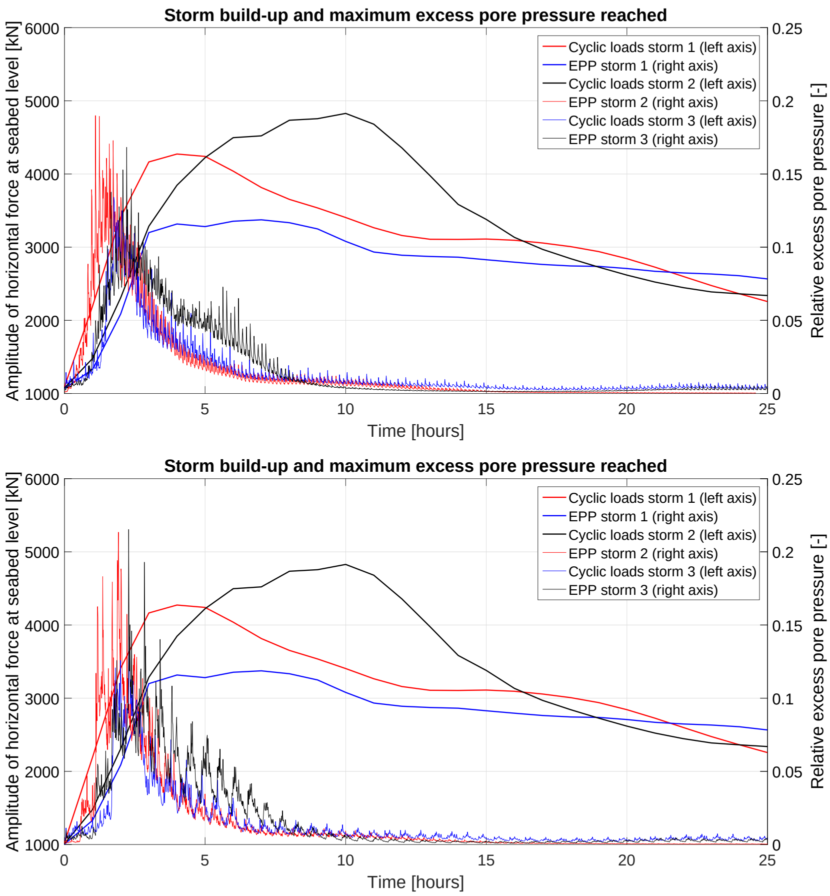

Figure 7.5: *Relative excess pore pressure build-up for the three storms creating the largest relative EPP, at seabed level, for two random generations for each of the storms (top and bottom). The storm developments in amplitude horizontal force at seabed is hourly averaged but has a cyclic nature as well, but this is not plotted since this would result in an unclear plot. The storm developments is plotted at the left axis, and EPP at the right axis.*

Based on the considered storms from the dataset and the used upper and lower thresholds, it was observed that the storms showing the largest maximum values in excess pore pressure, are not the largest storms (i.e. not the storms with the largest horizontal force amplitudes at seabed level) in the dataset. This was further investigated by comparing calculation results for the three storms showing the largest relative EPP (figure 7.6) with the three largest storms from the dataset. Since the irregular nature of the loads results in a distribution of maximum values of relative excess pore pressures, for each of these six storms 200 calculations were made. Based on the results, the values of the 90th percentile were found for both the maximum relative EPP and the duration to reach this value from the start of the storm. The 90th percentile represent the value of relative EPP which is exceeded in only 10% of the 200 calculations for the storm under consideration, while the 90th percentile of time represents the time from the start of the storm till the maximum value in EPP, which is only exceeded by 10% of the storms. The build-up of the storms is presented in figure 7.6, as well as the points in time when the maximum value of relative EPP is reached.

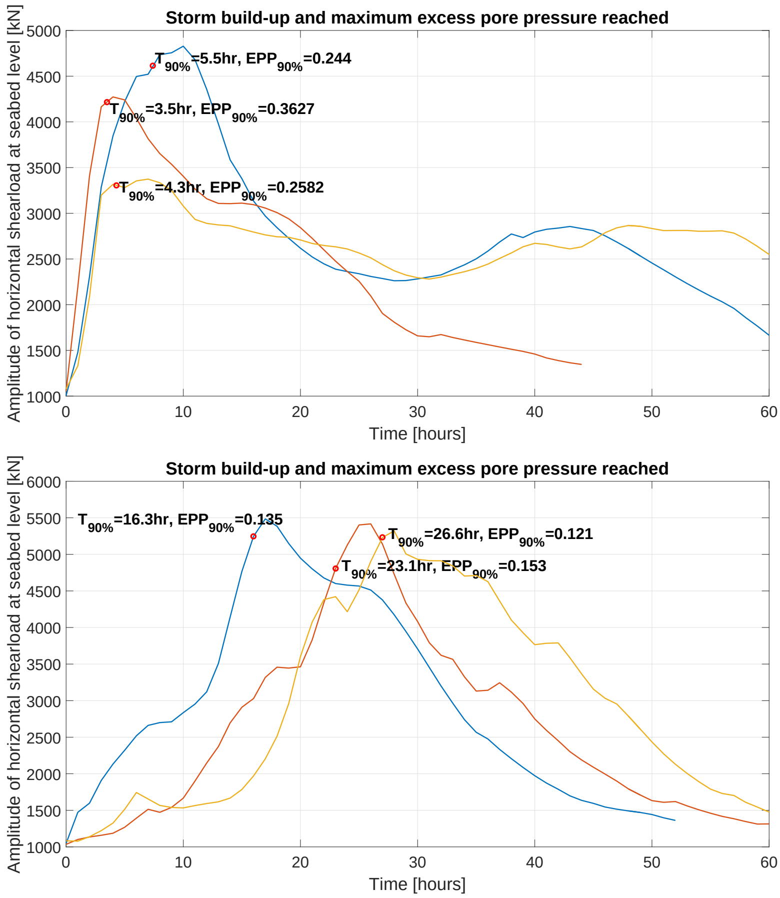

Figure 7.6: *Comparison between storms with the largest maximum relative excess pore pressure (top), and the largest storms in terms of amplitude in shear force at seabed level (bottom). The presented percentiles of duration to maximum relative EPP and maximum relative EPP values, are based on 200 calculations for 200 randomly generated time series for each of the six storms. The storms are based on the definition with a lower threshold level of 1250kN and upper threshold of 3000kN. The maximum values of pore pressures were are found at seabed level.*

The comparison shows that the largest storms from the dataset do not result in the largest relative EPP for the homogeneous sand deposit with a relative density of 60%. It is due to the longer build-up of these storms, at least 17 hours, resulting in significant drainage and strengthening of the soil to further pore pressure generation. The maximum EPP is therefore found in the storm with the fastest build-up. The three storms in the dataset with the fastest build-up, reach the maximum cyclic loads in less than 10 hours, which reduces the drainage time during the fast pore pressure generation in the quick build-up of the storm. The storm with the fastest build-up results in maximum relative EPP values which are below 0.36 in 90% of the cases (200 calculations), and are reached in less than 3.5 hours in 90% of the cases. The other storms, with the 2nd and 3rd fastest build-up respectively, show 90th percentile values of pore pressures and longer durations after which it is reached. It can clearly be observed by comparing both figures that the build-up speed of the storm is the governing parameter for the maximum relative EPP, at least for the considered case with storms from the CoastDat database and homogeneous sand with a relative density of 60% and the corresponding drainage characteristics. The storm with the fastest build-up increases to a significant wave height of 6.5 meter, peak period of 10.2 seconds and wind speed of 23 m/s, while the largest storm in the dataset reaches a significant wave height of 10.85 meter, a peak period of 17.9 seconds and a wind speed of 23 m/s.

The previously shown results of maximum excess pore pressures were all reached at seabed level, at the top of the soil deposit. The profiles of relative and absolute excess pore pressure as a function of depth are shown in figure 7.10. The largest generation of EPP takes place in the upper layers, due to the large CSSR-ratios at the top. Drainage takes place in radial direction below the GBF, and is due to the homogeneous profile initially evenly distributed over depth. Due to stiffness degradation, the consolidation coefficient decreases, reducing the drainage capacity, mainly of the upper soil layers.

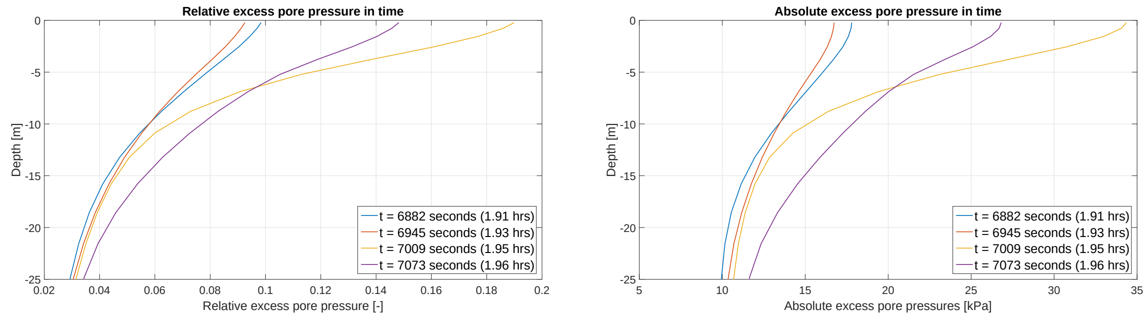

Figure 7.7: *Relative and absolute excess pore pressure below centre of GBF, for the time steps around the maximum relative excess pore pressure. Plotted for the storm with the 90% value of maximum excess pore pressure from figure 7.6.*

7.4.2. Threshold level

Comparing the storms producing the largest excess pore pressures with the largest storms from the dataset (figure 7.6), it is observed that the largest storms do not produce the largest excess pore pressures due to the far longer duration of build-up in the largest storms. In this longer build-up time, the soil has apparently densified to such an extent that even in the peak load of the largest storms the excess pore pressure remains lower. The storms producing the largest excess pore pressure show a faster build-up, which can best be described by the speed of storm build-up in kN cyclic load amplitude per hour (kN/hr). Considering load conditions only, this seems to be the most important parameter that is governing the maximum excess pore pressure in a storm. A faster build-up speed produces a larger maximum relative excess pore pressure (figure 7.8).

The definition of a storm is however still based on an artificial starting point in time, corresponding with a load amplitude at one of the threshold levels (figure 7.4). Since the build-up of the storms is very important in the final excess pore pressure that is reached, the sensitivity to the storm definition has been investigated. The maxima of relative excess pore pressures have been calculated for four combinations of upper and lower threshold levels, and have been averaged over five calculations for each of the storms and are compared with the build-up speed in kN/hour. This in total resulted in sets of 397*5, 205*5, 205*5 and 86*5 storms, in total 4465 calculations each of around 5 minutes for the homogeneous sand with relative density of 60%.

The maximum values of relative EPP are averaged over five calculations for each storm. It is right now not the purpose to obtain a distribution of relative EPPs, but to see whether or not the storm producing the largest relative EPP depends on the threshold. Since it is not achievable to make a set of for instance 100 irregular load histories for each storm and for each threshold level, only five calculations have been made for each of the storms. The maximum relative excess pore pressure values are plotted versus the build-up speed of the corresponding storm. The build-up speed is calculated from the maximum load amplitude in the storm and the duration till this maximum value from the starting point (lower threshold level). The results are presented in figure 7.8 for the four combinations of threshold levels. Each of the definitions show the same trend: the fastest build-up results in the largest excess pore pressures. Furthermore it was found that for all combinations of threshold levels the storm creating the largest (averaged) excess pore pressures is the same storm. This storm was present in all combinations of thresholds (resulting in 397, 205 and 86 storms). The storm producing the largest relative excess pore pressure is of further interest to investigate the effect of the irregular nature of the loads. For further investigations the lower threshold of 1250kN and the upper threshold of 2500kN is used.

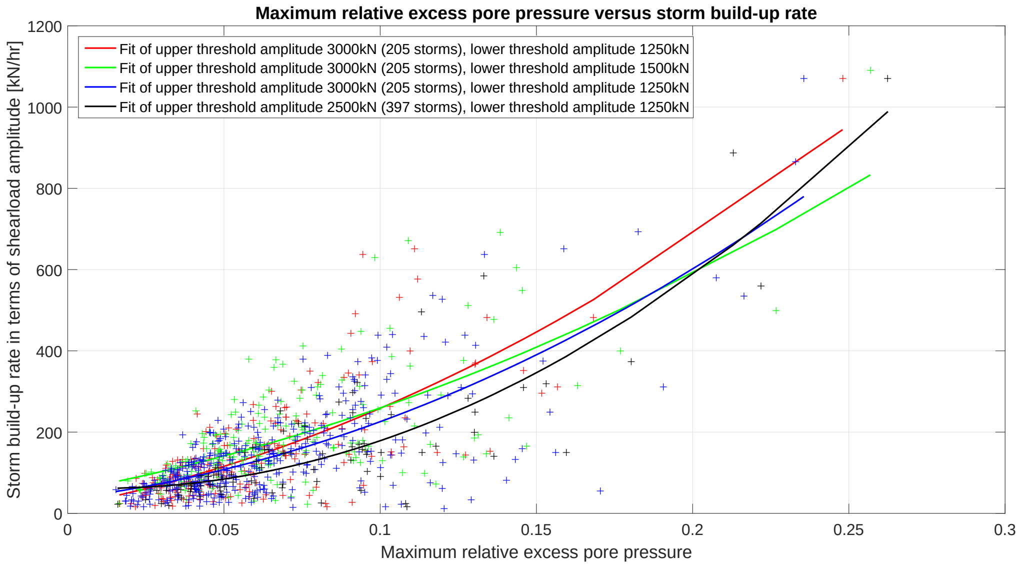

Figure 7.8: *Storm build-up speed [kN/hr] versus maximum relative excess pore pressure reached, presented for a lower threshold level of 1250kN and upper threshold of 3000kN. The pore pressures are all at seabed level, below the centre of the GBF. Calculation results are averaged for 5 generated irregular load time histories for each storm and each of the threshold levels.*

7.4.3. Irregular load histories

In addition to the real storm build-up, the effect of the irregular load histories at seabed level was taken into account by the application of a random-phase model in the load analysis in chapter 5. 200 irregular load histories were therefore generated for the storm producing the largest relative excess pore pressure. The results are used to fit probability density functions (PDF) to show the distribution and compare results from multiple storms. The probability distributions are obtained using a best fit method, using multiple distributions and a Bayesian information criterion to select the best fit. The distributions are not used further; therefore no emphasis is laid on which distribution should be used, neither on the parameters used.

The main focus has been on the maximum value of the relative excess pore pressure that is reached in a storm. The excess pore pressure will result in a significant reduction of strength of the subsoil, which should be taken into account in the GBF design to assess the stability during cyclic loading. Based on the observed result that the maximum EPP is already reached before the peak in load amplitude of the storm, which would imply that the stability of the GBF may be determined with a lower load amplitude at the time of reaching the maximum excess pore pressure. The load amplitude at the time of maximum EPP is lower than the maximum load amplitude in the storm. At the peak load amplitude in the storm, the excess pore pressure has reduced already due to drainage, which is beneficial for the strength of the soil in the extreme load cycle. However, at that moment the load amplitude has already increased.

The results of 200 calculations for the storm with the fastest build-up are presented in figures 7.9 and 7.10. The maximum values of relative excess pore pressures are presented in histograms. A best fit is obtained on the raw data, and the 90th percentile is indicated in each of the figures. The probability density curves are presented for the pore pressures at the moments of maximum relative excess pore pressure and at the moment of the maximum horizontal force amplitude in the storm. For these two moments, also the distributions of horizontal force amplitudes at seabed level are presented. From the results the maximum pore pressure is in 90% of the cases lower than 0.36, with a load amplitude lower than 6936kN in 90% of the cases. The maximum relative pore pressure will result in a significant decrease of soil strength, while the load amplitude remains relatively low when the maximum EPP is reached. However, at peak of the storm, the 90th percentile of the load amplitude increases to a value of 13214kN, but at that time the pore pressure remains below 0.17 in 90% of the cases, as a result of drainage. The load amplitude is significantly higher, and the excess pore pressure significantly lower. Based on the 200 load time histories, it is found that in the storm with the fastest build-up the maximum relative EPP is on average (50% of the cases) reached about one hour before the maximum cyclic load amplitude in the storm.

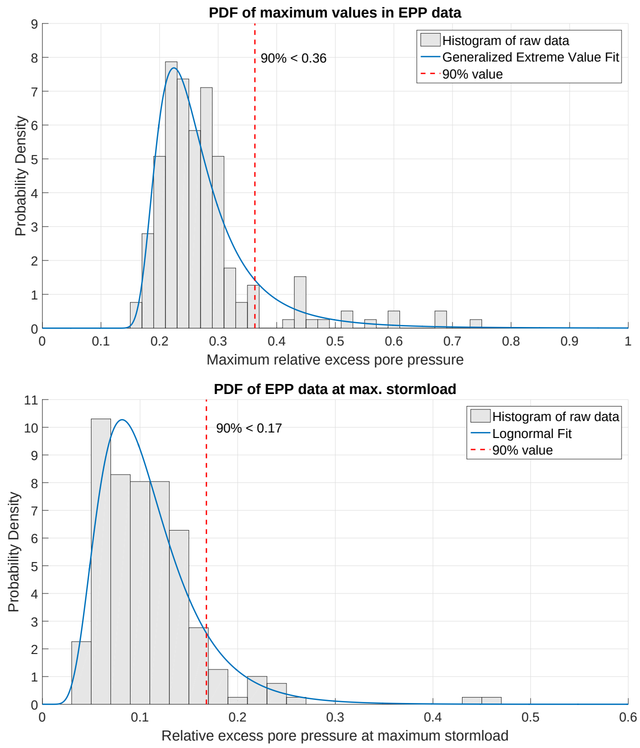

Figure 7.9: *90th percentile and best fit to data of maximum values of relative EPP (top) and to data of relative EPP at moment of maximum storm load (bottom). Both for a set of 200 irregular load time histories and homogeneous sand with relative density of 60%, for the storm with the fastest build-up*

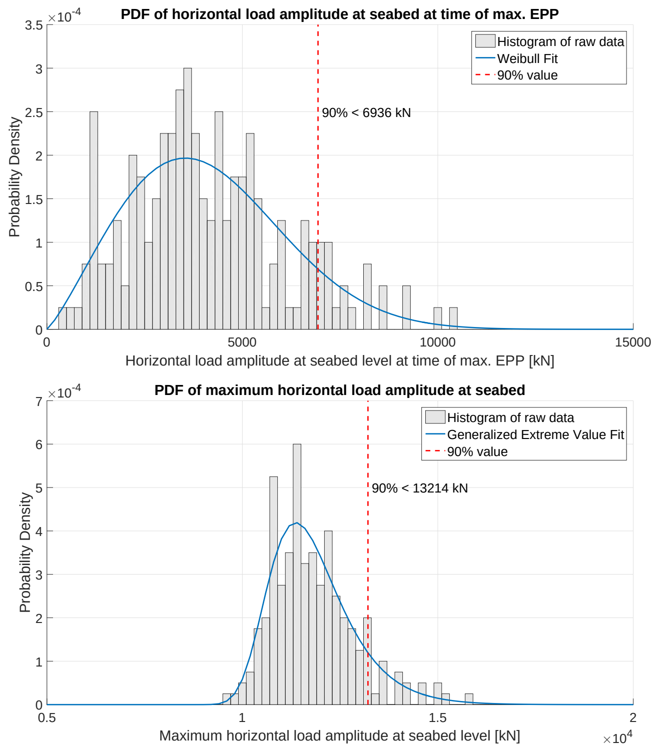

Figure 7.10: *90th percentile and best fit to data of horizontal force amplitudes at time of maximum relative EPP (top) and at the time of the maximum load in the storm (bottom). Both for a set of 200 irregular load time histories, for the storm with the fastest build-up*

It can furthermore be observed that a large spread in pore pressures is found due to the irregular load time histories. This shows that it is not possible to obtain a reliable estimate of the maximum pore pressure below the GBF using only a single load time history. For the 2nd and 3rd storm with the largest pore pressure generation from figure 7.8 a similar set of calculations was made with irregular load time histories corresponding to the storm. The results are visualised in figure 7.11. Only the obtained fits are presented, showing that for these storms the pore pressures also overlay. The 90% values however still show the same tendency in which the faster build-up results in the highest 90th percentile. The storm with the fastest build-up (called storm 1 in figure 7.8) still shows a significant increase compared to the two other storms (called storm 2 and 3 in the figure); 0.36 versus 0.26 and 0.24 respectively), due to its exceptional fast build-up with less time for drainage of pore pressures. The spread in pore pressures furthermore shows a larger spread for storm 1, which might be due to the larger increase of pore pressure when the pore pressure has already obtained a value of around 50%. This is implemented in the pore pressure generation model of Seed & Rahman, and seems to increase the spread in pore pressure in combination with the irregular load time histories that have been used. A group of load cycles with a relatively large amplitude results in a fast increase in pore pressure if significant pore pressure has already built up. Another clarification of the spread comes from the continuously changing relative density during drainage of EPP, increasing the strength for further build-up. Therefore a group of large load cycles at the start of the cyclic loading results in a fast build-up, while some large load cycles at the end produce less due to the already intensified soil. The largest excess pore pressures are therefore expected to result from a group of large load amplitudes at the start of the storm.

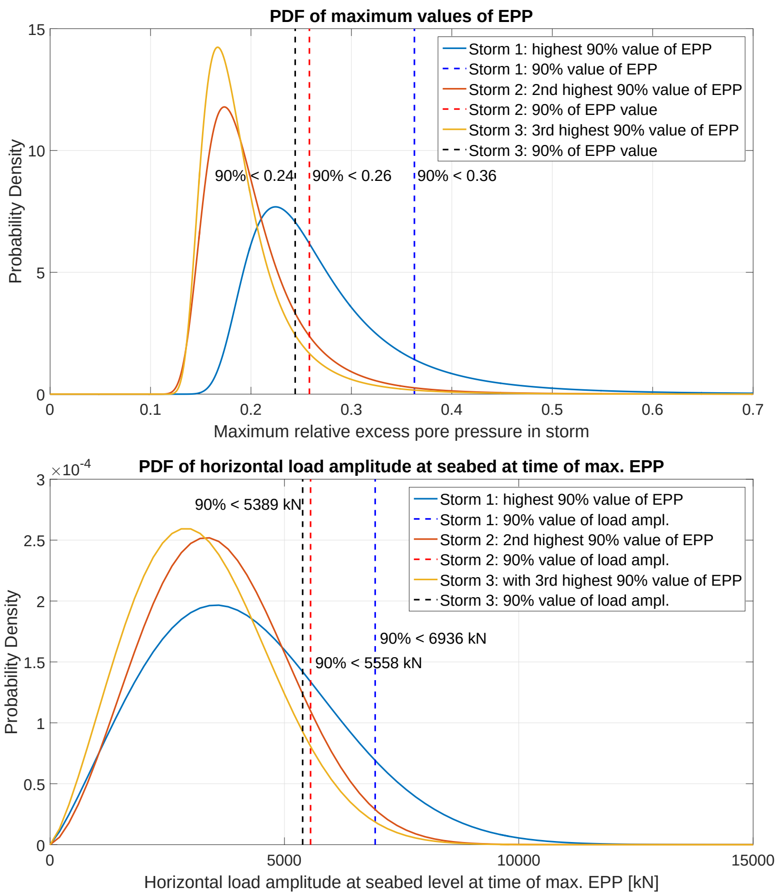

Figure 7.11: *90th percentile and best fit to data of maximum relative EPP values from 3 storms building up fastest (top) and horizontal force amplitudes at the time of the max. EPP in the storm (bottom). All for a set of 200 irregular load time histories.*

Based on the used dataset of storm build-up and the derived loads, the observations would imply that the stability check under cyclic loading, with the maximum excess pore pressure generated in the subsoil, can be less conservative by taking the actual cyclic load amplitude at that time into account. This would result in a less conservative design, since the GBF does not have to withstand the extreme load amplitude at the moment of reaching the maximum EPP.

This holds at least for the currently considered storm histories, cyclic loads and soil conditions. The maximum cyclic load at the storm peak has to be considered with a reduced pore pressure due to drainage. Which of the cases is governing the stability, should be determined in a constitutive model. It cannot beforehand be said which case is governing, or whether any other combination of excess pore pressure and cyclic load amplitude in between both points is governing.

Before any design can be based on a stability check with a reduced load amplitude at the time of the maximum excess pore pressure, a sound validation of the observed behaviour is required. The real load history of a storm, with the corresponding build-up speed, should for instance be used in an element test to see whether the maximum excess pore pressure is obtained before the cyclic load reaches its maximum. This also asks for continuous drainage, or regular intermediate drainage steps. This is discussed in section 8.3.

7.5. Sensitivity study

After the significant influence of drainage and densification in the build-up of a storm, it is interesting to investigate whether this behaviour is also observed is less permeable sands. Furthermore, a large influence and uncertainty is related to the preshear parameter X. For other parameters, such as relative density, the results can be predicted quite well based on the formulations in DCycle. These are therefore not further investigated to limit the number of calculations. The starting point is again homogeneous sand with a relative density of 60%, which will be investigated for various preshear values, for a gravel bed and for a silt layer.

7.5.1. Preshear value

The previously used value for the preshear parameter of 150 was based on results of element test with increasing load amplitude during the test. This represents the build-up of a storm. However, depending on the structure of the soil and the previous loading, other values might be more appropriate. The preshear value is directly related to the number of cycles to full liquefaction via the change in porosity after drainage of excess pore pressure (equation 2.5), and is therefore expected to have a significant influence on the results. Based on the previous calculations the drainage in the build-up of a storm was found to be highly relevant, and therefore the effect of preshearing in these partially drained conditions is expected to be highly relevant too. Two different values have been used, 50 and 500 respectively, and will be compared with the original value of 150. The soil profile used as input is presented again in table 7.3.

bottom [m]	RD [-]	n_{min} [-]	n_{max} [-]	γ_{wet} $[kN/m^3]$	c_v $[m^2/s]$	k [m/s]	a [-]	b [-]	θ [-]	preshear value [-]
30	0.6	0.33	0.45	20	0.5	1E-04	0.48	0.2	0.7	50
30	0.6	0.33	0.45	20	0.5	1E-04	0.48	0.2	0.7	500

Table 7.3: *2 separate soil profiles have been investigated, both a homogeneous sand layer of 30 meter deep with two preshear values*

The question that first needs to be answered is whether the storm with the fastest build-up is also the one with the highest excess pore pressures for different values of preshear parameter X. It was previously mentioned that the effect of preshearing on the maximum excess pore pressure in a combination of storms is hard to determine beforehand. A small storm results in less pore pressure build-up with a large preshear value, but may therefore reach a higher excess pore pressure in a second storm due to less densification after drainage of the lower pore pressure from the first storm. The reverse trend might be expected for a low value of preshearing. This might also be the case in the build-up of a storm: a storm with a very slow build-up might result in very little densification for a large preshear value, but when the peak of the storm with large load amplitudes arrives, it might then be possible to reach a higher excess pore pressure. For lower preshear values the storm with the fastest build-up is expected to result in the largest excess pore pressures. To investigate which storm is governing, again the dataset of storms with a lower threshold of 1250kN and upper threshold of 3000kN is used to find this storm. Since the irregular load time histories result in a distribution of excess pore pressures, five calculations have been made again for each storm and the maxima have been averaged. Although five calculations are not enough for a reasonable estimate of the spread in pore pressures, it is assumed to be large enough to find the storm producing the largest EPPs on average, and to limit the calculation time as well.

The results show the same trend for both preshear values. A faster build-up shows in general a larger excess pore pressure. It is however observed that also storms with a far lower build-up may result in high excess pore pressures as well. Part of this behaviour may be explained from the complex effect of preshearing, while another part may be attributed to the irregular load time histories, resulting in a large spread of pore pressures for each of the storms. The probability distributions will only be made for the storm with the fastest build-up, since it is not possible to make a large number of calculations for each of the storm.

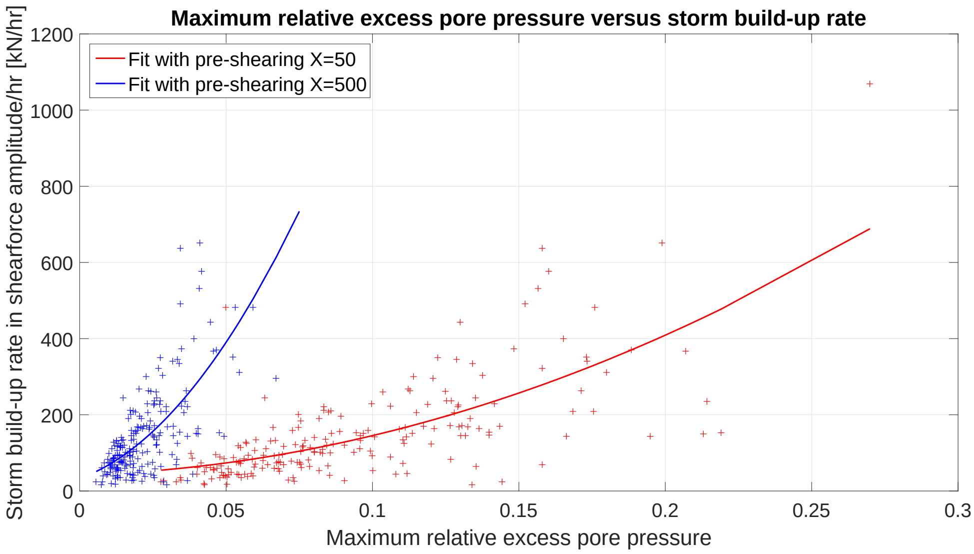

Figure 7.12: *Storm build-up speed versus maximum relative EPP reached, for 205 storms with a lower threshold of 1250kN and upper threshold of 3000kN, averaged over 5 irregular load time series, for preshear values of 50 and 500. The results for a preshear value of 150 can be found in figure 7.8*

For the storm with the fastest build-up, the distributions of relative excess pore pressures are presented in figures 7.13 for a set of 200 calculations for each of the preshear values. For a lower preshear value of 50, the maximum values of relative excess pore pressures significantly increase. The increase in the 90th percentile value is 40% for a decrease in preshear value from 150 to 50. This shows that the effect of preshearing is reducing the pore pressure build-up. This is due to the fact that a large amount of pore pressures already drain in the build-up of a storm, and the soil is therefore able to re-arrange and change its structure. This leads to an increase in liquefaction resistance.

In figure 7.14 the results are compared with the previous calculations for X=150, which was also obtained with a set of 200 calculations. The largest pore pressures are obtained with the lowest preshear value. Furthermore, the spread in pore pressures gets larger for larger pore pressures, which might due to the pore pressure generation model of Seed & Rahman, where the pore pressure increases faster after reaching relative excess pore pressures above 50%. For higher pore pressures therefore a group of larger load cycles results in a faster increase in pore pressures compared to lower pore pressures. It can furthermore be observed that the pore pressures have already dissipated significantly at the peak in storm load compared to the maximum values of pore pressures that are reached.

It was furthermore investigated whether the maximum pore pressures are reached before the peak in load amplitude of the storm, which was already observed for the preshear value of 150 in the previous calculations. In that case only 2% of the 200 calculations reached the maximum value after the peak load in the storm. For the preshear value of 500 also only 2% of the cases reaches its maximum after the peak of the storm, while for the preshear value of 50 this is 15%. This shows that for a lower preshear value the maximum pore pressure is often reached after a longer duration compared to larger preshear values. These larger pore pressures can be reached due to less increase in strength against liquefaction in the build-up of the storm, and these higher pore pressures are obviously reached after a longer duration, resulting in 15% of the irregular load time histories reaching its maximum after the peak in storm loading.

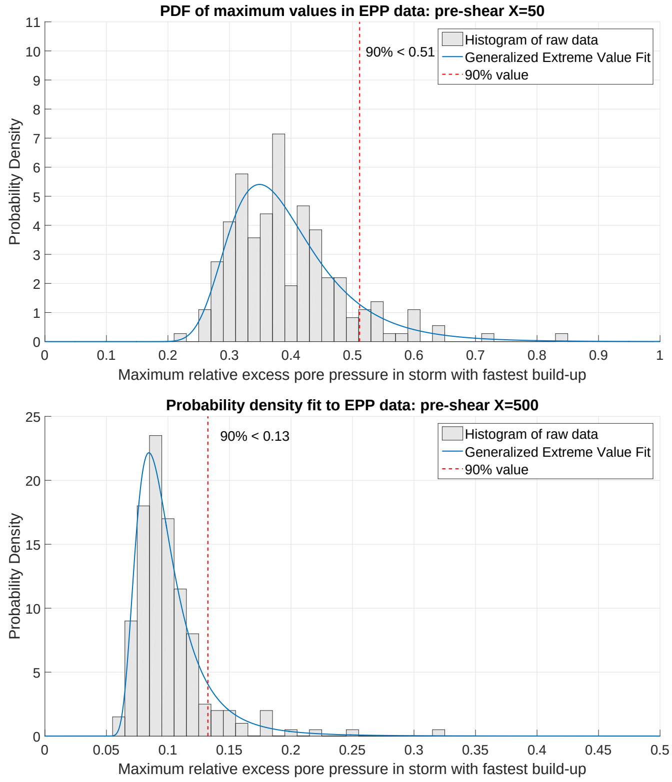

Figure 7.13: *Histogram, 90th percentile and best fit to data of maximum relative EPP values for 200 calculations of irregular load time histories, for preshear value X=50 (top) and preshear value X=500 (bottom)*

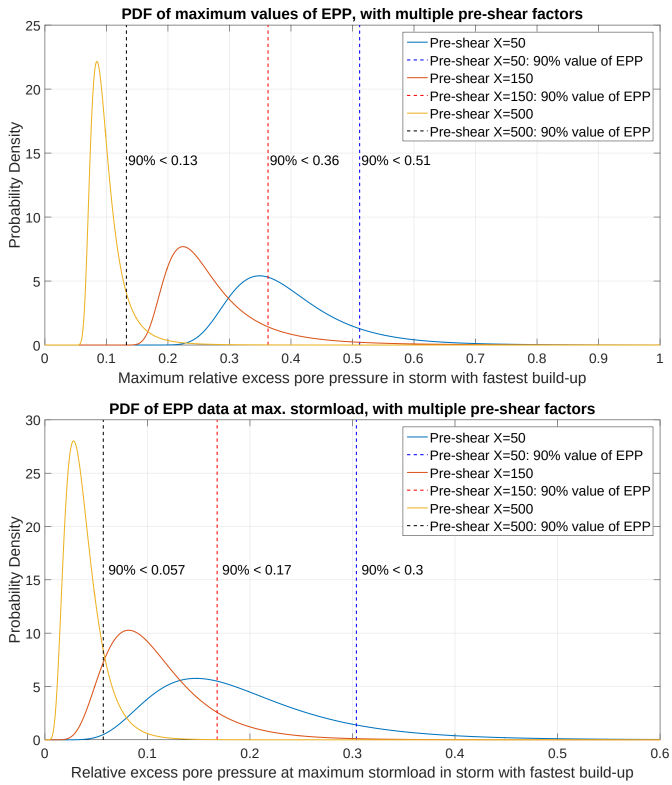

Figure 7.14: *90th percentile and best fit to data of maximum values of relative EPP for preshear value X=50 (top) and X=500 (bottom). Both for a set of 200 irregular load time histories*

7.5.2. Gravel bed

In practice a gravel bed will often be constructed to create a well draining layer below the GBF. Furthermore this will be used to create a better levelled bed and it can be used as a filter layer between the scour protection and sand bed. The gravel is modelled in DCycle with a higher consolidation coefficient and a higher permeability to represent the higher drainage capacity, indicated in table 7.4. In total 100 load time histories were generated and the excess pore pressure response was calculated.

bottom [m]	RD [-]	n_{min} [-]	n_{max} [-]	γ_{wet} $[kN/m^3]$	c_v $[m^2/s]$	k [m/s]	a [-]	b [-]	θ [-]
0.5	0.7	0.33	0.45	20	3.0	0.1	0.48	0.2	0.7
30	0.6	0.33	0.45	20	0.1	1E-04	0.48	0.2	0.7

Table 7.4: *Soil conditions for DCycle, a homogeneous sand layer with a gravel bed of 0.5 meter on top*

For a set of 100 irregular load time histories the results are shown in figure 7.15. The pore pressures clearly reduce significantly due to the gravel bed, the 90th percentile is found at a relative excess pore pressure of 0.078. This was also expected, since the large excess pore pressures were found in the top layers due to the largest CSSR-ratios, a well draining layer at the top will be able to reduce the pore pressures in an efficient manner. The radial drainage capacity below the GBF is improved by the gravel bed, and in combination with vertical dissipation results in a large reduction of pore pressures. In practical cases the gravel bed will not be placed to reduce the EPP only, a more important reason might be to replace the top few meter of loose soil deposit and replace it with a well draining layer of gravel. It can finally be used to create a properly flattened seabed for placement of the GBF.

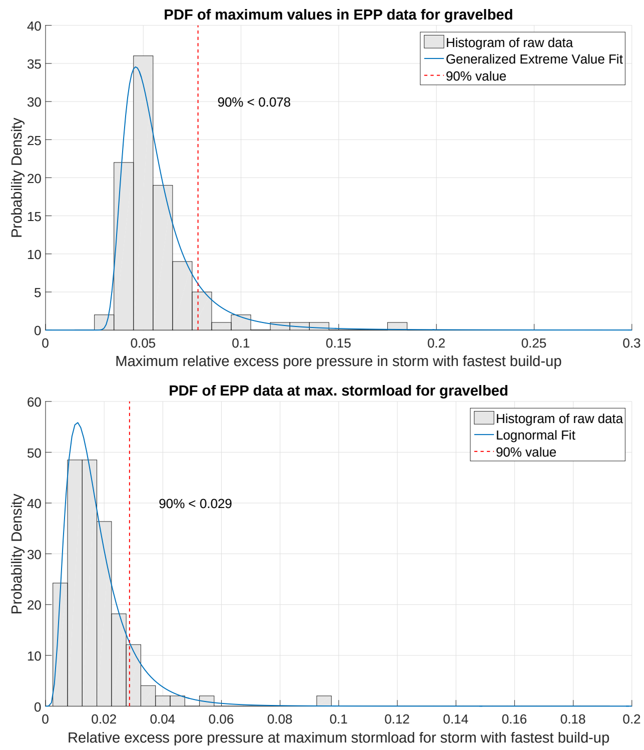

Figure 7.15: *90th percentile and best fit to data of maximum values of relative EPP (top) and to data of relative EPP at moment of maximum storm load (bottom). Both for a set of 100 irregular load time histories, for a gravel bed*

It can furthermore be observed that the spread in resulting maxima is less, which might be due to the fact that the lower pressures do not increase that much as long as the number of cycles remains far from the number of cycles for full liquefaction. This behaviour is implemented in the pore pressure generation model of Seed & Rahman, and is shown in the results from DCycle as well. The results as a function of depth also show that the largest EPP are not found at seabed level (figure 7.16), as such was the case for the sand deposit, but at a larger depth around 4 meter. This holds for both the absolute and relative excess pore pressures. The gravel bed clearly drains the upper few meter, but at larger depths the pore pressures are building up again. It is finally noted that for the gravel bed only 2% of the considered 100 irregular load time histories reach its maximum after the maximum storm load.

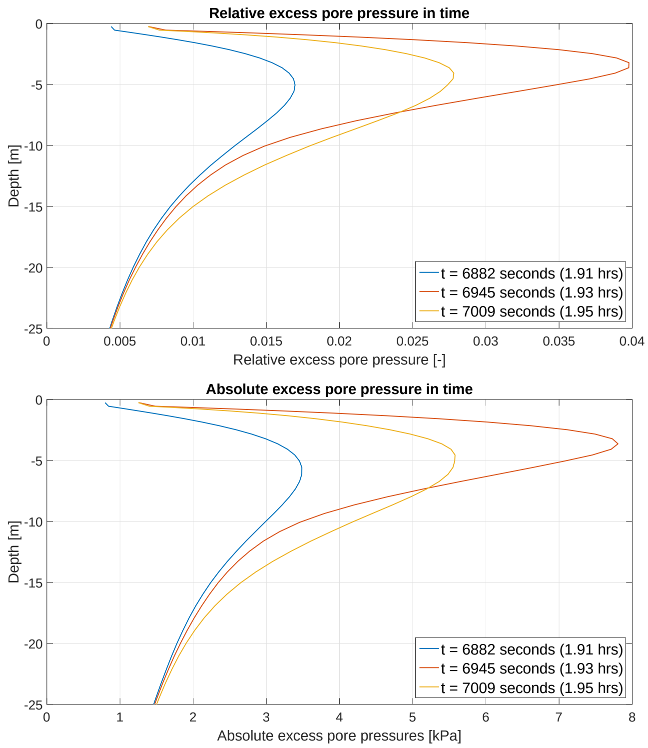

Figure 7.16: *Relative (top) and absolute (bottom) excess pore pressure in a vertical below centre of GBF, for the time steps around the maximum relative excess pore pressure.*

7.5.3. Silt layer

An interesting question is whether the obtained results also hold for sands with lower permeabilities, like silty sands. For well draining, clean sands with homogeneous properties, it was found that due to dissipation of pore pressures the maximum values are in 98% of the cases already reached before the peak in storm load. This is beneficial, since these maximum pore pressures are reached during lower cyclic load amplitudes, before the peak in the storm. This might be different for sands with lower drainage capacity, leading to different conclusions. The silt profile that has been used is presented in table 7.5, consists of a top layer of sand of 6 meter, a silt layer of 4 meter till a depth of 10 meter, and sand again up to 30 meter. The silt has a lower permeability, $10E-5$ and a lower consolidation coefficient of 0.01.

bottom [m]	RD [-]	n_{min} [-]	n_{max} [-]	γ_{wet} $[kN/m^3]$	c_v $[m^2/s]$	k [m/s]	a [-]	b [-]	θ [-]
6	0.6	0.33	0.45	20	0.1	1E-04	0.48	0.2	0.7
10	0.3	0.33	0.45	20	0.01	1E-05	0.48	0.2	0.7
30	0.6	0.33	0.45	20	0.1	1E-04	0.48	0.2	0.7

Table 7.5: *Soil conditions for DCycle, a homogeneous sand layer with an intermediate 4 meter thick silt layer*

The results show that the relative excess pore pressures are significantly larger compared to the homogeneous sand layer (figure 7.17). The 90% value has increased to 0.62, while it was 0.36 for homogeneous sand, an increase of 70%. The lower drainage capacity of the silt layer therefore largely influences the maximum values of EPP. It was expected that the maximum value would be reached later in time, and possibly even after the maximum storm load. This however is not the case: for all 100 irregular load time histories, the maximum value in EPP was on average reached after 2.95 hours, while the peak in the storm is reached after 4 hours.

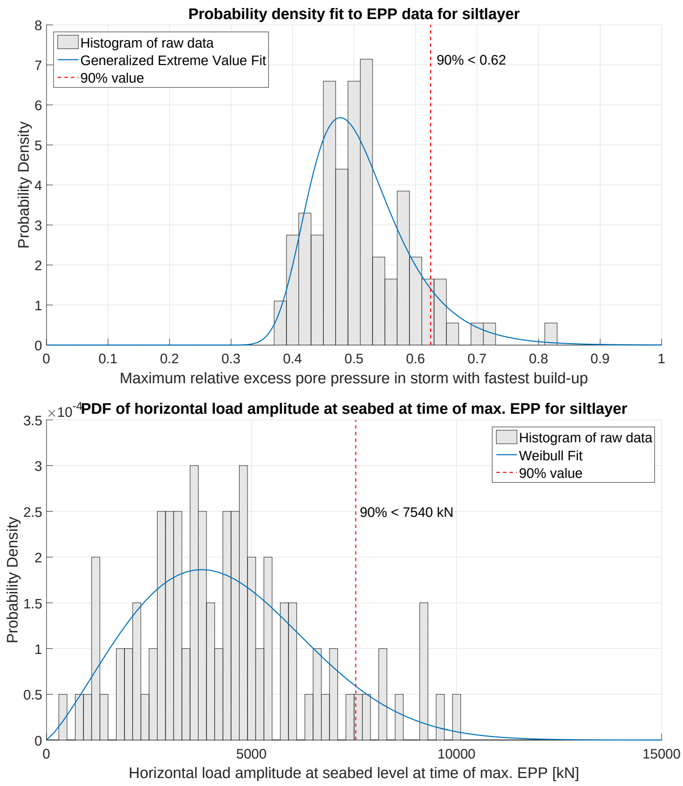

Figure 7.17: *90th percentile and best fit to data of maximum values of relative EPP (top) and to data of horizontal force amplitudes at time of max. relative EPP (bottom). Both for a set of 100 calculations for a soil profile with silt layer*

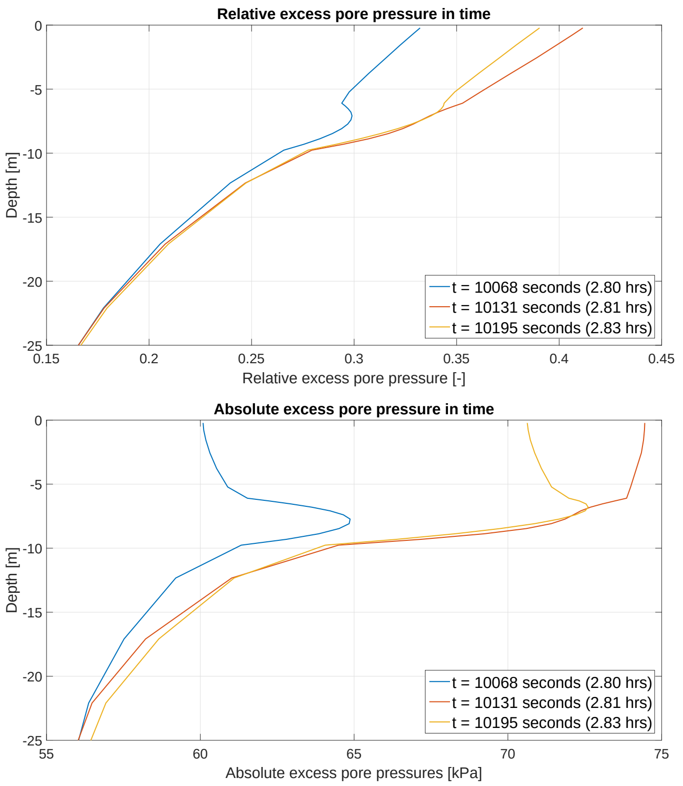

Figure 7.18: *Relative (top) and absolute (bottom) excess pore pressure in a vertical below centre of GBF, for the time steps around the maximum relative excess pore pressure.*

None of the generated time series resulted in a maximum in EPP after the peak in the storm. This is also visualised in the distribution of horizontal force amplitudes at the moment of reaching the maximum relative EPP, right figure of figure 7.17. The 90% value is significantly lower at the time of maximum value in relative EPP, 7540kN, compared to the 90% in load amplitude at the storm peak, figure 7.10, showing 13214kN.

In a profile over depth, it can be observed that the largest relative EPPs are still obtained at seabed level at the closed boundary below the GBF (figure 7.18). The absolute values show an increase at the level of the silt layer, which is due to the lower drainage capacity. The vertical profile is presented for a single load time history, but varies far less compared to the maximum values in EPP. Only the maximum value in the vertical will be different, but the distribution over depth is approximately the same. The profile does not differ significantly compared to the sand layer, as presented in figure 7.7. Only around the silt layer a slight increase in pore pressure can be observed just before the maximum value is reached, which is due to the lower drainage capacity of the silt layer. Below the silt layer no significant pore pressure build-up is seen, although the cyclic shear stress ratios have decreased below 0.15 below the silt layer, the silt layer is still able to drain the generated pore pressure towards the top.

7.6. Validation of the method

An important question after considering the various results of excess pore pressures is whether the followed simplified method can be validated. The largest uncertainty is expected in the scaling of the cyclic shear stress profile with the amplitude of each individual load cycle. Due to the changing soil stiffness during pore pressure build-up, the cyclic shear stress profile will continuously change. In the currently followed approach, the cyclic shear stress profile is kept constant during the whole storm duration, apart from a scaling factor in each load cycle. It is desirable to know the influence of a changing shear stress profile on the obtained (maximum) excess pore pressures.

Validation is often done against measurements from the field or against experimental results. The available information from measurements is however often incomplete, for instance from the measurements of excess pore pressures below the Ekofisk tank: the measured excess pore pressures are available but the storm characteristics are missing (only the maximum wave height is presented). The Ekofisk tank is on the other hand often used in model comparisons to compare developed models with predictions of excess pore pressures in the original design, for instance discussed in Rahman and Seed (1977), Lee and Focht (1975), Bjerrum (1973) and Clausen et al. (1975). Therefore these results will be used in this section to compare with the results from the followed approach used in this thesis.

The starting points are the Ekofisk tank characteristics and soil properties in figure 7.19. The tank with a radius of 46.5 meter is placed on a sand bed of 26 meter on top of a impermeable clay layer. The sand properties are a radial and vertical permeability of $1E-5m/s$, and a compressibility modulus of $1.73E-5$ [1/kPa], which results with a saturated volumetric weight of $17.3kN/m^3$ in a consolidation coefficient of $3.3E-2$ m/s. The relative density is 85%. In the available model results that will be discussed below, the clay layer is not modelled, and the properties will therefore not be discussed. The design storm input used for the Ekofisk tank, is presented in figure 7.19 as well. The design storm was at that time for sake of convenience constructed back to a equivalent storm which is assumed to have the same excess pore pressure development (figure 7.19 right, and table 7.6). The equivalent storm is also indicated, and was obtained using the procedure described by Seed and Rahman (1978) and already presented in chapter 3.

	wave height [m]	wave period [s]	nr. of cycles [-]
wave group 1	6.1	2.7	1328
wave group 2	12.2	4.7	148
wave group 3	18.3	13.6	98
wave group 4	12.2	4.7	148
wave group 5	6.1	2.7	1328

Table 7.6: *Equivalent storm characteristics*

The loads on the Ekofisk tank were investigated for various wave heights by Rahman (Rahman and Seed (1977)). For a wave height of 12.5 meter they determined the bending moments and horizontal forces at

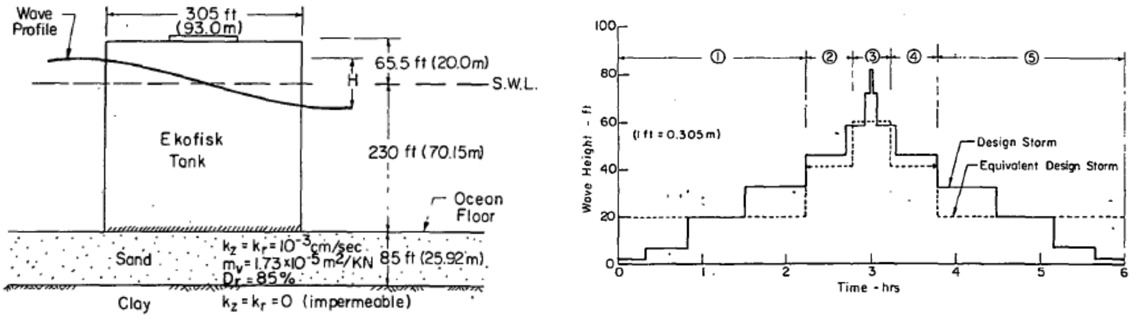

Figure 7.19: *Ekofisk tank with main characteristics (left) and design storm and equivalent storm (right, Rahman and Seed (1977))*

seabed level, and determined the cyclic shear stress ratios below and around the tank. The obtained values will be used in this analysis as well. The dead weight of the tank amounted 1900MN, with a radius of 46.5 meter resulting in an on-bottom stress of around 280 kPa.

Rahman used the pore pressure generation model from Seed and Rahman (1978) and added vertical and radial dissipation. The number of cycles to liquefaction was determined based on the actual results form cyclic simple shear tests performed on sand from the Ekofisk location. For relative densities of 77% and 85% the results of cyclic shear stress ratios are presented, but the actual values used in the pore pressure generation model are not presented. It is however indicated that the cyclic simple shear tests were pre-loaded by four smaller storms, and were allowed to drain in between. This indicates that some effect of preshearing is present in the obtained results, and consequently also in the used values for the pore pressure generation model.

Taiebat (Taiebat (1999)) presented a semi-analytical 3D finite element method for liquefaction analysis of marine structures. The model is based on an elastic soil skeleton and the pore pressure generation model of Seed and Rahman (1978) is implemented in the created mesh, corresponding to the hybrid type of models as discussed in chapter 3. Consolidation is taken into account as well. The major advantage over standard 3D finite element methods is the semi-analytical approach, which reduces computational time significantly since not every load cycle needs to be modelled separately. Therefore both the stress distribution and pore pressure generation and dissipation are taken into account in 3D. The model is validated with results from the Ekofisk tank using the same storm and soil input as was used by Seed & Rahman, presented previously. Taiebat used a mesh of 150 meter wide and 50 meter deep, including the 26 meter sand and an impermeable clay layer beneath. The clay layer was used to prevent the effect of rigid boundaries on the stress distribution in the sand layer. The clay layer is impermeable and the boundary between the foundation and sand as well. For the other boundaries perfect drainage was assumed.

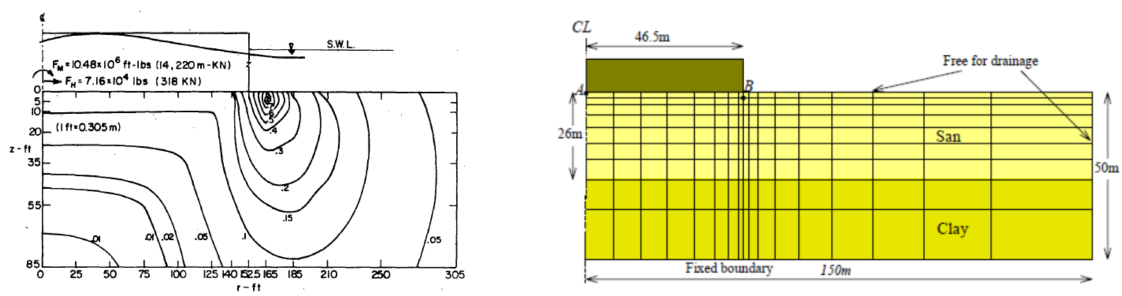

Figure 7.20: *Cyclic shear stress ratio for a wave height of 12.5 meter. Dimensions are in feet (left, Rahman and Seed (1977)) Finite Element mesh used by Taiebat (right, Taiebat (1999)). In this figure also points A and B are indicated, were the output will be presented. Point A is located at the centre below the tank, at seabed level, while point B is located below the edge of the tank foundation, 1.5 meter below seabed.*

For the case considered it should be noted that Rahman (Rahman and Seed (1977)) used the horizontal cyclic shear stresses for the generation of pore pressures, while Taiebat uses the radial cyclic shear stresses. The results presented by Rahman and by Taiebat are presented in figure 7.21. The output points at the centra and off edge are represented by points A and B respectively in figure 7.20. The output at the middle of the foundation is at the top of the sand layer, while the output off edge, at the edge of the foundation, is at 1.5 meter below seabed level. The predictions obtained by Taiebat are greater than obtained by Rahman, at the

Depth [m]	CSSR-value [-]
0	0.125
1.5	0.125
3.1	0.100
6.1	0.07
12.2	0.02
26	0.01

Table 7.7: *CSSR profile used in DCycle*

centre nearly double as high and at the edge for the largest part of the storm duration larger as well. The differences are attributed by Taiebat to the different stress distribution between models. It would however be expected that the 3D analysis results in a more stress spreading compared to the 2D situation considered by Rahman, and consequently less cyclic shear forces and less pore pressure development. The calculations of Rahman have however been based on test results of simple shear test with some preshearing, which was not taken into account by Taiebat. This might clarify the lower relative excess pore pressures found by Rahman.

The calculations have been made in DCycle as well, with the same approach as used throughout this thesis for various storm histories. The CSSR profile was derived from figure 7.20 at the centre of the foundation, presented in table 7.7. This was derived for a wave height of 12.5 meter. In the calculations each wave load will therefore be scaled with the CSSR profile corresponding to the 12.5 meter high wave. The same equivalent storm input which was used by Rahman and Taiebat has been used.

The obtained results from the DCycle calculations are shown as well in the right figure of 7.20 at seabed level below the centre of the foundation. Without preshearing a maximum relative excess pore pressure just above 0.5 is found, while with a preshear factor of X=150 a value around 0.3 is reached. The first result is higher than the value obtained by Taiebat at the centre of the foundation. However, the cyclic shear stress ratios were derived by Rahman in a 2D schematisation. In a 3D schematisation stresses are expected to spread out, resulting in lower cyclic stress ratios, and consequently lower pore pressures from the calculations by Taiebat. This therefore matches the expectations. Furthermore, the radial drainage in DCycle is implemented as a correction on the 2D drainage, which might result in a lower drainage capacity compared to the full 3D drainage by Taiebat. The calculation with preshearing shows lower values than the calculation by Taiebat, which can be explained by the fact that there was no preshearing included in the 3D model. Comparing the DCycle results with the results from Rahman, far larger relative excess pore pressures are obtained, even if preshearing is taken into account, which was also taken into account in the empirical values for the pore pressure generation model used by Rahman.

In general it can be concluded that the procedure adapted in this thesis in which every individual load cycle is scaled with a CSSR-profile produces reasonable results compared to a 3D semi-analytical constitutive model. The relative excess pore pressures are overestimated but therefore result in a conservative value. This is mainly attributed to the different stress distribution in the 3D model, resulting in larger stress spreading and lower CSSR-ratios. Also drainage might be larger in the 3D model, resulting in lower overall pore pressures.

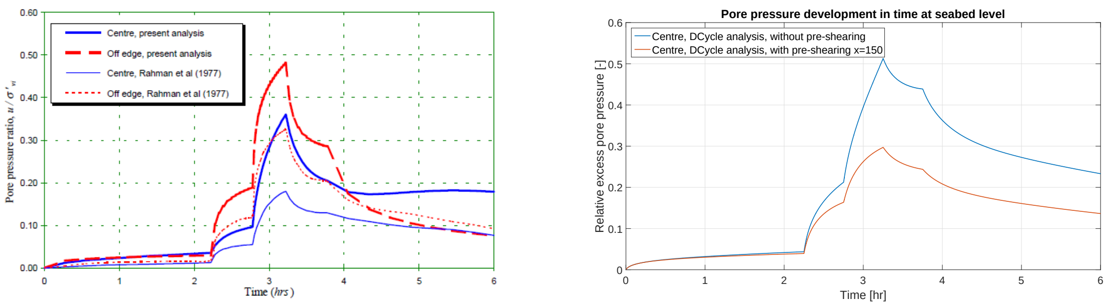

Figure 7.21: *Results of pore pressure calculations from Taiebat and Rahman (left, Taiebat (1999)) and based on DCycle calculations (right). In the left figure the legend "present analysis" refers to the results from Taiebat, and not to the results obtained in this thesis, since these are presented in the figure at the right. The results from DCycle are at the centre of the foundation and should be compared with the blue lines in the left figure. The results at centre level are in both cases at seabed level.*

7.7. Assumptions and limitations

The followed approach and the resulting excess pore pressures, are based on a set of assumptions. The conclusions drawn from this section, should therefore be read with the following limitations in mind, divided into excess pore pressures, soil behaviour and structure and loads:

Excess Pore Pressures

- The calculated excess pore pressures are based on synthetic data from the CoastDat database (Weisse et al. (2005)) at the location of Blyth, and the selected storms from this dataset. The conclusions are based on the observed storm conditions from the dataset, and may therefore vary for other locations around the world with other storm characteristics.
- The excess pore pressures have been calculated using the governing CSSR profile found just outside the edge of the GBF. The EPPs are calculated in a single vertical below the middle of the GBF, where the limited drainage should result in the largest EPP. The resulting EPP is therefore a conservative estimate, since the cyclic shear stresses in the middle below the GBF are less than just outside the edge of the GBF.
- Dissipation of pore pressures is taken into account based on a corrected 1D consolidation equation. The equation has been corrected for the radial dissipation below the GBF. Furthermore, the default values for the pore pressure generation model have been used, based on Seed and Rahman (1978).

Soil behaviour

- The CSSR profile that has been used, is based on a schematised model of the GBF, and based on a single load cycle. The assumptions and limitations from this model also hold for the results here. These mainly are the linear-elastic soil modelling to superpose the maximum and minimum loads in a single cycle, and undrained behaviour of the soil during a single cyclic load cycle. The other assumptions are listed in section 6.6 and are based on a schematised soil profile as well.
- The basic assumptions for the preshearing effect is a limited shear strain in the subsoil, as already discussed in 2.2.6. The shear strains have not been assessed in this research, but it should definitely be checked whether the strains remain limited (for instance smaller than 0.5%) and whether preshearing may actually be taken into account. Furthermore, the preshear parameter X is based on element tests by Bhatia (1982) for increasing load amplitude for instance in the build-up of a storm, after Meijers and Luger (2012). Whether this value however also applies to the specific sand profile used here, is not investigated.

Structure and loads

- All results are based on the loads from the reference geometry, with its own assumptions and limitations. Furthermore, these only hold for the water depth of 30 meter. The assumptions and limitations of the loads are listed in 5.6.
- The CSSR profile has been scaled with the amplitude of individual load cycles. It is therefore implicitly assumed that the load amplitude and cyclic shear stress ratio are related in a linear way. Due to the non-linear soil behaviour, this might however not be correct. Furthermore, this also means that the static part of the load is scaled along in a load cycle, but since the static and dynamic amplitude of the load are not necessarily linearly related, this might not be correct.

7.8. Concluding remarks

This chapter started with the outline of the general approach to calculate excess pore pressures. The results from chapters 5 and 6 have been combined in the excess pore pressure calculations, and with the final results the research question related to the load history can be answered. For various storm definitions, the excess pore pressures have been calculated. The results clearly showed that the build-up of a storm up to the highest cyclic horizontal force amplitude in the storm determines the maximum relative excess pore pressure that is reached. The speed of build-up, in kN/hr, seems to be the most important parameter for the relation between the cyclic loads and resulting pore pressure build-up, at least for the selected storms from the dataset and for the homogeneous sand profile with a relative density of 60%.

Based on the literature review, it was expected that the governing load history would consist of a series of storms. From the results in this chapter, the build-up of the first storm was found to be the governing part for the maximum excess pore pressure. A series of storms following after each other did not result in higher excess pore pressures, due to the relatively long build-up of the first storm. This results in significant densification and strengthening of the soil to further pore pressure generation. The densification results from previously generated excess pore pressures and dissipation, indicating the importance of drainage in the build-up of a storm.

The irregular load time history has a significant influence on the spread in the obtained maximum values of relative excess pore pressures. Based on 200 irregular load time histories, a 90th percentile for the relative excess pore pressure of 0.36 is obtained for homogeneous sand with a relative density of 0.60. Due to the observed build-up of pore pressures, the cyclic load amplitude at the moment of the maximum excess pore pressures, is significantly lower compared to the maximum cyclic load amplitude in the storm. The 90th percentile values are respectively 6939kN versus 13214kN. At the moment of the maximum load amplitude the relative excess pore pressure has already reduced to 0.17 for 90% of the cases. This would imply that a final stability check can be based on a lower load amplitude a the moment of the maximum pore pressures, but before this can actually be used the results should be validated. It is in general observed that no reliable estimate of the relative excess pore pressure can be obtained by considering only a single load time history.

No full liquefaction was observed for sand with a relative density of 60% and a preshear value of 150. This indicates that full liquefaction of the seabed below the reference geometry of the GBF is not likely to occur in the storm conditions considered and with the cyclic shear stresses found below the GBF. For a silt layer larger pore pressures were observed, in 90% of the cases lower than 0.62, but no full liquefaction either. A gravel bed drains the top layers very well, and is therefore an efficient manner to limit pore pressure build-up.

In the next chapter, these findings will be presented and discussed, together with recommendations for further research.

8

Conclusions, discussion and recommendations

8.1. Conclusions

After seven chapters describing the steps taken to answer the research question, in this final chapter the conclusions, discussion and recommendations will be presented. For the sake of completeness, each of the research questions as defined in chapter 1 will be repeated again before the conclusions is presented. The starting point of this chapter is the main research question.

- Main question: How to assess the liquefaction potential of a gravity based foundation for an offshore wind turbine under cyclic loads?
- Sub question 1: How to determine a cyclic shear stress profile below a gravity based foundation taking into account the load configuration and cyclic loads?
- Sub question 2: How to determine a representative load history to assess the liquefaction potential of a gravity based foundation under cyclic loads?
- Sub question 3: How should this be related to the current norms and standards?

8.1.1. Main research question

How to assess the liquefaction potential of a gravity based foundation for an offshore wind turbine under cyclic loads?

Based on the investigation of modelling cyclic loading of sands, it was found that both the irregular nature of the cyclic loads and the real build-up of a storm in the calculations of excess pore pressures should be taken into account. For most methods it is still necessary to translate the irregular loads into discretized sequences with equal amplitude, where the irregular nature and the real development of a storm are lost (Safinus et al. (2011) and Andersen (2007)).

By deriving the wind loads, wave loads and turbine loads in the frequency domain for the reference geometry of gravity based foundation (GBF) and offshore wind turbine (OWT), a large number of load histories in the time domain has been generated with a random phase-amplitude model. With this approach the irregular nature of the loads is taken into account, and using the CoastDat database (Weisse et al. (2005)) the real storm development at the reference location (Blyth, UK) has been taken into account.

Based on the reference geometry of a GBF, OWT and a cyclic shear stress profile from a linear elastic FEM-calculation in a single extreme load cycle in medium dense sand, the largest liquefaction potential was found just outside the circular base area of the GBF. In the areas around the edges of the structure, the cyclic shear stresses are still high while the initial effective stresses are significantly lower than below the GBF, resulting in the largest liquefaction potential.

Combining both the irregular load time series for various storms from the CoastDat dataset and for multiple realisations of each storm, together with the governing cyclic shear stress profile, the excess pore pressures below the reference geometry of the GBF have been assessed in DCycle. In this model the pore pressure generation as well as drainage and preshearing are taken into account. Based on the irregular load time histories, a large spread was found in the obtained maxima of relative excess pore pressures for each of the storms. Based on this it can be concluded that no reliable estimate of the maximum relative excess pore pressure can be found by considering only a single load time history.

Looking back at the problem in general, the liquefaction assessment of a gravity based foundation for an offshore wind turbine asks for an integrated approach ranging over multiple disciplines, from structural dynamics, hydrodynamics to soil mechanics. This research has shown that the topic gets complicated due to the large number of engineering fields that have to be consulted before any conclusion can be drawn. An integrated approach enables the understanding of the problem, prevents conservative designs and enables optimizations in the design.

8.1.2. Sub question 1

How to determine a cyclic shear stress profile below a gravity based foundation taking into account the load configuration and cyclic loads?

A representative cyclic shear stress profile was derived from the extreme load cycle with Plaxis. Using different definitions of the cyclic shear stress ratio (CSSR) it was found that the largest shear stress amplitude over initial effective stresses results in the governing ratios over depth. For different locations below the gravity based foundation, the largest cyclic shear stress profile was found just outside the base slab of the foundation. This is caused by the fact that below the GBF the initial effective stresses are high, while they reduce significantly outside the area below the GBF, where the shear stresses are still high. This therefore produces the highest liquefaction potential just outside the base slab of the GBF, based on the used CSSR definition.

From multiple FEM calculations it was found that the horizontal loads represent the largest contribution to the CSSR profile. The wave loads have the largest contribution in horizontal loads and therefore in CSSR ratios, while the wind loads show a large static bending moment and a relatively small cyclic horizontal component, resulting in significantly lower CSSR ratios.

8.1.3. Sub question 2

How to determine a representative load history to assess the liquefaction potential of a gravity based foundation under cyclic loads?

The answer to this sub question is divided into the *Load contributions* and the *Excess pore pressure and load history.*

Part 1: Load contributions
Wind loads contribute significantly to the spectral density of the fore-aft bending moments at seabed level, although only at low frequencies and only when the turbine is operating. A comparable part of the spectral density of bending moments is located at the natural frequency of the system of GBF and OWT. This shows the large contribution of the system dynamics to the dominant frequencies of the wind loads that are transferred to the subsoil, if the turbine is operating.

Considering the spectral development of fore-aft horizontal loads at seabed level, the spectral density around the natural frequency is nearly constant during the storm build-up. The spectral density around the wave frequency increases in the storm build-up with increasing wave height. This shows that for the horizontal loads at seabed the contribution of the system dynamics is of less influence compared to bending moments. The wave frequency plays a more significant role in the frequencies of horizontal loads at seabed level.

Part 2: Excess pore pressures and load history
Based on the selected storms from the CoastDat dataset, the generated irregular load histories and a homogeneous sand profile of 60% relative density, it was found that the maximum relative excess pore pressures are reached in the build-up of the first storm. This is due to the relatively long build-up of the storms. The

processes of drainage, densification and preshearing result in a significant increase in soil strength in the build-up of the storm, reducing further pore pressure generation.

It was observed that the maximum excess pore pressures are not reached in the largest storms from the dataset, but in the storms with the fastest build-up in cyclic shear force amplitude at seabed level per unit of time. The storm with the fastest build-up results in less time for drainage and densification, and consequently less strengthening for further pore pressure generation at the maximum storm load, compared to the largest storms with a longer build-up time. This results in the largest maxima in relative excess pore pressures for storms with the fastest build-up.

After investigating the three storms with the fastest build-up further, it was found that the maximum values of relative excess pore pressures (EPP) are on average reached before the maximum cyclic load in the storm. For the homogeneous sand profile with a relative density of 60% and preshear factor X=150, only 2% of the 200 irregular load time histories of the storm with the fastest build-up showed a maximum value after the maximum load amplitude in the storm. On average the maximum relative excess pore pressure was reached about one hour before the maximum load amplitude. 90% of the maximum relative excess pore pressures are below 0.36 for the storm with the fastest build-up, which reduces to a 90% value of 0.17 at the time of the maximum cyclic load amplitude in the storm. This results in a significant reduction of relative excess pore pressure at the moment of maximum loading in the storm.

For a lower preshear value of X=50, 15% of 200 irregular load time histories reached the maximum value in EPP after the maximum cyclic load amplitude. This might be due to the slower increase in strength for further pore pressure generation with lower preshear values. For this lower preshear value higher pore pressures are reached, with 90% below 0.51. For less permeable sand profiles, for instance with a silt layer, larger relative excess pore pressures were found with 90% below 0.62, but on average still reached about one hour before the maximum load amplitude in the storm. This shows that even for less permeable sands and for lower preshear values, the effects of drainage and densification in the development of a storm are very significant, preventing full liquefaction and resulting in a maximum relative excess pore pressure before the maximum load amplitude.

8.1.4. Sub question 3

How should this be related to the current norms and standards?

It was observed that for the homogeneous sand deposit with a relative density of 0.6 and the considered storms and resulting loads, the maximum values of relative excess pore pressures are on average reached before the maximum cyclic load amplitude in the storm. At the moment of the maximum cyclic shear load amplitude in the storm the pore pressure has already reduced significantly due to drainage. For a final analysis in which the stability is checked with the generated excess pore pressures and the cyclic load amplitude (both shear force and bending moment), this would imply either a check with the maximum value of excess pore pressure and a reduced cyclic load amplitude, or a reduced excess pore pressure with the maximum cyclic load amplitude. Any combination that is reached in the storm duration in between these two points may however also be governing the stability.

How this relates to the norms and standards cannot be completely answered yet. The probability density distributions of both maximum values of excess pore pressures and the cyclic shear load amplitudes should be combined to determine a general probability of failure. Whether failure or loss of stability occurs was not determined in this thesis, but can for instance be investigated in a finite element model. With the observations in this research, a significant reduction of either the excess pore pressure or cyclic shear load amplitude may be present due to the phase difference between pore pressure and load amplitude, resulting in a less conservative design. Before this observation can be used however, a decent validation in the laboratory or in reality is desired, which will be discussed in the recommendations.

8.2. Discussion

After the conclusions of this research, the results will be discussed and compared with the original thoughts and expectations. This will be done for respectively *The load history*, *The comparison with literature on cyclic liquefaction*, *The areas of largest liquefaction potential* and *The 1-dimensional approach.*

Load history

Based on Meijers and Luger (2012) and Meijers et al. (2014), it was expected that the load history with the maximum EPP would consist of a combination of storms in time. Although this was based on the case of a horizontal seabed loaded by waves, and in Meijers and Luger (2012) only with regular loads, the questions of the load history and the expectations remain evenly relevant. In these papers it was observed that a small storm before a large storm works beneficial for the maximum excess pore pressure in the largest storm, but if the design storm is applied at the start of the load history, full liquefaction could easily be reached. This resulted in the hypothesis that the storm sequence and the storm size within the sequence would determine the maximum excess pore pressure.

This was contradictory to the expectations: would full liquefaction really happen if the design storm occurs as the first storm during the lifetime of the structure? Or is it just the very low probability of having the design storm first in the lifetime which makes that it is never observed in reality? Although various failures have been reported, also discussed in chapter 2 of this research based on Oumeraci (1994), it was often found that full liquefaction was never reached due to excess pore pressures only. Often other reasons, such as the induced movements of the structure due to the cyclic wave loads, contributed to the pore pressure increase.

This hypothesis was based on hypothetical storms, in which the maximum cyclic loads in the storm were based on a design value (i.e. often the wave height and resulting wave load), while the actual build-up towards this maximum load was assumed to occur in one, two or a few hours. From this research this assumption seems to be the main reason why the current results show that the EPP does not depend on the storm order but on the build-up speed in the single first storm. The build-up time during the storms is that long, on average over all storms 17 hours, that many load cycles have past, in which densification, drainage and preshearing have been able to strengthen the soil against further EPP generation. This process is found to be even that important that the maximum EPP is not reached at the peak of the storm loading, but already before the peak in cyclic loads. Although datasets with real storm developments are available, as well as the tools to model soil behaviour under cyclic loads, both have never been combined with a cyclic load model of a GBF with OWT to come up with a representative load history.

The starting point in this research was a combination of multiple storms in time as well. The starting point of a storm was defined as a threshold level in terms of the amplitude of the horizontal load at seabed level. Based on Meijers (2007), the threshold of a CSSR-value of 0.08 was used based on data from laboratory experiments described in literature. With this threshold, the starting point of each storm was identified, i.e. each storm was assumed to start at this threshold level, since below the threshold no densification and no pore pressure build-up was expected to occur. However, DCycle itself does not contain such a threshold level, and due to the large number of cycles, for instance in the first hours of a storm, pore pressure was generated anyway. This showed that a threshold level in terms of cyclic shear cannot be defined in this way, probably since it was actually based on a threshold in shear strain (section 2.2.6) and due to the fact that a large number of cycles will always cause any densification, even with a load amplitude just below a specified threshold. This observation resulted in a new storm definition, based on a far lower threshold and consequently in far longer build-up times of storms, resulting in the conclusion that especially this build-up is governing the final maximum EPP.

Comparison with literature on cyclic liquefaction

The cyclic loading on a gravity based foundation may lead to the cyclic liquefaction type of failure. During cyclic loading the excess pore pressure is expected to rise, since drainage will not allow the pore pressure to flow off immediately, resulting in build-up. From literature it was also found that the residual pore pressure generation is in any case not found to be responsible for full liquefaction failure. The motions of structures in literature, often vertical caisson breakwaters, largely contribute to the excess pore pressure developments. This result was also obtained from the calculated excess pore pressures below the gravity based foundation in various storm conditions: the maxima in relative excess pore pressures for homogeneous sand with a relative density of 60% showed a 90th percentile value of 0.36. This shows that the calculation results of this study fit in the expected behaviour, i.e. the cyclic liquefaction type of failure, but without losing all effective stresses. The resulting EPP may however be overestimated or underestimated: overestimated since the governing CSSR profile was derived just outside the base area, but applied in the middle below the structure with limited drainage, and underestimated because the movements of the GBF induced by cyclic loading were however not taken into account, increasing the EPP further.

Area of largest liquefaction potential
From literature, it was known that the largest liquefaction potential can be found around the edges of the structure, for instance investigated for the Ekofisk tank (Taiebat (1999)). The hypothesis would however be to find the largest liquefaction in the centre below the structure, where drainage is limited and where the cyclic loads transferred to the subsoil are expected to be largest. This results in the largest pore pressure generation, and with the lowest drainage capacities the centre was expected to show the highest excess pore pressures. However, from the cyclic shear stress profile similar results as from literature were obtained. The clarification is found in the definition of the cyclic shear stress, which results in the largest cyclic shear stresses in areas where shear stresses are high and initial effective stresses low, to be found just outside the edges of the structure. This subsequently results in the question whether the definition is right, and whether stress rotations in the area just outside the GBF ask for another definition. In the definition of the cyclic shear stress ratio, as proposed in Boeije et al. (1993), this is in fact already taken into account when one is looking for the plane under angle α with the largest shear stress amplitude (section 6.2). The other used definitions for the CSSR profile, showed even lower ratios, indicating that the followed procedure results in a governing cyclic load of the subsoil which is found to be largest just outside the base area of the GBF.

The 1-dimensional approach
The circular GBF is loaded by storms coming from multiple directions. Therefore the assessment of cyclic loading would ask for a method which takes account of the multi-directionality of the loads and consequently multi-directionality of the soil behaviour. However, in a first assessment this is hardly possible, due to the already very complex problem in a single direction. Since the governing CSSR-profile was found in an area just outside the GBF in a single vertical, the problem seems suitable to be captured quite accurately in a single load direction. In literature often a misalignment between wind and waves of 30 °is used in a preliminary design (Seidel et al. (2016)) to take the directionality of loads into account. Assuming them aligned then results in a conservative load estimate. Therefore, in general it is expected that the resulting excess pore pressures do not differ too much compared to a multi-directional approach of the loads. It is then assumed that after each storm the EPP have fully dissipated, which was found to be reasonable from the storms in the CoastDat database. If the pore pressures are not able to fully dissipate between storms, spreading of pore pressures generated by storms from different directions has to be taken into account as well. For the settlements and especially the differential settlements, the direction of loading is highly relevant however, since the cumulative effect of densification due to drained pore pressures from storms coming from different directions, might result in uneven settlements of the GBF.

8.3. Recommendations

The recommendations resulting from this thesis work have been listed below. The starting point will be some general recommendations, subsequently followed by more detailed recommendations about the soil modelling, the load modelling and the interaction between soil and structure.

General recommendations

- In general, the research has shown that different disciplines have to be combined before anything can be concluded about cyclic loading of the subsoil below the GBF. First of all, a general load derivation from turbine and wind loads asks for a comprehensive knowledge and understanding of the operating systems of wind turbines. The dynamic behaviour of the tower structure is even more complex, and results in design practice often in a large set of time series of loads at the level of the transition piece, or for the GBF, at the level of the connection with the support structure. Subsequently, the support structure should be designed to withstand both the interface loads from the turbine, and the wave loads acting on it. For the GBF, the latter aspect is again rather complex, asking for decent knowledge of hydrodynamics. Again a structural engineer should be involved to assess the dynamic behaviour of the GBF, and the interaction with the turbine, resulting in the overall dynamic behaviour. Finally, the geotechnical engineer has to assess the stability of the structure under extreme (cyclic loads), with input from a large set of load combinations to assess the governing excess pore pressure in storm conditions. This results in the final stability assessment of the GBF, which should be coupled back to the stability and the dynamic behaviour of the overall structure. This shows that the various disciplines involved make this topic complex, and especially the feedback between various disciplines asks for the understanding of various fields of engineering. This results in the recommendation to integrate the fields of struc-

tural, hydraulic and geotechnical engineering in design practice, to prevent conservative designs and to encourage overall optimizations of the structure as a whole.
- Next to this, the model results of pore pressures should be validated with laboratory tests, either element tests or centrifuge tests, to see whether the predicted pore pressures are also found in the laboratory. This asks for a test which implements continuous drainage and in which also the cyclic load build-up based on a storm can be followed. This can be used to see whether the maximum pore pressures are also reached before the maximum cyclic load amplitude. Furthermore, field measurements should provide another way to validate the model results. This can be performed with pore pressure sensors installed below foundations, but also asks for a detailed record of the storm history of wave heights, period and wind speed. Both the element tests and measurements from reality should enable a validation of the model results.
- In addition to a validation, a probabilistic approach is recommended to relate the probability density functions of maximum values of excess pore pressures with the probability density function of the cyclic load amplitudes, in combination with a stability assessment in which combinations of excess pore pressures and load amplitudes are related to a failure probability. This failure probability can be linked to a probability of failure described in norms and standards. Some complexities are already identified, such as the out-of-phase character of the pore pressures and the maximum load amplitude, and the distribution of pore pressures over depth, which is not taken into account when only a single (maximum) value over the vertical is considered.

Furthermore, some detailed recommendations are listed about the soil modelling, the load modelling and the interaction between soil and structure.

Soil modelling:

- The CSSR profile has been scaled linearly with the amplitude of each individual load cycle. The soil response however is not expected to behave in a linear way in each load cycle, since the soil stiffness changes during cyclic loading and during pore pressure generation. This in turn changes the stress distributions in the subsoil in terms of shear stresses and vertical stresses. However, this also asks for a coupling with the pore pressure developments and soil stiffness over time, leading to the next recommendation. The approach of the implicit and explicit steps in the pore pressure response could be the easiest way, though still complex, to reach this higher level of modelling. Another approach would be to implement the pore pressure generation model in a FEM-package, to ensure an easier to use model.
- The excess pore pressures are calculated in 1D, in a single vertical with a corrected consolidation equation for radial dissipation. For a detailed analysis a 2D or 3D model is desired to capture the distribution of excess pore pressures around and below the GBF better. Also the 3D drainage can then be taken into account without a correction on a 1D drainage term.
- The CSSR profile was obtained in a single undrained load cycle. This might be correct for deeper layers, but the top layers might even drain during a single load cycle. For a more realistic approach this could be taken into account with a drained top layer. Also the effect of layered soils on the pore pressure response should be investigated to approach reality better.

Load modelling:

- No directionality of the loads has been taken into account, i.e. only loading in the fore-aft direction is considered. During single storms in which the main focus is on excess pore pressures, this might still be an realistic and accurate approximation. For settlements on the other hand, the directionality might result in differential settlements due to various densification rates resulting from various directions of loading. This is especially relevant for the OWT, where the differential settlements should be limited for the operability of the turbine. The directionality can be taken into account in a more detailed study of the effects of cyclic loading.
- The dynamic behaviour the OWT (including GBF) was schematised into 1 and 2 mass-spring-dashpot systems. Although the first natural frequency was found to be mainly determined by the tower characteristics, and therefore expected to be represented quite well with the proposed mass-spring-dashpot systems, a more accurate prediction based on distributed masses is desired. Also the soil stiffness and the interaction with the GBF is modelled in a very simplistic way, not including any effects of changing soil stiffness during cyclic loading. The cyclic loading results in a time dependent stiffness and consequently a time dependent natural frequency. This should also be taken into account for a better prediction of the natural frequency, which is relevant due to the fact that it is found to be close to the

excitation frequencies of the loads.

- The wind loads on the turbine have been modelled with a thrust coefficient, which is frequency independent and does not incorporate any turbine operating system. In a detailed analysis the dynamic response of the turbine blades needs to be incorporated, for instance in a blade element model (BEM). This however asks for detailed information about the turbine operating system, which is often not available in a research project.
- The dynamic behaviour of the OWT has been taken into account with a single factor, the DAF. The reducing stiffness due to cyclic loading close to the natural frequency, which is the case for the GBF due to the loads from wind and wave being close to the natural frequency, has not been taken into account. In a detailed analysis this effect should be taken into account.
- The wave loads are based on linear wave theory. It was already found that for regular waves with certain characteristics of wave height and period in the water depth of 30 meter, higher order Stoke's theories should be applied. Furthermore, many effects such as the phase difference in maximum loads on base, cone and pile are not taken into account. Also the wave run-up and breaking wave loads are not taken into account. Although these extreme load cycles are not expected to influence the excess pore pressures too much, a more accurate prediction of wave loads is important due to their large contribution in horizontal loads at seabed.

Soil and structure

- In the current analysis the soil-structure interaction is not taken into account. From literature it is known however that the structural motions are responsible for a significant part of the pore pressure response. This was also found in the large scale model test of a wave loaded caisson by Kudella et al. (2006), where especially the bending moments (resulting in vertical loads) showed a clear correlation with the pore pressure build-up. Also the rocking (rotational) and sway (horizontal) motion might result in a significant build-up. Although very complex, it is recommended to investigate the motions of the structure and resulting pore pressure response further.
- Currently no vertical loads have been taken into account. Especially the wave loads induce a cyclic vertical component due to a change in water level and a resulting change in buoyancy force. Also the wind turbine will induce (1P) vertical loads. The effect of the vertical loads should be further investigated to see the relative contribution to the final excess pore pressure response.

Bibliography

Andersen, K. (2007). Bearing capacity under cyclic loading - offshore, along the coast, and on land. the 21st bjerrum lecture presented in oslo, 23 november 2007. *Canadian Geotechnical Journal*, Vol. 46:pp. 513–535.

Arany, L., Bhattacharya, S., Macdonald, J., and John Hogan, S. (2014). Simplified critical mudline bending moment spectra of offshore wind turbine support structures. *Wind Energy*, Vol. 18:pp. 2171–2197.

Arthur, J., Dunstan, T., Al-Ani, Q., and Assadi, A. (1977). Plastic deformation and failure in granular media. *Géotechnique*, Vol. 27(Nr. 1):pp. 53–74.

Been, K., Jefferies, M., and Hachey, J. (1991). The critical state of sands. *Géotechnique*, Vol. 41(No. 3):pp. 365–381.

Bhatia, S. (1982). *The Verification Of Relationships For Effective Stress Method To Evaluate Liquefaction Potential Of Saturated Sands*. PhD thesis, University Of British Columbia.

Bianchi, F., Battista, H., and Mantz, R. (2007). *Wind Turbine Control Systems. Principles, Modelling and Gain Schedulling Design. Advances in Industrial Control*. Springer.

Bjerrum, L. (1973). Geotechnical problems involved in foundations of structures in the north sea. *Geotechnique*, Vol. 23(No. 3):pp. 319–358.

Boeije, R., De Groot, M., and Meijers, P. (1993). Pore pressure generation and drainage underneath gravity structures. *International Offshore and Polar Engineering Conference*.

Christian, J., Taylor, P., Yen, J., and Erali, D. (1974). Large diameter underwater pipeline for nuclear plant designed against soil liquefaction. *Offshore Technology Conference*.

Clausen, J., Dibiagio, E., Duncan, J., and Andersen, K. (1975). Observed behaviour of the ekofisk oil storage tank foundation. In *Proc. 7th Offshore Technology Conference*, volume Vol. 3, pages 399–413, Houston.

De Groot, M., Bolton, M., Foray, P., Meijers, P., Palmer, A., Sandven, R., Sawicki, A., and Teh, T. (2006a). Physics of liquefaction phenomena around marine structures. *Journal of Waterway Port, Coastal, and Ocean Engineering*, Vol. 132(No. 4):pp. 227–243.

De Groot, M., Kudella, M., Meijers, P., and Oumeraci, H. (2006b). Liquefaction phenomena underneath marine gravity structures subjected to wave loads. *Journal of Waterway Port, Coastal, and Ocean Engineering*, Vol. 132(No. 4):pp. 325–335.

De Groot, M. and Meijers, P. (2004). Wave induced liquefaction underneath gravity structures. *Proceedings of the International Conference Bochum*, pages 399–406.

De Vries, W. (2010). Support structure concepts for deep water sites. Technical report, Delft University of Technology.

DNV (1992). Foundations, classification notes, no 30.4. Technical report, Det Norske Veritas.

DNV (2014). Design of offshore wind turbine structures (dnv-os-j101). Technical report, Det Norske Veritas.

DTI (2001). Monitoring & evaluation of blyth offshore wind farm. Technical report, Department of Trade and Industry (DTI).

European Commission (2010). Energy 2020: A strategy for competitive, sustainable and secure energy. Technical report, European Union.

European Commission (2011). Energy roadmap 2050. Technical report, European Union.

European Commission (2014). A policy framework for climate and energy in the period from 2020 up to 2030. Technical report, European Union.

EWEA (2016). The european offshore wind industry - key trends and statistics 2015. Technical report, EWEA.

Faccioli, E. (1973). A stochastic model for predicting seismic failure in a soil deposit. *Earthquake engineering and structural dynamics*, Vol. 1:pp. 293–307.

Finn, W., Siddharthan, R., and Martin, G. (1983). Response of seafloor to ocean waves. *Journal of Geotechnical Engineering*, vol.109(no. 4):pp.556–572.

Frohboese, P. and Schmuck, C. (2010). Thrust coefficients used for estimation of wake effects for fatigue load calculation. *European Wind Energy Conference*.

Hasselmann, K., Barnett, T., and Bouws, E. (1973). Measurements of wind wave growth and swell decay during the joint north sea wave project (jonswap). *Deutsche Hydrographische Zeitschrift*.

Holthuijsen, L. (2007). *Waves in Oceanic and Coastal waters*. Cambridge.

Huang, B., Liu, J., Lin, P., and Ling, D. (2014). Uplifting behavior of shallow buried pipe in liquefiable soil by dynamic centrifuge test. *The Scientific World Journal*.

IEC (2014). *NEN-EN-IEC 61400-2, Wind turbines - Part 2: Small wind turbines*.

Irvine, J. (2011). Blyth offshore demonstration project - appendix 3: Site selection, site design and alternatives considered. Technical report, National Energy Renewable Centre (NAREC).

ISO 19901-4 (2000). Petroleum and natural gas indistries - offshore structures - part 4: Geotechnical and foundation design considerations. Technical report, International Standardisation Organisation.

Jaspers Faijer, M. (2014). Underwater noise caused by pile driving impacts on marine mammals, regulations and offshore wind developments. Technical report, Pondera Consult.

Jonkman, J., Butterfield, S., Musial, W., and Scott, G. (2009). Definition of a 5-mw reference wind turbine for offshore system development. Technical report, National Renewable Energy Laboratory (NREL).

Jostad, H. and Page, A. (2014). Udcam and pdcam, soil models accounting for cyclic degradation. *ISSMGE Bulletin*.

Kudella, M., Oumeraci, H., De Groot, M., and Meijers, P. (2006). Large-scale experiments on pore pressure generation underneath a caisson breakwater. *Journal of Waterway Port, Coastal, and Ocean Engineering*, Vol. 132(No. 4):pp. 310–324.

Lee, K. and Focht, J. (1975). Liquefaction potential at ekofisk tank in the north sea. *Journal of the Geotechnical Engineering Division*, Vol. 101(No.):pp. 1–18.

Lupea, C. (2013). Long term effects of cyclic loading on suction caisson foundations. Master's thesis, Delft University of Technology.

Martin, P. (1975). *Nonlinear methods for dynamic analysis of ground reponse*. PhD thesis, University of California.

Meijers, P. (2007). *Settlement during vibratory sheet piling*. PhD thesis, Delft University of Technology.

Meijers, P. and Luger, D. (2012). On the modelling of wave-induced liquefaction, taking into account the effect of preshearing. *Proceedings of Twenty-second (2012) International Offshore and Polar Engineering conference*, Vol. 2:pp. 739–745.

Meijers, P., Raaijmakers, T., and Luger, D. (2014). The effect of a random wave field on wave induced pore pressure generation. *Proceedings of the Twenty-fourth (2014) International Ocean and Polar Engineering Conference*, pages 668–675.

Morison, J., O'Brien, M., Johnson, J., and Schaaf, S. (1950). The force exerted by surface waves on piles. *Petroleum Transactions*.

Oda, M., Kawamoto, K., Suzuki, K., Fujimori, H., and Sato, M. (2001). Microstructural interpretation on reliquefaction of saturated granular soils under cyclic loading. *Journal of Geotechnical and Geoenvironmental Engineering*, pages 416–423.

Oumeraci, H. (1994). Review and analysis of vertical breakwater failures. *Coastal Engineering*, 22:3–29.

Oumeraci, H., Allsop, N., De Groot, M., Crouch, R., and Vrijling, J. (1999). Mast iii/ probabilistic design tools for vertical breakwaters (proverbs). Technical report, European Union.

Pederstad, H., Kort, D., and Nowacki, F. (2015). Some key aspects in geotechnical design of gbs foundations on sand. In *Frontiers in Offshore Geotechnics III*.

Poulos, H. and Davis, E. (1974). *Elastic solutions for soil and rock mechanics*. Geotechnical Research Centra, University of Sydney.

Putnam, J. (1949). Loss of wave energy due to percolation in a permeable sea bottom. *Transactions, American Geophysical Union*, Vol. 30(No. 3):pp. 349–356.

Raaijmakers, T. (2005). Submarine slope development of dredged trenches and channels. Master's thesis, Delft University of Technology.

Rahman, M. and Jaber, W. (1986). A simplified drained analysis for wave induce liquefaction in ocean floor sands. *Soils and Foundations*, Vol. 26(No. 3):pp. 57–68.

Rahman, M. and Seed, H. (1977). Pore pressure development under offshore gravity structures. *Journal of geotechnical engineering*, Vol. 103(No. 12):pp. 1419–1436.

Robertson, P. (1994). Suggested terminology for liquefaction. *Proceedings of the 47th Canadian Geotechnical Conference*, 1(pp. 277–286.).

Robertson, P. (2010). Evaluation of flow liquefaction and liquefied strength using the cone penetration test. *Journal of geotechnical and geoenvironmental engineering*, pages 842–853.

Robertson, P. e. a. (2000). The canlex project: summary and conclusions. *Canadian Geotechnical Journal*, Vol. 37:pp. 563–591.

Safinus, S., Sedlacek, G., and Hartwig, G. (2011). Cyclic response of granular subsoil under a gravity base foundation for offshore wind turbines. *Proceedings of the International Conference on Offshore Mechanics and Arctic Engineering*, Vol. 7:pp. 875–882.

Seed, H. and Booker, J. (1976). Stabilization of potentially liquefiable sand deposits using gravel drain systems. Technical report, Earthquake engineering research centre.

Seed, H. and Rahman, M. (1978). Wave-induced pore pressure in relation to ocean floor stability of cohesionless soils. *Marine Geotechnology*, Vol. 3(No. 2):pp. 123–150.

Seed, H. e. a. (1975). Representation of irregular stress time histories by equivalent uniform stress series in liquefaction analysis. Technical report, Earthquake Engineering Research Centre.

Seidel, M., Voormeeren, S., and Van der Steen, J. (2016). State-of-the-art design processes for offshore wind turbine support structures. *Stahlbau*, Vol. 85(No. 9):pp. 583–590.

Smaling, H. (2014). Hydrodynamic loading on the shaft of a gravity based offshore wind turbine. Master's thesis, Delft University of Technology.

Smits, F., Andersen, K., and Gudehus, G. (The Netherlands, 1978). Pore pressure generation. *Proceedings of the Int. Symposium on Soil Mechanics Research and Foundation Design for the Oosterschelde Storm Surge Barrier*.

Song, E. (1990). *Elasto-Plastic Consolidation under steady and cyclic Loads*. PhD thesis, Delft University of Technology.

Taiebat, H. (1999). *Three dimensional liquefaction analysis of offshore foundations*. PhD thesis, The University of Sydney.

Uslu, A. e. a. (2009). Europe's onshore and offshore wind energy potential. Technical report, European Environmental Agency.

van der Hoven, I. (1957). Power spectrum of horizontal wind speed in the frequency range from 0.0007 to 900 cycles per hour. *Journal of Meteorology*.

Van der Tempel, J. (2006). *Design of Support Structures for Offshore Wind Turbines*. PhD thesis, Delft University of Technology.

Verruijt, A. (2012). *Soil Mechanics*. Delft University of Technology.

Vestas Wind Systems (2012). Vestas v164 8.0 mw. Technical report, Vestas Wind Systems A/S.

Vugts, J. and Harland, L. (1996). Analytical expression for the first natural frequency of a stepped tower. Delft University of Technology.

Weisse, R., Von Storch, H., and Feser, F. (2005). Northeast atlantic and north sea storminess as simulated by a regional climate model during 1958-2001 and comparison with observations. *Journal of Climate*, Vol. 18:pp. 465–479.

Yamamoto, T., Koning, H., Sellmeijer, H., and Van Hijum, E. (1978). On the response of a poro-elastic bed to water waves. *Journal of Fluid Mechanics*, Vol. 87:pp. 193–206.

Youd, T., Idriss, I., and Andrus, R. (2001). Liquefaction resistance of soils: Summary report from the 1996 nceer and 1998 nceer/nsf workshops on evaluation of liquefaction resistance of soils. *Journal of Geotechnical and Geoenvironmental Engineering*, Vol. 127(No. 10):pp. 817–833.

Zaaijer, M. (2005). Design methods for offshore wind turbines at exposed sites (owtes). Technical report, Delft University of Technology.

Zaaijer, M. (2007-2008). Introduction to wind energy, relevant to offshore wind farm design. Technical report, DUWIND TU Delft.

A

Appendix A: Multiple storms

A.1. Multiple storms

The results in chapter 7 were all based on time series of single storms, no series of multiple storms were considered. In this appendix a combination of two storms with various preshear parameters will be investigated, to see whether or not a second storm might result in a higher relative EPP compared to the first storm. The soil properties that are used are presented in table A.1.

bottom [m]	RD [-]	n_{min} [-]	n_{max} [-]	γ_{wet} $[kN/m^3]$	c_v $[m^2/s]$	k [m/s]	a [-]	b [-]	θ [-]
30	0.7	0.33	0.45	20	0.5	1E-04	0.48	0.2	0.7

Table A.1: *Soil conditions for DCycle, for a homogeneous sand layer of 30 meter deep. No soil improvements such as a gravel bed are implemented.*

The relative density at the end of the first storm will be the main parameter which represents the influence of the first storm on the excess pore pressure development in the second storm. The most critical situation would therefore be to have first the storm creating the lowest relative density at the end of the storm, and second the storm with the maximum EPP build-up. Furthermore, a very important but complex parameter is the preshear factor X. A low value will result in larger EPP in the first storm, but large densification after drainage, and in the second storm the maximum EPP is hard to predict: the densification from the first storm acts as an decrease in pore pressure build-up, while the low value of preshearing acts as an increase in pore pressure build-up. A high value for preshearing results in less densification after the first storm, but would result in a lower maximum EPP in the second storm due to the large preshearing, and a higher EPP due to the lower densification. This explanation shows that it is hard to predict which of the processes is governing the final result in maximum EPP, and therefore a set of calculations is made for various cases.

The considered values for the preshear parameter are again 50, 150 and 500, the same as used for the previous sensitivity study. For each of these values the storm with the lowest final density at the end of the storm is obtained using again the defined lower threshold of 1250kN and upper threshold level of 2500kN. The relative density shows a very small spread due to the irregular nature of the loads. Although the development of the densification during the first storm shows small differences, at the end the same relative density is reached. This might be due to the fact that not the maximum value of the excess pore pressure determines the increase in relative density, but the total amount of pore pressure which dissipates. The total amount is less sensitive to the irregular nature of the loads and this might result in the same relative densities at the end of the first storm.

The development of the relative density during the storm is shown in figure A.1. For each of the preshear values, a different storm results in the lowest densification at the end, which can also be seen on the development of relative density over time. Due to the varying duration of the storms the lines do not end at the same moment in time.

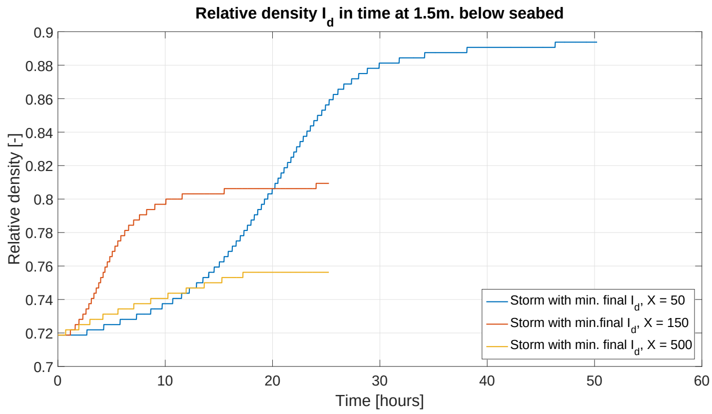

Figure A.1: *Development of relative density in time for three storms creating the lowest relative density at the end of the storm, for multiple preshear parameters. Development over time is plotted for the duration of each of the storms, at a depth of 1.5 meter below seabed.*

After the resulting storms with the minimum relative density at the end of the first storm, the storm producing the maximum EPP in a first storm is applied as a second storm. The latter storm is the storm with the fastest build-up, which was found to produce the largest excess pore pressures when it is the first storm in the lifetime of the GBF. As an example, the resulting pore pressures over time is shown in figure A.2 for a single randomly generated time serie of the storm combination. Both storms can clearly be seen in the time record. It is now desirable to obtain probability distributions of the maximum excess pore pressures for the three storm combinations in each of the two storms within the combination, to see whether or not a second storm can produce a higher excess pore pressure.

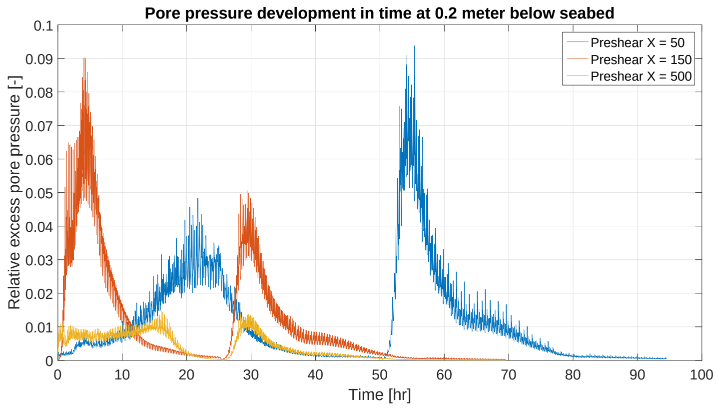

Figure A.2: *Maximum EPP in first and second storm, for multiple values of preshear parameter X. Results based on a single irregular time series.*

The obtained distributions of maximum excess pore pressures for preshear values of 50, 150 and 500 respectively, are shown in figures A.3, A.4 and A.5. The distributions of maximum values in the first storm (top figure) and the maximum values in the second storm (bottom figure) are both plotted. The distributions are based on 100 irregular load time histories for each of the preshear values.

The results show that for all preshear values the 90% value of the maximum EPP in the second storm is located below the 90% value of the maximum EPP in the first storm. It is however still possible that for a certain irregular load time serie the maximum EPP in the second storm is higher than in the first storm. For each of the preshear values 100 load time histories were generated, and from these results is was found that for the preshear value of X=50 only 12% of the load histories show a larger maximum EPP in the second storm than in the first storm. For the preshear value of X=150 this was 4% and for the preshear value of 500 this was 5%.

Based on these results, for the low preshear value X=50 it is concluded that in a worst case combination of two storms a second storm might still produce a higher EPP. This is only the case when the first storm produces the lowest relative density from all the considered storms, and when the second storm is the storm with the fastest build-up. For this combination still only 12% of the investigated cases show a larger maximum EPP in

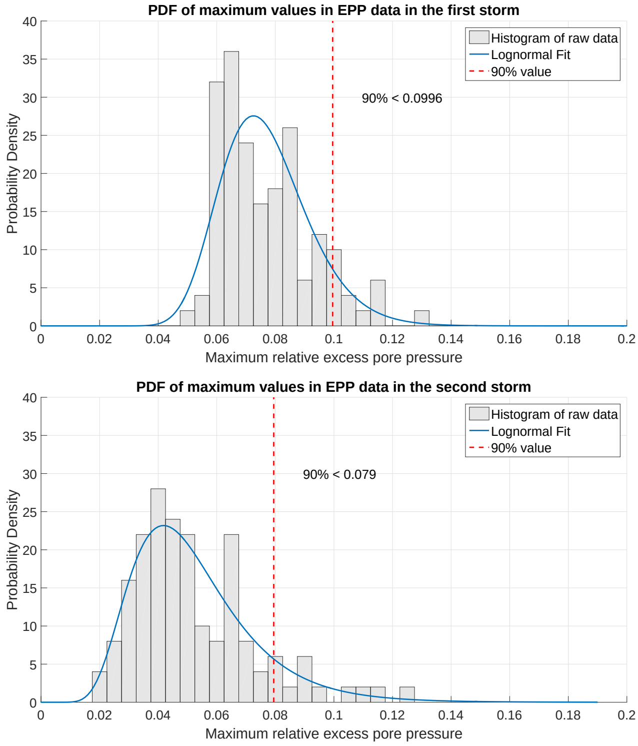

Figure A.3: *90% value and best fit to data of maximum values of relative excess pore pressures for preshear value of X=50, in the first storm (top) and in the second storm (bottom). Based on 100 generated irregular load time histories.*

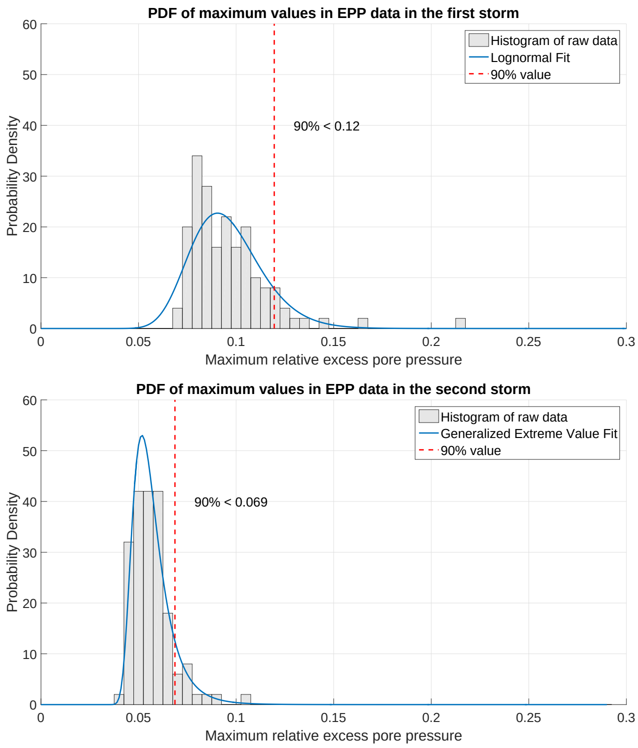

Figure A.4: *90% value and best fit to data of maximum values of relative excess pore pressures for preshear value of X=150, in the first storm (top) and in the second storm (bottom). Based on 100 generated irregular load time histories.*

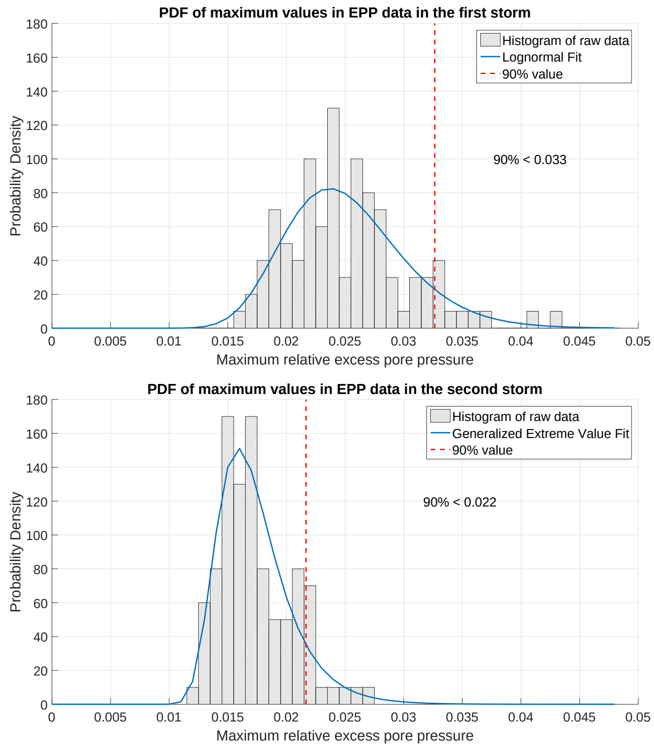

Figure A.5: *90% value and best fit to data of maximum values of relative excess pore pressures for preshear value of X=500, in the first storm (top) and in the second storm (bottom). Based on 100 generated irregular load time histories.*

the second storm, and the increase in relative EPP is on average 0.02.

It is concluded that a combination of storms does not result in a significant increase in maximum excess pore pressure in a second storm. Only for relatively low preshear values (X=50), the second storm might produce a higher value (12% of the cases), but only in the worst case (i.e. first the storm with smallest densification at the end, and subsequently the storm with the fastest build-up) and without a significant increase in maximum EPP. For higher preshear values less cases show an increase in maximum EPP in the second storm. Since the soil strengthening will continue due to drainage and densification in between the storms, more storms after the second storm are not expected to result in higher maximum EPP values. For the previously used preshear parameter X=150, the worst case combination of storms shows that only 4% reaches a higher maximum EPP in the second storm. It is therefore considered to be acceptable to take only the first storm into account to investigate maximum values of relative EPP for this preshear value, at least for the homogeneous sand deposit and the storms from the CoastDat dataset.

The obtained results are based on homogeneous sand with a relative density of 0.7 and with the storms from the CoastDat dataset. Only the effect of the preshear parameter has been investigated. The permeability and consolidation coefficient might also affect the results, but this was not further investigated.

B

Appendix B: Model of Seed & Rahman

B.1. Model of Seed & Rahman

In this section the derivation of the pore pressure generation model of Seed & Rahman will be presented. Since this model is also implemented in DCycle, which has been used in the previous calculations, it is important to know the basic assumptions and limitations of the model. The focus is on the derivation of the pore pressure generation term A, as already presented in equation 3.7.

The pore pressure generation model developed by Seed and Rahman (Seed and Rahman (1978) and Rahman and Seed (1977)) is based on the flow of water by Darcy's law. Based on continuity in vertical and radial direction the pore pressure response is derived. The basic equation to start with is equation B.1, based on Darcy and on elastic behaviour and only taking the radial and vertical direction into account.

$$\frac{\partial}{r\partial r}\left(r\frac{k_r}{\gamma_w}\frac{\partial u}{\partial r}\right)+\frac{\partial}{\partial z}\left(\frac{k_z}{\gamma_w}\frac{\partial u}{\partial z}\right)=\frac{\partial \epsilon_{vol}}{\partial t} \tag{B.1}$$

With:

u	= excess pore pressure [kPa]
k_z, k_r	= vertical and radial hydraulic permeability [m/s]
γ_w	= volumetric weight pore water [kPa]
ϵ_{vol}	= volumetric strain [-]

The volumetric strain rate will now be linked to the pore pressure generation. The starting point of the derivation is a pore pressure change Δu in time instant Δt in an elemental soil volume. This soil volume is loaded cyclically and a pore pressure increase resulting from the pore pressure generation term A [kPa/s] takes place in time instant Δt equal to $A\Delta t$ [kPa]. Therefore, the dissipated volume of pore water is equal to the difference between the generated pore pressure and the change in pore pressure $A\Delta t - \Delta u$. The amount of dissipated pore pressure results in a change in soil volume due to a rearrangement of the grains. The underlying assumptions in this derivation is therefore that no pore pressure is expected to flow into the soil sample, and therefore the derivation is only applicable to undrained conditions.

The volume change is now caused only by a change in deviator effective stress level, $\Delta\sigma_d^{'}$, in equation B.2. Using the stress strain relationship, this can be rewritten into equation B.3 and B.4 with m_v the coefficient of volume compressibility. This will be used to determine the expression for the pore pressure generation coefficient A.

$$\Delta\sigma_d^{'} = -(A\Delta t - \Delta u) \tag{B.2}$$

$$\Delta\epsilon_{vol} = m_v(\Delta u - A\Delta t) \tag{B.3}$$

$$\frac{\Delta\epsilon_{vol}}{\Delta t} = m_v(\frac{\Delta u}{\Delta t} - A) \tag{B.4}$$

If $\Delta t \rightarrow 0$ this results in equation B.5:

$$\frac{\partial\epsilon_{vol}}{\partial t} = m_v(\frac{\partial u}{\partial t} - A) \tag{B.5}$$

The pore pressure generation A can be rewritten into equation B.6, based on Seed and Booker (1976). In this equation u_g represents the generated pore pressure and N the number of cycles.

$$A = \frac{\partial u_g}{\partial t} = \frac{\partial u_g}{\partial N}\frac{\partial N}{\partial t} \tag{B.6}$$

The pore pressure per cycle is based on the pore pressure generation measured in undrained tests, equation B.7. This formula is based on fitted data for a large set of cyclic simple shear tests (Seed (1975)). It is known to depend on various factors such as relative density and stress conditions. A general constitutive relation to take this into account is however not yet available, and therefore often the value for θ of 0.7 as proposed by Seed, based on his laboratory results, is used to give approximate results.

$$\frac{u_g}{\sigma'_{v0}} = \frac{2}{\pi}\arcsin\left(\frac{N}{N_{liq}}\right)^{\frac{1}{2\theta}} \tag{B.7}$$

Differentiating this equation to N and expressing the cycle ratio in the pore pressure ratio results the desired pore pressure generation term A in equation B.9. The derivate of the number of cycles to time is defined by the load input.

$$\frac{\partial u_g}{\partial N} = \frac{\sigma'_{v0}}{\theta\pi N_{liq}}\frac{1}{\sin^{(2\theta-1)}(\frac{\pi}{2}r_u)\cos\left(\frac{\pi}{2}r_u\right)} \tag{B.8}$$

$$A = \frac{\partial u_g}{\partial t} = \frac{\sigma'_{v0}}{\theta\pi N_{liq}}\frac{1}{\sin^{(2\theta-1)}(\frac{\pi}{2}r_u)\cos\left(\frac{\pi}{2}r_u\right)}\frac{\partial N}{\partial t} \tag{B.9}$$

Finally only the number of cycles to full liquefaction, N_{liq}, has to be determined in equation B.9. This is based on the work of Rahman (Rahman and Jaber (1986)). By fitting a curve through measured data from cyclic simple shear tests, a relation was obtained between the cyclic shear stress ratio, the relative density and the number of cycles to liquefaction, as already presented in equation 2.3, presented again in equation B.10. Values of a and b were determined by Faccioli (Faccioli (1973)): $a = 0.48$ and $b = 0.2$.

$$\frac{\Delta\tau/\sigma'_{vo}}{I_d} = aN_{liq}^{-b} \tag{B.10}$$